CONFIDENTIAL

Copy 74

RM A53G08

NACA

RESEARCH MEMORANDUM

A METHOD FOR CALCULATING THE LIFT AND CENTER OF PRESSURE OF WING-BODY-TAIL COMBINATIONS AT SUBSONIC, TRANSONIC, AND SUPERSONIC SPEEDS

By Jack N. Nielsen, George E. Kaattari,
and Robert F. Anastasio

Ames Aeronautical Laboratory
Moffett Field, Calif.

NATIONAL ADVISORY COMMITTEE
FOR AERONAUTICS

WASHINGTON

November 12, 1953

CONFIDENTIAL

NATIONAL ADVISORY COMMITTEE FOR AERONAUTICS

RESEARCH MEMORANDUM

A METHOD FOR CALCULATING THE LIFT AND CENTER OF PRESSURE OF WING-BODY-TAIL COMBINATIONS AT SUBSONIC, TRANSONIC, AND SUPERSONIC SPEEDS

By Jack N. Nielsen, George E. Kaattari, and Robert F. Anastasio

SUMMARY

A method is presented for calculating the lift and pitching-moment characteristics of circular cylindrical bodies in combination with triangular, rectangular, or trapezoidal wings or tails through the subsonic, transonic, and supersonic speed ranges. The method covers unbanked wings, sweptback leading edges or sweptforward trailing edges, low angles of attack, and the effects of wing and tail incidence. The wing-body interference is handled by the method presented in NACA RM's A51J04 and A52B06, and the wing-tail interference is treated by assuming one completely rolled-up vortex per wing panel and evaluating the tail load by strip theory. A computing table and set of design charts are presented which reduce the calculations to routine operations. Comparison is made between the estimated and experimental characteristics for a large number of wing-body and wing-body-tail combinations. Generally speaking, the lifts were estimated to within ±10 percent and the centers of pressure were estimated to within ±0.02 of the body length. The effect of wing deflection on wing-tail interference at supersonic speeds was not correctly predicted for triangular wings with supersonic leading edges.

INTRODUCTION

In recent years the problems of the interference among the components of airplanes or missiles have received much attention because of their great importance in high-speed aircraft design. This increased importance is due to the current design trends toward larger fuselage radii and tail spans relative to the wing span. With regard to wing-body interference, one of the notable methods for its determination at

subsonic speeds is that of Lennertz, reference 1; recent data supporting the work of Lennertz are presented in references 2 and 3. Laborious methods are available (refs. 4, 5, and 6) for computing the interference load distributions of wing-body (or tail-body) combinations at supersonic speeds, and simple engineering methods are available for estimating the effects of wing-body interference on lift and pitching moment at these speeds (refs. 7, 8, and 9). With regard to wing-tail interference, one of the notable methods for its calculation in subsonic aircraft design is that of Silverstein and Katzoff in references 10 and 11. For supersonic speeds, Morikawa (ref. 12) has examined the four limiting cases of zero and infinite aspect ratio for wing and tail and has found that the loss of lift due to interference can be as large as the lift of the wing itself for equal wing and tail spans. Using slender-body theory, Lomax and Byrd (ref. 13) have analyzed the wing-tail interference of a family of combinations having swept wings. Several authors have studied problems of the nonuniform downwash field behind wings in combination with a body at supersonic speeds; Lagerstrom and Graham (ref. 14) present solutions for certain vortex models representing the downwash field. Spahr and Dickey (ref. 15) have compared experimental measurements of downwash with the theoretical values and have found that the assumption of one fully rolled-up vortex per wing panel provides a good prediction for low-aspect-ratio triangular wings at small angles of attack. However, for large aspect ratios or high angles of attack more than one vortex per wing panel is needed to provide agreement between theory and experiment. With regard to the problem of determining the tail loads due to the nonuniform downwash field, Lagerstrom and Graham (ref. 14) advocate the use of strip theory. Alden and Schindel (ref. 16) have developed a method based on linear theory for determining the tail load in certain cases. With regard to over-all lift and moment for wing-body-tail combinations, Grigsby (ref. 17), Edwards (ref. 18), Edelman (ref. 19), and Rainey (ref. 20) have compared experiment and theory on the basis of one fully rolled-up vortex per wing panel and have usually obtained good agreement for the specific configurations they have analyzed.

The present report can be considered an extension of references 7, 8, and 9 to include subsonic speeds and wing-body-tail combinations. Its purpose is threefold: first, to present a unified procedure for calculating interference effects and to examine the assumptions underlying the procedure; second, to compare the predictions of the method with experiment to estimate the accuracy of the predictions and the range of application; and third, to make suggestions for future research to improve the accuracy and increase the scope of the method.

SYMBOLS

A_T	tail-alone[1] aspect ratio
A_W	wing-alone[1] aspect ratio
c_r	chord at wing-body juncture or tail-body juncture, in.
c_t	tip chord of tail or wing, in.
C_L	lift coefficient based on wing-alone area
C_{L_α}	lift-curve slope, per deg (unless otherwise specified)
$\left(C_{L_\alpha}\right)_T$	lift-curve slope of tail based on tail-alone area
C_m	pitching-moment coefficient based on wing-alone area
f_T	wing vortex semispan at tail position, in.
f_W	wing vortex semispan at wing trailing edge, in.
f_∞	wing vortex semispan for large downstream distances, in.
$F(\eta)$	Alden-Schindel influence coefficient at spanwise distance η
g_T	image vortex semispan at tail position, in.
g_W	image vortex semispan at wing position, in.
h_T	height of wing vortex above body axis at tail center of pressure, in.
i	tail interference factor
k	ratio of lift component to lift of wing alone or tail alone for variable wing or tail incidence
K	ratio of lift component to lift of wing alone or tail alone for variable angle of attack
K_N	ratio of lift of body nose to lift of wing alone

[1]The wing alone or tail alone is defined to be the exposed panels of the wing or tail joined together.

l	length of wing-body-tail combination, in.
l_W	distance from most forward point of body to wing leading edge and body intersection, in.
l_M	distance from most forward point of body to center of moments, in.
l_N	distance from most forward point of body to shoulder of body nose, in.
l_T	distance from most forward point of body to tail leading edge and body intersection, in.
$\bar{l}$	distance from most forward point of body to center of pressure of combination, in.
l_r	moment reference length, in.
L	lift force, lb
$L_{T(V)}$	lift on tail section due to wing vortices, lb
$L_{B(V)}$	lift on body section between wing and tail due to wing vortices, lb
m	cotangent of leading-edge sweep angle
M_o	free-stream Mach number
q	free-stream dynamic pressure, lb/sq in.
r_N	body radius at shoulder of nose, in.
r_W	body radius at wing, in.
r_T	body radius at tail, in.
R	Reynolds number based on mean aerodynamic chord of exposed wing
s_T	semispan of tail in combination, in.
S_N	cross-sectional area of nose at maximum section, sq in.
S_R	reference area of combination lift coefficient, sq in.
S_T	tail-alone area, sq in.

S_W wing-alone area, sq in.

V_o free-stream velocity, in./sec

V_N volume of body nose up to shoulder, cu in.

$\bar{x}$ distance to center of pressure measured from wing leading edge and body intersection for wing quantities and from tail leading edge and body intersection for tail quantities, in.

x_H distance from leading edge and body intersection to wing hinge line, in.

α angle of attack of body center line, deg

β $\sqrt{|M^2 - 1|}$

Γ_m circulation at wing-body juncture of combination, $in.^2/sec$

Γ circulation, positive counterclockwise facing upstream, $in.^2/sec$

δ_T tail incidence angle, deg

δ_W wing incidence angle, deg

λ_T tail taper ratio, $(c_t/c_r)_T$

λ_W wing taper ratio, $(c_t/c_r)_W$

$\Lambda_{L.E.}$ sweep angle of leading edge, deg

ρ_o free-stream density, slugs/cu in.

Subscripts

B body alone

C combination, either body-wing or body-wing-tail

F forebody

N body nose

T tail alone

V wing vortex

W wing alone

AS Alden-Schindel theory

B(T) body in presence of tail

B(W) body in presence of wing

ST strip theory

T(B) tail in presence of body

W(B) wing in presence of body

α α variable, δ constant

δ δ variable, α constant

LIFT THEORY

The lift theory as developed is for the angle-of-attack range over which the lift and moment curves are linear and is equally applicable to subsonic and supersonic speeds unless otherwise noted. The methods developed in references 7 and 9 for determining the various components of the lift have been substantiated for supersonic speeds. These methods are summarized and their applicability to subsonic speed shown.

Attention is focused on pointed bodies having wings and tails mounted on body sections of uniform diameter. For the sake of being specific, the forward lifting surfaces are termed the wings, even in cases of canard configurations. Both wings and tails may have variable incidence, but cases of differential incidence are beyond the scope of this paper.

The terminology used is indicated in figure 1. The nose is that part of the body in front of the wing. However, when the wing is mounted on an expanding section of the body, the nose is taken to be the entire expanding part of the body. The principal lift components are (neglecting wing-tail interference):

1. Lift on nose including forebody, L_N
2. Lift on wing in presence of body, $L_{W(B)}$
3. Lift on body due to wing, $L_{B(W)}$
4. Lift on tail in presence of body, $L_{T(B)}$
5. Lift on body due to tail, $L_{B(T)}$

The additional lift components due to the wing trailing vortices are:

6. Lift on tail section due to wing vortices, $L_{T(V)}$
7. Lift on wing afterbody due to wing vortices, $L_{B(V)}$

All lift coefficients, except those for the tail alone, are based on the wing-alone area. All lift components are referred to experimental or theoretical values of C_{L_W} or C_{L_T}, through which Mach number effects enter. Experimental values of C_{L_W} or C_{L_T} should be used when these are available, otherwise any discrepancies between experiment and theory for these component parts of a combination will also carry over to the characteristics of the complete configuration. The lift results for tail-body interference are identical to those for wing-body interference, except for a term to refer the tail-body interference lifts to the wing area and, therefore, will not be treated separately.

Lift on Body Nose

The method given in reference 7 for specifying the lift on the nose makes use of the equation

$$C_{L_N} = K_N\left(C_{L_\alpha}\right)_W \alpha_B \tag{1}$$

wherein the coefficient K_N is defined as

$$K_N = \frac{L_N}{L_W} \tag{2}$$

for equal angles of attack of wing and nose. For many applications it is sufficiently accurate to evaluate L_N by use of slender-body theory

$$L_N = 2\pi r_N^2 \alpha_B q \tag{3}$$

$$L_F = 0 \tag{4}$$

so that

$$K_N = \frac{2\pi(r_N^2)}{S_W\left(C_{L_\alpha}\right)_W} \tag{5}$$

It is known that slender-body theory is usually not sufficiently accurate to determine body-alone lifts in cases such as nonslender bodies, hypersonic speeds, or large angles of attack. These effects are discussed in references 21, 22, and 23, respectively. However, for combinations which are not predominantly body, the nose lift is not a large part of the total lift, and slender-body theory gives satisfactory results in most instances.

Lift on Wing in Presence of Body

The lift on the wing in the presence of the body is given in reference 9 as

$$C_{L_{W(B)}} = \left[K_{W(B)}\ \alpha + k_{W(B)}\ \delta_W\right]\left(C_{L_\alpha}\right)_W \tag{6}$$

The factor $K_{W(B)}$ is defined as

$$K_{W(B)} = \frac{L_{W(B)}}{L_W} \text{ with } \delta_W = 0 \tag{7}$$

and is greater than unity because of body upwash. The factor $k_{W(B)}$ is defined as

$$k_{W(B)} = \frac{L_{W(B)}}{L_W} \text{ with } \alpha = 0 \tag{8}$$

and is less than unity because of the effects of interference on wing lift in the absence of body upwash. The lift ratios $K_{W(B)}$ and $k_{W(B)}$ have been determined from slender-body theory and are presented in figure 2 as taken from reference 9. The use of slender-body values of $K_{W(B)}$ and $k_{W(B)}$ for combinations employing wings of large aspect ratio has been justified in references 7, 9, and 24 for supersonic speeds.

It might be surmised that the present method of determining the lift on a wing in the presence of the body is applicable at subsonic

speeds since the slender-body-theory values of $K_{W(B)}$ and $k_{W(B)}$ on which it is based are not dependent on Mach number and the effect of Mach number enters only through $\left(C_{L_\alpha}\right)_W$. This supposition will subsequently be shown to be borne out by experimental data. Spreiter made the observation in reference 25 that the loading on the minimum drag wing-body combination of Lennertz (ref. 1) is identical at low speeds to that of a slender wing-body combination with a body of uniform diameter. The division of lift between wing and body based on this loading is shown in figure 3. Since the present method is based on the division of lift as given by Spreiter, the equality of the results of Spreiter and Lennertz is further evidence of the applicability of the present method to subsonic speeds.

At this point, it is desirable to consider the effects of span loading on the division of lift between wing and body because this information has bearing on the validity of the vortex model used in determining some later results. Besides his result for minimum drag, Lennertz also determined the division of load between wing and body for uniform span loading. This result, which corresponds to replacing each side of the combination by a horseshoe vortex, is shown in figure 3, wherein the part of the lift carried by the body is shown as a function of the ratio of body radius to vortex semispan. For the same value of the abscissa there is not much difference between the fractions of the lift acting on the body for the two cases. Generally, the span of a horseshoe vortex replacing a wing is less than the wing span. If account is taken of this fact in the comparison, the existing difference would largely disappear. Thus, the representation of the wing-body combination by a horseshoe vortex on each side is compatible with the present method of determining the division of lift between wing and body.

Lift on Body Due to Wing

The same general scheme used to compute the lift on the wing in the presence of the body is used to compute the lift on the body due to the wing. In fact, the equation analogous to equation (6) is

$$C_{L_{B(W)}} = \left[K_{B(W)}\,\alpha + k_{B(W)}\,\delta_W\right]\left(C_{L_\alpha}\right)_W \tag{9}$$

The factors $K_{B(W)}$ and $k_{B(W)}$, defined so that equation (9) is valid under the assumptions of linearity, are

$$K_{B(W)} = \frac{L_{B(W)}}{L_W} \text{ with } \delta_W = 0 \tag{10}$$

$$k_{B(W)} = \frac{L_{B(W)}}{L_W} \text{ with } \alpha = 0 \qquad (11)$$

Generally, the values of $K_{B(W)}$ based on slender-body theory are used, and these values are given in figure 2. However, for the high-aspect-ratio range at supersonic speeds, a special design chart was developed in reference 7 by use of the planar model shown in figure 4. This design chart is presented in figure 5(a).

The case of no afterbody behind the wing or tail is investigated in Appendix A for the high-aspect-ratio range at supersonic speeds. The analysis is based on the planar model of figure 4, and the lift is assumed to carry over onto the body only back to the wing (or tail) trailing edge. The design chart based on this assumption is presented in figure 5(b). The difference between the afterbody and no-afterbody cases for the low-aspect-ratio range at supersonic speeds has not been considered.

A comparison of $K_{B(W)}$ as determined from figure 5(a) with that from figure 5(b) gives an indication of the importance of the afterbody for any particular configuration. For small values of the ratio $2\beta(r/c_r)_W$ there is very little effect of the afterbody on $K_{B(W)}$ but, for large values, the effect can be as large as several hundred percent. At subsonic speeds no distinction will be made between the afterbody and no-afterbody cases. The difference between the two cases, which is usually small in terms of total lift at supersonic speeds, is further reduced at subsonic speeds because of the lesser tendency of lift to be carried downstream.

Slender-body theory is the only general means available for the determination of $k_{B(W)}$. The values of $k_{B(W)}$ so determined are presented in figure 2 (see ref. 9). These values are used for both subsonic and supersonic speeds.

Lift on Tail Section Due to Wing Vortices

Wing-tail interference results from downwash in the region of the tail caused by the wing vortices. The problem of determining wing-tail interference breaks down into the problems, first, of determining the number, strengths, and positions of the wing vortices at the tail and, second, of determining the reaction of the tail section to the nonuniform flow field induced by the wing vortices. This component of the combination lift is the most laborious to calculate. The same method will be used for subsonic and supersonic speeds.

Line-vortex theory is used in the solution of the wing-tail-interference problem following the general lines of other investigators. The model to be used is illustrated in figure 6. This model of the wing is the same as the Lennertz model for uniform loading previously discussed and is thus compatible with the method used here for calculating wing-body interference. Only one trailing vortex per wing panel is considered although more vortices per panel could be used to obtain greater accuracy at the expense of greater complication. The wing trailing vortices stream backward but undergo lateral and vertical deflections as a result of the body cross-flow field and the interaction between vortices. Image vortex lines are introduced inside the body at the image position of the trailing vortices to satisfy the boundary condition for a circular body. Sufficiently far downstream the external vortices approach an asymptotic spacing.

Number of vortices per panel.- For ease of calculation it will be assumed that one fully rolled-up vortex is discharged from each wing panel. While this model simulates the flow behind the wing panels of many combinations, there are cases where it does not. For instance, the work of Spahr and Dickey, reference 15, shows that for panels of high aspect ratio the flow behind the panel can consist of a flat sheet or several vortices, and for high angles of attack body vortices appear in the flow. Thus, it is a fact that the simplified model of one vortex per wing panel is not always an adequate basis for computing downwash. However, several investigators, such as Grigsby, Edwards, Edelman, and Rainey, (refs. 17, 18, 19, and 20) have successfully applied this simplified model to the computation of tail loads. These results indicate that the total tail load of each of the configurations investigated is insensitive to the details of the vortex flow although the downwash and spanwise distribution of tail load are not. This conjecture is substantiated in part by the theoretical work of Morikawa, reference 12, who has calculated the tail lifts of slender wing-body-tail combinations using one fully rolled-up vortex per wing panel and using a flat vortex sheet. Only for fully rolled-up vortices in the immediate vicinity of the tail tip does any appreciable difference between the two cases occur. The results of Lomax and Byrd, reference 13, for a family of swept wing-body-tail combinations are in accord with the findings of Morikawa. It was on the basis of this evidence and because of its great simplicity that the use of one wing vortex per panel was adopted. The accuracy of this assumption and its range of application will subsequently be determined by comparison between experiment and theory.

Vortex strength.- The circulation distribution at the wing trailing edge determines the strength Γ_m and the spanwise position f_W of the vortex at the trailing edge. The actual circulation distribution is replaced by an equivalent horseshoe vortex corresponding to the Lennertz model for uniform loading. Figure 7 illustrates this model. Note that figure 7 contains the tacit assumption that the maximum value of the

circulation is at the wing-body juncture. Since the lift of the bound vortex is $\rho_o V_o \Gamma_m$ per unit span, the value of Γ_m can be estimated from the following series of equations:

$$\Gamma_m = \frac{L_{W(B)}}{2\rho_o V_o (f_W - r_W)} = \frac{L_{B(W)}}{2\rho_o V_o (r_W - g_W)} = \frac{L_{W(B)} + L_{B(W)}}{2\rho_o V_o (f_W - g_W)} \tag{12}$$

$$f_W g_W = r_W^2 \tag{13}$$

to satisfy the boundary condition that the body is circular. The first form of the equation will be used for determining Γ_m. From equations (6) and (12) it follows that

$$\Gamma_m = \frac{V_o [K_{W(B)} \alpha + k_{W(B)} \delta_W]}{4(f_W - r_W)} \left(C_{L_\alpha}\right)_W S_W \tag{14}$$

Vortex lateral position.- The problem of determining the lateral positions of the wing vortices must be solved before the foregoing equation can be used to evaluate Γ_m. The assumption is made that the vortices of the wing in combination are discharged at the center of vorticity of the panels of the wing alone as determined by lifting-line theory or linear theory. This assumption is necessary because the circulation distribution is not generally known for the wing-body combination. The validity of this assumption can be examined for slender wing-body combinations for which the span loading is known and from which the lateral position of the vortex can be determined. In fact, the lateral vortex position on the basis of slender-body theory is given as

$$\left(\frac{f-r}{s-r}\right)_W = \frac{\frac{\pi}{4} - \frac{\pi}{4}\left(\frac{r}{s}\right)_W^2 - \left(\frac{r}{s}\right)_W + \frac{\left[1 + \left(\frac{r}{s}\right)_W^2\right]^2}{2\left[1 - \left(\frac{r}{s}\right)_W^2\right]} \sin^{-1}\left[\frac{1 - \left(\frac{r}{s}\right)_W^2}{1 + \left(\frac{r}{s}\right)_W^2}\right]}{2\left[1 - \left(\frac{r}{s}\right)_W\right]} \tag{15}$$

This equation gives the lateral position of the vortex as a fraction of the semispan of the exposed wing panel and as a function of the radius-semispan ratio. The maximum deviation between the values given by this equation and the wing-alone value of 0.786 (or $\pi/4$) is about 3 percent. This result is independent of the plan form of the wing or body in front of the maximum span position since in slender-body theory the potential and, hence, the circulation depend only on the cross-flow plane under consideration.

For nonslender wing-body combinations the lateral position can easily be determined if the wing lift coefficient and the loading at the root chord are known. The necessary equation is

$$f_W = \frac{(C_L)_W S_W}{2(c_l c)} \tag{16}$$

In this equation $(c_l c)$ is the product of the section lift coefficient at the center line of the wing and the chord at that position. Inherent in the equation is the assumption that the maximum circulation occurs at the center line of the wing.

A series of charts has been prepared for wings of unswept leading edges, midchord lines, and trailing edges to give the vortex location as a fraction of the wing-alone semispan and as a function of the effective aspect ratio with taper ratio as parameter. The charts for subsonic speeds, shown in figure 8, are based on the lift charts of DeYoung and Harper, reference 26. It is noteworthy that for low aspect ratios the lateral positions of the vortices all tend toward the slender-body value of $\pi/4$. No systematic set of lift charts similar to those of DeYoung and Harper is available for supersonic speeds. However, where linear-theory results were available, they were used to obtain the curves shown solid in figure 9, which is the supersonic analog of figure 8. To complete the charts the solid lines have been continued as dashed lines toward the slender-body value of $\pi/4$ at zero aspect ratio for the cases in which it was felt that the extrapolation could be made safely. For the $\lambda = 0$ case with no leading-edge sweep, there is a possibility that the circulation distribution does not have its maximum at the center line of the wing as assumed in equation (16). The linear-theory solution for the load distribution for the reversed triangular wing is unknown for $\beta A_W < 4$.

While the foregoing charts give the vortex lateral position at the wing, the lateral position at the tail, f_T, is required for calculating wing-tail interference. The simple assumption can be made that f_T is equal to f_W. The determination of f_W has been discussed by Spreiter and Sacks in reference 27. Also f_T can be set equal to f_∞, the asymptotic vortex lateral position, as determined from reference 14. (A step-by-step calculation of f_T using the graphical aids of reference 28 can be made, if desired.) To determine which of the approximations to f_T, f_W, or f_∞, is more accurate, the experimental lateral positions are compared with f_W and f_∞ in figures 10, 11, and 12 for three triangular wing and body combinations reported by Spahr and Dickey in reference 15. As the angle of attack increases, the vortices become more rolled up at a given downstream station and are spaced closer together. Grigsby, reference 17, has also found similar results. However, the data of figures 10, 11, and 12 exhibit certain behavior that must be considered if accurate vortex positions at the tail are to be

predicted. In the first place, more than one vortex per wing panel sometimes occurs in the field for the higher aspect ratios. Secondly, at high angles of attack body vortices appear in the flow and affect the positions of the wing vortices. Further work is required before accurate predictions can be made of the vortex positions at the tail. On the basis of the comparison between theory and experiment, neither f_W nor f_∞ is superior for predicting the vortex spacing at the tail because of the appearance of other vortices in the flow. Until more data are available on vortex positions to justify a more elaborate estimate, the value of f_W will be used.

Vortex vertical positions.- The vertical position of the vortex at the tail can be estimated by the step-by-step calculative procedure described in reference 15, but the process is generally too lengthy. Two alternate methods are considered. In the first method, the vortex is assumed to stream backward in the free-stream direction from the wing trailing edge. The second method, suggested by Lagerstrom and Graham, reference 14, is to ignore the effects of the image vortices, which are nearly equal and opposite, but to consider crossflow and the mutual effects of the external vortices. A comparison between the two positions predicted by these methods and the positions measured by Spahr and Dickey are shown in figures 10(b), 11(b), and 12(b). Because of the occurrence of more than one wing vortex per panel and of body vortices, neither theoretical method appears superior. Therefore, it seems best to use the simpler of the two methods which assumes that the vortices stream back from the trailing edge in the free-stream direction. This assumption leads to the following equation for vortex vertical location:

$$h_T = -\left(c_r - x_H\right)_W \sin \delta_W + \left[\bar{l}_{T(B)} - \bar{l}_W - \left(c_r\right)_W\right] \sin \alpha \qquad (17)$$

The height is measured above the body axis and normal to it at the center of pressure of the tail panels.

Lift due to wing vortices.- The load transmitted to the tail section because of the wing vortices depends on the vortex positions at the tail and the vortex strengths. For estimating the loads on the tail section, strip theory is generally applicable but the method of Alden and Schindel, reference 16, can be applied when the necessary theoretical span loadings are known. In specifying the tail load, use will be made of a tail interference factor

$$i = \frac{L_{T(V)}/\left(L_T\right)_\alpha}{57.3\ \Gamma_m/2\pi\alpha\ V_o\left(s_T - r_T\right)} \qquad (18)$$

where $(L_T)_\alpha$ is the lift of the tail alone at angle of attack α. The interference factor represents a nondimensional quantity useful for computing tail loads. The factor i depends on the parameters λ_T, $(r/s)_T$, $(c_r/\beta s)_T$, $(f/s)_T$, and $(h/s)_T$. For a fixed body-tail configuration, the factor depends only on the vortex positions in the cross-flow plane of the tail.

Whether the factor i is calculated by strip theory or by the Alden-Schindel technique, several simplifying assumptions are required regarding the wing-tail interference. The first assumption is one already used in determining $K_{B(W)}$ for large aspect ratios at supersonic speeds - that the nonplanar tail section can be reduced to an equivalent planar model similar to that shown in figure 4. The body is assumed to be flat and to act at zero angle of attack, while the tail angle of attack α_T varies spanwise. The second assumption is that the lift on the tail section due to wing-tail interference is all developed by the tail panels, even though part of it is transferred to the body. In the application of strip theory to determine this lift, Lagerstrom and Van Dyke in reference 29 have shown that an exact value (within the realm of linear theory) will be obtained for the over-all lift of the planar model if the leading edge is supersonic and the trailing edge is straight, as for a triangular wing of effective aspect ratio greater than 4. It is to be noted that the second assumption circumvents the question of whether an afterbody occurs behind the tail. Generally, the lift acting on the body is only a small fraction of that acting on the tail section due to wing-tail interference, so that no precise consideration of the tail afterbody is usually required.

Strip theory has been used to calculate a series of design charts for the estimation of i. The details of the calculations are given in Appendix B, and the charts are presented in figure 13. The charts of this figure show contours of constant values of i in the cross-flow plane of the tail with the parameters λ_T and $(r/s)_T$ varying from chart to chart. It is to be noted that strip theory is independent of the chord-span ratio $(c/\beta s)_T$. In fact, strip theory represents the limiting case of linear theory as $(c/\beta s)_T \longrightarrow 0$. The charts give an immediate idea of the regions wherein wing-tail interference is most important. For triangular tails ($\lambda_T = 0$) it is to be noted that the interference is a finite maximum when the vortex is in the plane of the tail and slightly inboard of the tip. For all other taper ratios, however, an infinite maximum effect occurs when the vortex is at the tail tip. Strip theory is, thus, not accurate for positions of the vortex near the tail tip, except in the case of triangular wings with supersonic leading edges, in which case it is accurate to the order of linear theory.

An alternate method for the determination of i is the method of Alden and Schindel, which will serve as a basis for assessing the accuracy of strip theory. The essential result of the method is that the

lift of a lifting surface with supersonic edges in a nonuniform flow field that varies spanwise can be evaluated to the accuracy of linear theory by the equation

$$L = \int_{span} w(y)F(y)dy \tag{19}$$

where $w(y)$ is the vertical velocity at the spanwise position y and $F(y)$ is proportional to the span loading of the tail at uniform angle of attack in reversed flow. Heaslet and Spreiter in reference 30 have extended the range of equation (19) to include surfaces with subsonic edges. For triangular tails with supersonic leading edges, the reversed tail is uniformly loaded so that $F(y)$ is proportional to the local chord. Thus, strip theory and the Alden-Schindel method give identical results for this case. Generally speaking, the Alden-Schindel technique is not suited for an analytical determination of i because, in some cases, the necessary function $F(y)$ is not known or leads to complicated integrations. (A clever electromagnetic device for performing these integrations has been described by Hill in ref. 31.) The Alden-Schindel method leads to results in closed form for rectangular tail and body combinations, and the calculation has been carried out in Appendix C. The values of i for the vortex in the plane of a rectangular tail and for a radius-semispan ratio of 0.2 are given in figure 14 for four values of $(c/\beta s)_T$. For a value of $(c/\beta s)_T = 0$ the Alden-Schindel technique and strip theory are identical. Thus, a comparison of the curves for other values of $(c/\beta s)_T$ with those for zero gives an indication of the error due to the use of strip theory for large chord-span ratios. The first result is that the infinity at $(f/s)_T = 1$ (for values of $(c/\beta s)_T$ not equal to zero) has been eliminated by using the Alden-Schindel technique. For vortex positions outboard of the tail tip, the effect of $(c/\beta s)_T$ is very small. However, for vortex positions inboard of the tip, a larger effect of $(c/\beta s)_T$ is indicated. To obtain an idea of where the discrepancy due to the use of strip theory is large and where small, a figure has been prepared showing the ratio of $(i_{AS} - i_{ST})/i_{AS}$ as a measure of the error incurred in using strip theory for $(c/\beta s)_T=0.5$. This ratio is shown as a function of vortex position in figure 15. For positions of the vortex outboard of the tail tip, the error is generally very small except in the immediate vicinity of the tip. For positions of the wing vortex inboard of the tail tip, a maximum error of about 35 percent can be incurred by the use of strip theory. This error decreases with distance from the tail. The reason that larger errors are incurred for positions of the vortex inboard of the tail tip is that here the net effect of the vortex is the small difference of large positive and negative lifts, while for outboard positions the vortex induces negative lift across the entire tail. It is believed that the use of strip theory is more accurate for tapered wings than for rectangular wings since it is known to be exact for triangular wings with

supersonic edges. Despite the fact that strip theory does not possess the accuracy of linear theory for purposes of estimating tail loads, it has several decisive advantages over the linear theory (exemplified at supersonic speeds by the Alden-Schindel method). First, the necessary theoretical information is not available for using linear theory in some cases at supersonic speeds. Second, separate determinations would be required for different $(c/\beta s)_T$ values and for subsonic and supersonic speeds, making the construction of design charts extremely difficult. For these reasons and because of its great simplicity, strip theory is used in this report for computing the tail interference factors except for rectangular tails at supersonic speeds.

The contribution of wing-tail interference to the lift coefficient is now derived. The contribution is by definition

$$C_{L_{T(V)}} = \frac{L_{T(V)}}{qS_W} \tag{20}$$

With the aid of equations (14) and (18) there is obtained

$$C_{L_{T(V)}} = \frac{57.3 \left(C_{L_\alpha}\right)_W \left(C_{L_\alpha}\right)_T \left[K_{W(B)}\ \alpha + k_{W(B)}\ \delta_W\right] i(s_T - r_T)}{2\pi\ A_T(f_W - r_W)} \tag{21}$$

The values of $K_{W(B)}$ or $k_{W(B)}$ are obtained from figure 2, the value of i from figure 13, and the value of f_W from figures 8 or 9. For rectangular tails at supersonic speeds the value of i calculated by use of the Alden and Schindel technique is recommended.

Lift on Wing Afterbody Due to Wing Vortices

In the previous work it was assumed that no change in lateral vortex spacing occurred between the wing and tail because, for the purposes of this report, the extra work to compute the change is usually not warranted. However, if for some reason a step-by-step calculation of the vortex path is made, the lift on the wing afterbody can be estimated. The model shown in figure 6 is used in the estimation. The lift represented by a horseshoe vortex is $\rho_o V_o \Gamma_m$ per unit span. The lift represented by the vortex system at the wing trailing edge is thus $2\rho_o V_o \Gamma_m (f_W - g_W)$ and at the tail location is $2\rho_o V_o \Gamma_m (f_T - g_T)$. The net lift retained on the body between the wing and the tail is thus

$$L_{B(V)} = -2\rho_o V_o \Gamma_m [(f_W - g_W) - (f_T - g_T)] \tag{22}$$

With the aid of the relationships

$$g_W = \frac{r_W^2}{f_W} \tag{23}$$

$$g_T = \frac{r_T^2}{\sqrt{f_T^2 + h_T^2}} \tag{24}$$

equation (22) becomes in lift coefficient form

$$C_{L_{B(V)}} = -\frac{4\Gamma_m}{S_W V_o}\left[\frac{(f_W^2 - r_W^2)}{f_W} - f_T + \frac{r_T^2}{\sqrt{f_T^2 + h_T^2}}\right] \tag{25}$$

Lagerstrom and Graham (ref. 14) have derived this same result using a different method. Generally, the change in f between wing and tail is not known unless the step-by-step solution mentioned in reference 15 is performed. In this case both the total lift and distribution of lift on the body due to the trailing vortices is known. However, if only an upper bound on the value of $C_{L_{B(V)}}$ is desired, then the value of f_∞ can be used for f_T in equation (25).

Summary of Lift Components of Wing-Body-Tail Combinations

The seven components of the lift acting on a wing-body-tail combination are outlined as follows:

1. Lift on body nose,

$$(C_L)_N = K_N \left(C_{L_\alpha}\right)_W \alpha_B \tag{26}$$

2. Lift on wing in presence of body,

$$(C_L)_{W(B)} = \left[K_{W(B)}\ \alpha + k_{W(B)}\ \delta_W\right]\left(C_{L_\alpha}\right)_W \tag{27}$$

3. Lift on body due to wing,

$$(C_L)_{B(W)} = \left[K_{B(W)}\ \alpha + k_{B(W)}\ \delta_W\right]\left(C_{L_\alpha}\right)_W \tag{28}$$

4. Lift on tail in presence of body (neglecting wing vortices),

$$(C_L)_{T(B)} = \left[K_{T(B)}\ \alpha + k_{T(B)}\ \delta_T \right] \left(C_{L_\alpha} \right)_T \left(\frac{S_T}{S_W} \right) \tag{29}$$

5. Lift on body due to tail (neglecting wing vortices),

$$(C_L)_{B(T)} = \left[K_{B(T)}\ \alpha + k_{B(T)}\ \delta_T \right] \left(C_{L_\alpha} \right)_T \left(\frac{S_T}{S_W} \right) \tag{30}$$

6. Lift on tail section due to wing vortices,

$$(C_L)_{T(V)} = \frac{57.3 \left(C_{L_\alpha} \right)_W \left(C_{L_\alpha} \right)_T \left[K_{W(B)}\ \alpha + k_{W(B)}\ \delta_W \right] i (s_T - r_T)}{2\pi A_T (f_W - r_W)} \tag{31}$$

7. Lift on wing afterbody due to wing vortices,

$$(C_L)_{B(V)} = -\frac{4\Gamma_m}{S_W V_o} \left[\frac{(f_W^2 - r_W^2)}{f_W} - f_T + \frac{r_T^2}{\sqrt{f_T^2 + r_T^2}} \right] \tag{32}$$

A calculative form for determining the lift and moment characteristics of wing-body-tail combinations utilizing the foregoing results will subsequently be presented. However, the last lift component will not be incorporated into the form since it is only of importance in rare instances, and since it can only be computed after a step-by-step computation of the type discussed in reference 15. A chart summarizing the lift-curve slopes of wings at supersonic speeds as determined from linear theory is included as figure 16 for use with these formulas.

CENTER-OF-PRESSURE THEORY

In the section on lift theory the differences between subsonic and supersonic speeds were given only passing attention since the lift theory as developed applies in the same form to both speed ranges. The primary effect of Mach number was manifest through the quantities $\left(C_{L_\alpha} \right)_W$ and $\left(C_{L_\alpha} \right)_T$. However, in the center-of-pressure theory the Mach number has a direct effect on the centers of pressure of several of the lift components, and a definite distinction must be made between the subsonic and supersonic cases for these components.

Several conventions are adopted with regard to center-of-pressure position in this report. All positions for the complete configuration are ultimately given in fractions of the body length behind the most forward point of the body. The design chart for the centers of pressure of $L_{B(W)}$, $L_{W(B)}$, $L_{T(B)}$, and $L_{B(T)}$ are given in fractions of the root chord (at the juncture with the body) behind the juncture of the leading edge with the body. All length symbols having bars over them represent center-of-pressure lengths.

Center of Pressure of Body Nose

For most purposes the center of pressure of the body nose can be estimated with sufficient accuracy by slender-body theory. The result is obtained that

$$\bar{l}_N = l_N \left(1 - \frac{V_N}{\pi r_N^2 l_N}\right) \tag{33}$$

wherein V_N, r_N, and l_N are the volume, radius, and length of the body nose. For bodies with noses of small fineness ratio or even for bodies with slender noses at high Mach numbers, some lift is carried over onto the body behind the nose, tending to make $\bar{l}_N$ greater than the value given by equation (33). If the lift on the nose is a substantial fraction of the total lift, the effect can be significant. In such cases linear theory is better than slender-body theory, although experimental values of $\bar{l}_N$ are always to be preferred. In this report, slender-body theory will be used when theoretical values are used.

Center of Pressure of Wing in Presence of Body

The center of pressure of the wing in the presence of the body depends slightly on whether the lift is developed by varying the body angle of attack at fixed wing incidence or varying the wing incidence at constant body angle of attack. The difference in centers of pressure for these lift components, determined experimentally for triangular all-movable wings and reported in reference 9, amounts at supersonic speeds to about 2 percent of the root chord or 3 percent of the mean aerodynamic chord. If account is taken of the difference, the center of pressure for the wing in the presence of the body is

$$\left(\frac{\bar{x}}{c_r}\right)_{W(B)} = \frac{K_{W(B)\alpha}\left(\frac{\bar{x}}{c_r}\right)_{W(B)\alpha} + k_{W(B)}\,\delta_W\left(\frac{\bar{x}}{c_r}\right)_{W(B)\delta}}{K_{W(B)}\,\alpha + k_{W(B)}\,\delta_W} \tag{34}$$

Generally speaking, the theoretical values of $(\bar{x}/c_r)_{W(B)\alpha}$ and $(\bar{x}/c_r)_{W(B)\delta}$ are not known so that some approximate method of estimating them is required. In reference 9 the values of $(\bar{x}/c_r)_{W(B)\alpha}$ and $(\bar{x}/c_r)_{W(B)\delta}$ for triangular wings in combination with a round body are given as computed on the basis of slender-body theory. Also, the values of $(\bar{x}/c_r)_{W(B)\delta}$ for rectangular wings of effective aspect ratio 2 or greater are reported as determined by linear theory. For other cases the following approximate result is recommended in lieu of more specific information:

$$\left(\frac{\bar{x}}{c_r}\right)_{W(B)} = \left(\frac{\bar{x}}{c_r}\right)_W \tag{35}$$

The distance of the center of pressure of the wing in the presence of the body measured from the most forward point of the body is, then

$$\bar{l}_{W(B)} = l_W + (c_r)_W \left(\frac{\bar{x}}{c_r}\right)_{W(B)} \tag{36}$$

At subsonic speeds the charts of DeYoung and Harper, reference 26, may be used for estimating $(\bar{x}/c_r)_W$ for a wide range of aspect ratios, taper ratios, and sweep angles. A chart presenting the results is shown as figure 17. The results have been extrapolated from values of $\beta A = 2$ to the slender-body values at $\beta A = 0$. Cross-plotting aided in the extrapolation. A set of charts for supersonic speeds is presented as figure 18. These charts are based on linear theory and have been extrapolated to the slender-body values at zero aspect ratio when linear theory was not available for the low-aspect-ratio range. The curve for $\lambda = 0$ and no leading-edge sweep could not be extrapolated with any degree of assurance.

Center of Pressure of Body Due to Wing

The center of pressure acting on the body due to the wing is determined by different methods, depending on whether subsonic or supersonic flow is considered. For the supersonic case the method of reference 8 is used. In this method the planar model of figure 4 is used with the

assumption that the wing is at a uniform angle of attack. Generally speaking, the model is applicable only if the tip Mach cones do not intersect the wing-body juncture, thereby influencing the wing-body interference. For this high-aspect-ratio range two cases are distinguished: that of an afterbody behind the wing and that of no afterbody. The afterbody case is approximated by integrating the pressure field on the body to the trailing-edge Mach waves, as shown in figure 4, and the no afterbody case is approximated by integrating only up to an extension of the wing trailing edge. Based on these models, charts for determining $(\bar{x}/c_r)_{B(W)}$ for the afterbody and no afterbody cases are presented in figures 19(a) and 19(b), respectively.

While the charts of figure 19 can be used for an approximation to $(\bar{x}/c_r)_{B(W)}$ even for the low-aspect-ratio range, as indeed was done in reference 9, nevertheless, a somewhat more accurate method can be derived for this range. In the more accurate method the independent variables are taken to be aspect ratio and taper ratio, with radius-semispan ratio as parameter. The values of $(\bar{x}/c_r)_{B(W)}$ for $\beta A = 0$ are those given by slender-body theory, and the values for $(r/s)_W = 0$ are those for the wing alone as given by linear theory. On the basis of this information it is possible to extrapolate the high-aspect-ratio theory to $\beta A = 0$, as has been done in figure 20 for the afterbody case. These charts are to serve as design charts for the aspect-ratio range. Similar charts can easily be formulated for the no afterbody case by use of the results of figure 19(b). In establishing the slender-body values at $\beta A = 0$, it was assumed that no lift was developed downstream of the maximum wing span. The extrapolation was not attempted for $\lambda = 0$ and no leading-edge sweep.

Hitherto, no method seems to have been available for estimating $(\bar{x}/c_r)_{B(W)}$ at subsonic speeds. For this purpose, the lifting-line model shown in figure 21 has been used. The lifting line is placed along the quarter-chord line of the wing and its image is introduced inside the body. The external lifting line is divided into a number of bound vortices, the strengths of which are proportional to the circulation distribution. The lifting line is not uniformly loaded although the horseshoe vortices are. The external vortices have their internal images which produce the lift on the body, this lift being produced at the bound part of the horseshoe vortex. Since the lift on the body due to each elemental image horseshoe vortex is proportional to the product of its strength times the length of its bound element, and since its lift acts at the bound element, it is easy to determine the center of lift of all the image horseshoe vortices. The formulas for the calculation are presented in Appendix D and the results are presented in figure 22 as a series of design charts for $(\bar{x}/c_r)_{B(W)}$ at subsonic speeds. In Appendix D, the lifting line was assumed to be

elliptically loaded. This assumption should be valid for most cases since the calculation is not sensitive to the span loading and since efficient wings tend to be elliptically loaded. No difference between $(\bar{x}/c_r)_{B(W)\alpha}$ and $(\bar{x}/c_r)_{B(W)\delta}$ has been considered since any such differences will be small and are beyond the scope of available theory.

The charts of figure 22 give results for unswept leading edges, midchord lines, and trailing edges as a function of βA and (r/s). The results for $\beta A \geq 4$ represent the results of lifting-line theory. It is to be noted that no dependence on aspect ratio is found on the basis of lifting-line theory. It is known that at low aspect ratios the loading on the wing-body combination approaches the slender-body loading for which the center of pressure on the body is known. The value from slender-body theory is plotted on the charts of figure 22 at $\beta A = 0$. Furthermore, for $r/s = 0$ it is clear that $(\bar{x}/c_r)_{B(W)}$ equals the center of pressure of the loading at the root chord of the wing alone. For rectangular and triangular wings of low aspect ratio this quantity has been obtained from the work of reference 32. The results for $r/s = 0$ at low aspect ratio agree with good accuracy with the lifting-line-theory results for $r/s = 0$ at about $\beta A = 4$. Therefore, lifting-line theory has been adopted for $\beta A > 4$, and for $\beta A < 4$ the curves have been extrapolated to the slender-body values at $\beta A = 0$ with the $r/s = 0$ results used as a guide. The extrapolated curves are shown dotted in figure 22. The distance of the center of pressure from the body point is given as

$$\bar{l}_{B(W)} = l_W + (c_r)_W \left(\frac{\bar{x}}{c_r}\right)_{B(W)} \tag{37}$$

Center of Pressure of Tail in Presence of Body

The center of pressure of the tail in the presence of the body (wing-tail interference being neglected) is given by the same procedure as that for the wing. For supersonic speeds the value of $(\bar{x}/c_r)_T$ as determined from figure 18 is used as an approximation to $(\bar{x}/c_r)_{T(B)}$. For subsonic speeds the charts of reference 26 or those of figure 17 are available for estimating $(\bar{x}/c_r)_T$. The distance from the most forward point of the body to the tail center of pressure is thus given as

$$\bar{l}_{T(B)} = l_T + (c_r)_T \left(\frac{\bar{x}}{c_r}\right)_{T(B)} \tag{38}$$

Center of Pressure on Body Due to Tail

The center of pressure on the body due to the tail, wing-tail interference being neglected, is determined by the same procedure as that due to the wing. For supersonic speeds the charts of figures 19 and 20 are used for cases of afterbody and no afterbody. For subsonic speeds the charts of figure 22 are used in estimating $(\bar{x}/c_r)_{B(T)}$. From these values the distance from the point of the body to the center of pressure is given

$$\bar{l}_{B(T)} = l_T + (c_r)_T \left(\frac{\bar{x}}{c_r}\right)_{B(T)} \tag{39}$$

Center of Pressure of Tail Section Due to Wing Vortices

The flow over the tail due to the wing vortices varies greatly as the position of the vortex varies with respect to the tail. It follows that the center of pressure of the lift due to the effect of the vortices on the tail section is also dependent on the position of the vortices with respect to the tail. It is possible on the basis of strip theory to take account of this effect. However, the refinement is hardly warranted in view of the fact that the distance from the center of moments to the tail is usually large so that great precision in the location of the center of pressure of the load on the tail section due to the wing vortices is unnecessary. A good approximation is to take the center of pressure as that for the tail panels in combination with the body. Thus

$$\bar{l}_{T(V)} = \bar{l}_{T(B)} \tag{40}$$

Summary of Center-of-Pressure Positions of Wing-Body-Tail Combination

The components of the lift, with the exception of the lift on the wing afterbody due to the wing vortices, have center-of-pressure positions estimated as follows:

1. Center of pressure of body nose,

$$\bar{l}_N = l_N\left(1 - \frac{V_N}{\pi r_N^2 l_N}\right) \tag{41}$$

2. Center of pressure of wing in presence of body,

$$\bar{l}_{W(B)} = l_W + \left(\frac{\bar{x}}{c_r}\right)_{W(B)} (c_r)_W \tag{42}$$

with

$$\left(\frac{\bar{x}}{c_r}\right)_{W(B)} = \frac{K_{W(B)}\ \alpha \left(\frac{\bar{x}}{c_r}\right)_{W(B)\alpha} + k_{W(B)}\ \delta_W \left(\frac{\bar{x}}{c_r}\right)_{W(B)\delta}}{K_{W(B)}\ \alpha + k_{W(B)}\ \delta_W} \tag{43}$$

3. Center of pressure on body due to wing,

$$\bar{l}_{B(W)} = l_W + (c_r)_W \left(\frac{\bar{x}}{c_r}\right)_{B(W)} \tag{44}$$

4. Center of pressure of tail in the presence of body,

$$\bar{l}_{T(B)} = l_T + (c_r)_T \left(\frac{\bar{x}}{c_r}\right)_{T(B)} \tag{45}$$

5. Center of pressure on body due to tail,

$$\bar{l}_{B(T)} = l_T + (c_r)_T \left(\frac{\bar{x}}{c_r}\right)_{B(T)} \tag{46}$$

6. Center of pressure of tail section due to wing vortices,

$$\bar{l}_{T(V)} = \bar{l}_{T(B)} \tag{47}$$

The center of pressure for the entire combination is thus

$$\bar{l}_c = \frac{\bar{l}_N (C_L)_N + \bar{l}_{W(B)} (C_L)_{W(B)} + \bar{l}_{B(W)} (C_L)_{B(W)} + \bar{l}_{B(T)} (C_L)_{B(T)} + \bar{l}_{T(B)} (C_L)_{T(B)} + \bar{l}_{T(V)} (C_L)_{T(V)}}{(C_L)_N + (C_L)_{W(B)} + (C_L)_{B(W)} + (C_L)_{B(T)} + (C_L)_{T(B)} + (C_L)_{T(V)}}$$

COMPUTATIONAL TABLE FOR DETERMINING LIFT COMPONENTS AND CENTERS OF PRESSURE

To organize and illustrate the calculations of the lift and center-of-pressure characteristics of wing-body-tail combinations, a computational table, based on the equations and charts already presented, is presented as table I. A numerical example is included in the table, which is self-explanatory. The reference area and moment reference point and length are arbitrary. Angular measures are always to be taken in degrees.

A possible confusion in the use of the computing table is the manner of using figure 13 when interpolations must be made with respect to λ and r/s. Normally, one can interpolate at constant values of the vortex lateral and vertical positions. However, for positions of the vortex near the body, interpolating in r/s may carry the vortex inside the body. Under such circumstances, it is recommended that the interpolation be made at constant values of $(f_W - r_T)/(s_W - r_T)$, the vortex lateral position as a fraction of the span of the exposed wing panel.

Again, it is advocated that experimental values of the lift-curve slopes $\left(C_{L_\alpha}\right)_W$, $\left(C_{L_\alpha}\right)_T$, and $\left(C_{L_\alpha}\right)_B$ be used if available. If the experimental values of $\left(C_{L_\alpha}\right)_W$ and $\left(C_{L_\alpha}\right)_T$ are unavailable and if the theoretical values are not obtainable from the material at hand, then references 26, 33, or 34 should be consulted. It is to be noted that in the calculative form, the body radius can be variable since the quantities r_N, r_W, and r_T are all considered separately. If the body radius is varying at the wing or tail location, an average radius should be used at each location. The assumption has been used in determining the lateral vortex position at the tail that the wing vortex streams back in the free-stream direction. For variable body radius the assumption is made that in the plan view, the wing vortex streams back parallel to the side of the body. This assumption is incorporated into the computing table. A special figure to aid in determining the center of pressure of ogival noses is presented in figure 23 and used in the computing table.

RESULTS AND DISCUSSION

To test the method of this report, a series of calculations have been performed to estimate the characteristics of a number of combinations, and these characteristics have been compared with experiment. The geometric and aerodynamic characteristics of those combinations for

which the comparisons have been made are summarized in table II for wing-body combinations and in table III for wing-body-tail combinations. The experimental data have been taken from references 35 to 65, inclusive.

In summarizing the aerodynamic data, little difficulty was experienced with wing-body combinations because their lift and moment characteristics, being usually linear at low angles of attack, are well represented by lift-curve slope and center of pressure at $\alpha = 0$. However, these quantities are not sufficient to describe the nonlinear characteristics exhibited by many wing-body-tail combinations. Some of the moment characteristics were so nonlinear that it was impossible to determine the center-of-pressure position at $\alpha_B = 0$ accurately, and in these cases the information was not entered in table III. Curves of the nonlinear characteristics will subsequently be presented.

The discussion of the main lift and center-of-pressure correlations between experiment and theory is for no deflection of wing or tail. The effects of wing deflection on wing-body interference were discussed in reference 9. Some effects of wing deflection on wing-tail interference are discussed after the main lift and center-of-pressure results.

Lift

In presenting the lift results attention is first focused on subsonic wing-body combinations. No results are presented for supersonic combinations since it has already been shown in reference 7 that the present method is applicable to combinations employing rectangular, triangular, and trapezoidal wings at supersonic speeds to within an error of about ±10 percent for lift.

Wing-body combinations.- In figure 24 the experimental values of $\beta(dC_L/d\alpha)_C$ for subsonic wing-body combinations are plotted against the estimated values. A 45° line of perfect agreement is shown in the figure together with lines of ±10-percent error. Certain of the correlation points have flags to indicate that they represent the Mach number range 0.9 to 1.0. It is apparent that the present method of predicting $(dC_L/d\alpha)_C$ is accurate to within about ±10 percent for wing-body combinations at subsonic speeds, as well as supersonic speeds, except for certain combinations in the transonic range.

Figure 25 is presented to show how the present method predicts the trend with Mach number of the lift-curve slopes of wing-body combinations. In general, the trends are well represented by the theory and the magnitudes are within the expected accuracy, except for certain combinations in the transonic range. For these combinations the wing-alone lift-curve

slopes in the transonic range are greater than the value given by linear theory because of nonlinear transonic effects. McDevitt (ref. 66) has shown that for rectangular wings having NACA 65AOXX sections, good agreement between linear theory and experiment is obtained near $M_o = 1$ for lift if the transonic similarity parameter $A(t/c)^{1/3}$ is less than unity. No well-defined dependence of the agreement between experiment and theory on this parameter was noted for the various plan forms represented in figure 25.

For some combinations the theory shows a peak in the lift-coefficient variation at $M_o = 1$, while for other combinations the peak occurs on the supersonic side. For $M_o = 1$, the effective aspect ratio is zero, and the slender-body value of the lift-curve slope, $(\pi/2)A$, has been used in the theory. On the supersonic side of $M_o = 1$ the values of βA are small and the wing lift-curve slope has been obtained from low-aspect-ratio linear theory. If the lift-curve slope so obtained is greater than that obtained from slender-body theory, then the maximum lift-curve slope occurs on the supersonic side of $M_o = 1$. The behavior of the lift variation with Mach number around $M_o = 1$ thus depends on the low-aspect-ratio lift characteristics of the wing alone.

While the agreement between the estimated and experimental lift-curve slopes for the large number of combinations compared is evidence suggesting that the division of lift between wing and body is correctly given by the present method, nevertheless, more direct evidence is needed to prove the point. Such evidence has been obtained for supersonic speeds and is available in reference 67. At subsonic speeds data in references 2 and 3 give the same division of lift between wing and body as a function of diameter-span ratio as the present method. The comparison of the data of these reports is with the theoretical division as given by the Lennertz theory which, as previously pointed out, is numerically the same as that given by slender-body theory on which the present method is based.

Wing-body-tail combinations.- The values of $\beta(dC_L/d\alpha)_C$ at $\alpha = 0$ obtained from experiment are plotted against the estimated values in figure 26 for subsonic speeds and in figure 27 for supersonic speeds. To illustrate the importance of wing-tail interference, the points are shown as squares for no wing-tail interference and as circles for wing-tail interference included in the estimated values. It is apparent that effects of wing-tail interference can be very large on a percentage basis, 30 to 40 percent. However, after the effects of wing-tail interference have been included in the theory, the errors are generally within ±10 percent. Therefore, the accuracy of prediction of the wing-tail interference in the worst cases must be within about ±25 to 30 percent.

Sufficient data have been analyzed to present some effects of angle of attack and Mach number on the lift characteristics of wing-body-tail combinations. The nonlinear variations of C_L with α for subsonic wing-body-tail combinations are shown in figure 28. The theory with and without wing-tail interference is shown. The theory including wing-tail interference is in good accord with the experiment. As expected, in the high-angle-of-attack range the measured lift tends to be greater than the estimated lift, probably as a result of body cross flow. Comparison has been made between experiment and theory for supersonic speeds in figure 29. Again, in the low-angle-of-attack range the agreement between the experimental and theoretical values of the lift coefficient is good. The variations of lift-curve slope for zero angle of attack and of lift coefficient for several angles of attack with Mach number are shown in figures 30(a) through 30(j) for a number of combinations. It is clear that the trends with Mach number are well predicted for the combinations considered. Where the theory has not been extended to $M_O = 1$ from the subsonic or supersonic range, the wing-alone or tail-alone lift-curve slopes could not be predicted accurately for the low effective aspect ratios involved. The large transonic effects exhibited by some of the combinations are predicted by the theory. Unfortunately, the wing-body-tail characteristics were not available for any wing-body combination exhibiting nonlinear transonic characteristics, so it was impossible to see the effect of adding a tail in such a case.

Center of Pressure

Wing-body combination.- The center-of-pressure locations for wing-body combinations at supersonic speeds are not considered since the problem is discussed in reference 8, where it was shown that the center of pressure of wing-body combinations employing triangular, rectangular, or trapezoidal wings could be estimated to within about $\pm 0.016l$ or less at supersonic speeds by the present method.

The center-of-pressure positions for subsonic wing-body combinations as determined experimentally have been plotted as a function of the estimated positions in figure 31. Lines of $\pm 0.02l$ error have been included in the figure. Generally speaking, the configurations correlated lie within the $\pm 0.02l$ error limits. It is to be noted that the errors are randomly distributed about the line of perfect agreement. Comparison is made between theory and experiment for subsonic and supersonic speeds in figure 32 in which the variation with Mach number of the centers of pressure is presented for a number of wing-body combinations. The theory for supersonic speeds has been presented in two manners. The solid line represents the theory without correction, while the dashed lines represented the theory with the corrections advocated in reference 8. Generally speaking, the variation with Mach number of

the center of pressure is not large so long as the transonic range is not traversed. However, through the transonic range, changes in center of pressure of appreciable magnitude can occur. The magnitudes of the shift are fairly well predicted by the theory when the correction of reference 8 is made. It should be remembered that the correction applies only to wing-body combinations at supersonic speeds.

Wing-body-tail combinations.- A correlation of the center-of-pressure positions for $\alpha = 0$ as determined experimentally and as estimated are presented in figure 33 for subsonic wing-body-tail combinations. It is clear that including the effects of wing-tail interference is sufficient to move the points into the correlation band for almost all cases.

The results corresponding to figure 33 are shown in figure 34 for supersonic wing-body-tail combinations. The effects of wing-tail interference are larger generally than for the subsonic wing-body combinations. The correlation is accurate to within $\pm 0.02l$ for nearly all the combinations.

The effects of Mach number and angle of attack on the center-of-pressure position of wing-body-tail combinations can be very large. The effects of angle of attack are illustrated in figure 28 for subsonic combinations and in figure 29 for supersonic combinations. In figure 28 the theory with and without wing-tail interference is shown. The effects of wing-tail interference are generally large for the combinations illustrated and the effects are generally predicted to within $0.02l$. One important observation is that some large rearward changes in center-of-pressure location with angle of attack are observed and predicted for combinations such as number 101, changes that are comparable in magnitude to the effects of wing-tail interference itself. The rearward shift is due to a decrease in the tail download caused by the wing vortices as the angle of attack increases. An examination of figure 29 for supersonic speeds discloses results similar to those of figure 28. The most significant difference is that the supersonic configurations exhibit more drastic angle-of-attack effects than the subsonic combinations.

One of the important problems of aircraft and missile design, the center-of-pressure travel in the transonic range, is considered in figure 35. The wing-body-tail combinations shown in this figure exhibit very small to large rearward shifts in center-of-pressure position. Another important effect shown is the large rearward shift due to changing the angle of attack. The changes due to angle of attack are in one instance greater than those due to Mach number. With regard to the comparison between experiment and theory, it can be said that the trends with angle of attack and Mach number are well predicted and that the absolute values of the center-of-pressure position are within the $\pm 0.02l$ given as the accuracy of the method by the correlation curves.

Effects of Wing Incidence

Varying the incidence of the wing affects the wing-body and wing-tail interference, while varying the tail incidence affects only the tail-body interference. The effects of wing and tail deflection on wing-body and tail-body interference have already been considered in reference 9, wherein it was shown that the present method predicts the effects with engineering accuracy. Thus, there remain to discuss only the effects of wing deflection on wing-tail interference.

Deflecting a wing positively will normally cause an upload on the wing, but the resulting wing vortex causes a download on the tail. As a result, a considerable pitching moment is developed. For slender wing-body-tail combinations with tail spans greater than the wing span, Morikawa, in reference 12, pointed out that the lift on the tail due to interference is equal and opposite to that on the wing. Under these circumstances a pure couple is developed on the airplane due to wing deflection so that the center of pressure moves forward. The forward movement can be large.

To determine the validity of the present computational method for estimating the effects of wing incidence on the lift and moment interference of complete configurations, estimates are made of the lift and moment characteristics of those combinations for which data for variable wing incidence are available. The estimated and experimental characteristics are compared in figures 36 to 40, inclusive, for several combinations differing widely in Mach number and wing and tail plan form. All combinations exhibit the forward movement of the center of pressure. In the low-angle-of-attack range where the theory applies, the agreement between theory and experiment is good except for the combination of figure 39. This combination, which was tested at supersonic speeds and which has a triangular wing with supersonic leading edges, exhibits a behavior which is not explainable in terms of the theoretical model with one fully rolled-up vortex per wing panel.

A closer examination of figure 39 reveals that the predicted lift due to wing deflection is in good agreement with experiment, but the predicted moment is not realized. Since the predicted moment is due primarily to tail download, it follows that the tail download is not developed. This behavior is explainable in terms of span loading. As yet unpublished experimental results and theoretical results (ref. 4) indicate that for rectangular wings of sufficiently large aspect ratio, the span loading at the juncture of the wing and body is considerably below the maximum span loading on the wing for variable wing incidence at zero angle of attack. This means that the shed vorticity inboard has the opposite sense of rotation of that shed outboard, and upwash

is generated inboard. Under these circumstances it appears that two vortices per wing panel are the least number that can adequately represent the trailing-vortex system. The combination of figure 39 possesses a triangular rather than a rectangular wing, but its effective aspect ratio is 6.8 so that the foregoing effect may be anticipated. A complicating factor is that the shock wave is detached from the wing for all angles greater than about 3° so that the flow is, in part, transonic. Also, the tail span is considerably less than the wing span so that the tail is located largely behind the inboard portions of the wing. For these reasons it is felt that the theoretical model of one vortex per wing panel is inapplicable and that two vortices per wing panel is the minimum number that can describe the gross effects of the phenomenon. However, more experimental work must be done before an accurate theory can be developed to cover this case.

Limitations and Extensions of the Method

In the application of any method such as the present one, the important question of its limitations arises. Because of the very large number of variables specifying a wing-body-tail combination, it is not practical to present correlations covering all possible combinations. For this reason the limitations and possible extensions of the method are best determined by an examination of the assumptions made with regard to configuration geometry, angle of attack, and Mach number.

With regard to configuration effects, the assumption was made that the leading edges are not swept forward nor are the trailing edges swept back. For sweptforward leading edges or sweptback trailing edges, the solution of slender-body theory used to determine $K_{W(B)}$ and $K_{B(W)}$ is not applicable because no account is taken of the trailing-vortex system that passes through the cross-flow planes of the wing-body combination. The use of the correct cross-flow solution, determined by the method of Lomax and Byrd in reference 13, should circumvent this difficulty. However, some successful preliminary correlations between data on swept wing-body combinations and the estimates of the present method (ignoring the sweep of the trailing edges) indicate that the effect may not be large. While the present method is worked out only for unbanked configurations with two wing panels, it seems possible by use of the appropriate slender-body-theory solution to extend the method to banked configurations with any number of wing panels. For interdigitated or high tails the method can be easily generalized. For differential incidence of the wing panels, the method is still applicable if a step-by-step calculation of the type mentioned in reference 15 is used to determine the vortex position at the tail. The model on which the present method is based corresponds to the case of the maximum circulation of the wing-body juncture. A violation of this assumption invalidates the model.

Such a condition could conceivably arise through the use of inverse taper, sweptforward wings, high-aspect-ratio deflected wing panels with supersonic leading edges, or wing panels having large gaps between wing and body.

With regard to angle-of-attack effects, it has already been stated that the assumption of linearity in the present method limits the useful angle-of-attack and wing-deflection ranges of the theory. Body vortices and more than one vortex per wing panel can occur in flow at high angles of attack, as shown by reference 15. With regard to Mach number effects in the transonic and hypersonic ranges, the present method will fail where nonlinear effects become important. However, since the division of lift is not sensitive to span loading, the lift ratios may be applicable in the nonlinear range.

CONCLUSIONS

On the basis of the comparison between predicted and measured lifts and center-of-pressure positions of a large number of wing-body and wing-body-tail combinations, the following conclusions can be drawn:

1. It was determined that the present method predicts lift-curve slope to within ±10 percent for most combinations through the speed range. However, in the transonic range nonlinear effects may reduce the accuracy of the lift prediction.

2. For wing-body and wing-body-tail combinations at subsonic speeds, the center-of-pressure positions are predicted to within ±0.02 of the body length. At supersonic speeds the same accuracy is obtained for wing-body-tail combinations.

3. The effects of wing-tail interference may change the combination lifts by as much as 35 to 40 percent and may change the center-of-pressure positions by as much as 10 to 20 percent of the body length.

4. The nonlinear effects of angle of attack on center-of-pressure position and lift may be as important as those of Mach number.

Ames Aeronautical Laboratory
National Advisory Committee for Aeronautics
Moffett Field, Calif., July 8, 1953

APPENDIX A

DETERMINATION OF $K_{B(W)}$ AND $K_{B(T)}$ FOR NO BODY BEHIND WING OR TAIL TRAILING EDGE

The method for determining $K_{B(W)}$ or $K_{B(T)}$ for the case of no afterbody parallels closely the method used in reference 7 for the afterbody case. Referring to figure 41 the pressure distribution acting on the top of the plan-form area of the body is

$$P = \frac{2}{\pi} \frac{\alpha_W m}{\sqrt{m^2\beta^2-1}} \cos^{-1}\left(\frac{\frac{\xi}{\beta} + m\beta\eta}{\eta + m\xi}\right) \tag{A1}$$

for supersonic leading edges and

$$P = \frac{4\alpha_W(\beta m)^{3/2}}{\pi\beta(m\beta + 1)} \sqrt{\frac{\frac{\xi}{\beta} - \eta}{m\xi + \eta}} \tag{A2}$$

for subsonic edges, where P is the pressure coefficient and α_W is in radians. These results have been taken from references 68 and 69. The lift acting on the body due to using both panels is then

$$L = 4q \int_0^d d\eta \int_{\beta\eta}^{c_r} P \, d\xi \tag{A3}$$

where d is the body diameter. Carrying out this integration and dividing by the lift of the wing alone yields

$$K_{B(W)}\left[\beta\left(C_{L_\alpha}\right)_W\right](\lambda+1)\left(\frac{s}{r} - 1\right) =$$

$$\frac{8}{\pi\sqrt{\beta^2m^2-1}}\left(\frac{\beta d}{c}\right)\left[\left(1+\frac{mc}{d}\right)^2 \cos^{-1}\left(\frac{m\beta+\frac{c}{\beta d}}{1+\frac{mc}{d}}\right) - m^2\beta^2\left(\frac{c}{\beta d}\right)^2 \cos^{-1}\left(\frac{1}{m\beta}\right) + \right.$$

$$\left. m\beta\left(\frac{c}{\beta d}\right)^2 \sqrt{m^2\beta^2-1}\,\sin^{-1}\frac{\beta d}{c} - \sqrt{m^2\beta^2-1}\,\cosh^{-1}\frac{c}{\beta d}\right]; \beta m > 1, \frac{c}{\beta} > d \tag{A4}$$

$$K_{B(W)}\left[\beta\left(C_{L_\alpha}\right)_W\right](\lambda+1)\left(\frac{s}{r}-1\right) =$$

$$\frac{16\sqrt{m\beta}}{\pi(m\beta+1)}\left(\frac{\beta d}{c}\right)\left\{\left(1+\frac{mc}{d}\right)\sqrt{\left(\frac{c}{\beta d}-1\right)\left(\frac{mc}{d}-1\right)}-\left(\frac{c}{\beta d}\right)^2(m\beta)^{3/2}+\right.$$

$$m\beta\left(\frac{c}{\beta d}\right)^2(\beta m+1)\left[\tan^{-1}\sqrt{\frac{1}{\beta m}}-\tan^{-1}\sqrt{\left(\frac{c}{\beta d}-1\right)\Big/\left(\frac{mc}{d}+1\right)}\right]-$$

$$\left.\frac{(m\beta+1)}{\sqrt{m\beta}}\tanh^{-1}\sqrt{m\beta\left(\frac{c}{\beta d}-1\right)\Big/\left(\frac{mc}{d}+1\right)}\right\};\quad \beta m<1,\quad \frac{c}{\beta}>d \qquad (A5)$$

The restriction that $\frac{c}{\beta}>d$ is not a serious one. For $d>\frac{c}{\beta}$ it is clear that the lift transmitted to the body is the same as for $d=\frac{c}{\beta}$ so that $K_{B(W)}$ is constant. The value of the parameter $K_{B(W)}\left[\beta\left(C_{L_\alpha}\right)_W\right](\lambda+1)\left(\frac{s}{r}-1\right)$ is a function only of $m\beta$ and $\beta d/c$, and has been plotted as a function of these two variables in figure 5(a). The figure is so constructed for $\beta d/c>1$ that $K_{B(W)}$ is constant for a given wing panel.

APPENDIX B

DETERMINATION OF TAIL INTERFERENCE FACTOR BY USE OF STRIP THEORY AND SLENDER-BODY THEORY

The tail interference factor to be evaluated is

$$i = \frac{L_T(V)/(L_T)_\alpha}{57.3\,\Gamma_m/2\pi\alpha\,V_o(s_T - r_T)} \tag{B1}$$

The lift ratio is readily evaluated by a combination of strip theory and slender-body theory. The model used to obtain the vertical velocity at the tail induced by the wing vortices is the slender-body model given by figure 42. From the Biot-Savart law for an infinite line vortex, the vertical velocity due to the right external vortex is

$$w = -\frac{\Gamma_m(f - \eta)}{2\pi\,[h^2 + (f - \eta)^2]} \tag{B2}$$

In this equation Γ_m is positive counterclockwise facing upstream, and w is positive upward. The tail is effectively twisted because of the variation of w across its span. All geometric quantities in the derivation are understood to be those of the tail rather than the wing so that no subscript will be used.

The application of strip theory to obtain the load on the tail due to the vortex involves an integration across the exposed part of the tail. As previously discussed, the lift evaluated by this procedure appears partly on the tail panels and partly on the body. If the section lift coefficient is taken as $4/\beta$, the lift due to the right external vortex on the right external panel is

$$L_1 = -\frac{q}{2\pi}\int_r^s \left(\frac{4}{\beta}\right)\frac{\Gamma_m\,(f - \eta)}{h^2 + (f - \eta)^2}\,c_\eta\,d\eta \tag{B3}$$

The value of L_1 obtained by integrating equation (B3) is obtained with

the aid of the following function:

$$L\left(\lambda, \frac{r}{s}, \frac{f}{s}, \frac{h}{s}\right) = \left\{\frac{(s - r\lambda) - f(1 - \lambda)}{2(s - r)} \ln \frac{h^2 + (f - s)^2}{h^2 + (f - r)^2} - \right.$$

$$\left. \frac{(1 - \lambda)}{(s - r)} \left[(s - r) + h \tan^{-1}\left(\frac{f - s}{h}\right) - h \tan^{-1} \frac{f - r}{h}\right]\right\} \quad (B4)$$

as

$$L_1 = \frac{4q \Gamma_m c_r}{2\pi\beta V_o} L\left(\lambda, \frac{r}{s}, \frac{f}{s}, \frac{h}{s}\right) \quad (B5)$$

The lift on the right panel due to the left vortex is

$$L_2 = -\frac{4q \Gamma_m c_r}{2\pi\beta V_o} L\left(\lambda, \frac{r}{s}, -\frac{f}{s}, \frac{h}{s}\right) \quad (B6)$$

Consider the image vortices having coordinates f_i and h_i given by the following equation:

$$\left.\begin{aligned} f_i &= \frac{fr^2}{f^2 + h^2} \\ h_i &= \frac{hr^2}{f^2 + h^2} \end{aligned}\right\} \quad (B7)$$

The lifts of the right and left image vortices are then given, respectively, by

$$L_3 = -\frac{4q \Gamma_m c_r}{2\pi\beta V_o} L\left(\lambda, \frac{r}{s}, \frac{fi}{s}, \frac{hi}{s}\right) \quad (B8)$$

$$L_4 = \frac{4q \Gamma_m c_r}{2\pi\beta V_o} L\left(\lambda, \frac{r}{s}, -\frac{fi}{s}, \frac{hi}{s}\right) \quad (B9)$$

The total lift due to the wing vortices and their images is

$$L_T(V) = \frac{8q\Gamma_m c_r}{2\pi\beta V_o}\left[L\left(\frac{f}{s}\right) - L\left(-\frac{f}{s}\right) - L\left(\frac{fi}{s}\right) + L\left(-\frac{fi}{s}\right)\right] \quad (B10)$$

To obtain the tail interference factor, i, requires a determination of the lift of the tail alone by strip theory to nondimensionalize the foregoing lift quantity.

$$(L_T)_\alpha = \frac{2q\alpha}{57.3}\int_r^s \left(\frac{4}{\beta}\right) c_\eta \, d\eta \quad (B11)$$

Integration gives

$$(L_T)_\alpha = \frac{4\alpha q(s-r)c_r(1+\lambda)}{57.3\ \beta} \quad (B12)$$

Forming the ratio given by equation (B1) yields the following result for i:

$$i = \frac{2}{1+\lambda}\left[L\left(\lambda,\frac{r}{s},\frac{f}{s},\frac{h}{s}\right) - L\left(\lambda,\frac{r}{s},-\frac{f}{s},\frac{h}{s}\right) - L\left(\lambda,\frac{r}{s},\frac{fi}{s},\frac{hi}{s}\right) + L\left(\lambda,\frac{r}{s},-\frac{fi}{s},\frac{hi}{s}\right)\right] \quad (B13)$$

APPENDIX C

DETERMINATION OF TAIL INTERFERENCE FACTOR FOR RECTANGULAR TAILS USING ALDEN-SCHINDEL TECHNIQUE

The technique of Alden and Schindel described in reference 16 can be used for estimating the load on the tail section due to wing vortices. Figure 43 shows the model which is analyzed. The assumption is made that the lift due to the vortices originates on the exposed tail panels even though some of this lift may be carried over onto the body. Thus, an integration across the exposed wing panels gives all the lift. This assumption is the same as that made in evaluating the tail interference factor by strip theory and has been previously discussed. The analysis is carried out with $\beta = 1$ to simplify the algebra, and the β's are reintroduced into the final charts. The essential idea of the Alden-Schindel technique is that the total lift acting on a wing of arbitrary twist can be evaluated by a strip technique wherein the weighting factor for the local strip corresponds to the span loading at the strip for the same plan form at uniform angle of attack in reversed flow. In mathematical form this result is stated as

$$L = \int_{\text{span}} w(\eta)\, F(\eta)\, d\eta \tag{C1}$$

wherein $F(\eta)$ is the weighting factor and $w(\eta)$ is the vertical component of velocity. With reference to figure 43 for model and coordinates, the weighting factor is given for the three regions as

Region I.:

$$F(\eta) = \frac{4qc}{V_o} \tag{C2}$$

Region II.:

$$F(\eta) = \frac{4qc}{V_o}\left[\frac{1}{\pi}\cos^{-1}\left(1 + \frac{2\eta}{c} - \frac{2s}{c}\right) + \frac{2}{\pi}\sqrt{\left(\frac{s}{c} - \frac{\eta}{c}\right) - \left(\frac{s}{c} - \frac{\eta}{c}\right)^2}\right] \tag{C3}$$

Region III.:

$$F(\eta) = \frac{4qc}{V_o}\left[\frac{1}{\pi}\cos^{-1}\left(1 - \frac{2\eta}{c} - \frac{2s}{c}\right) + \frac{2}{\pi}\sqrt{\left(\frac{s}{c} + \frac{\eta}{c}\right) - \left(\frac{s}{c} + \frac{\eta}{c}\right)^2}\right] \tag{C4}$$

The vertical velocity component due to the right external vortex is

$$w(\eta) = -\frac{\Gamma_m(f-\eta)}{2\pi\left[h^2 + (f-\eta)^2\right]} \tag{C5}$$

To evaluate the lift due to the right external vortex the following integration must be performed:

$$L_1 = \int_{-s}^{-s+c} F(\eta)\, w(\eta)\, d\eta + \int_{-s+c}^{-a} F(\eta)\, w(\eta)\, d\eta + \int_{a}^{s-c} F(\eta)\, w(\eta)\, d\eta + \int_{s-c}^{s} F(\eta)\, w(\eta)\, d\eta \tag{C6}$$

Performing the integrations presents some algebraic difficulty. However, the answer was obtained in closed form in terms of the following function:

$$\chi\left(\frac{f}{c},\frac{h}{c},\frac{s}{c},\frac{r}{c}\right) = \frac{L_1}{\Gamma_m q s/\pi V_0} = \frac{2c}{s}\left\{\frac{1}{2}\ln\frac{(\delta_2+1)^2+\left(\frac{2h}{c}\right)^2}{(\delta_1+1)^2+\left(\frac{2h}{c}\right)^2} + (\delta_2-\delta_1) + \right.$$

$$\frac{1}{2}\ln\left[\frac{\delta_1^2 + \left(\frac{2h}{c}\right)^2 + \gamma_1 + \sqrt{2}\,|\delta_1|\sqrt{\alpha_1+\gamma_1} + \sqrt{2}\left(\frac{2h}{c}\right)\sqrt{-\alpha_1+\gamma_1}}{\delta_2^2 + \left(\frac{2h}{c}\right)^2 + \gamma_2 + \sqrt{2}\,|\delta_2|\sqrt{\alpha_2+\gamma_2} + \sqrt{2}\left(\frac{2h}{c}\right)\sqrt{-\alpha_2+\gamma_2}}\right] +$$

$$\frac{\sqrt{2}\,\delta_1\left(\frac{2h}{c}\right)\sqrt{-\alpha_1+\gamma_1}}{\gamma_1} + \frac{\alpha_1\delta_1\sqrt{\alpha_1+\gamma_1}}{\sqrt{2}|\delta_1|\gamma_1} - \frac{\sqrt{2}\,\delta_2\left(\frac{2h}{c}\right)\sqrt{-\alpha_2+\gamma_2}}{\gamma_2} -$$

$$\left.\frac{\alpha_2\delta_2\sqrt{\alpha_2+\gamma_2}}{\sqrt{2}|\delta_2|\gamma_2} + \frac{1}{2}\ln\left[\frac{h^2+(f-s+c)^2}{h^2+(f-r)^2}\right]\left[\frac{h^2+(f+r)^2}{h^2+(f+s-c)^2}\right]\right\} \tag{C7}$$

where

$$\left.\begin{aligned} \delta_1 &= \frac{2f}{c} - \frac{2s}{c} + 1 \\ \delta_2 &= -\frac{2f}{c} - \frac{2s}{c} + 1 \\ \alpha_{1,2} &= \delta_{1,2}^2 - 1 - \left(\frac{2h}{c}\right)^2 \\ \gamma_{1,2} &= \sqrt{\left[\delta_{1,2}^2 - \left(\frac{2h}{c}\right)^2 - 1\right]^2 + 4\,\delta_{1,2}^2 \left(\frac{2h}{c}\right)^2} \end{aligned}\right\} \tag{C8}$$

In terms of the function χ, the lift is

$$L_1 = \frac{\Gamma_m q s}{\pi V_o} \chi\left(\frac{f}{c}, \frac{h}{c}, \frac{s}{c}, \frac{r}{c}\right) \tag{C9}$$

The contribution of the image vortex to the lift must now be determined. The coordinates of the image vortex to the right are

$$\left.\begin{aligned} f_i &= \frac{r^2 f}{f^2+h^2} \\ h_i &= \frac{r^2 h}{f^2+h^2} \end{aligned}\right\} \tag{C10}$$

In terms of these coordinates the lift due to the image vortex, taking into account the change in the sign of the circulation, is

$$L_2 = -\frac{\Gamma_m q s}{\pi V_o} \chi\left(\frac{f_i}{c}, \frac{h_i}{c}, \frac{s}{c}, \frac{r}{c}\right) \tag{C11}$$

The χ function is determined in terms of the following parameters:

$$\left.\begin{aligned}
\delta_3 &= \frac{2f_i}{c} - \frac{2s}{c} + 1 \\
\delta_4 &= -\frac{2f_i}{c} - \frac{2s}{c} + 1 \\
\alpha_{3,4} &= \delta_{3,4}{}^2 - 1 - \left(\frac{2h_i}{c}\right)^2 \\
\gamma_{3,4} &= \sqrt{\left[\delta_{3,4}{}^2 - \left(\frac{2h_i}{c}\right)^2 - 1\right]^2 + 4\,\delta_{3,4}{}^2 \left(\frac{2h_i}{c}\right)^2}
\end{aligned}\right\} \qquad (C12)$$

The lift due to the two external vortices and the two internal vortices is thus

$$2(L_1 + L_2) = \frac{2\Gamma_m qs}{\pi V_o}\left[\chi\left(\frac{f}{c},\frac{h}{c},\frac{s}{c},\frac{r}{c}\right) - \chi\left(\frac{f_i}{c},\frac{h_i}{c},\frac{s}{c},\frac{r}{c}\right)\right] \qquad (C13)$$

The lift so determined is exact within the limits of linear theory. It is necessary to obtain the lift of the wing alone, as given by linear theory, to form the ratio given by the tail interference factor i.

$$i = \frac{2(L_1+L_2)/(L_T)_\alpha}{57.3\,\Gamma_m/2\pi V_o \alpha(s-r)} \qquad (C14)$$

The lift-curve slope of a rectangular tail per radian is

$$\frac{dC_L}{d\alpha} = 4\left(1 - \frac{1}{2A_T}\right) \qquad (C15)$$

so that

$$(L_T)_\alpha = \frac{2c(s-r)q\alpha}{57.3}\,\frac{\left[4\left(1-\frac{r}{s}\right) - \frac{c}{s}\right]}{\left(1-\frac{r}{s}\right)} \qquad (C16)$$

The lift ratio is obtained by division

$$\frac{2(L_1+L_2)}{(L_T)_\alpha} = \left[\frac{57.3\Gamma_m}{\alpha V_o(s-r)}\right]\frac{\left(\frac{s}{c}\right)\left(1-\frac{r}{s}\right)}{\pi\left[4\left(1-\frac{r}{s}\right)-\frac{c}{s}\right]}\left[\chi\left(\frac{f}{c},\frac{h}{c}\right)-\chi\left(\frac{f_i}{c},\frac{h_i}{c}\right)\right] \qquad (C17)$$

or

$$i = \frac{2\left(1-\frac{r}{s}\right)\left(\frac{s}{c}\right)}{\left[4\left(1-\frac{r}{s}\right)-\frac{c}{s}\right]}\left[\chi\left(\frac{f}{c},\frac{h}{c}\right)-\chi\left(\frac{f_i}{c},\frac{h_i}{c}\right)\right] \tag{C18}$$

APPENDIX D

DETERMINATION OF CENTER OF BODY LIFT DUE TO WING AT SUBSONIC SPEEDS

Hitherto, no subsonic method has been available for estimating the center of the lift transferred by a wing or tail to the body. An approximate method for accomplishing this, based on lifting-line theory, is now presented. It is known that a good approximation of the lift and moment characteristics of swept wings at subsonic speeds can be gained by placing a lifting line of variable loading at the wing quarter chord and satisfying the tangency conditions at the three-quarter chord. See, for instance, reference 26. An extension of this model to include the body is shown in figure 21. The image of the quarter-chord line inside the body is obtained by reflecting each point of the quarter-chord line into the body in its cross-flow plane. Since the quarter-chord line is not uniformly loaded, trailing vortices will stream backward from the line proportional in strength to the gradient of the span-loading curve. A series of three horseshoe vortices representing the span loading is shown in figure 21 Image vortices inside the body are also illustrated. In the mathematical treatment that follows, the number of vortices increases without limit.

Consider the quarter-chord line with an elliptical loading

$$\Gamma = \Gamma_m \sqrt{1 - \left(\frac{\eta - r}{s - r}\right)^2} \tag{D1}$$

The strength of the bound vortices is proportional to Γ, for both the external flow and the internal flow. The lift due to the bound part of an elementary horseshoe vortex is proportional to the product of its strength times its length

$$dL \sim \Gamma d\eta_i \sim \Gamma\, d\left(\frac{r^2}{\eta}\right) \sim -\Gamma r^2 \frac{d\eta}{\eta^2} \tag{D2}$$

The lift due to any horseshoe vortex is concentrated at its bound vortex so that the moment about the leading-edge quarter-chord intersection is

$$dM \sim -\frac{\Gamma r^2 \xi d\eta}{\eta^2} \sim -\frac{\Gamma r^2 (\eta - r) \tan \Lambda_{1/4}\, d\eta}{\eta^2} \tag{D3}$$

$$\bar{x}_{B(W)} - \frac{c_r}{4} = \frac{M}{L} = \frac{\tan \Lambda_{1/4} \int_r^s \frac{\Gamma(\eta - r)}{\eta^2} d\eta}{\int_r^s \Gamma \frac{d\eta}{\eta^2}} \tag{D4}$$

$$\bar{x}_{B(W)} - \frac{c_r}{4} = \tan \Lambda_{1/4} \frac{\int_r^s \frac{\sqrt{(s-r)^2 - (\eta-r)^2}}{\eta^2} (\eta - r)\, d\eta}{\int_r^s \frac{\sqrt{(s-r)^2 - (\eta-r)^2}}{\eta^2} d\eta} \tag{D5}$$

The value of $\bar{x}_{B(W)}$ as determined by integrating equation (D5) is

$$\bar{x}_{B(W)} = \frac{c_r}{4} + (s-r) \tan \Lambda_{1/4} \left[\frac{r}{r-s} + \frac{\sqrt{s(s-2r)} \cosh^{-1}\left(\frac{s-r}{r}\right) - (s-r) + \frac{\pi r}{2}}{\frac{(s-r)r}{\sqrt{s(s-2r)}} \cosh^{-1}\left(\frac{s-r}{r}\right) + \frac{(s-r)^2}{r} - \frac{\pi}{2}(s-r)} \right]; \quad s > 2r \tag{D6}$$

REFERENCES

1. Betz, A.: Applied Airfoil Theory. Airfoils or Wings of Finite Span. Vol. IV of Aerodynamic Theory, div. K, ch. III, sec. 1, W.F. Durand, ed., Julius Springer (Berlin), 1934, pp. 152-157.

2. Hopkins, Edward J., and Carel, Hubert C.: Experimental and Theoretical Study of the Effect of Body Size on the Aerodynamic Characteristics of an Aspect Ratio 3.0 Wing-Body Combination. NACA RM A51G24, 1951.

3. Hopkins, Edward J., and Carel, Hubert C.: Experimental and Theoretical Studies of the Interference at Low Speeds Between a Slender Body and Triangular Wings. NACA RM A53A14, 1953.

4. Nielsen, Jack N., and Pitts, William C.: Wing-Body Interference at Supersonic Speeds with an Application to Combinations with Rectangular Wings. NACA TN 2677, 1952.

5. Ferrari, Carlo: Interference Between Wing and Body at Supersonic Speeds - Theory and Numerical Application. Jour. Aero. Sci., vol. 15, 1948, pp. 317-336.

6. Morikawa, George K.: The Wing-Body Problem for Linearized Supersonic Flow. Calif. Inst. of Tech., Doctoral Thesis, 1949.

7. Nielsen, Jack N., and Kaattari, George E.: Method for Estimating Lift Interference of Wing-Body Combinations at Supersonic Speeds. NACA RM A51J04, 1951.

8. Kaattari, George E., Nielsen, Jack N., and Pitts, William C.: Method for Estimating Pitching-Moment Interference of Wing-Body Combinations at Supersonic Speeds. NACA RM A52B06, 1952.

9. Nielsen, Jack N., Kaattari, George E., and Drake, William C.: Comparison Between Prediction and Experiment for All-Movable Wing and Body Combinations at Supersonic Speeds - Lift, Pitching Moment, and Hinge Moment. NACA RM A52D29, 1952.

10. Silverstein, Abe: Toward a Rational Method of Tail-Plane Design. Jour. Aero. Sci., vol. 6, 1939, pp. 361-369.

11. Silverstein, Abe, and Katzoff, S.: Design Charts for Predicting Downwash Angles and Wake Characteristics Behind Plain and Flapped Wings. NACA Rep. 648, 1939.

12. Morikawa, George: Supersonic Wing-Body-Tail Interference. Jour. Aero. Sci., vol. 19, no. 5, 1952, pp. 333-340.

13. Lomax, Harvard, and Byrd, Paul F.: Theoretical Aerodynamic Characteristics of a Family of Slender Wing-Tail-Body Combinations. NACA TN 2554, 1951.

14. Lagerstrom, Paco A., and Graham, Martha E.: Aerodynamic Interference in Supersonic Missiles. Douglas Aircraft Co., Rep. No. SM-13743, 1950.

15. Spahr, Richard J., and Dickey, Robert R.: Vortex Wake and Downwash Field Behind Triangular Wings and Wing-Body Combinations at Supersonic Speeds. NACA RM A53D10, 1952.

16. Alden, Henry L., and Schindel, Leon H.: The Calculation of Wing Lift and Moments in Nonuniform Supersonic Flows. M.I.T. Meteor Rep. 53, 1950.

17. Grigsby, Carl E.: The Use of the Rolled-Up Vortex Concept for Predicting Wing-Tail Interference and Comparison with Experiment at Mach Number of 1.62 for a Series of Missile Configurations Having Tandem Cruciform Lifting Surfaces. NACA RM L52H05, 1952.

18. Edwards, Samuel S.: Experimental and Theoretical Study of Factors Influencing the Longitudinal Stability of an Air-to-Air Missile at a Mach Number of 1.4. NACA RM A52J19, 1952.

19. Edelman, Gilbert M.: Wing-Body and Wing-Body-Tail Interaction at Supersonic Speeds for Generalized Missile Configurations at High Angles of Attack. U. S. Navy Symposium on Aeroballistics, May 13-14, 1952.

20. Rainey, Robert W.: An Investigation of Several Supersonic Missile Configurations Directed Toward Minimizing Center-of-Pressure Travel. NACA RM L52G01, 1952.

21. Tsien, Hsue-Shen: Supersonic Flow Over an Inclined Body of Revolution. Jour. Aero. Sci., vol. 5, no. 12, Oct. 1938, pp. 480-483.

22. Canning, Thomas C., and Denardo, Billy Pat: Investigation of the Lift and Center of Pressure of Low-Aspect-Ratio, Cruciform, Triangular, and Rectangular Wings in Combination With a Slender Fuselage at High Supersonic Speeds. NACA RM A52C24, 1952.

23. Allen, H. Julian, and Perkins, Edward W.: Characteristics of Flow Over Inclined Bodies of Revolution. NACA RM A50L07, 1951.

24. Nielsen, Jack N., Katzen, Elliot D., and Tang, Kenneth K.: Lift and Pitching-Moment Interference Between a Pointed Cylindrical Body and Triangular Wings of Various Aspect Ratios at Mach Numbers of 1.50 and 2.02. NACA RM A50F06, 1950.

25. Spreiter, John R.: Aerodynamic Properties of Slender Wing-Body Combinations at Subsonic, Transonic, and Supersonic Speeds. NACA Rep. 962, 1950.

26. DeYoung, John, and Harper, Charles W.: Theoretical Symmetric Span-Loading at Subsonic Speeds for Wings Having Arbitrary Planform. NACA TR 921, 1948.

27. Spreiter, John R., and Sacks, Alvin H.: The Rolling-Up of the Trailing Vortex Sheet and Its Effect on Downwash Behind Wings. Jour. Aero. Sci., vol. 18, no. 1, 1951, pp. 21-32.

28. Edwards, Sherman, and Hikido, Katsumi: A Method for Estimating the Rolling Moments Caused by Wing-Tail Interference for Missiles at Supersonic Speeds. NACA RM A53H18, 1953.

29. Lagerstrom, Paco A., and Van Dyke, M. D.: General Considerations About Planar and Non-Planar Lifting Systems. Douglas Aircraft Co., Rep. No. SM-13432, 1949.

30. Heaslet, Max. A., and Spreiter, John R.: Reciprocity Relations in Aerodynamics. NACA TN 2700, 1952.

31. Hill, J. A. F.: An Electrical Analog for Studying Wing-Tail Interference on Guided Missiles. Description of Method. U. S. Navy Symposium on Aeroballistics, May 13-14, 1952

32. Lawrence, H. R.: The Lift Distribution on Low Aspect Ratio Wings at Subsonic Speeds. Jour. Aero. Sci., vol. 18, no. 10, 1951, pp. 683-695.

33. Lagerstrom, Paco A., Wall, D., and Graham, M. E.: Formulas in Three-Dimensional Wing Theory. Douglas Aircraft Co., Rep. No. SM-11901, 1946.

34. Lapin, Ellis: Charts for the Computation of Lift and Drag of Finite Wings at Supersonic Speeds. Douglas Aircraft Co., Rep. No. SM-13480, 1949.

35. Johnson, Ben H., Jr., and Rollins, Francis W.: Investigation of a Thin Wing of Aspect Ratio 4 in the Ames 12-Foot Pressure Wind Tunnel. V. - Static Longitudinal Stability and Control Throughout the Subsonic Speed Range of a Semispan Model of a Supersonic Airplane. NACA RM A9I01, 1949.

36. Lauritsen, Charles H.: Wind Tunnel Tests at Transonic Speeds of the MX-770 Missile Without Ram-Jets. North American Aviation, Inc., Rep. No. AL-629, 1948.

37. Strohmeyer, William E.: Supersonic Wind Tunnel Tests at M = 1.73 of MX-770 Canard and Conventional Configurations. North American Aviation, Inc., Rep. No. AL-545, 1948.

38. Magnus, R. J., Beal, R. R., and Kutschinski, C. R.: Sparrow 13-D, Analysis of Force and Moment Characteristics from Subsonic Wind-Tunnel Tests of a 50-Percent-Scale Model. Douglas Aircraft Co., Rep. No. SM-13632, 1950.

39. Beek, Charles R., and Anderson, Arnold W.: Wind-Tunnel Tests of the XSSM-N-6 (Rigel) Pilotless Aircraft. Part II. - Longitudinal and Lateral Stability Characteristics of a 1/4-Scale Model with Single Booster. David W. Taylor Model Basin Rep. C-201, Aero. 760, 1949.

40. Heitmeyer, John C.: Lift, Drag, and Pitching Moment of Low-Aspect-Ratio Wings at Subsonic and Supersonic Speeds - Plane Triangular Wing of Aspect Ratio 3 with NACA 0003-63 Section. NACA RM A51H02, 1951.

41. Reese, David E., and Phelps, E. Ray: Lift, Drag, and Pitching Moment of Low-Aspect-Ratio Wings at Subsonic and Supersonic Speeds - Plane Tapered Wing of Aspect Ratio 3.1 With 3-Percent-Thick Biconvex Section. NACA RM A50K28, 1951.

42. Cahn, Maurice S., and Bryan, Carroll R.: A Transonic-Wing Investigation in the Langley 8-Foot High-Speed Tunnel at High Subsonic Mach Numbers and at a Mach Number of 1.2 Wing-Fuselage Configuration Having a Wing with 0° Sweepback, Aspect Ratio 4.0, Taper Ratio 0.6, and NACA 65A006 Airfoil Section. NACA RM L51A02, 1951.

43. Smith, Donald W., and Heitmeyer, John C.: Lift, Drag, and Pitching Moment of Low-Aspect-Ratio Wings at Subsonic and Supersonic Speeds - Plane Triangular Wings of Aspect Ratio 2 With NACA 0008-63 Section. NACA RM A50K20, 1951.

44. Heitmeyer, John C.: Lift, Drag, and Pitching Moment of Low-Aspect-Ratio Wings at Subsonic and Supersonic Speeds - Plane Triangular Wing of Aspect Ratio 4 with 3-Percent-Thick Biconvex Section. NACA RM A51D30, 1951.

45. Weber and Kehl: Wind-Tunnel Measurements on the Henschel Missile "Zitterrochen" in Subsonic and Supersonic Velocities. NACA TM 1159, 1948.

46. Smith, Donald W., and Heitmeyer, John C.: Lift, Drag, and Pitching Moment of Low-Aspect-Ratio Wings at Subsonic and Supersonic Speeds - Plane Triangular Wing of Aspect Ratio 2 with NACA 0005-63 Section. NACA RM A50K21, 1951.

47. Heitmeyer, John C., and Hightower, Ronald C.: Lift, Drag, and Pitching Moment of Low-Aspect-Ratio Wings at Subsonic and Supersonic Speeds - Plane Triangular Wing of Aspect Ratio 4 with 3-Percent-Thick Rounded Nose Section. NACA RM A51F21, 1951.

48. Anderson, Adrien E.: An Investigation at Low Speed of a Large-Scale Triangular Wing of Aspect Ratio Two. III. Characteristics of Wing with Body and Vertical Tail. NACA RM A9H04, 1949.

49. Polhamus, Edward C., and King, Thomas J. Jr.: Aerodynamic Characteristics with Fixed and Free Transition of a Modified Delta Wing in Combination with a Fuselage at High Subsonic Speeds. NACA RM L50C21, 1950.

50. House, Rufus O., and Wallace, Arthur R.: Wind-Tunnel Investigation of Effect of Interference on Lateral-Stability Characteristics of Four NACA 23012 Wings, an Elliptical and a Circular Fuselage, and Vertical Fins. NACA Rep. 705, 1941.

51. McKay, James M., and Hall, Albert W.: The Effects on the Aerodynamic Characteristics of Reversing the Wing of a Triangular Wing-Body Combination at Transonic Speeds as Determined by the NACA Wing-Flow Method. NACA RM L51H23, 1951.

52. Smalley, J. H.: Wind-Tunnel Investigation of a 3/4-Scale Model of the XAAM-N-4 (Oriole) Guided Missile. David W. Taylor Model Basin Rep. C-305 Aero.785, 1950.

53. Payne, W. Randolph: Wind-Tunnel Tests of the XSSM-N-6 (Rigel) Pilotless Aircraft. Part I - Longitudinal and Lateral Stability Characteristics of a 1/5-Scale Model. David W. Taylor Model Basin Rep. C-161, Aero.760, 1948.

54. Niewald, Roy J., and Moul, Martin T.: The Longitudinal Stability, Control Effectiveness, and Control Hinge-Moment Characteristics Obtained from a Flight Investigation of a Canard Missile Configuration at Transonic and Supersonic Speeds. NACA RM L50I27, 1950.

55. Brown, Clarence A., and Lundstrom, Reginald R.: Flight Investigation From Mach Number 0.8 to Mach Number 2.0 to Determine Some Effects of Wing-to-Tail Distance on the Longitudinal Stability and Control Characteristics of a 60° Delta-Wing-Canard Missile. NACA RM L52C26, 1952.

56. Spahr, J. Richard, and Robinson, Robert A.: Wind-Tunnel Investigation at Mach Numbers of 1.5 to 2.0 of a Canard Missile Configuration. NACA RM A51C08, 1951.

57. Rainey, Robert W.: Langley 9-Inch Supersonic Tunnel Tests of Several Modifications of a Supersonic Missile Having Tandem Cruciform Lifting Surfaces. Three-Component Data Results of Models Having Ratios of Wing Span to Tail Span Equal to and Less Than 1 and Some Static Rolling-Moment Data. NACA RM L50G07, 1951.

58. Ellis, Macon C., and Grigsby, Carl E.: Aerodynamic Investigation of Mach Number of 1.92 of a Rectangular Wing and Tail and Body Configuration and Its Components. NACA RM L9L28a, 1950.

59. Grigsby, Carl E.: Tests at Mach Number of 1.62 of a Series of Missile Configurations Having Tandem Cruciform Lifting Surfaces. NACA RM L51J15, 1952.

60. Fischer, H. S.: Supersonic Wind-Tunnel Tests of a 0.075 Scale Model of the Nike 482 Missile. Douglas Aircraft Co., Rep. No. SM-13848, 1950.

61. Harshman, J., and Uddenberg, R. C.: Supersonic Wind Tunnel Tests of GAPA Models at a Mach Number of 1.28 in the Aberdeen Tunnel. Boeing Aircraft Company Document No. D-7817, 1946.

62. Uddenberg, R. C.: Supersonic Wind Tunnel Tests of GAPA Models at a Mach Number of 1.72 in the Aberdeen Tunnel. Boeing Aircraft Company Document No. D-7818, 1946.

63. Uddenberg, R. C.: Supersonic Wind Tunnel Tests of GAPA Models at a Mach Number of 1.72 in the Aberdeen Tunnel Supplement A - Results From the Fourth Aberdeen Test Period. Boeing Aircraft Company Document No. D-7818A, 1947.

64. Beal, R. R.: Analysis of Force and Moment Characteristics From Supersonic Wind-Tunnel Tests of a 13.5-Percent-Scale Model of the Sparrow 14-B at Mach Number 1.50 Including the Effects of Systematic Variations of Wing Planform. Douglas Aircraft Co., Rep. No. SM-20175, 1951.

65. Mead, Merrill H.: Experimental Investigation of the Aerodynamic Characteristics of an Air-to-Air Missile Employing Cruciform Wings and Tails of Rectangular Plan Form at Mach Numbers of 1.4 and 1.9. NACA RM A52K14, 1953.

66. McDevitt, John B.: A Correlation by Means of Transonic Similarity Rules of the Experimentally Determined Characteristics of 22 Rectangular Wings of Symmetrical Profile. NACA RM A51L17b, 1952.

67. Coletti, Donald E.: Investigation of Interference Lift, Drag, and Pitching Moment of a Series of Rectangular Wing and Body Combinations at Mach Numbers of 1.62, 1.93, and 2.41. NACA RM L52E26, 1952.

68. Jones, R. T.: Thin Oblique Airfoils at Supersonic Speeds. NACA TN 1107, 1946.

69. Lagerstrom, P. A.: Linearized Supersonic Theory of Conical Wings. NACA TN 1685, 1948.

TABLE I.- WING-BODY-TAIL INTERFERENCE CALCULATING FORM

1	M_o = 1.99
2	R = 0.81×10^6
3	l_M = 5.25
4	S_R = 5.062
5	l_R = 10.5
6	$\beta = \sqrt{\lvert M_o^2 - 1 \rvert}$ = 1.72

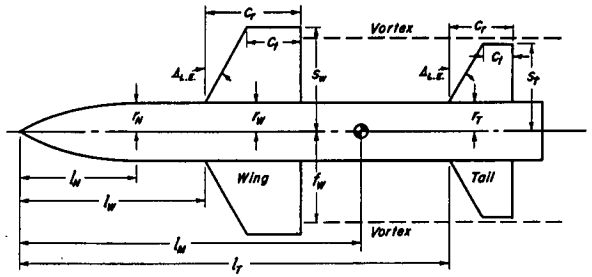

Wing-body				Tail-body				Body-nose			
7	r_W = 0.5625	16	(⑧-⑦)(⑨+⑩) = S_W = 5.062	23	r_T = 0.5625	32	(㉔ - ㉓)(㉕ + ㉖) = S_T = 1.5625	39	r_N = 0.5625		
8	s_W = 2.8125	17	$4⑥(⑧-⑦)^2/⑯$ = βA_W = 6.88	24	s_T = 1.8125	33	$4⑥(㉔-㉓)^2/㉜$ = βA_T = 6.88	40	$S_N = \pi (39)^2$ = 0.994		
9	c_t = 0	18	$\beta d/c_r = 2⑥⑦/⑩$ = 0.86	25	c_t = 0	34	$\beta d/c_r = 2⑥㉓/㉖$ = 1.548	41	l_N = 3.19		
10	c_r = 2.25	19	$⑰(1+1/⑮)(1+⑬)$ = $\beta A(1+1/m\beta)(1+\lambda)$ = 10.875	26	c_r = 1.25	35	$㉝(1+1/㉛)(1+㉙)$ = $\beta A(1+1/m\beta)(1+\lambda)$ = 10.87	42	V_N = 1.56 (2)		
11	$\Lambda_{L.E.}$ = 45°	20	x_h = 1.375	27	$\Lambda_{L.E.}$ = 45°	36	$S_T/S_W = ㉜/⑯$ = 0.3087	43			
12	l_W = 3.75	21	$[⑩-⑳]/57.3$ = 0.0153	28	l_T = 9.16	37		44			
13	$\lambda_W = ⑨/⑩ = c_t/c_r$ = 0			29	$\lambda_T = ㉕/㉖$ = 0			45			
14	$(r/s)_W = ⑦/⑧$ = 0.2			30	$(r/s)_T = ㉓/㉔$ = 0.3104			46			
15	$(m\beta) = ⑥\text{ctn}⑪$ = 1.72			31	$(m\beta) = ⑥\text{ctn}㉗$ = 1.72						
	Instructions		Items		Instructions		Items		Items		
47	Fig. 2		$K_{W(B)}$ = 1.16	63	Fig. 2		$K_{T(B)}$ = 1.27	79	$S_N/S_R = ㊵/⑭$ = 0.1963		
48	Fig. 2; $M_o>1$, ⑲>4, Fig. 5		$K_{B(W)}$ = 0.231	64	Fig. 2; $M_o>1$, ㉟>4, Fig. 5		$K_{B(T)}$ = 0.129 (no afterbody)	80	$K_N = (C_{L_\alpha})_B ㊴/㊷$ = 0.169(4)		
49	Fig. 2 if $\delta_W \neq 0$		$k_{W(B)}$ = 0.94	65	Fig. 2, if $\delta_T \neq 0$		$k_{T(B)}$ = 0.93	81	$V_N/S_N = ㊷/㊵$ = 1.57(2)		
50	Fig. 2 if $\delta_W \neq 0$		$k_{B(W)}$ = 0.23	66	Fig. 2, if $\delta_T \neq 0$		$k_{B(T)}$ = 0.33	82	$\bar{l}_N = ㊶ - ㉛$ = 1.62 (2)		
51	$M_o<1$, Fig. 17 or Ref. 26		$(\bar{x}/c_r)_{W(B)\alpha}$ (3)	67	$M_o<1$, Fig. 17 or Ref. 26		$(\bar{x}/c_r)_{T(B)\alpha}$ (3)	83	$\bar{l}_N/l_N$ = (3)		
52	$M_o>1$, Fig. 18		$(\bar{x}/c_r)_{W(B)\delta}$ = 0.667	68	$M_o>1$, Fig. 18		$(\bar{x}/c_r)_{T(B)\delta}$ = 0.667	84	$\bar{l}_N = ㉝ ㊶$ (3)		
53	⑫ + (51) ⑩		$\bar{l}_{W(B)\alpha}$ = 5.25	69	㉘ + (67) ㉖		$\bar{l}_{T(B)\alpha}$ = 9.994	85	$l_M - \bar{l}_N = ③ - \bar{l}_N$ = 3.63		
54	⑫ + (52) ⑩		$\bar{l}_{W(B)\delta}$ = 5.25	70	㉘ + (68) ㉖		$\bar{l}_{T(B)\delta}$ = 9.994	86			
55	③ - (53)		$l_M - \bar{l}_{W(B)\alpha}$ = 0	71	③ - (69)		$l_M - \bar{l}_{T(B)\alpha}$ = -4.744	87			
56	③ - (54)		$l_M - \bar{l}_{W(B)\delta}$ = 0	72	③ - (70)		$l_M - \bar{l}_{T(B)\delta}$ = -4.744				
57	$M_o<1$; Fig. 22; $M_o>1$, Fig. 19(a-b) if ⑲>4; $M_o>1$, Fig. 20(a-i) if ⑲<4		$(\bar{x}/c_r)_{B(W)}$ = 0.938	73	$M_o<1$, Fig. 22; $M_o>1$, Fig. 19(a-b) if ㉟>4; $M_o>1$, Fig. 20(a-i) if ㉟<4		$(\bar{x}/c_r)_{B(T)}$ = 0.667				
58	⑫ + (57) ⑩		$\bar{l}_{B(W)}$ = 5.861	74	㉘ + (73) ㉖		$\bar{l}_{B(T)\alpha}$ = 9.994				
59	③ - (58)		$l_M - \bar{l}_{B(W)}$ = -0.611	75	③ - (74)		$l_M - \bar{l}_{B(T)}$ = -4.744				
60	$M_o<1$, Fig. 8; $M_o>1$, Fig. 9		$(f-r)_W/(s-r)_W$ = 0.678	76							
61	⑧ - ⑦		$(s-r)_W$ = 2.250	77	㉔ - ㉓		$(s-r)_T$ = 1.250				
62	$M_o<1$, Ref. 26; $M_o>1$, Ref. 33-34 or experiment $\left((C_{L_\alpha})_W = 0.0406\right)$		$⑯\left(C_{L_\alpha}\right)_W/⑭$ = 0.0406 (1)	78	$M_o<1$, Ref. 26; $M_o>1$, Ref. 33-34 or experiment $\left((C_{L_\alpha})_T = 0.0406\right)$		$㉜\left(C_{L_\alpha}\right)_T/⑭$ = 0.0125 (1)				

Combination - No wing-tail interference

88	$C_{L_\alpha} = \left[\left((80)+(47)+(48)\right)(62)+\left((63)+(64)\right)(78)\right] = 0.0808$	91	$C_{m_\alpha} = \left[\left((80)(85)+(47)(55)+(48)(59)\right)(62)+\left((63)(71)+(64)(75)\right)(78)\right]/(5) = -0.00607$
89	$C_{L_{\delta_W}} = \left((49)+(50)\right)(62) = 0.0475$	92	$C_{M_{\delta_W}} = \left((49)(56)+(50)(59)\right)\frac{(62)}{(5)} = -0.000543$
90	$C_{L_{\delta_T}} = \left((65)+(66)\right)(78) = 0.0158$	93	$C_{M_{\delta_T}} = \left((65)(72)+(66)(75)\right)\frac{(78)}{(5)} = -0.00712$

Lift							Moment				
94	95	96	97	98	99	100	101	102	103	104	105
			(88)(94)	(89)(95)	(90)(96)	(97)+(98)+(99)	(91)(94)	(92)(95)	(93)(96)	(101)+(102)+(103)	(104)/(100)
α°	δ_W°	δ_T°				C_{L_c}				C_{M_c}	$(l_M-\bar{l})/l_r$
0	4.9	0	0	0.2328	0	0.233	0	-0.0027	0	-0.0027	-0.0116
5	↓	↓	.4040	↓	↓	.637	-.0304	↓	↓	-.0331	-.0520
10			.8080			1.041	-.0607			-.0634	-.0609
15			1.2120			1.445	-.0911			-.0938	-.0649

Combination - With wing-tail interference

106	$\frac{(62)(78)(6)(77)(4)\ 57.3}{2\pi\ (33)(60)(61)(32)} = 0.00307$	108	$f_w/e_t = \frac{(60)(61)+(7)}{(24)} = 1.152$ (6)
107	$\left[(69)-(12)-(10)\right]/57.3 = 0.0697$	109	

Lift									Moment		
112	113	114	115(6)	116	117	118	119	120	121	122	123
(107)(94)	(95)(21)	(112)-(113)/(24)	Fig. 13	(47)(94)	(49)(95)	(116)+(117)	(109)(115)(116)	(119)+(100)	(119)(71)/(5)	(104)+(121)	(122)/(120)
		(h/e_T)	$\bar{l}$					C_{L_c}		C_{M_c}	$(l_M-\bar{l})/l_r$
0	0.075	-0.042	-2.16	0	4.606	4.606	-0.0306	0.2022	0.0138	0.0111	0.0549
.349	↓	.151	-2.02	5.80	↓	10.406	-.0646	.5722	.0292	-.0039	-.0068
.697		.343	-1.71	11.60		16.206	-.0851	.9557	.0384	-.0250	-.0262
1.046		.536	-1.44	17.40		22.006	-.0973	1.3475	.0440	-.0498	-.0370

SUMMARY OF LIFT AND MOMENT COMPONENTS

		BODY	BODY-WING	BODY-TAIL	BODY-WING-TAIL
124	$(C_{L_\alpha})_{\alpha=\delta_W=0}$	$(80)(62) = 0.0068$	$\left((80)+(47)+(48)\right)(62) = 0.0631$	$\left[(63)+(64)\right](78) = 0.0175$	$(68)+(106)(47)(115) = 0.0731$
125	$(C_{m_\alpha})_{\alpha=\delta_W=0}$	$\frac{(124)(85)}{(5)} = 0.00237$	$\left[(80)(85)+(47)(55)+(48)(59)\right]\frac{(62)}{(5)} = 0.00182$	$\left[(63)(71)+(64)(75)\right]\frac{(78)}{(5)} = -0.00785$	$(91)+\frac{(106)(47)(115)(71)}{(5)} = -0.00259$
126	$(C_{L_{\delta_W}})_{\alpha=\delta_W=0}$		$(89) = 0.0475$		$(89)+(106)(49)(115) = 0.0413$
127	$(C_{m_{\delta_W}})_{\alpha=\delta_W=0}$		$(92) = -0.000543$		$(92)+\frac{(106)(49)(115)(71)}{(5)} = 0.00228$

Notes

(1)	Lift-curve slope per degree
(2)	Omit for ogival noses
(3)	See reference 9 for more detailed information on these quantities
(4)	Use experimental value per degree based on S_N. If not available, use slender-body value: $C_{L_{\alpha_B}} = 2/57.3$
(5)	Ogival nose only, Figure 23.
(6)	For rectangular tails at (108) <1 use equations C-7 and C-18 to obtain i.

NACA

TABLE II.- SUMMARY OF GEOMETRIC AND AERODYNAMIC CHARACTERISTICS AND TEST CONDITIONS FOR WING-BODY COMBINATIONS

(a) Geometric Characteristics

No.	Sketch	M_o	R	r_N	l_R	l_M	l	Section	$\frac{t}{c}$	12_c	A_W	βA	$\Lambda_{L.E.}$	λ	r_W	$\left(\frac{r}{s}\right)_M$	Ref.	Facility
1a		0.20	1.86×10^6	6.48	18.67	70.5	146	[2]hex.	0.042	17.40	64.20	3.43	9.45°	0.546	6.43	0.179	35	Ames 12 ft
b		.50	1.86×10^6	6.48	18.67	70.5	146	hex.	.042	17.40	64.20	3.02	9.45°	.546	6.43	.179	35	Ames 12 ft
c		.70	1.86×10^6	6.48	18.67	70.5	146	hex.	.042	17.40	64.20	2.49	9.45°	.546	6.43	.179	35	Ames 12 ft
d		.80	1.86×10^6	6.48	18.67	70.5	146	hex.	.042	17.40	64.20	2.10	9.45°	.546	6.43	.179	35	Ames 12 ft
e		.90	1.86×10^6	6.48	18.67	70.5	146	hex.	.042	17.40	64.20	1.52	9.45°	.546	6.43	.179	35	Ames 12 ft
2a		.80	$.78\times10^6$	.8125	1.625	6.575	13.075	[3]b.c.	- - -	2.91	8.06	1.03	45°	.401	.812	.258	36	OAL
b		.90	- - -	.8125	1.625	6.575	13.075	b.c.	- - -	2.91	8.06	.744	45°	.401	.812	.258	36	OAL
c		1.10	$.67\times10^6$	.8125	1.625	6.575	13.075	b.c.	- - -	2.91	8.06	.782	45°	.401	.812	.258	36	OAL
d		1.73	1.60×10^6	.8125	1.625	6.575	13.075	b.c.	- - -	2.91	8.06	2.41	45°	.401	.812	.258	37	OAL
3a		.80	$.36\times10^6$	.8125	1.625	6.575	13.075	b.c.	- - -	1.34	1.51	1.18	45°	.341	.546	.308	36	OAL
b		.90	- - -	.8125	1.625	6.575	13.075	b.c.	- - -	1.34	1.51	.856	45°	.341	.546	.308	36	OAL
c		1.10	$.31\times10^6$	.8125	1.625	6.575	13.075	b.c.	- - -	1.34	1.51	.900	45°	.341	.546	.308	36	OAL
d		1.73	$.74\times10^6$	.8125	1.625	6.575	13.075	b.c.	- - -	1.34	1.51	2.77	45°	.341	.546	.308	37	OAL
4a	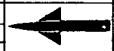	.465	1.95×10^6	2.0	8.38	36.46	64.41	[4]d.w.	.029	8.38	23.24	2.06	60°	0	2.0	.216	38	CAL & CWT
b		.70	1.33×10^6	2.0	8.38	36.46	64.41	d.w.	.029	8.38	23.24	1.66	60°	0	2.0	.216	38	CAL & CWT
c		.90	1.05×10^6	2.0	8.38	36.46	64.41	d.w.	.029	8.38	23.24	1.01	60°	0	2.0	.216	38	CAL & CWT
5a	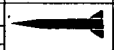	.465	$.91\times10^6$	2.0	8.38	36.46	64.41	d.w.	.030	3.92	57.53	3.54	45°	0	2.0	.254	38	CAL & CWT
b		.70	$.62\times10^6$	2.0	8.38	36.46	64.41	d.w.	.030	3.92	57.53	2.86	45°	0	2.0	.254	38	CAL & CWT
c		.90	$.49\times10^6$	2.0	8.38	36.46	64.41	d.w.	.030	3.92	57.53	1.74	45°	0	2.0	.254	38	CAL & CWT
[5]6	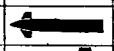	.204	$.30\times10^6$	3.50	7.00	76.26	80.41	d.w.	.05	2.69	11.14	2.46	26.6°	.500	3.45	.514	39	DTMB
[5]7	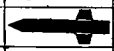	.204	$.82\times10^6$	3.50	7.00	76.26	80.41	hex.	.06	7.45	50.69	2.86	14°	.462	3.50	.250	39	DTMB
8a	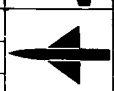	.60	4.1×10^6	2.38	14.39	28.11	46.93	NACA 0003-63	.03	12.27	20.50	2.40	53.1°	0	2.38	.147	40	Ames 6x6 ft
b		.90	4.1×10^6	2.38	14.39	28.11	46.93	NACA 0003-63	.03	12.27	20.50	1.31	53.1°	0	2.38	.147	40	Ames 6x6 ft
c		1.20	4.1×10^6	2.38	14.39	28.11	46.93	NACA 0003-63	.03	12.27	20.50	1.99	53.1°	0	2.38	.147	40	Ames 6x6 ft
d		1.40	4.1×10^6	2.38	14.39	28.11	46.93	NACA 0003-63	.03	12.27	20.50	2.94	53.1°	0	2.38	.147	40	Ames 6x6 ft
e		1.53	4.1×10^6	2.38	14.39	28.11	46.93	NACA 0003-63	.03	12.27	20.50	3.47	53.1°	0	2.38	.147	40	Ames 6x6 ft
f		1.70	4.1×10^6	2.38	14.39	28.11	46.93	NACA 0003-63	.03	12.27	20.50	4.13	53.1°	0	2.38	.147	40	Ames 6x6 ft
9a		.60	2.22×10^6	2.38	11.32	23.88	46.93	b.c.	.03	10.50	20.29	2.26	19.1°	.427	2.38	.145	41	Ames 6x6 ft
b		.70	2.22×10^6	2.38	11.32	23.88	46.93	b.c.	.03	10.50	20.29	2.02	19.1°	.427	2.38	.145	41	Ames 6x6 ft
c		.80	2.22×10^6	2.38	11.32	23.88	46.93	b.c.	.03	10.50	20.29	1.69	19.1°	.427	2.38	.145	41	Ames 6x6 ft
d		.90	2.22×10^6	2.38	11.32	23.88	46.93	b.c.	.03	10.50	20.29	1.23	19.1°	.427	2.38	.145	41	Ames 6x6 ft
e		1.20	2.22×10^6	2.38	11.32	23.88	46.93	b.c.	.03	10.50	20.29	1.87	19.1°	.427	2.38	.145	41	Ames 6x6 ft
f		1.40	2.22×10^6	2.38	11.32	23.88	46.93	b.c.	.03	10.50	20.29	2.77	19.1°	.427	2.38	.145	41	Ames 6x6 ft
g		1.60	2.22×10^6	2.38	11.32	23.88	46.93	b.c.	.03	10.50	20.29	3.53	19.1°	.427	2.38	.145	41	Ames 6x6 ft
h		1.90	2.22×10^6	2.38	11.32	23.88	46.93	b.c.	.03	10.50	20.29	4.56	19.1°	.427	2.38	.145	41	Ames 6x6 ft

TABLE II.- SUMMARY OF GEOMETRIC AND AERODYNAMIC CHARACTERISTICS AND TEST CONDITIONS FOR WING-BODY COMBINATIONS - Continued

(b) Aerodynamic Characteristics

No.	M_o	K_N	$K_{W(B)}$	$K_{B(W)}$	Theoretical								Experimental		
					e_{Lift}			Center of pressure					e_{Lift}		c.p.
					$\beta C_{L_{\alpha_W}}$	$\beta C_{L_{\alpha_N}}$	$\beta C_{L_{\alpha_C}}$	$\bar{l}_N$	$\bar{l}_{W(B)}$	$\bar{l}_{B(W)}$	$\bar{l}_C$	$\left(\frac{\bar{l}}{l}\right)_C$	$\beta C_{L_{\alpha_B}}$	$\beta C_{L_{\alpha_C}}$	$\left(\frac{\bar{l}}{l}\right)_C$
1a	0.20	0.077	1.14	0.24	3.47	0.27	5.05	33.4	70.76	70.05	68.67	0.470		4.70	0.471
b	.50	.072	1.14	.24	3.16	.23	4.59	33.4	70.76	69.99	68.78	.471		4.35	.468
c	.70	.067	1.14	.24	2.83	.19	4.10	33.4	70.76	69.82	68.87	.472		3.94	.470
d	.80	.063	1.14	.24	2.51	.16	3.62	33.4	70.76	69.60	68.94	.472		3.56	.470
e	.90	.057	1.14	.24	2.02	.12	2.90	33.4	70.76	69.23	69.02	.473		3.08	.475
2a	.80	(.214)	1.22	.38	1.43	.194	2.60	2.52	9.73	9.39	8.80	.673	(0.305)	2.51	.690
b	.90	(.232)	1.22	.38	1.04	.141	1.90	2.52	9.70	9.32	8.71	.667	(.242)	1.82	.695
c	1.10	(.176)	1.22	.38	1.26	.147	2.24	2.52	10.10	10.25	9.39	.718	(.221)	2.49	.710
d	1.73	(.130)	1.22	.29	3.29	.457	5.40	2.52	10.39	11.22	9.92	.759	(.427)	5.44	.730
3a	.80	(.814)	1.26	.46	1.56	.81	3.95	2.52	2.35	2.17	2.38	.182	(1.27)	4.17	.187
b	.90	(.855)	1.26	.46	1.18	.59	3.04	2.52	2.35	2.16	2.38	.182	(1.01)	3.40	.195
c	1.10	(.615)	1.26	.46	1.50	.62	3.50	2.52	2.55	2.69	2.57	.197	(.92)	3.75	.187
d	1.73	(.520)	1.26	.34	3.42	1.91	7.25	2.52	2.65	3.23	2.71	.207	(1.78)	7.56	.180
4a	.465	.109	1.18	.31	2.25	.25	3.60	11.6	30.18	28.74	28.62	.446		4.00	.460
b	.70	.104	1.18	.31	1.90	.20	3.03	11.6	30.20	28.86	28.71	.448		3.39	.462
c	.90	.094	1.18	.31	1.28	.12	2.03	11.6	30.39	29.09	29.00	.452		2.22	.465
5a	.465	.206	1.21	.37	3.14	.65	5.61	11.6	60.74	60.03	55.00	.854		5.65	.835
b	.70	.187	1.21	.37	2.78	.52	4.91	11.6	60.76	60.08	55.44	.864		4.46	.878
c	.90	.162	1.21	.37	1.97	.32	3.43	11.6	60.80	60.20	56.05	.875		3.25	.925
6	.204	1.578	1.47	.82	2.82	4.45	10.91	7.21	13.05	12.37	10.54	.131		11.40	.122
7	.204	.163	1.21	.36	3.08	.50	5.35	7.21	53.71	53.34	49.26	.613		5.15	.609
8a	.60	.045	1.11	.20	2.49	.11	3.37	12.23	30.62	28.01	29.64	.632		3.68	.634
b	.90	.038	1.11	.20	1.59	.06	2.14	12.23	30.88	28.69	30.04	.640		2.42	.648
c	1.20	.036	1.11	.18	2.58	.09	3.42	12.23	32.77	31.36	32.03	.684		3.34	.678
d	1.40	.041	1.11	.17	3.36	.14	4.45	12.23	32.77	32.09	32.05	.684		4.28	.676
e	1.53	.044	1.11	.17	3.72	.16	4.92	12.23	32.77	32.55	32.06	.685		4.55	.675
f	1.70	.048	1.11	.16	4.00	.19	5.28	12.23	32.77	33.10	32.07	.685		5.15	.672
9a	.60	.038	1.11	.20	2.65	.10	3.58	12.23	24.68	23.83	24.21	.508		3.82	.510
b	.70	.037	1.11	.20	2.46	.09	3.32	12.23	24.68	23.75	24.21	.508		[a]3.80	.510
c	.80	.035	1.11	.20	2.17	.08	2.92	12.23	24.68	23.64	24.21	.508		[a]3.50	.510
d	.90	.032	1.11	.20	1.71	.05	2.30	12.23	24.62	23.43	24.15	.507		[a]3.30	.461
e	1.20	.028	1.11	.19	3.04	.09	4.05	12.23	26.68	29.13	26.73	.561		3.74	.558
f	1.40	.036	1.11	.17	3.48	.13	4.60	12.23	26.99	30.20	27.00	.567		4.51	.565
g	1.60	.044	1.11	.16	3.64	.16	4.81	12.23	27.10	30.96	27.08	.569		4.97	.570
h	1.90	.054	1.11	.16	3.78	.20	5.01	12.23	27.14	31.90	27.10	.569		5.05	.575

TABLE II.- SUMMARY OF GEOMETRIC AND AERODYNAMIC CHARACTERISTICS AND TEST CONDITIONS FOR WING-BODY COMBINATIONS - Continued

(c) Geometric Characteristics

No.	Sketch	M_o	R	r_N	l_R	l_M	l	Section	$\frac{t}{c}$	$12\frac{z}{c}$	l_W	βA	$\Lambda_{L.E.}$	λ	r_W	$\left(\frac{r}{s}\right)_W$	Ref.	Facility
10a		0.60	1.66×10^6	1.667	6.125	20.0	33.33	NACA 65A006	0.06	5.89	18.23	2.85	3.6°	0.635	1.667	0.139	42	Langley 8 ft
b		.70	1.79×10^6	1.667	6.125	20.0	33.33	NACA 65A006	.06	5.89	18.23	2.55	3.6°	.635	1.667	.139	42	Langley 8 ft
c		.80	1.88×10^6	1.667	6.125	20.0	33.33	NACA 65A006	.06	5.89	18.23	2.14	3.6°	.635	1.667	.139	42	Langley 8 ft
d		.90	1.93×10^6	1.667	6.125	20.0	33.33	NACA 65A006	.06	5.89	18.23	1.56	3.6°	.635	1.667	.139	42	Langley 8 ft
e		1.20	1.86×10^6	1.667	6.125	20.0	33.33	NACA 65A006	.06	5.89	18.23	2.37	3.6°	.635	1.667	.139	42	Langley 8 ft
[9]11a		.24	2.46×10^6	3.06	22.67	38.12	60.44	NACA 0008-63	.08	18.60	27.24	1.94	63.4°	0	3.06	.180	43	Ames 12 ft
b		.60	2.46×10^6	3.06	22.67	38.12	60.44	NACA 0008-63	.08	18.60	27.24	1.60	63.4°	0	3.06	.180	43	Ames 12 ft
c		.80	2.46×10^6	3.06	22.67	38.12	60.44	NACA 0008-63	.08	18.60	27.24	1.20	63.4°	0	3.06	.180	43	Ames 12 ft
d		.90	2.46×10^6	3.06	22.67	38.12	60.44	NACA 0008-63	.08	18.60	27.24	.87	63.4°	0	3.06	.180	43	Ames 12 ft
e		.95	2.46×10^6	3.06	22.67	38.12	60.44	NACA 0008-63	.08	18.60	27.24	.62	63.4°	0	3.06	.180	43	Ames 12 ft
f		1.30	2.46×10^6	3.06	22.67	38.12	60.44	NACA 0008-63	.08	18.60	27.24	1.66	63.4°	0	3.06	.180	43	Ames 6x6 ft
g		1.53	2.46×10^6	3.06	22.67	38.12	60.44	NACA 0008-63	.08	18.60	27.24	2.32	63.4°	0	3.06	.180	43	Ames 6x6 ft
h		1.70	2.46×10^6	3.06	22.67	38.12	60.44	NACA 0008-63	.08	18.60	27.24	2.75	63.4°	0	3.06	.180	43	Ames 6x6 ft
[10]12a		.60	3.63×10^6	2.38	12.46	27.40	46.93	[3]b.c.	.03	10.90	20.43	3.20	45°	0	2.38	.127	44	Ames 6x6 ft
b		.80	3.63×10^6	2.38	12.46	27.40	46.93	b.c.	.03	10.90	20.43	2.40	45°	0	2.38	.127	44	Ames 6x6 ft
c		.90	3.63×10^6	2.38	12.46	27.40	46.93	b.c.	.03	10.90	20.43	1.74	45°	0	2.38	.127	44	Ames 6x6 ft
d		1.20	3.63×10^6	2.38	12.46	27.40	46.93	b.c.	.03	10.90	20.43	2.65	45°	0	2.38	.127	44	Ames 6x6 ft
e		1.40	3.63×10^6	2.38	12.46	27.40	46.93	b.c.	.03	10.90	20.43	3.92	45°	0	2.38	.127	44	Ames 6x6 ft
f		1.70	3.63×10^6	2.38	12.46	27.40	46.93	b.c.	.03	10.90	20.43	5.50	45°	0	2.38	.127	44	Ames 6x6 ft
13a	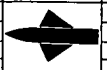	.50	4.25×10^5	.50	1.00	9.79	9.79	b.c.	.063	2.08	3.723	1.73	26.5°	0	.50	.243	45	German
b		.70		.50	1.00	9.79	9.79	b.c.	.063	2.08	3.723	1.43	26.5°	0	.50	.243	45	German
c		.90	6.58×10^5	.50	1.00	9.79	9.79	b.c.	.063	2.08	3.723	.872	26.5°	0	.50	.243	45	German
d		1.45	2.76×10^5	.50	1.00	9.79	9.79	b.c.	.063	2.08	3.723	2.10	26.5°	0	.50	.243	45	German
e		1.99	2.34×10^5	.50	1.00	9.79	9.79	b.c.	.063	2.08	3.723	3.45	26.5°	0	.50	.243	45	German
14a		.50	5.60×10^5	.50	1.00	9.79	9.79	b.c.	.037	2.74	3.475	.866	45°	0	.50	.327	45	German
b		.70		.50	1.00	9.79	9.79	b.c.	.037	2.74	3.475	.714	45°	0	.50	.327	45	German
c		.90	8.67×10^5	.50	1.00	9.79	9.79	b.c.	.037	2.74	3.475	.436	45°	0	.50	.327	45	German
d		1.45	3.64×10^5	.50	1.00	9.79	9.79	b.c.	.037	2.74	3.475	1.05	45°	0	.50	.327	45	German
e		1.99	3.08×10^5	.50	1.00	9.79	9.79	b.c.	.037	2.74	3.475	1.72	45°	0	.50	.327	45	German
[9]15a		.24	2.46×10^6	3.06	22.67	38.12	60.44	NACA 0005-53	.05	18.60	27.24	1.94	63.4°	0	3.06	.180	46	Ames 12 ft
b		.60	2.46×10^6	3.06	22.67	38.12	60.44	NACA 0005-53	.05	18.60	27.24	1.60	63.4°	0	3.06	.180	46	Ames 12 ft
c		.80	2.46×10^6	3.06	22.67	38.12	60.44	NACA 0005-53	.05	18.60	27.24	1.20	63.4°	0	3.06	.180	46	Ames 12 ft
d		.90	2.46×10^6	3.06	22.67	38.12	60.44	NACA 0005-53	.05	18.60	27.24	.87	63.4°	0	3.06	.180	46	Ames 12 ft
e		1.30	2.46×10^6	3.06	22.67	38.12	60.44	NACA 0005-53	.05	18.60	27.24	1.66	63.4°	0	3.06	.180	46	Ames 6x6 ft
f		1.53	2.46×10^6	3.06	22.67	38.12	60.44	NACA 0005-53	.05	18.60	27.24	2.32	63.4°	0	3.06	.180	46	Ames 6x6 ft
g		1.70	2.46×10^6	3.06	22.67	38.12	60.44	NACA 0005-53	.05	18.60	27.24	2.75	63.4°	0	3.06	.180	46	Ames 6x6 ft

TABLE II.- SUMMARY OF GEOMETRIC AND AERODYNAMIC CHARACTERISTICS AND TEST CONDITIONS FOR WING-BODY COMBINATIONS - Continued

(d) Aerodynamic Characteristics

No.	M_O	K_N	$K_{W(B)}$	$K_{B(W)}$	Theoretical								Experiment		
					e_{Lift}			Center of pressure					e_{Lift}		c.p.
					$\beta C_{L_{\alpha_W}}$	$\beta C_{L_{\alpha_N}}$	$\beta C_{L_{\alpha_C}}$	$\bar{l}_N$	$\bar{l}_{W(B)}$	$\bar{l}_{B(W)}$	$\bar{l}_C$	$\left(\frac{\bar{l}}{l}\right)_C$	$\beta C_{L_{\alpha_B}}$	$\beta C_{L_{\alpha_C}}$	$\left(\frac{\bar{l}}{l}\right)_C$
10a	0.60	0.038	1.11	0.19	3.07	0.11	4.11	7.88	20.02	19.93	19.66	0.590		[a]4.01	0.575
b	.70	.036	1.11	.19	2.88	.10	3.85	7.88	20.02	19.89	19.68	.590		[a]3.72	.577
c	.80	.034	1.11	.19	2.58	.09	3.45	7.88	20.02	19.82	19.68	.590		[a]3.73	.572
d	.90	.031	1.11	.19	2.07	.06	2.75	7.88	20.02	19.65	19.69	.591		[a]3.12	.601
e	1.20	.030	1.11	.18	3.28	.10	4.33	7.88	21.27	22.98	21.20	.636		[a]3.77	.617
11a	.24	.068	1.15	.25	2.15	.15	3.15	12.44	42.74	39.28	40.75	.674		3.30	.676
b	.60	.066	1.15	.25	1.84	.12	2.70	12.44	42.88	39.62	40.95	.678		2.79	.681
c	.80	.061	1.15	.25	1.47	.09	2.15	12.44	43.02	39.93	41.21	.682		2.24	.685
d	.90	.058	1.15	.25	1.13	.07	1.65	12.44	43.33	40.20	41.56	.688		1.78	.691
e	.95	.054	1.15	.25	.87	.05	1.26	12.44	43.75	40.46	42.01	.695		1.36	.706
f	1.30	.055	1.15	.22	2.26	.12	3.22	12.44	45.84	44.02	44.26	.733		3.27	.723
g	1.53	.061	1.15	.21	2.87	.18	4.07	12.44	45.84	45.14	44.30	.733		4.04	.723
h	1.70	.064	1.15	.20	3.22	.21	4.56	12.44	45.84	45.75	44.31	.733		4.48	.723
12a	.60	.036	1.10	.17	2.96	.11	3.86	9.65	29.40	26.63	28.50	.598		4.24	[a].606
b	.80	.032	1.10	.17	2.49	.08	3.24	9.65	29.43	26.92	28.62	.601		3.47	[a].612
c	.90	.030	1.10	.17	1.97	.06	2.55	9.65	29.50	27.33	28.76	.604		2.92	[a].620
d	1.20	.028	1.10	.15	3.14	.09	4.01	9.65	31.29	30.38	30.71	.645		3.78	.645
e	1.40	.033	1.10	.14	3.96	.13	5.04	9.65	31.29	31.03	30.70	.645		4.61	.645
f	1.70	.046	1.10	.15	4.00	.18	5.17	9.65	31.29	32.14	30.62	.643		5.17	.644
13a	.50	.142	1.20	.35	1.97	.28	3.34	1.00	(4.19)	4.42	3.97	.405		3.36	.408
b	.70	.136	1.20	.35	1.70	.23	2.86	1.00	(4.19)	4.38	3.97	.405		3.04	.408
c	.90	.125	1.20	.35	1.13	.16	1.89	1.00	(4.19)	4.32	3.98	.406		2.18	.408
d	1.45	.127	1.20	.35	2.69	.34	4.50	1.00	(4.67)	5.93	4.66	.476		4.40	.428
e	1.99	.151	1.20	.35	3.71	.55	6.31	1.00	(4.67)	6.19	4.66	.476		5.95	.428
14a	.50	.27	1.28	.49	1.22	.33	2.48	1.00	4.46	4.25	3.96	.404		2.49	.418
b	.70	.26	1.28	.49	1.02	.27	2.08	1.00	4.44	4.21	3.94	.402		2.05	.408
c	.90	.25	1.28	.49	.65	.16	1.32	1.00	4.36	4.15	3.89	.397		1.50	.408
d	1.45	.20	1.28	.49	2.01	.40	3.96	1.00	4.63	5.46	4.48	.457		3.35	.444
e	1.99	.23	1.28	.49	2.83	.65	5.66	1.00	4.81	5.96	4.66	.475		5.12	.449
15a	.24	.068	1.15	.25	2.15	.15	3.15	12.44	42.74	39.28	40.75	.674		3.33	.679
b	.60	.066	1.15	.25	1.84	.12	2.70	12.44	42.88	39.62	40.95	.678		2.79	.682
c	.80	.061	1.15	.25	1.47	.09	2.15	12.44	43.02	39.93	41.21	.688		2.26	.689
d	.90	.058	1.15	.25	1.13	.07	1.65	12.44	43.33	40.20	41.56	.695		1.77	.695
e	1.30	.055	1.15	.22	2.26	.12	3.22	12.44	45.84	44.02	44.26	.733		3.24	.728
f	1.53	.061	1.15	.21	2.87	.18	4.07	12.44	45.84	45.14	44.30	.733		4.04	.728
g	1.70	.064	1.15	.20	3.22	.21	4.56	12.44	45.84	45.75	44.31	.733		4.48	.727

NACA

TABLE II.- SUMMARY OF GEOMETRIC AND AERODYNAMIC CHARACTERISTICS AND TEST CONDITIONS FOR WING-BODY COMBINATIONS - Continued

(e) Geometric Characteristics

No.	Sketch	M_o	R	r_N	l_R	l_M	l	Section	$\frac{t}{c}$	l_c	l_w	βA	Λ L.E.	λ	r_w	$\left(\frac{r}{s}\right)_w$	Ref.	Facility
[10]16a	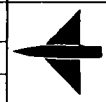	0.60	3.63×10^6	2.38	12.46	27.40	46.93	[3]b.c.	0.03	10.90	20.43	3.20	45°	0	2.38	0.127	47	Ames 6x6 ft
b		.80	3.63×10^6	2.38	12.46	27.40	46.93	b.c.	.03	10.90	20.43	2.40	45°	0	2.38	.127	47	Ames 6x6 ft
c		.90	3.63×10^6	2.38	12.46	27.40	46.93	b.c.	.03	10.90	20.43	1.74	45°	0	2.38	.127	47	Ames 6x6 ft
d		1.20	3.63×10^6	2.38	12.46	27.40	46.93	b.c.	.03	10.90	20.43	2.65	45°	0	2.38	.127	47	Ames 6x6 ft
e		1.40	3.63×10^6	2.38	12.46	27.40	46.93	b.c.	.03	10.90	20.43	3.92	45°	0	2.38	.127	47	Ames 6x6 ft
f		1.70	3.63×10^6	2.38	12.46	27.40	46.93	b.c.	.03	10.90	20.43	5.50	45°	0	2.38	.127	47	Ames 6x6 ft
17	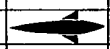	.13	12.7×10^6	26.94	196.40	358.6	673.9	[4]d.w.	.048	161.20	264.1	2.00	63.0°	0	26.94	.196	48	Ames 40x80 ft
18a	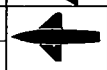	.40	2.84×10^6	3.10	14.20	27.0	51.8	NACA 64_1A012	.12	12.80	20.02	2.51	35°	.352	3.10	.160	49	Langley 7x10 ft
b		.60	3.67×10^6	3.10	14.20	27.0	51.8	NACA 64_1A012	.12	12.80	20.02	2.19	35°	.352	3.10	.160	49	Langley 7x10 ft
c		.80	4.65×10^6	3.10	14.20	27.0	51.8	NACA 64_1A012	.12	12.80	20.02	1.64	35°	.352	3.10	.160	49	Langley 7x10 ft
d		.90	4.89×10^6	3.10	14.20	27.0	51.8	NACA 64_1A012	.12	12.80	20.02	1.19	35°	.352	3.10	.160	49	Langley 7x10 ft
19		.100	$.57\times10^6$	3.44	9.40	13.0	40.31	NACA 20312	.12	9.40	10.5	5.62	0°	.88	3.44	.115	50	Langley 7x10 ft
20		.100	$.62\times10^6$	3.44	9.85	13.0	40.31	NACA 20312	.12	10.20	7.47	5.52	18.3°	.38	3.44	.115	50	Langley 7x10 ft
21		.100	$.62\times10^6$	3.44	9.85	13.0	40.31	NACA 20312	.12	10.20	8.98	5.52	9.3°	.38	3.44	.115	50	Langley 7x10 ft
22	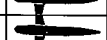	.100	$.62\times10^6$	3.44	9.85	13.0	40.31	NACA 20312	.12	10.20	10.51	5.52	0°	.38	3.44	.115	50	Langley 7x10 ft
23a	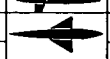	.747	1.27×10^6	.583	4.07	8.49	14.0	b.c.	.06	3.40	5.43	1.49	60°	0	.572	.158	51	Wing Flow (Langley)
b		.851	1.31×10^6	.583	4.07	8.49	14.0	b.c.	.06	3.40	5.43	1.18	60°	0	.572	.158	51	Wing Flow (Langley)
c		1.067	1.25×10^6	.583	4.07	8.49	14.0	b.c.	.06	3.40	5.43	.834	60°	0	.572	.158	51	Wing Flow (Langley)
24a		.747	1.31×10^6	.583	3.87	8.92	14.0	b.c.	.06	3.66	6.99	1.60	0°	0	.502	.139	51	Wing Flow (Langley)
b		.851	1.44×10^6	.583	3.87	8.92	14.0'	b.c.	.06	3.66	6.99	1.26	0°	0	.502	.139	51	Wing Flow (Langley)
c		1.067	1.29×10^6	.583	3.87	8.92	14.0	b.c.	.06	3.66	6.99	.90	0°	0	.502	.139	51	Wing Flow (Langley)
25		.183	$.74\times10^6$	4.125	8.25	66.15	106.5	d.w.	.04	7.09	47.73	2.53	24°	.272	4.125	.333	52	D.T.M.B.

TABLE II.- SUMMARY OF GEOMETRIC AND AERODYNAMIC CHARACTERISTICS AND TEST CONDITIONS FOR WING-BODY COMBINATIONS - Concluded

(f) Aerodynamic Characteristics

No.	M_o	K_N	$K_{W(B)}$	$K_{B(W)}$	Theoretical								Experiment		
					[6]Lift			Center of pressure					[6]Lift		c.p.
					$\beta C_{l_{\alpha_W}}$	$\beta C_{l_{\alpha_N}}$	$\beta C_{l_{\alpha_C}}$	$\bar{l}_N$	$\bar{l}_{W(B)}$	$\bar{l}_{B(W)}$	$\bar{l}_C$	$\left(\frac{\bar{l}}{l}\right)_C$	$\beta C_{l_{\alpha_B}}$	$\beta C_{l_{\alpha_C}}$	$\left(\frac{\bar{l}}{l}\right)_C$
16a	0.60	0.036	1.10	0.17	2.96	0.11	3.86	9.65	29.40	26.63	28.50	0.598		4.30	0.608
b	.80	.032	1.10	.17	2.49	.08	3.24	9.65	29.43	26.92	28.62	.601		3.47	.612
c	.90	.030	1.10	.17	1.97	.06	2.55	9.65	29.50	27.33	28.76	.604		2.89	.617
d	1.20	.028	1.10	.15	3.14	.09	4.01	9.65	31.29	30.38	30.71	.645		3.78	.647
e	1.40	.033	1.10	.14	3.96	.13	5.04	9.65	31.29	31.03	30.70	.645		4.61	.646
f	1.70	.046	1.10	.15	4.00	.18	5.17	9.65	31.29	32.14	30.62	.643		5.17	.644
17	.13	.069	1.15	.25	2.19	.15	3.22	139.1	398.5	368.2	381.0	.566		3.38	.567
[11]18a	.40	.052	1.13	.22	2.72	.14	3.81		28.02	26.19				3.84	.522
b	.60	.050	1.13	.22	2.51	.13	3.51		28.04	26.16				3.64	.522
c	.80	.045	1.13	.22	2.07	.09	2.88		28.06	26.21				3.15	.522
d	.90	.042	1.13	.22	1.63	.07	2.26		27.99	26.26				2.63	.509
19	.100	.145	1.09	.155	4.13	.60	5.30	4.04	12.85	12.97	12.62	.315		5.81	.323
20	.100	.141	1.09	.155	4.12	.58	5.27	4.04	13.62	11.68	13.12	.328		4.83	.323
21	.100	.141	1.09	.155	4.12	.58	5.27	4.04	13.46	12.72	13.11	.328		4.83	.323
22	.100	.141	1.09	.155	4.12	.58	5.27	4.04	13.09	13.73	12.92	.323		4.83	.323
23a	.747	.052	1.13	.23	1.76	.092	2.48	3.04	8.29	7.67	7.98	.570		2.40	.560
b	.851	.049	1.13	.23	1.46	.072	2.06	3.04	8.33	7.73	8.05	.575		1.95	.564
c	1.067	.042	1.13	.21	1.22	.051	1.68	3.04	8.83	8.18	8.56	.611		1.53	.589
24a	.747	.048	1.11	.188	1.84	.090	2.48	3.04	7.81	7.92	7.66	.546		2.38	.502
b	.851	.046	1.11	.188	1.53	.071	2.05	3.04	7.78	7.84	7.63	.545		2.19	.503
c	1.067	.038	1.11	.188	1.31	.050	1.74	3.04	7.54	8.09	7.49	.535		1.76	.538
25	.183	.366	1.285	.50	2.72	1.00	5.85	10.8	51.09	50.63	44.13	.414		5.74	.394

[1]- denotes nonuniform or unknown t/c, thickness-chord ratio

[2]hex. indicates hexagonal

[3]b.c. indicates biconvex

[4]d.w. indicates double wedge

[5]Configuration tested with extended tail boom coaxial with body

[6]βC_{l_α} per radian based on exposed wing area

[7]() denotes experimental value used in theory for combination

[8]Experimental data nonlinear near $\alpha=0^\circ$

[9]Nos. 11 and 15 identical except wing thickness

[10]Nos. 12 and 16 identical except wing thickness distribution

[11]No experimental or theoretical value available for $\bar{l}_N$

[12]$\bar{c}$ based on exposed wing area

TABLE III.- SUMMARY OF GEOMETRIC AND AERODYNAMIC CHARACTERISTICS AND TEST CONDITIONS FOR BODY-WING-TAIL COMBINATIONS

(a) Geometric Characteristics

No.	Sketch	M_o	l_R	r_N	l_R	l_M	l	Surface	Section	$\frac{z_t}{c}$	$\frac{z}{c}$	$\frac{l_W}{l_T}$ or	βA	$A_{L.E.}$	λ	r	$\frac{r}{s}$	Ref.	Facility
101		0.183	0.79×10^6	4.125	8.25	66.15	106.5	wing	[3]d.v.	0.042	7.09	47.73	2.53	24°	0.272	4.125	0.333	52	DTMB
								tail	d.v.	.042	7.48	93.40	2.55	24°	.270	4.125	.321		
102		.184	$.71\times10^6$	2.815	5.63	34.18	56.37	wing	[4]hex.	- - -	3.72	14.60	2.64	13.9°	.500	2.815	.369	53	DTMB
								tail	hex.	.06	6.69	37.74	2.64	14°	.499	2.815	.246		
103		.184	$.71\times10^6$	2.815	5.63	34.18	56.37	wing	hex.	- - -	2.64	15.30	2.68	13.8°	.500	2.815	.448	53	DTMB
								tail	hex.	.06	6.69	37.74	2.64	14°	.499	2.815	.246		
104		.184	$.71\times10^6$	2.815	5.63	34.18	56.37	wing	hex.	- - -	6.47	10.54	1.43	70°	0	2.815	.443	53	DTMB
								tail	d.v.	.06	6.69	37.74	2.64	14°	.499	2.815	.246		
105a		.20	1.86×10^6	6.48	18.67	70.50	146	wing	hex.	.042	17.38	64.20	3.43	9.45°	.546	6.43	.179	35	Ames 12 ft
								tail	hex.	.042	8.72	130.71	3.43	9.45°	.548	3.16	.176		
b		.50	1.86×10^6	6.48	18.67	70.50	146	wing	hex.	.042	17.38	64.20	3.02	9.45°	.546	6.43	.179	35	Ames 12 ft
								tail	hex.	.042	8.72	130.71	3.03	9.45°	.548	3.16	.176		
c		.70	1.86×10^6	6.48	18.67	70.50	146	wing	hex.	.042	17.38	64.20	2.49	9.45°	.546	6.43	.179	35	Ames 12 ft
								tail	hex.	.042	8.72	130.71	2.50	9.45°	.548	3.16	.176		
d		.80	1.86×10^6	6.48	18.67	70.50	146	wing	hex.	.042	17.38	64.20	2.10	9.45°	.546	6.43	.179	35	Ames 12 ft
								tail	hex.	.042	8.72	130.71	2.10	9.45°	.548	3.16	.176		
e		.90	1.86×10^6	6.48	18.67	70.50	146	wing	hex.	.042	17.38	64.20	1.52	9.45°	.546	6.43	.179	35	Ames 12 ft
								tail	hex.	.042	8.72	130.71	1.53	9.45°	.548	3.16	.176		
106a		.89	6.0×10^6	3.50	17.89	60.0	114.2	wing	hex.	- - -	4.62	25.87	1.05	60°	0	3.50	.467	54	Flight
								tail	hex.	- - -	13.87	68.20	1.05	60°	0	3.50	.226		
b		1.25	9.2×10^6	3.50	17.89	60.0	114.2	wing	hex.	- - -	4.62	25.87	1.73	60°	0	3.50	.467	54	Flight
								tail	hex.	- - -	13.87	68.20	1.73	60°	0	3.50	.226		
107a		.83	3.9×10^6	3.50	17.57	91.3	154.2	wing	hex.	- - -	3.47	26.70	1.29	60°	0	3.50	.538	55	Flight
								tail	hex.	- - -	13.60	108.20	1.31	59.3°	0	3.50	.226		
b		1.38	8.4×10^6	3.50	17.57	91.3	154.2	wing	hex.	- - -	3.47	26.70		60°	0	3.50	.538	55	Flight
								tail	hex.	- - -	13.60	108.20		59.3°	0	3.50	.226		
108a		.80	$.78\times10^6$	.8125	1.625	6.575	13.075	wing	[5]b.c.	- - -	2.90	1.51	1.18	45°	.341	.546	.308	36	OAL
								tail	b.c.	- - -	1.35	8.06	1.03	45°	.401	.812	.258		
b		.90		.8125	1.625	6.575	13.075	wing	b.c.	- - -	2.90	1.51	.856	45°	.341	.546	.308	36	OAL
								tail	b.c.	- - -	1.35	8.06	.744	45°	.401	.812	.258		
c		1.10	$.67\times10^6$	.8125	1.625	6.575	13.075	wing	b.c.	- - -	2.90	1.51	.900	45°	.341	.546	.308	36	OAL
								tail	b.c.	- - -	1.35	8.06	.782	45°	.401	.812	.258		
d		1.73	1.6×10^6	.8125	1.625	6.575	13.075	wing	b.c.	- - -	2.90	1.51	2.77	45°	.341	.546	.308	37	OAL
								tail	b.c.	- - -	1.35	8.06	2.41	45°	.401	.812	.258		
109a		.465	1.95×10^6	2.00	8.38	36.46	64.41	wing	d.w.	.029	8.38	23.24	2.06	60°	0	2.00	.216	38	CAL & CWT
								tail	d.w.	.030	3.92	57.53	3.54	45°	0	2.00	.254		
b		.70	1.33×10^6	2.00	8.38	36.46	64.41	wing	d.w.	.029	8.38	23.24	1.66	60°	0	2.00	.216	38	CAL & CWT
								tail	d.w.	.030	3.92	57.53	2.86	45°	0	2.00	.254		
c		.90	1.05×10^6	2.00	8.38	36.46	64.41	wing	d.w.	.029	8.38	23.24	1.01	60°	0	2.00	.216	38	CAL & CWT
								tail	d.w.	.030	3.92	57.53	1.74	45°	0	2.00	.254		
d		1.15	1.26×10^6	1.80	7.54	29.14	[6]57.97	wing	d.w.	.029	7.54	20.92	1.31	60°	0	1.80	.216		Ames 6x6 ft
								tail	d.w.	.030	3.53	51.77	2.27	45°	0	1.80	.254		
e		1.40	1.26×10^6	1.80	7.54	29.14	57.97	wing	d.w.	.029	7.54	20.92	2.26	60°	0	1.80	.216		Ames 6x6 ft
								tail	d.w.	.030	3.53	51.77	3.92	45°	0	1.80	.254		
f		1.70	1.26×10^6	1.80	7.54	29.14	57.97	wing	d.w.	.029	7.54	20.92	3.18	60°	0	1.80	.216		Ames 6x6 ft
								tail	d.w.	.030	3.53	51.77	5.50	45°	0	1.80	.254		
[6]110a		.204	$.82\times10^6$	3.50	7.00	76.27	80.41	wing	d.w.	.05	2.69	11.14	2.46	26.6°	.500	3.45	.514	39	DTMB
								tail	hex.	.06	7.45	50.69	2.89	14°	.461	3.50	.250		
b		1.50		.50	1.00	5.75	11.49	wing	d.w.	.06	.39	1.72	2.98	26.6°	.500	.46	.486	56	Ames 1x3 ft
								tail	hex.	.06	1.06	7.24	3.30	14°	.461	.50	.250		
c		2.00		.50	1.00	5.75	11.49	wing	d.w.	.06	.39	1.72	4.62	26.6°	.500	.46	.486	56	Ames 1x3 ft
								tail	hex.	.06	1.06	7.24	5.11	14°	.461	.50	.250		
111		1.93	$.33\times10^6$	.416	.832	4.747	9.10	wing	hex.	- - -	1.02	4.42	1.69	60°	.323	.416	.465	57	Langley 9 in.
								tail	hex.	.049	.85	7.91	2.03	60°	.305	.416	.465		
112		1.93	$.33\times10^6$	.416	.832	5.135	9.49	wing	hex.	- - -	1.02	4.81	1.69	60°	.323	.416	.465	57	Langley 9 in.
								tail	hex.	.064	.50	8.99	5.51	0°	1	.416	.333		
113		1.93	$.33\times10^6$	.416	.832	5.135	9.49	wing	hex.	- - -	1.02	4.810	1.69	60°	.323	.416	.465	57	Langley 9 in.
								tail	hex.	- - -	.74	8.476	3.16	45°	.352	.416	.388		
114		1.93	$.83\times10^6$	.416	.832	5.135	9.49	wing	hex.	- - -	.86	2.757	1.69	60°	.323	.416	.508	57	Langley 9 in.
								tail	hex.	- - -	2.57	6.037	1.03	70°	.400	.416	.356		
115		1.93	$.83\times10^6$	.416	.832	5.135	9.49	wing	hex.	- - -	.35	3.834	3.81	60°	0	.416	.579	57	Langley 9 in.
								tail	hex.	- - -	2.57	6.037	1.03	70°	.400	.416	.356		
116		1.93	$.83\times10^6$	.416	.832	5.135	9.49	wing	hex.	- - -	.52	3.573	3.81	60°	0	.416	.479	57	Langley 9 in.
								tail	hex.	- - -	2.57	6.037	1.03	70°	.400	.416	.356		
117		1.93	$.83\times10^6$	.416	.832	5.135	9.49	wing	hex.	- - -	.70	3.311	3.81	60°	0	.416	.408	57	Langley 9 in.
								tail	hex.	- - -	2.57	6.037	1.03	70°	.400	.416	.356		
118		1.92	$.40\times10^6$	.35	1.25	4.177	8.75	wing	b.c.	.06	1.25	3.569	5.64	0°	1	.350	.140	58	Langley 9 in.
								tail	b.c.	.06	.616	8.054	5.14	0°	1	.285	.228		
119		1.92	$.40\times10^6$	.35	1.25	4.927	8.75	wing	b.c.	.06	1.25	4.319	5.64	0°	1	.350	.140	58	Langley 9 in.
								tail	b.c.	.06	.616	8.054	5.14	0°	1	.285	.228		

TABLE III.- SUMMARY OF GEOMETRIC AND AERODYNAMIC CHARACTERISTICS AND TEST CONDITIONS FOR BODY-WING-TAIL COMBINATIONS - Continued
(b) Aerodynamic Characteristics

No.	$\frac{S_T}{S_W}$	K_N	$K_{W(B)}$	$K_{B(W)}$	$K_{T(B)}$	$K_{B(T)}$	Theoretical														Experimental		
							C_{L_α} Lift					$\bar{l}$ Center of pressure									C_{L_α} Lift		c.p.
							$\beta C_{L_{\alpha_W}}$	$\beta C_{L_{\alpha_T}}$	$\beta C_{L_{\alpha_B}}$	[a] $\beta C_{L_{\alpha_C}}$	$\beta C_{L_{\alpha_C}}$	$\bar{l}_N$	$\bar{l}_{W(B)}$	$\bar{l}_{B(W)}$	$\bar{l}_{T(B)}$	$\bar{l}_{B(T)}$	[a] $\bar{l}_C$	[a] $\left(\frac{\bar{l}}{l}\right)_C$	$\left(\frac{\bar{l}}{l}\right)_C$	$\beta C_{L_{\alpha_B}}$	$\beta C_{L_{\alpha_C}}$	$\left(\frac{\bar{l}}{l}\right)_C$
101	1.115	0.338	1.29	0.50	1.28	0.48	2.95	2.97	1.00	10.87	8.17	10.83	51.05	50.56	96.90	96.39	69.59	60.46	0.653	0.568		8.45	0.576
102	3.227	.481	1.32	.56	1.21	.35	2.94	2.94	.44	6.76	5.86	5.05	16.07	15.89	40.39	40.04	31.84	30.49	.565	.541		4.90	.545
103	6.286	.930	1.40	.70	1.21	.35	2.96	2.94	.44	6.03	5.52	5.05	16.35	16.24	40.39	40.04	33.76	33.14	.599	.588		4.68	.575
104	3.249	.842	1.39	.70	1.21	.35	1.69	2.94	.44	6.08	5.52	5.05	16.00	15.34	40.39	40.04	33.45	32.74	.593	.581		4.75	.565
105a	.252	.077	1.14	.24	1.14	.24	3.47	3.48	.27	6.45	5.56	33.43	70.76	70.05	134.00	133.63	81.23	76.10	.557	.521		5.20	.505
b	.252	.072	1.14	.24	1.14	.24	3.16	3.16	.23	5.71	5.16	33.43	70.76	69.99	134.00	133.61	81.23	75.71	.557	.519		4.85	.500
c	.252	.067	1.14	.24	1.14	.24	2.83	2.83	.19	4.70	4.21	33.43	70.76	69.82	134.00	133.52	82.50	76.66	.565	.525		4.25	.493
d	.252	.063	1.14	.24	1.14	.24	2.51	2.51	.16	4.50	4.02	33.43	70.76	69.60	134.00	133.42	81.48	75.13	.558	.515		3.87	.489
e	.252	.057	1.14	.24	1.14	.24	2.02	2.02	.12	3.60	3.17	33.43	70.76	69.23	134.00	133.23	81.65	74.48	.559	.510		3.11	.483
106a	9.00	.957	1.42	.74	1.19	.32	1.32	1.32	.14	2.51	2.06	11.88	29.82	29.32	80.06	78.00	68.77	66.33	.602	.581		1.97	.583
b	9.00	.890	1.42	.62	1.19	.27	2.34	2.34	.23	4.17	3.40	11.88	30.49	32.04	82.07	81.51	71.63	69.29	.627	.607		3.38	.603
107a	15.69	1.762	1.49	.87	1.19	.32	1.56	1.59	.18	2.81	2.46	11.83	29.65	29.31	119.75	118.01	105.08	102.90	.681	.667		2.62	.650
b	15.69	1.690	1.49	.72	1.19	.26	2.77	2.81	.30	4.74	4.14	11.83	30.17	32.47	121.81	122.01	107.66	105.36	.698	.683		4.23	.678
108a	4.16	[q](.814)	1.26	.46	1.22	.38	1.56	1.43	.19	3.20	2.78	2.52	2.35	2.17	9.73	9.39	7.47	7.14	.571	.546	(0.30)	2.85	.555
b	4.16	(.855)	1.26	.46	1.22	.38	1.18	1.04	.14	2.67	2.35	2.52	2.35	2.16	9.70	9.32	7.32	7.01	.560	.536	(.24)	2.27	.553
c	4.16	(.615)	1.26	.46	1.22	.38	1.50	1.26	.15	2.86	2.36	2.52	2.55	2.69	10.10	10.25	7.86	7.39	.601	.565	(.22)	2.34	.577
d	4.16	(.520)	1.26	.34	1.22	.29	3.42	3.29	.46	6.72	5.91	2.52	2.65	3.23	10.39	11.22	8.50	8.20	.650	.627	(.43)	5.96	.599
109a	.381	.109	1.18	.31	1.21	.37	2.25	3.14	.25	5.53	4.26	11.6	30.18	28.74	60.74	60.03	39.90	33.70	.620	.523		4.35	.505
b	.381	.104	1.18	.31	1.21	.37	1.90	2.78	.20	4.66	3.56	11.6	30.20	29.86	60.76	60.08	40.19	33.95	.624	.526		3.63	.509
c	.381	.094	1.18	.31	1.21	.37	1.28	1.97	.12	3.22	2.34	11.6	30.39	29.09	60.80	60.20	40.71	34.01	.632	.518		2.24	.503
d	.381	.084	1.18	.27	1.21	.22	1.86	2.84	.16	4.39	2.99	10.4	28.46	27.64	55.29	55.55	37.03	28.54	.639	.496		2.86	.516
e	.381	.095	1.18	.25	1.21	.17	2.83	3.96	.27	6.46	4.72	10.4	28.46	28.44	55.29	55.20	36.40	29.59	.628	.509		4.49	.522
f	.381	.111	1.18	.24	1.21	.14	3.41	4.00	.38	7.33	5.91	10.4	28.46	29.18	55.29	55.20	35.18	30.20	.606	.521		6.15	.535
110a	8.84	1.578	1.47	.82	1.21	.36	2.82	3.08	.50	6.06	5.67	7.21	13.05	12.37	53.71	53.34	44.77	44.11	.558	.549		5.25	.514
b	8.83	1.503	1.44	.56	1.21	.29	3.49	3.56	.58	6.73	6.28	1.03	2.01	2.44	7.89	8.51	6.69	6.61	.583	.575	.60	6.45	.557
c	8.83	2.591	1.44	.50	1.21	.27	3.73	3.78	.89	7.54	7.25	1.03	2.02	2.66	7.92	8.78	6.40	6.33	.557	.550	1.09	7.96	[10].567
111	.839	(.819)	1.41	.63	1.41	.26	2.94	3.12	2.01	12.77	8.70	(1.50)	5.22	5.82	8.63	8.70	5.78	4.44	.635	.488	2.41	8.39	[10]
112	.931	(.819)	1.41	.63	1.29	.057	2.94	3.64	2.01	12.87	11.73	(1.12)	5.61	6.22	9.23	9.32	6.14	5.85	.647	.616	2.41	11.15	.599
113	1.01	(.819)	1.41	.63	1.34	.14	2.94	3.67	1.99	13.81	10.31	(1.12)	5.61	6.22	9.10	9.15	6.29	5.33	.662	.561	2.39	10.72	.555
114	5.74	(1.155)	1.46	.69	1.31	.54	2.94	1.94	.49	4.98	4.26	(1.12)	3.43	4.09	7.88	8.24	6.32	5.93	.666	.625	.59	[10]3.90	[10].595
115	23.10	(3.479)	1.54	.70	1.31	.54	3.91	1.94	.49	4.54	4.16	(1.12)	4.18	4.79	7.88	8.24	6.82	6.69	.718	.705	.59	3.77	.683
116	10.30	(1.554)	1.43	.54	1.31	.54	3.91	1.94	.49	4.92	4.16	(1.12)	4.10	4.67	7.88	8.24	6.62	6.40	.698	.675	.59	3.82	.663
117	5.79	(.873)	1.36	.44	1.31	.54	3.91	1.94	.49	5.39	4.26	(1.12)	4.09	4.57	7.88	8.24	6.38	5.97	.672	.629	.59	4.00	[10].604
118	.221	(.067)	1.11	.12	1.19	.069	3.65	3.60	.23	5.73	5.45	(.317)	4.12	4.78	8.35	8.47	4.79	4.63	.548	.529	.23	5.24	.527
119	.221	(.067	1.11	.12	1.19	.069	3.65	3.60	.23	5.73	5.45	(.317)	4.92	5.53	8.35	8.47	5.38	5.21	.615	.595	.23	5.31	.599

TABLE III.- SUMMARY OF GEOMETRIC AND AERODYNAMIC CHARACTERISTICS AND TEST CONDITIONS FOR BODY-WING-TAIL COMBINATIONS - Continued

(c) Geometric Characteristics

No.	Sketch	M_0	l_R	r_N	l_R	l_M	l	Surface	Section	$\frac{z_t}{c}$	$\tan\varepsilon$	$\frac{l_W}{l_t}$ or $\frac{l_W}{l_t}$	βA	$\Lambda_{L.E.}$	λ	r	$\frac{r}{s}$	Ref.	Facility
120		1.92	0.40×10^6	0.350	1.25	5.677	8.75	wing	[3]b.c.	0.06	1.25	5.673	5.64	0°	1	0.350	0.140	58	Langley 9 in.
								tail	b.c.	.06	.616	8.054	5.14	0°	1	.285	.228		
121		1.62	$.23\times10^6$	.350	.700	4.375	9.00	wing	[4]hex.	- - -	.667	3.20	3.31	0°	0	.350	.350	59	Langley 9 in.
								tail	hex.	- - -	.667	7.92	3.31	0°	0	.350	.350		
122		1.62	$.23\times10^6$	.350	.700	4.375	9.00	wing	hex.	- - -	.667	4.70	3.31	0°	0	.350	.350	59	Langley 9 in.
								tail	hex.	- - -	.667	7.92	3.31	0°	0	.350	.350		
123		1.62	$.23\times10^6$	.350	.700	4.375	9.00	wing	hex.	- - -	.667	3.20	3.31	57°	0	.350	.350	59	Langley 9 in.
								tail	hex.	- - -	.667	7.92	3.31	0°	0	.350	.350		
124		1.62	$.23\times10^6$	.350	.700	4.375	9.00	wing	hex.	- - -	.667	4.70	3.31	57°	0	.350	.350	59	Langley 9 in.
								tail	hex.	- - -	.667	7.92	3.31	0°	0	.350	.350		
125		1.62	$.23\times10^6$	.350	.700	4.375	9.00	wing	hex.	- - -	.667	3.20	3.31	57°	0	.350	.350	59	Langley 9 in.
								tail	hex.	- - -	.667	7.92	3.31	57°	0	.350	.350		
126		1.62	$.23\times10^6$	.350	.700	4.375	9.00	wing	hex.	- - -	.667	4.70	3.31	57°	0	.350	.350	59	Langley 9 in.
								tail	hex.	- - -	.667	7.92	3.31	57°	0	.350	.350		
127		1.62	$.35\times10^6$	.350	.700	4.375	9.00	wing	hex.	.06	1.00	3.20	1.66	0°	1	.350	.350	59	Langley 9 in.
								tail	hex.	.06	1.00	7.91	1.66	0°	1	.350	.350		
128		1.62	$.35\times10^6$	.350	.700	4.375	9.00	wing	hex.	.06	1.00	4.70	1.66	0°	1	.350	.350	59	Langley 9 in.
								tail	hex.	.06	1.00	7.91	1.66	0°	1	.350	.350		
129		1.62	$.52\times10^6$	.350	.700	4.375	9.00	wing	hex.	.03	1.50	2.94	1.11	0°	1	.350	.350	59	Langley 9 in.
								tail	hex.	.03	1.00	7.91	1.66	0°	1	.350	.350		
130		1.62	$.52\times10^6$	.350	.700	4.375	9.00	wing	hex.	.03	1.50	4.44	1.11	0°	1	.350	.350	59	Langley 9 in.
								tail	hex.	.03	1.00	7.91	1.66	0°	1	.350	.350		
131		1.72	1.24×10^6	.450	4.12	10.68	19.075	wing	hex.	.078	1.03	1.96	2.24	68.2°	0	.308	.331	60	BRL
								tail	hex.	.025	3.00	10.89	1.50	75°	0	.450	.272		
132		1.28	1.12×10^6	.625	1.25	9.125	15.00	wing	hex.	- - -	2.60	8.021	1.07	0°	1	.625	.265	61	BRL
								tail	hex.	- - -	1.71	12.58	1.07	60°	.268	.625	.379		
133		1.28	1.24×10^6	.625	1.25	9.125	15.00	wing	hex.	- - -	2.89	6.69	1.07	60°	.268	.625	.265	61	BRL
								tail	hex.	- - -	1.71	12.58	1.07	60°	.268	.625	.379		
134		1.28	$.79\times10^6$	.625	1.25	9.125	15.00	wing	hex.	- - -	1.84	8.34	1.07	0°	1	.625	.338	61	BRL
								tail	hex.	- - -	1.71	12.58	1.07	60°	.268	.625	.379		
135		1.28	$.87\times10^6$	.625	1.25	9.125	15.00	wing	hex.	- - -	2.02	7.40	1.07	60°	.268	.625	.338	61	BRL
								tail	hex.	- - -	1.71	12.58	1.07	60°	.268	.625	.379		
136		1.72	1.11×10^6	.625	1.25	9.125	15.00	wing	hex.	- - -	2.57	6.69	3.31	59.4°	0	.625	.215	62	BRL
								tail	hex.	- - -	1.68	12.61	2.80	50°	.253	.625	.294		
137		1.72	$.56\times10^6$	.625	1.25	9.125	15.00	wing	hex.	- - -	1.30	8.60	7.48	0°	1	.625	.153	62	BRL
								tail	hex.	- - -	1.68	12.61	2.80	50°	.253	.625	.294		
138		1.72	1.34×10^6	.625	1.25	9.125	15.00	wing	hex.	- - -	3.11	6.69	1.87	60°	.130	.625	.265	62	BRL
								tail	hex.	- - -	1.68	12.61	2.80	50°	.253	.625	.294		
139		1.72	1.17×10^6	.625	1.25	9.125	15.00	wing	hex.	- - -	2.73	7.53	1.87	30°	.444	.625	.265	62	BRL
								tail	hex	- - -	1.68	12.61	2.80	50°	.253	.625	.294		
140		1.72	1.12×10^6	.625	1.25	9.125	15.00	wing	hex.	- - -	2.60	8.02	1.87	0°	1	.625	.265	62	BRL
								tail	hex.	- - -	1.68	12.61	2.80	50°	.253	.625	.294		
141		1.72	1.24×10^6	.625	1.25	9.125	15.00	wing	hex.	- - -	2.89	6.69	1.87	60°	.268	.625	.265	62	BRL
								tail	hex.	- - -	1.68	12.61	2.80	50°	.253	.625	.294		
142		1.72	$.83\times10^6$	.625	1.25	9.125	15.00	wing	hex.	- - -	1.99	7.43	4.00	40°	.250	.625	.198	63	BRL
								tail	hex.	- - -	1.68	12.61	2.80	50°	.253	.625	.294		
143		.49	1.90×10^6	2.00	8.38	36.46	64.41	wing	[5]d.w.	.029	7.54	23.24	2.03	60°	0	2.00	.216	38	CAL & CWT
								tail	d.w.	.030	3.92	57.53	3.49	45°	0	2.00	.254		
144		1.50	1.2×10^6	.54	2.26	9.62	19.90	wing	d.w.	.029	2.26	7.70	2.59	60°	0	.54	.216	64	CAL
								tail	d.w.	.030	1.21	17.40	4.47	45°	0	.54	.230		
145		1.99	$.81\times10^6$	.563	10.5	5.25	10.5	wing	d.w.	.08	1.50	3.75	6.88	45°	0	.563	.200		Ames 1x3 ft
								tail	d.w.	.08	.835	9.16	6.88	45°	0	.563	.310		
146		1.90	1.51×10^6	1.8	11.31	29.14	57.31	wing	d.w.	.03	11.31	22.28	1.87	0°	1	1.80	.216	65	Ames 6x6 ft
								tail	plate	.02	10.94	46.37	.782	0°	1	1.80	.405		

NACA

TABLE III.- SUMMARY OF GEOMETRIC AND AERODYNAMIC CHARACTERISTICS AND TEST CONDITIONS FOR BODY-WING-TAIL COMBINATIONS - Concluded

(d) Aerodynamic Characteristics

No.	$\frac{S_T}{S_W}$	K_N	$K_{W(B)}$	$K_{B(W)}$	$K_{T(B)}$	$K_{B(T)}$	Theoretical: [7]Lift $\beta C_{L_{\alpha_W}}$	$\beta C_{L_{\alpha_T}}$	$\beta C_{L_{\alpha_N}}$	[8]$\beta C_{L_{\alpha_C}}$	$\beta C_{L_{\alpha_C}}$	Theoretical: Center of pressure $\bar{l}_N$	$\bar{l}_{W(B)}$	$\bar{l}_{B(W)}$	$\bar{l}_{T(B)}$	$\bar{l}_{B(T)}$	[8]$\bar{l}_C$	$\bar{l}_C$	[8]$\left(\frac{l}{l}\right)_C$	$\left(\frac{l}{l}\right)_C$	Experimental: [7]Lift $\beta C_{L_{\alpha_B}}$	$\beta C_{L_{\alpha_C}}$	c.p. $\left(\frac{l}{l}\right)_C$
120	0.221	[8](0.067)	1.11	0.12	1.19	0.069	3.65	3.60	0.23	5.73	5.45	(0.317)	5.67	6.29	8.35	8.47	5.97	5.78	0.602	0.661	0.23	5.36	0.673
121	1.00	(.477)	1.30	.53	1.30	.53	3.62	3.62	1.51	14.97	9.78	(1.46)	3.51	4.05	8.23	8.58	5.48	4.01	.609	.446	(1.72)	9.09	[10].486
122	1.00	(.477)	1.30	.53	1.30	.53	3.62	3.62	1.51	14.97	9.78	(1.46)	5.11	5.55	8.23	8.58	6.18	5.08	.686	.564	(1.72)	9.94	.570
123	1.00	(.477)	1.30	.39	1.30	.53	3.62	3.62	1.51	14.53	10.73	(1.46)	3.87	4.15	8.23	8.58	5.65	4.70	.628	.522	(1.72)	10.02	.515
124	1.00	(.477)	1.30	.39	1.30	.53	3.62	3.62	1.51	14.53	10.73	(1.46)	5.37	5.65	8.23	8.58	6.28	5.59	.698	.621	(1.72)	9.82	.615
125	1.00	(.477)	1.30	.39	1.30	.20	3.62	3.62	1.51	13.29	9.49	(1.46)	3.87	4.15	8.59	8.58	5.52	4.43	.613	.492	(1.72)	9.00	.486
126	1.00	(.477)	1.30	.39	1.30	.20	3.62	3.62	1.51	13.29	9.49	(1.46)	5.37	5.65	8.59	8.58	6.21	5.40	.690	.600	(1.72)	9.00	.580
[11]127	1.00	(.310)	1.30	.39	1.30	.53	2.79	2.79	.76	11.02	6.79	(1.46)	3.63	4.15	8.34	8.57	5.74	4.11	.638	.457	(.87)	6.99	[10]
[11]128	1.00	(.310)	1.30	.39	1.30	.53	2.79	2.79	.76	11.02	6.79	(1.46)	5.13	5.65	8.34	8.57	6.43	5.23	.714	.581	(.87)	7.05	.588
[11]129	.667	(.263)	1.30	.53	1.30	.53	2.19	2.76	.50	7.96	4.67	(1.46)	3.30	3.70	8.34	8.57	5.44	3.34	.604	.371	(.58)	4.55	.392
[11]130	.667	(.263)	1.30	.53	1.30	.53	2.19	2.76	.50	7.96	4.67	(1.46)	4.80	5.20	8.34	8.57	6.20	4.63	.689	.514	(.58)	4.48	[10]
131	5.64	(.727)	1.28	.40	1.23	.34	2.81	2.08	.33	4.41	3.61	(2.13)	2.30	3.19	13.89	13.93	11.65	11.15	.611	.585	(.36)	3.38	.559
132	.35	(.129)	1.22	.38	1.33	.41	2.13	1.79	.22	4.76	3.71	(4.17)	8.94	9.70	14.00	14.11	9.96	8.82	.664	.588	(.28)	3.26	.535
133	.35	(.154)	1.22	.35	1.33	.41	1.79	1.79	.22	4.12	3.21	(4.17)	9.08	9.31	14.00	14.11	10.09	9.04	.672	.602	(.28)	[12]3.25	[12].575
134	.70	(.259)	1.29	.51	1.33	.41	2.13	1.79	.44	6.55	3.98	(4.17)	9.00	9.69	14.00	14.11	10.38	8.05	.692	.537	(.56)	3.74	.545
135	.70	(.306)	1.29	.46	1.33	.41	1.82	1.79	.44	5.95	3.62	(4.17)	9.08	9.40	14.00	14.11	10.50	8.27	.700	.551	(.56)	3.64	.575
136	.513	(.131)	1.18	.24	1.25	.23	3.61	3.68	.39	8.18	6.49	3.17	9.26	9.56	14.06	14.17	10.46	9.56	.698	.637	.47	[12]6.10	[12].620
137	.500	(.123)	1.12	.12	1.25	.23	3.73	3.68	.38	7.86	7.37	3.17	9.24	10.10	14.06	14.17	10.64	10.44	.710	.696	.46	[12]7.26	[12].691
138	.500	(.150)	1.22	.37	1.25	.23	3.06	3.68	.38	8.10	5.61	3.17	9.22	9.93	14.06	14.17	10.66	9.16	.710	.611	.46	[12]5.30	[12].608
139	.500	(.149)	1.22	.38	1.25	.23	3.08	3.68	.38	8.18	5.45	3.17	9.17	10.27	14.06	14.17	10.66	8.96	.710	.597	.46	[12]5.72	[12].591
140	.500	(.157)	1.22	.38	1.25	.23	2.93	3.68	.38	7.94	5.05	3.17	9.16	10.23	14.06	14.17	10.69	8.79	.713	.586	.46	[12]5.50	[12].608
141	.500	(.157)	1.22	.30	1.25	.23	2.94	3.68	.38	7.70	4.89	3.17	9.20	9.51	14.06	14.17	10.64	8.69	.710	.580	.46	4.74	.565
142	.500	.128	1.16	.22	1.25	.23	3.59	3.68	.38	8.18	6.89	3.17	9.24	9.76	14.06	14.17	10.60	9.97	.706	.665	.46	7.26	[12].691
143	.381	.108	1.18	.31	1.21	.37	2.22	3.12	.24	5.40	4.25	11.6	30.19	28.79	60.75	60.04	39.80	33.33	.618	.518		3.75	.509
144	.492	.100	1.18	.25	1.19	.16	3.10	4.00	.31	7.37	5.45	3.13	9.95	10.03	19.10	19.10	12.98	10.78	.652	.542		5.57	.553
145	.309	.169	1.16	.23	1.27	.12	4.00	4.00	.68	7.99	7.20	1.62	5.25	5.86	9.99	9.99	6.03	5.62	.575	.535		7.74	.550
146	.392	.076	1.18	.31	1.36	.62	2.93	1.50	.22	5.74	5.19	10.4	27.26	31.33	49.51	53.35	32.02	29.18	.559	.508		5.00	.485

[1] R based on $\bar{c}$ of larger lifting surface

[2] - denotes nonuniform or unknown t/c, thickness-chord ratio

[3] d.w. indicates double wedge

[4] hex. indicates hexagonal

[5] b.c. indicates biconvex

[6] Slight variation between subsonic and supersonic model wing proportions, subsonic configuration tested with extended, cylindrical tail boom coaxial with body.

[7] All lift curve slopes (per radian) referred to exposed area of larger lifting surface except $\beta C_{L_{\alpha_W}}$ or $\beta C_{L_{\alpha_T}}$.

[8] Value by neglecting wing-tail interference

[9] () indicates experimental value used in theory for combination

[10] Experimental C_L or C_m curve nonlinear near $\alpha = 0$.

[11] Alden-Schindel technique applied in estimating interference.

[12] Experimental lift or moment curves v.s. α do not pass through origin for symmetrical models.

[13] $\bar{c}$ based on exposed area

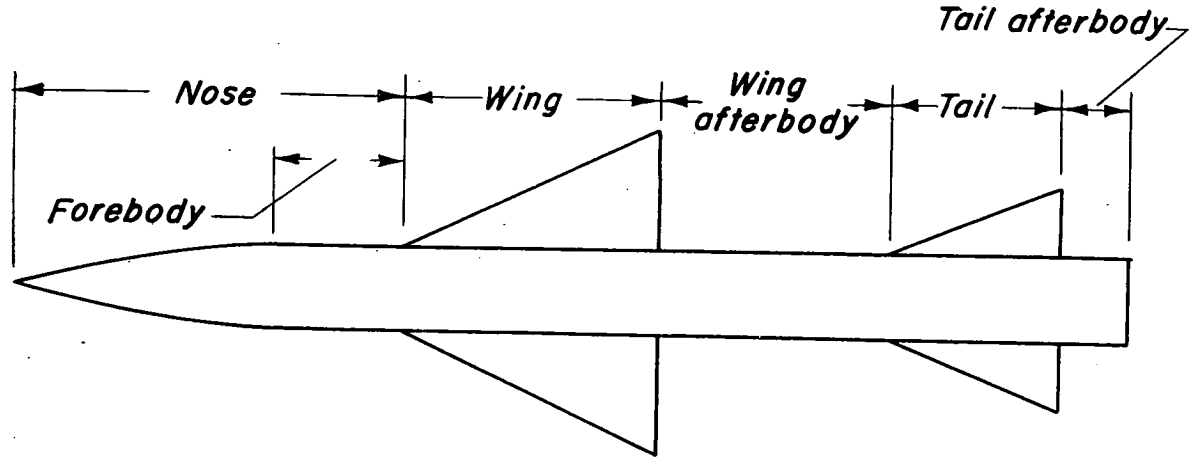

(a) Parts of a wing-body-tail combination.

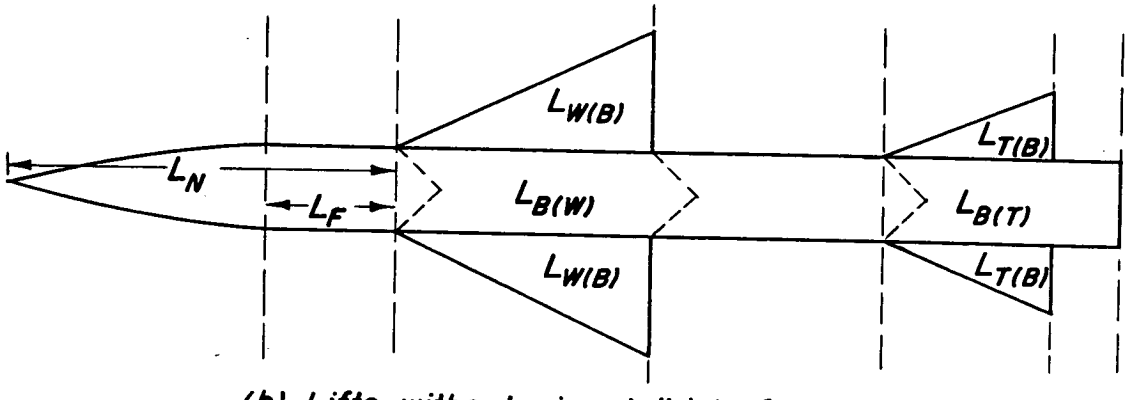

(b) Lifts without wing-tail interference.

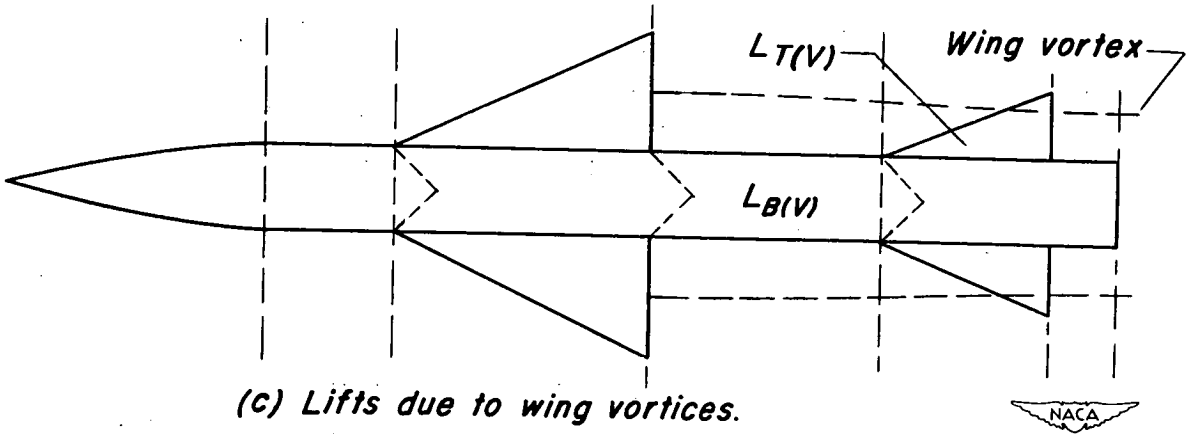

(c) Lifts due to wing vortices.

Figure 1.-Parts and lift components of a wing-body-tail combination.

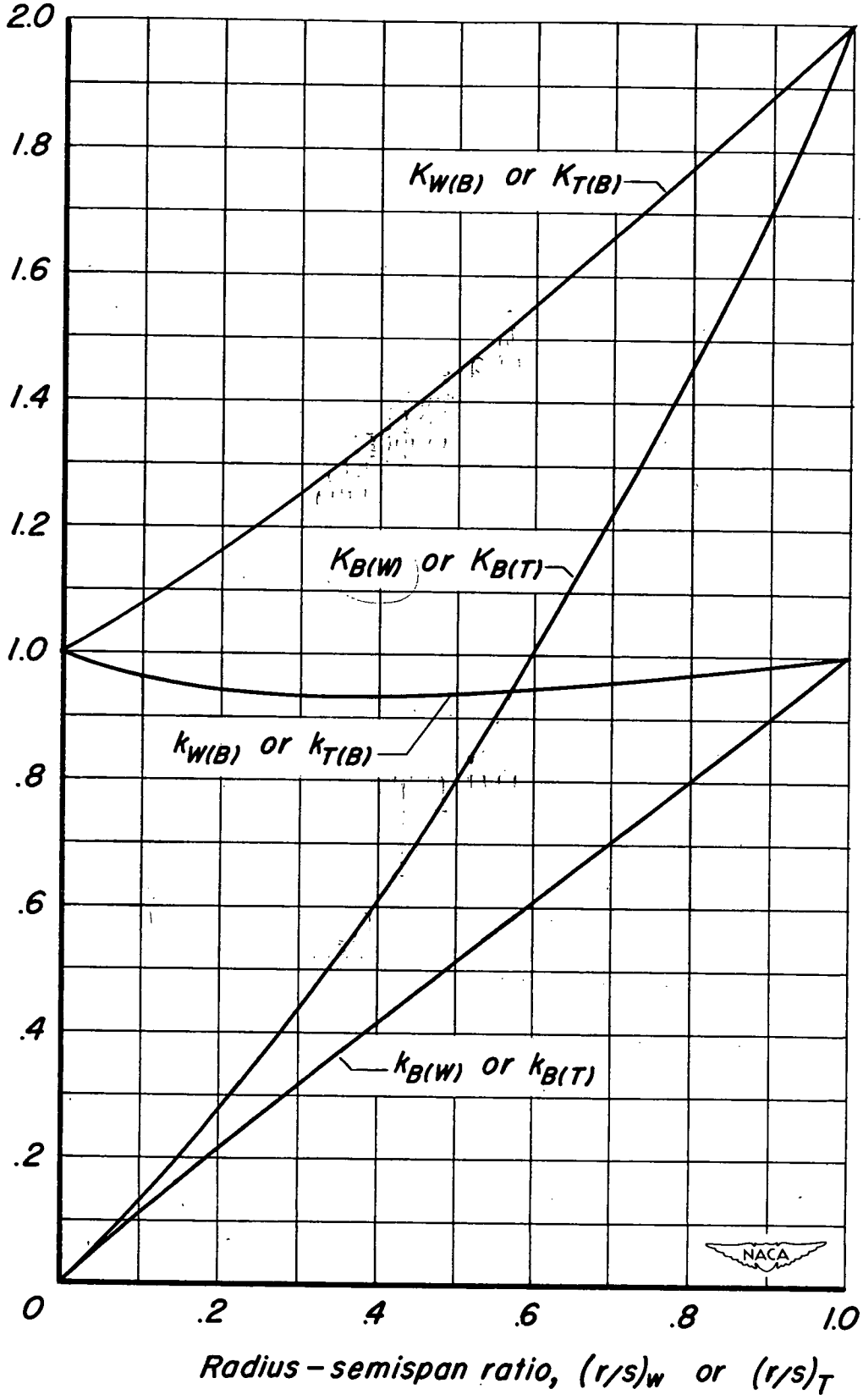

Figure 2. – Values of lift ratios based on slender-body theory.

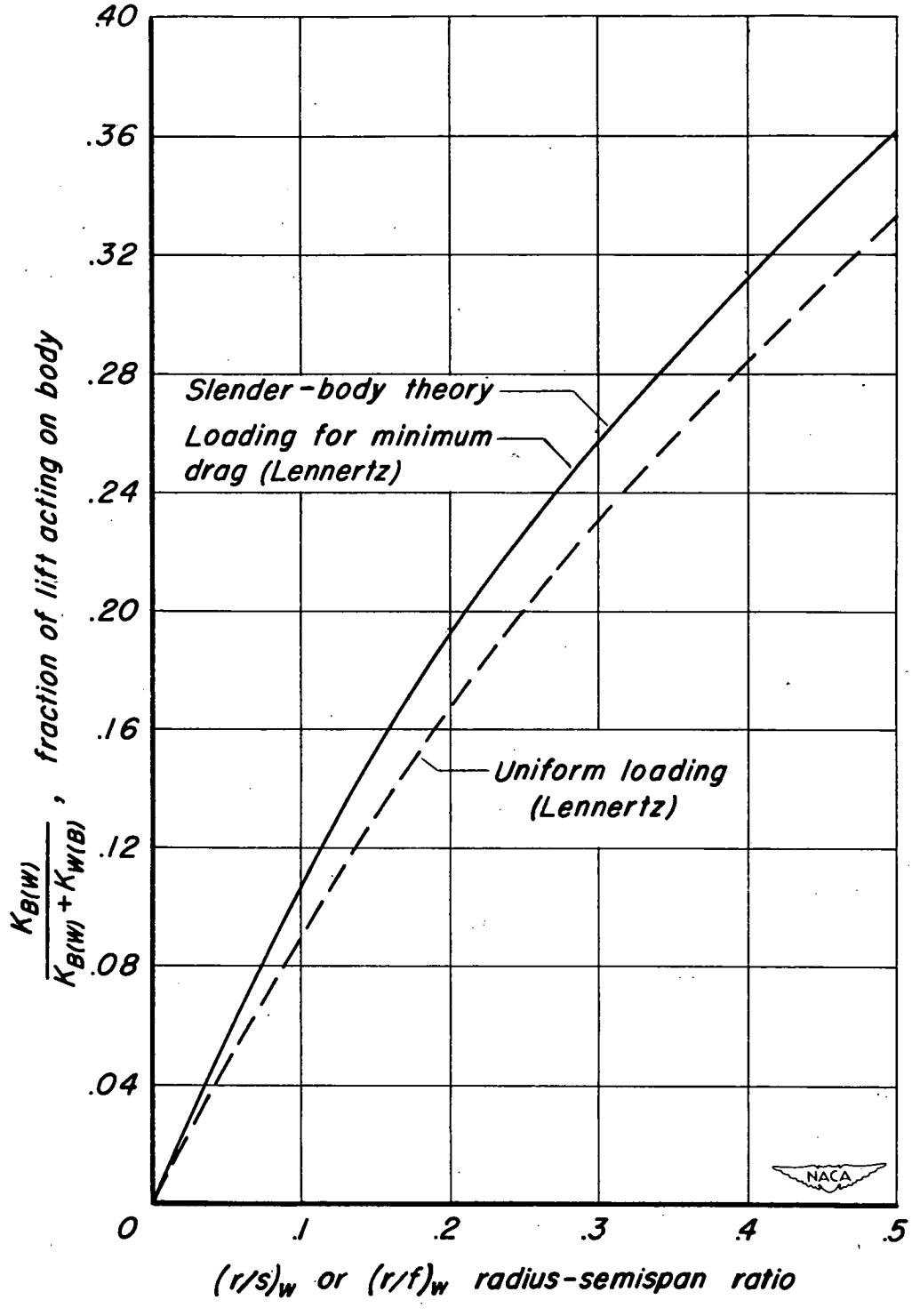

Figure 3.- Comparison of slender-body theory and theory of Lennertz for fraction of lift carried by body.

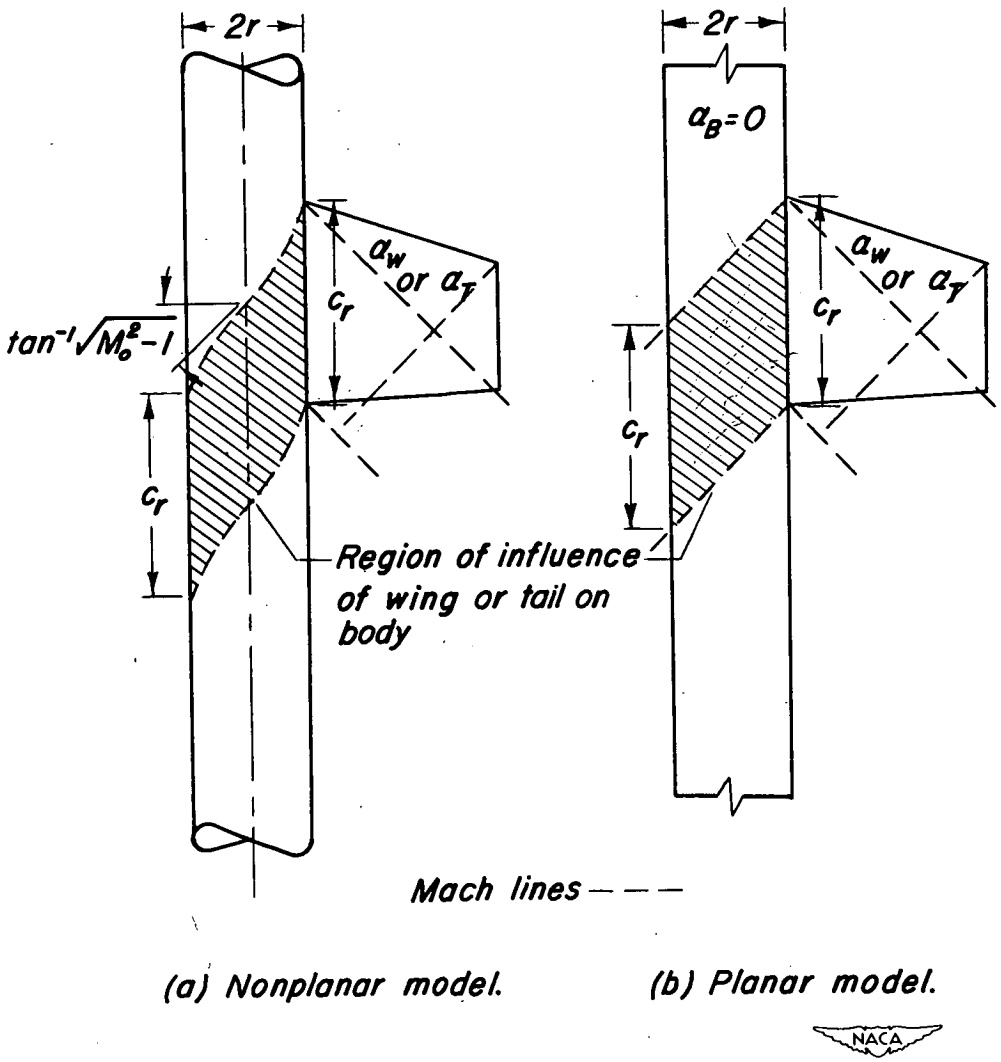

Figure 4.- Equivalent planar model for determination of $K_{B(W)}$ and $K_{B(T)}$ for high-aspect-ratio range at supersonic speeds.

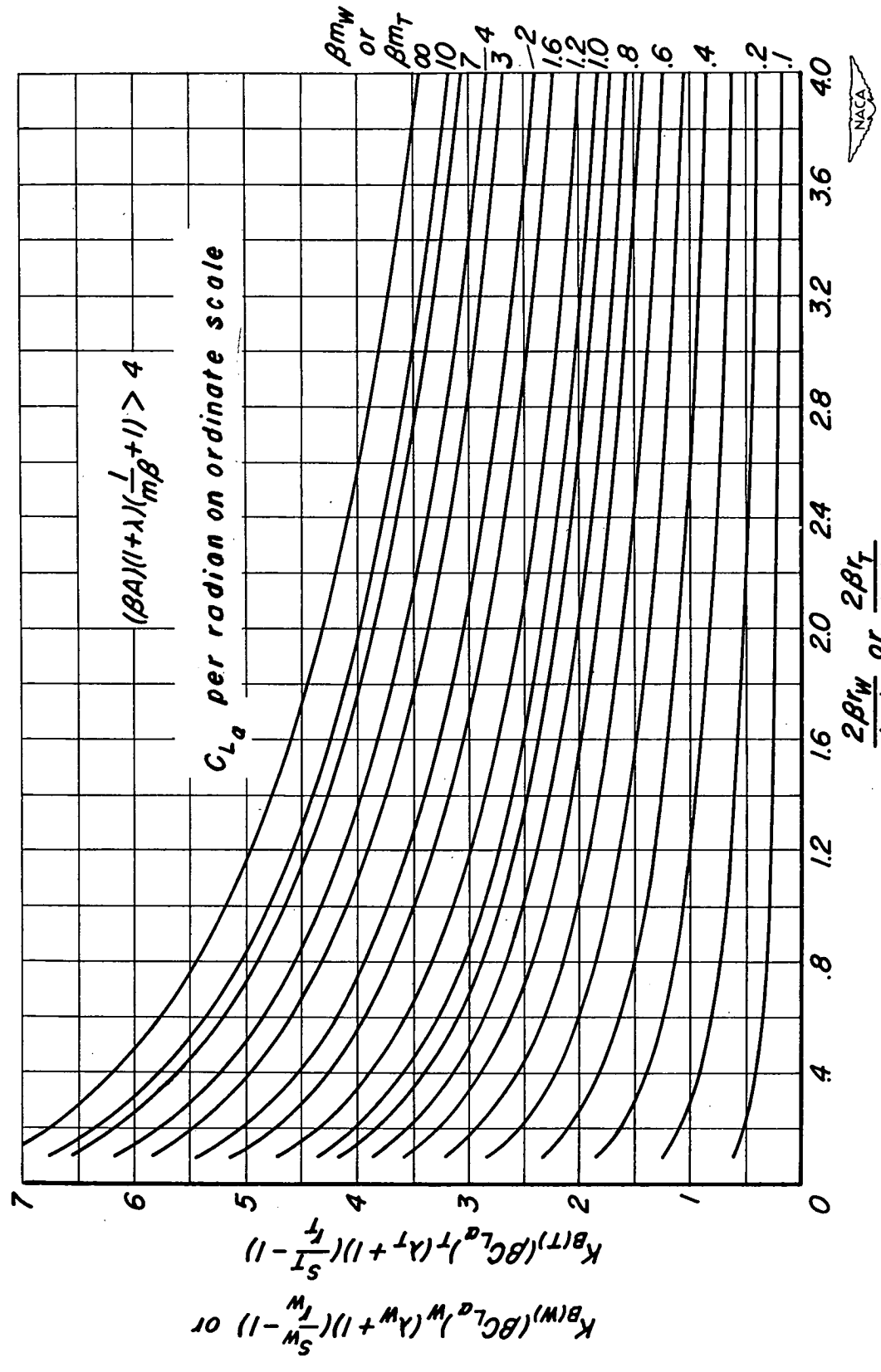

Figure 5.- Design charts for determining $K_{B(W)}$ and $K_{B(T)}$ for high-aspect-ratio range at supersonic speeds.

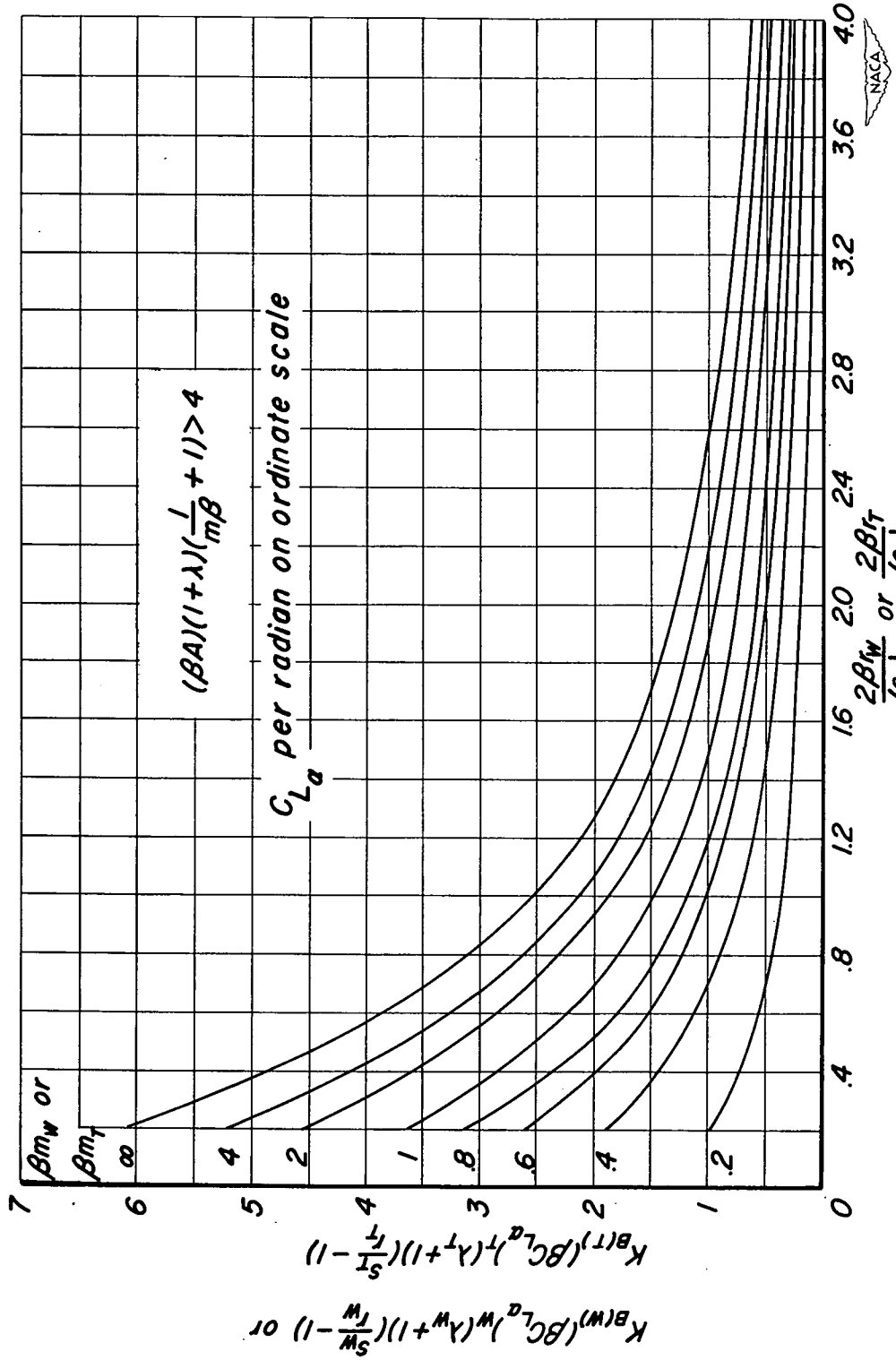

(b) No afterbody.

Figure 5.- Concluded.

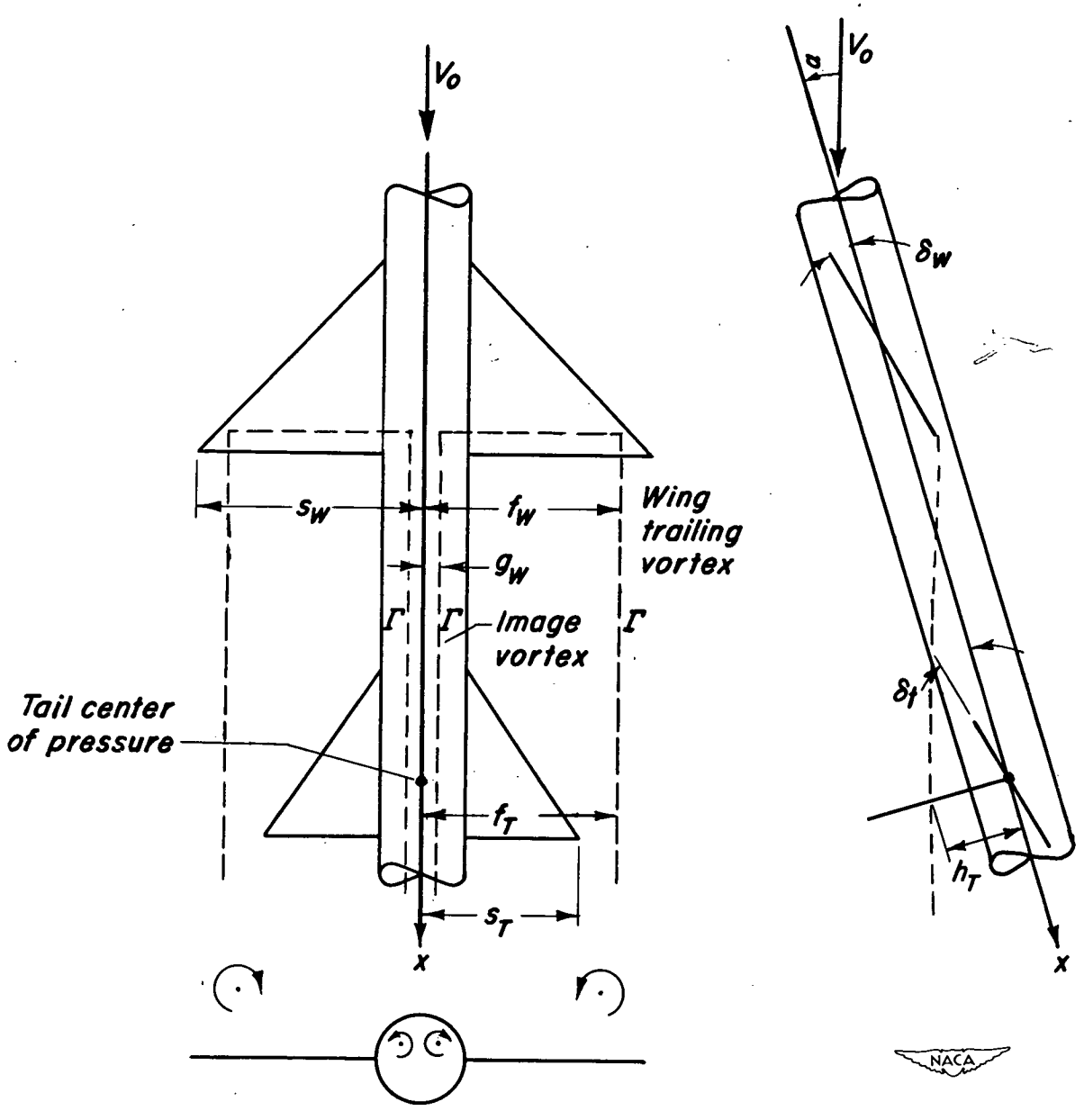

Figure 6.- Vortex model used in determination of wing-tail interference.

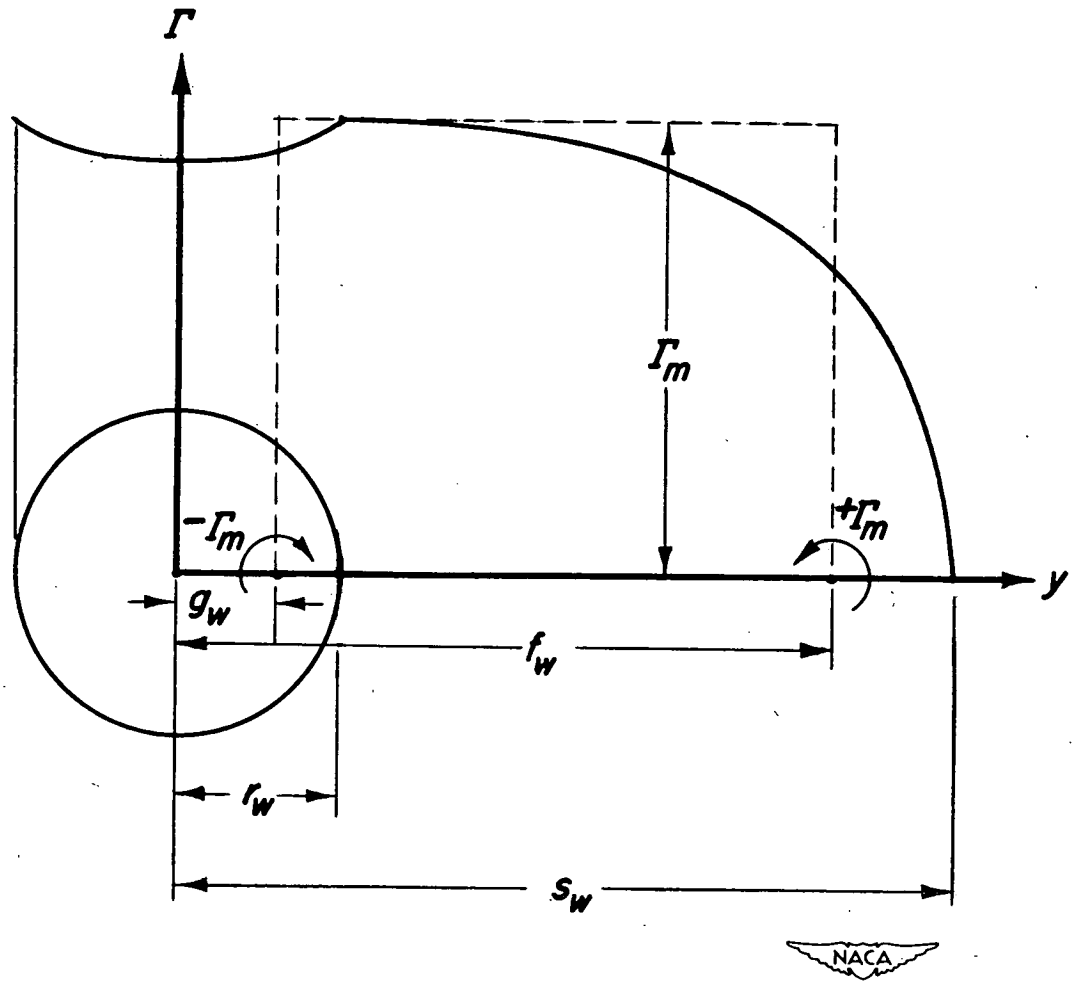

Figure 7.– Circulation distribution at wing trailing edge and equivalent horseshoe vortex.

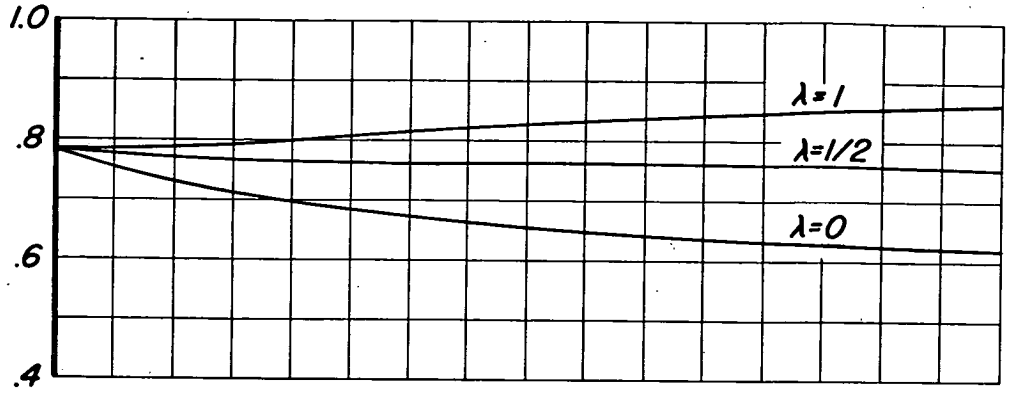

(a) No leading-edge sweep.

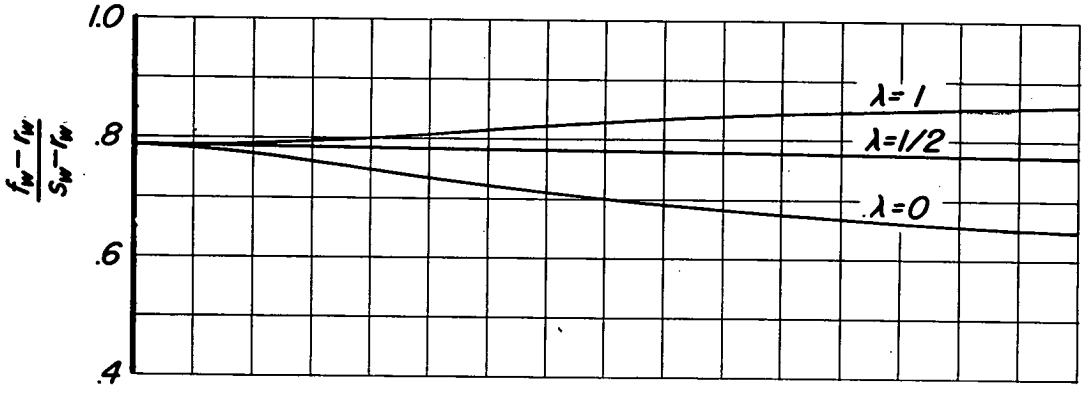

(b) No midchord sweep.

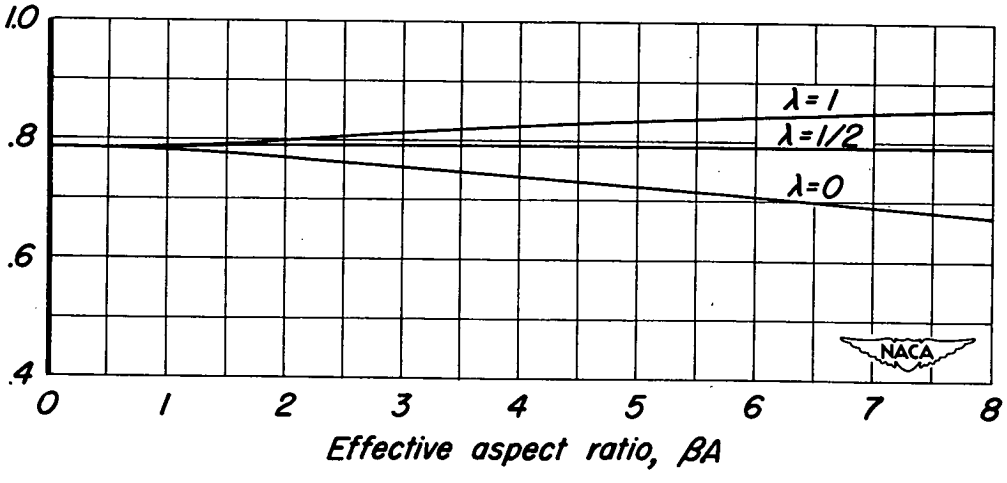

(c) No trailing-edge sweep.

Figure 8.—Chart for determination of wing vortex lateral positions at subsonic speeds.

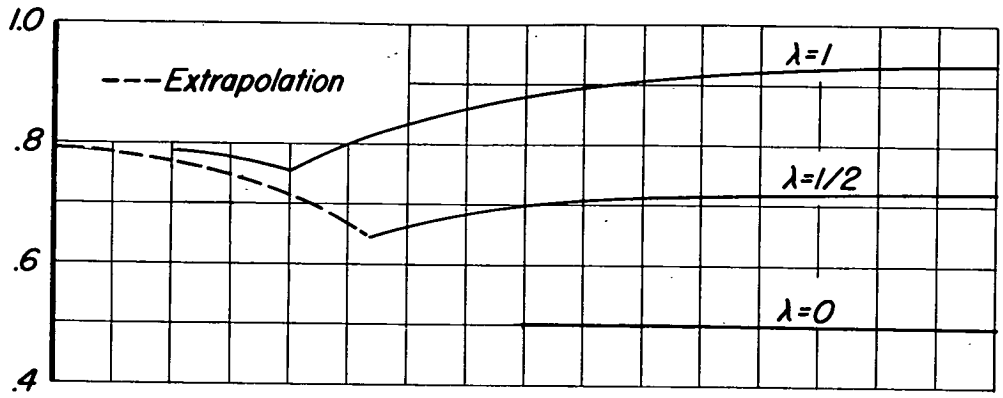

(a) No leading-edge sweep.

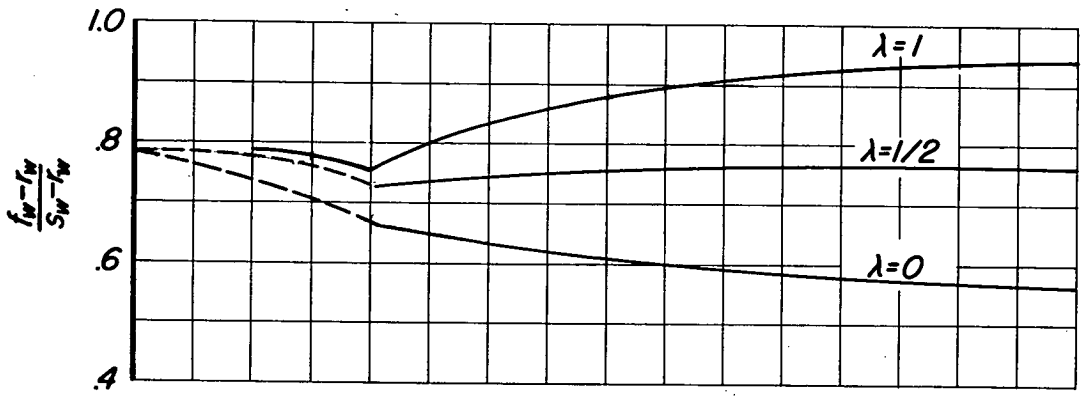

(b) No midchord sweep.

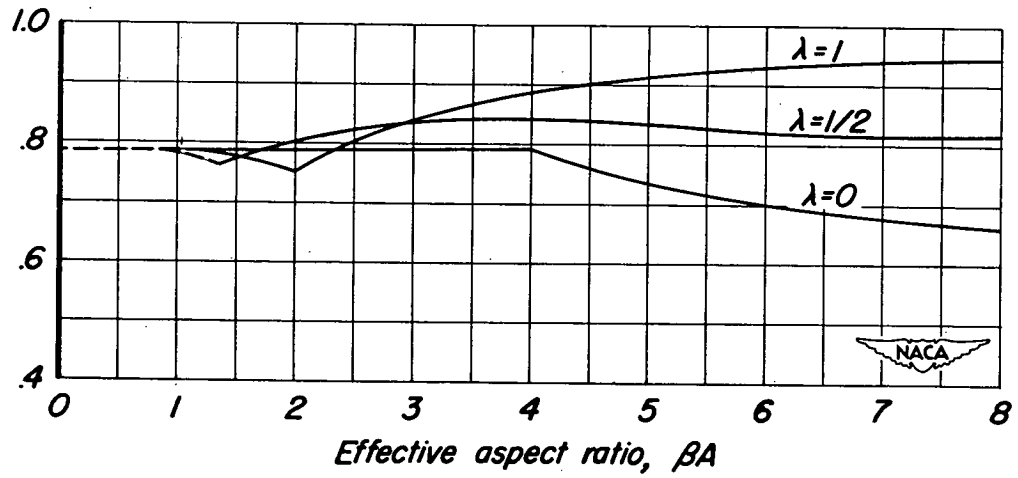

(c) No trailing-edge sweep.

Figure 9.—Chart for determination of wing vortex lateral positions at supersonic speeds.

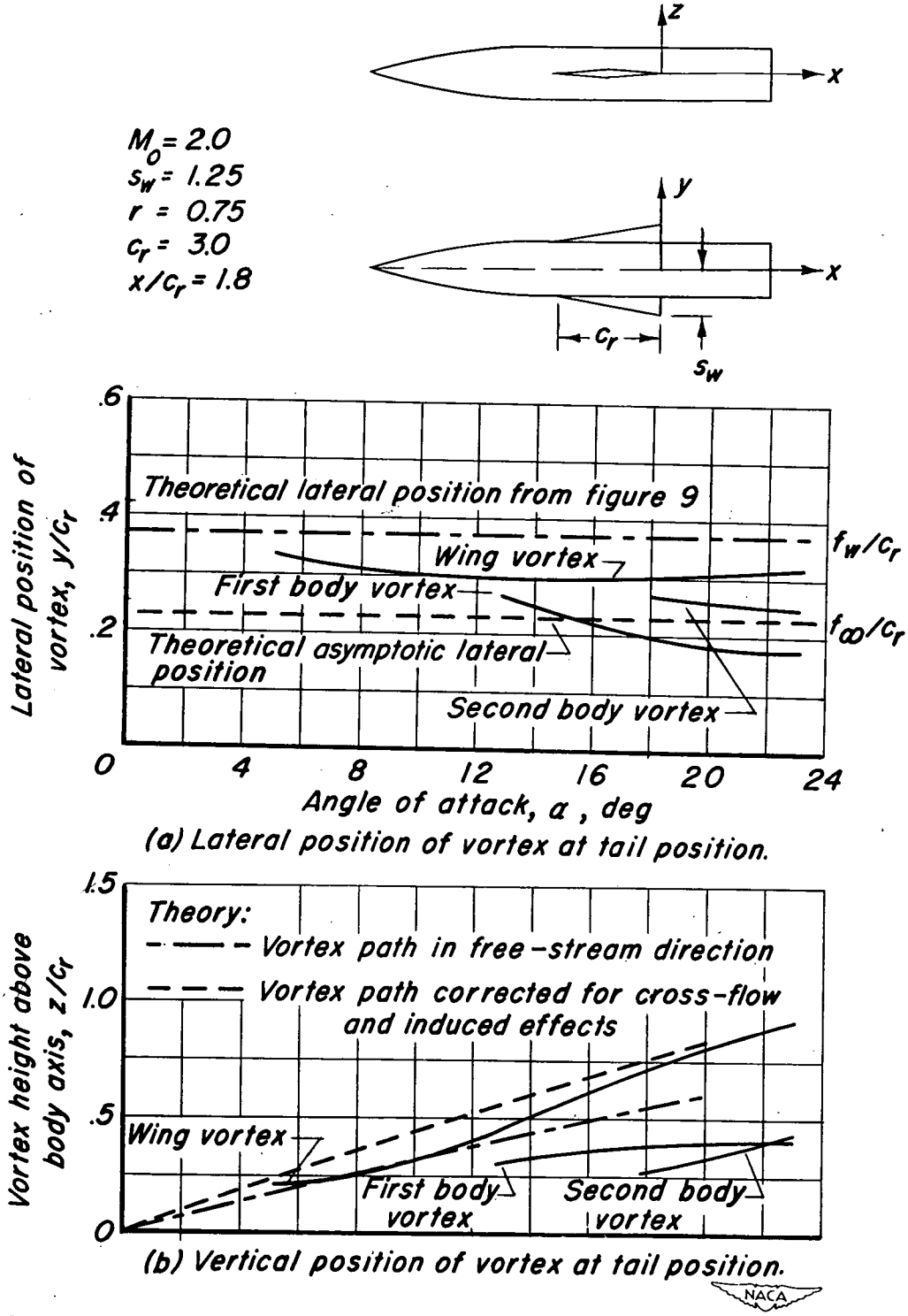

Figure 10. - Comparison between theory and experiment for lateral and vertical positions at wing vortex at tail position of aspect ratio 2/3 triangular wing and body combination.

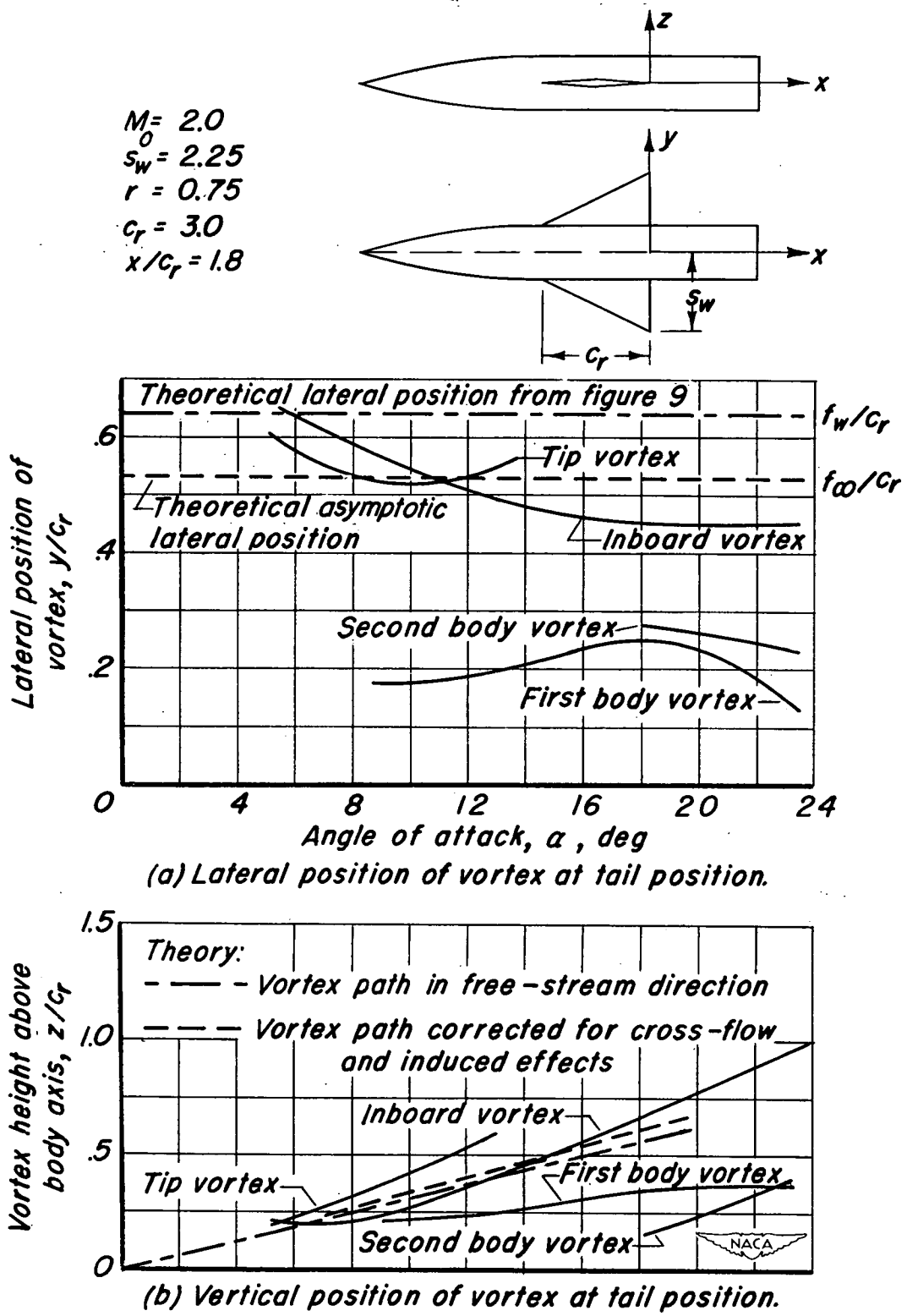

Figure 11.- Comparison between theory and experiment for lateral and vertical positions of wing vortex at tail position of aspect ratio 2 triangular wing and body combination.

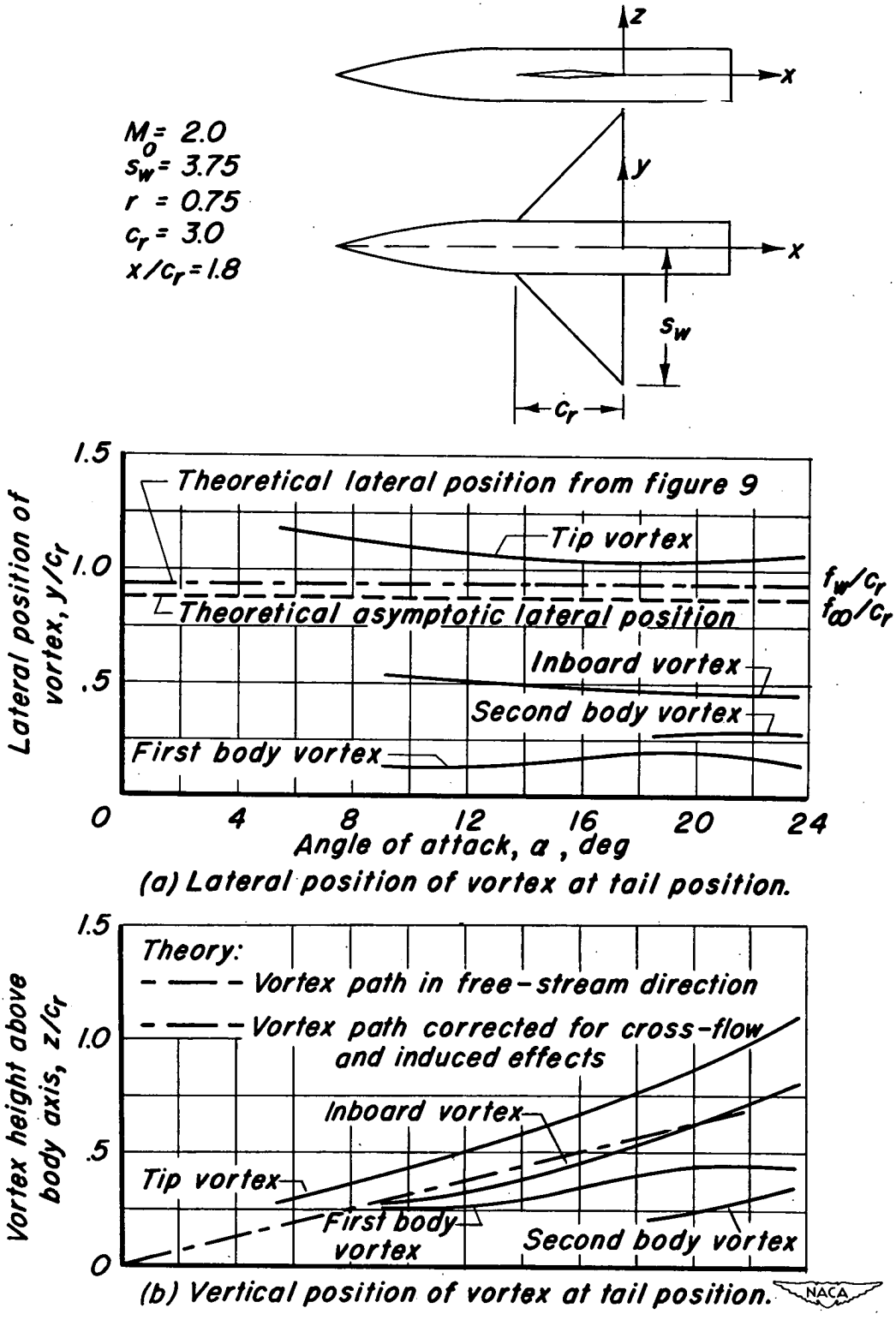

Figure 12.—Comparison between theory and experiment for lateral and vertical positions of wing vortex at tail position of aspect ratio 4 triangular wing and body combination.

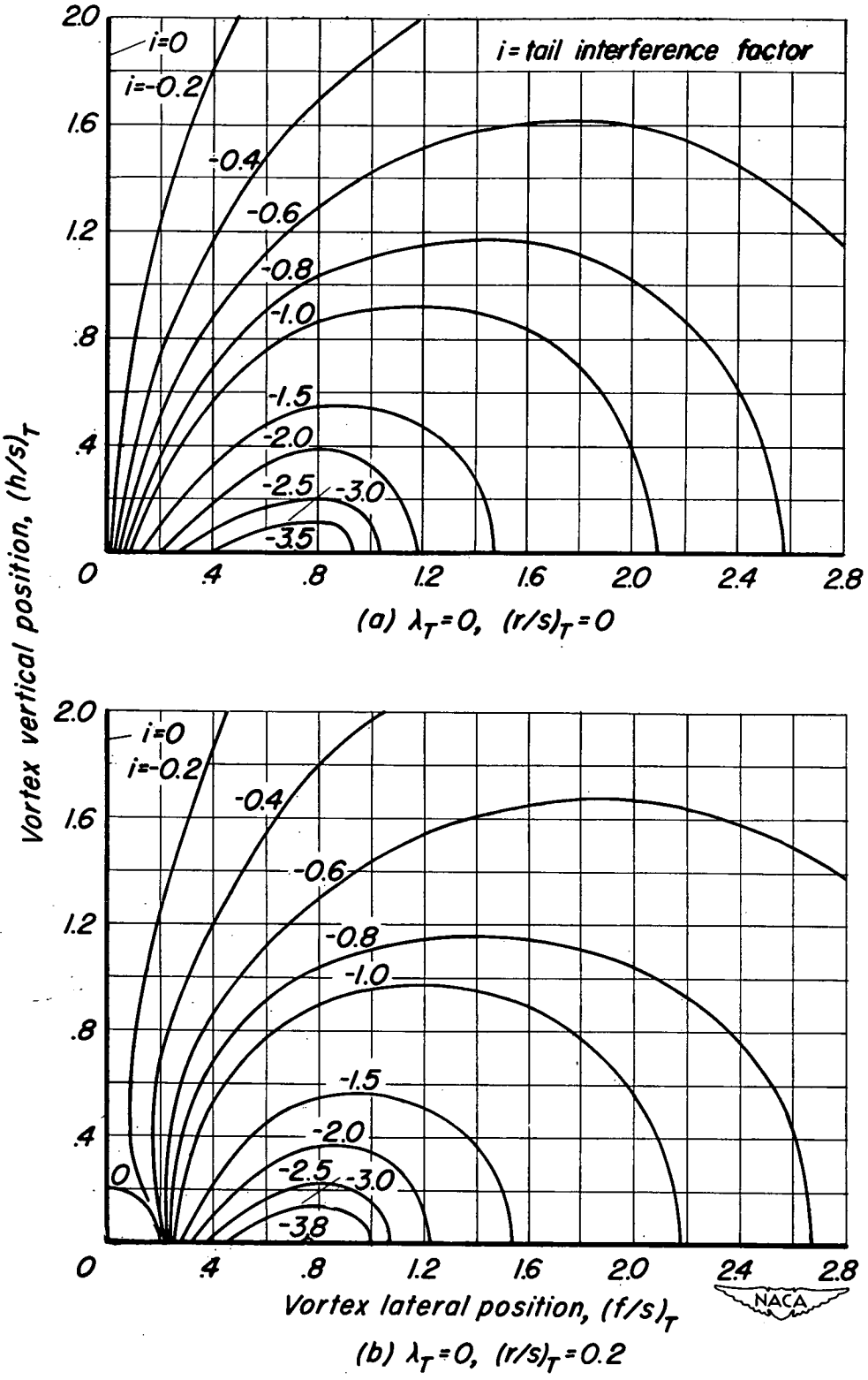

Figure 13.—Charts for determination of tail interference factor as determined by strip theory.

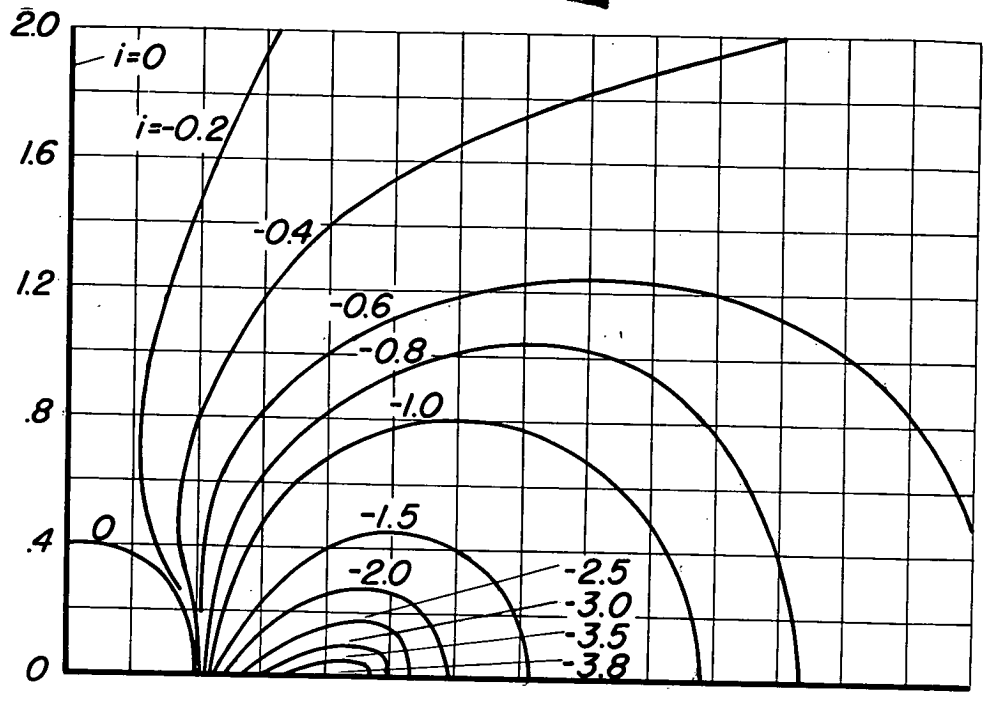

(c) $\lambda_T = 0$, $(r/s)_T = 0.4$

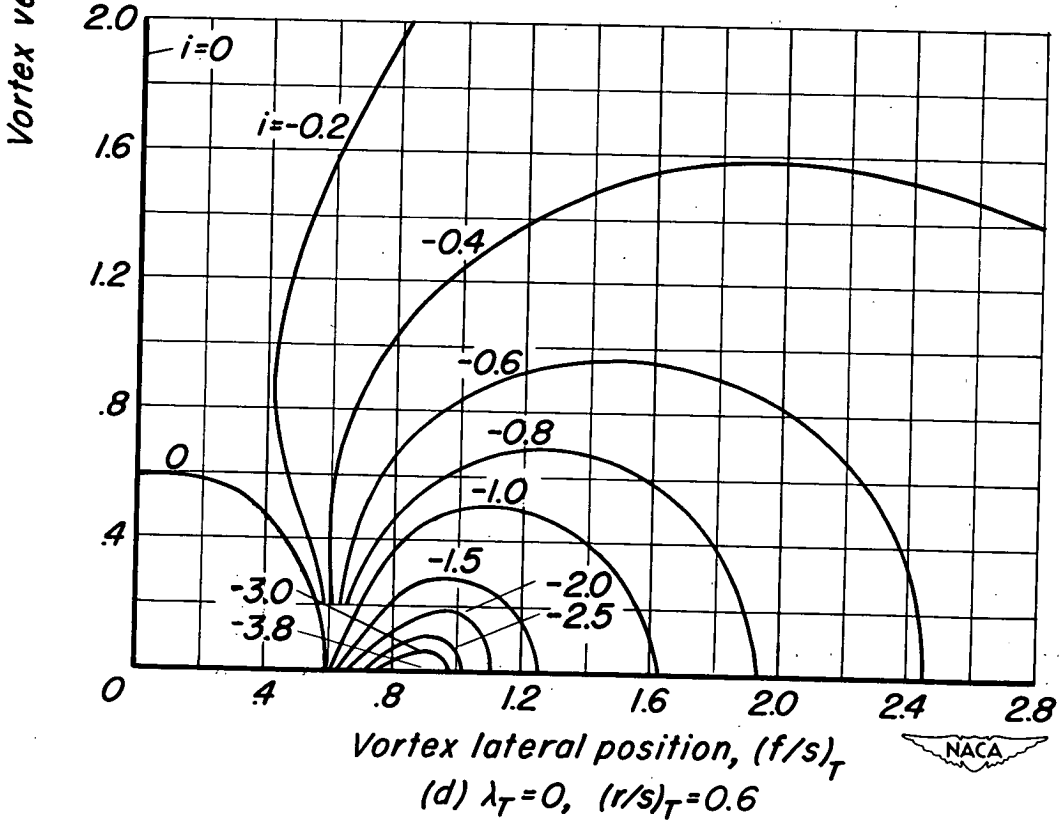

(d) $\lambda_T = 0$, $(r/s)_T = 0.6$

Figure 13. – Continued.

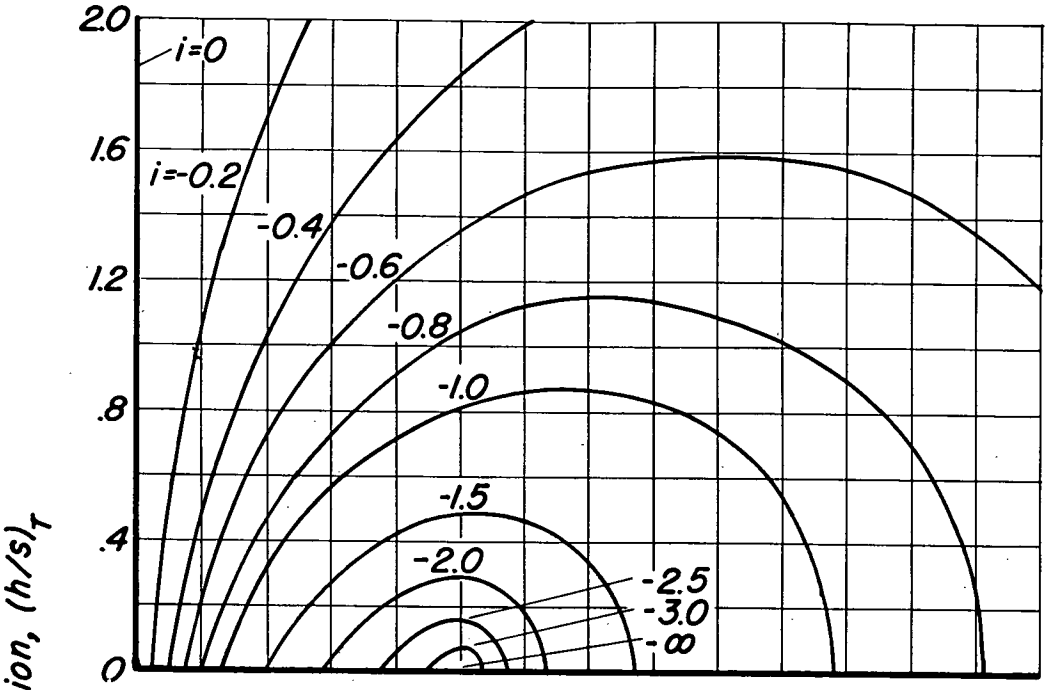

(e) $\lambda_T = 1/2$, $(r/s)_T = 0$

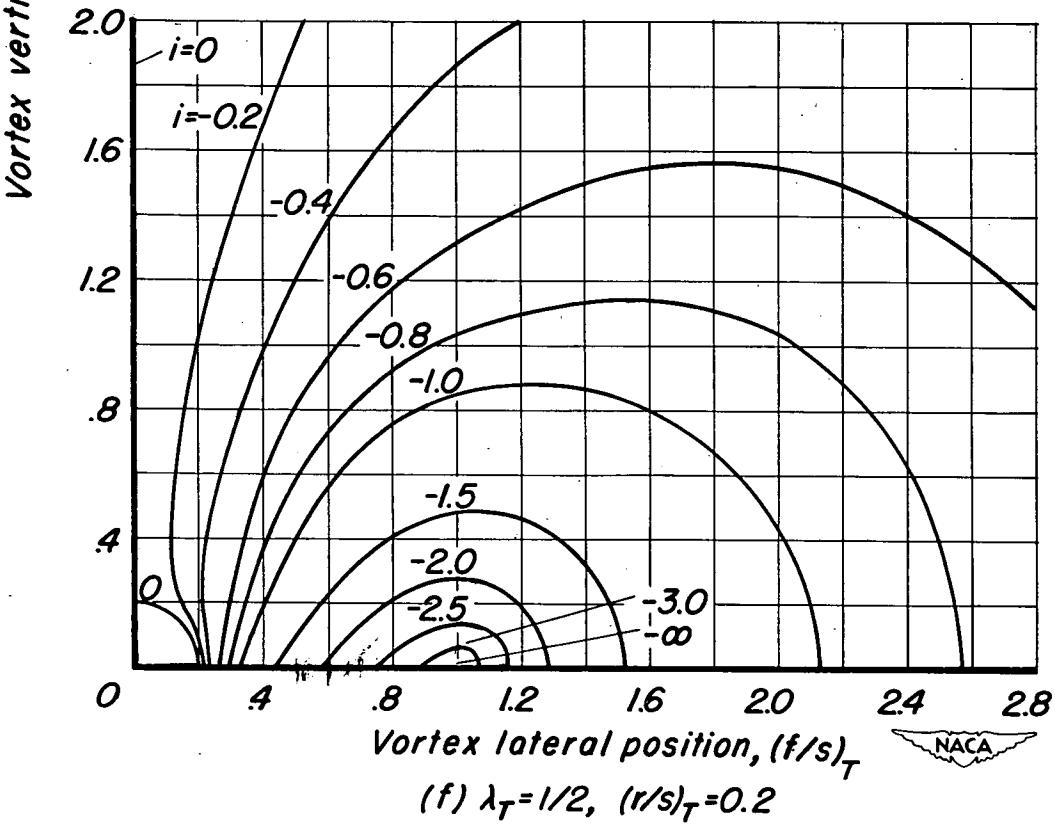

(f) $\lambda_T = 1/2$, $(r/s)_T = 0.2$

Figure 13. – Continued.

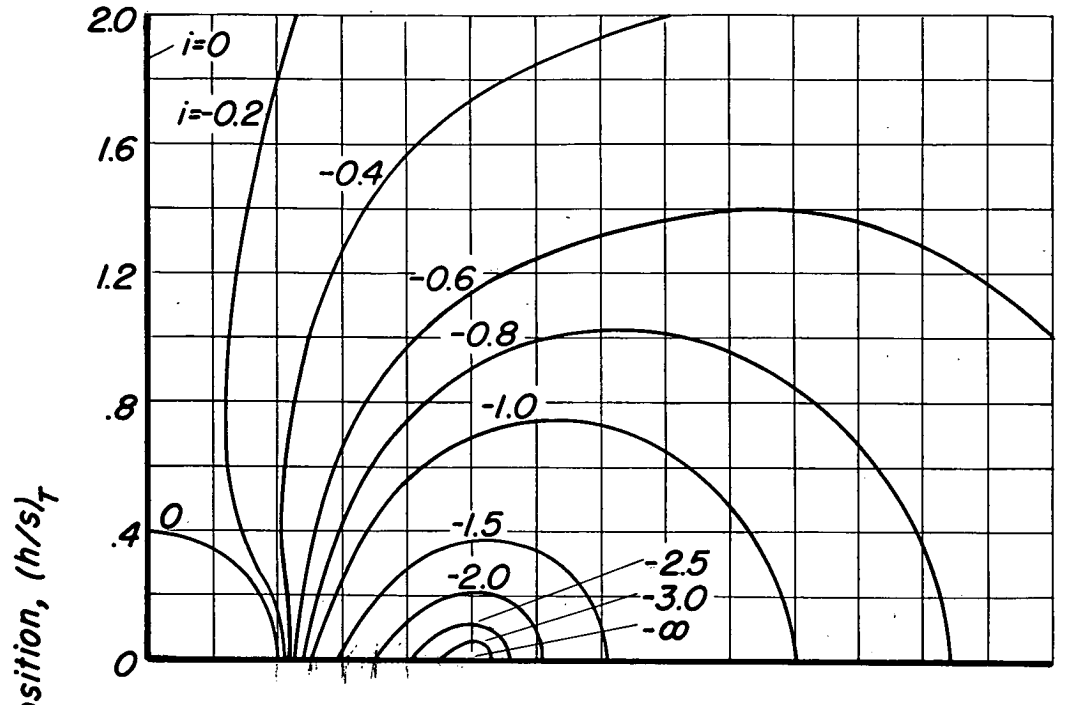

(g) $\lambda_T = 1/2$, $(r/s)_T = 0.4$

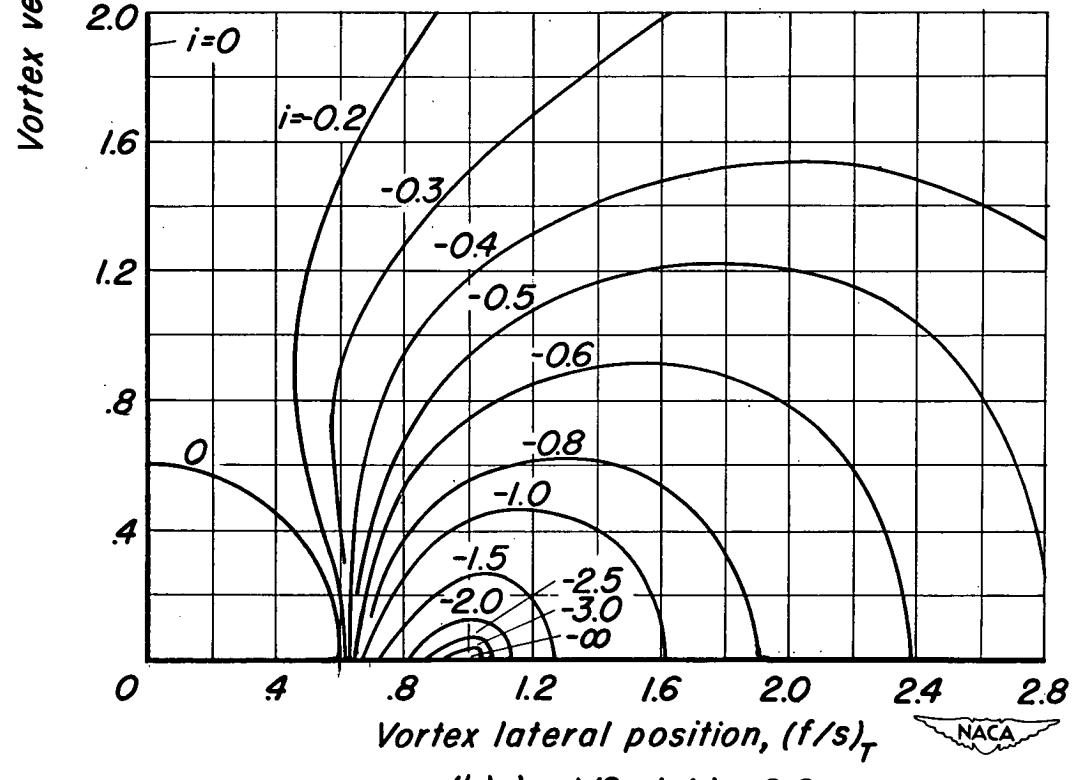

(h) $\lambda_T = 1/2$, $(r/s)_T = 0.6$

Figure 13.—Continued.

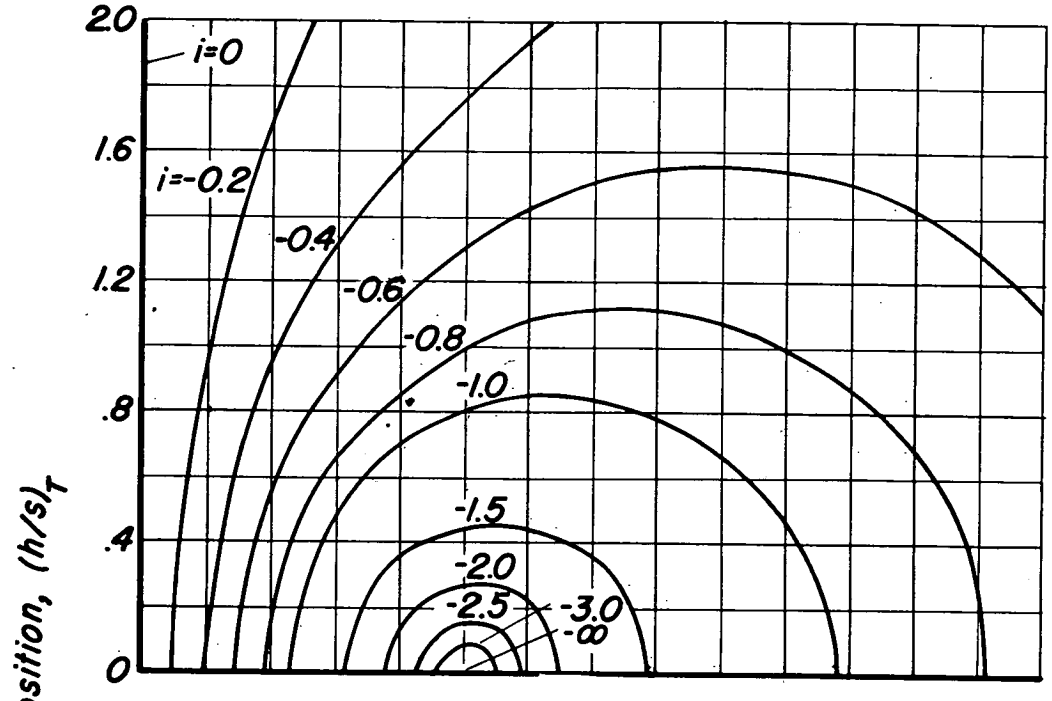

(i) $\lambda_T = 1$, $(r/s)_T = 0$

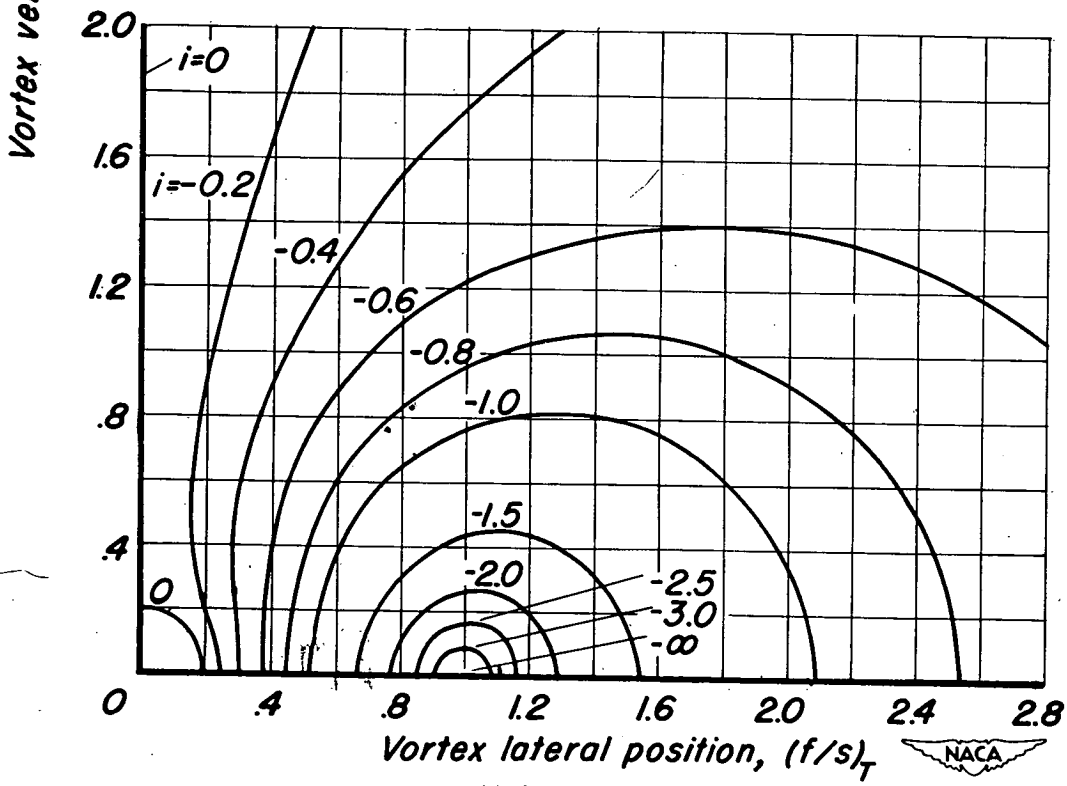

(j) $\lambda_T = 1$, $(r/s)_T = 0.2$

Figure 13. – Continued.

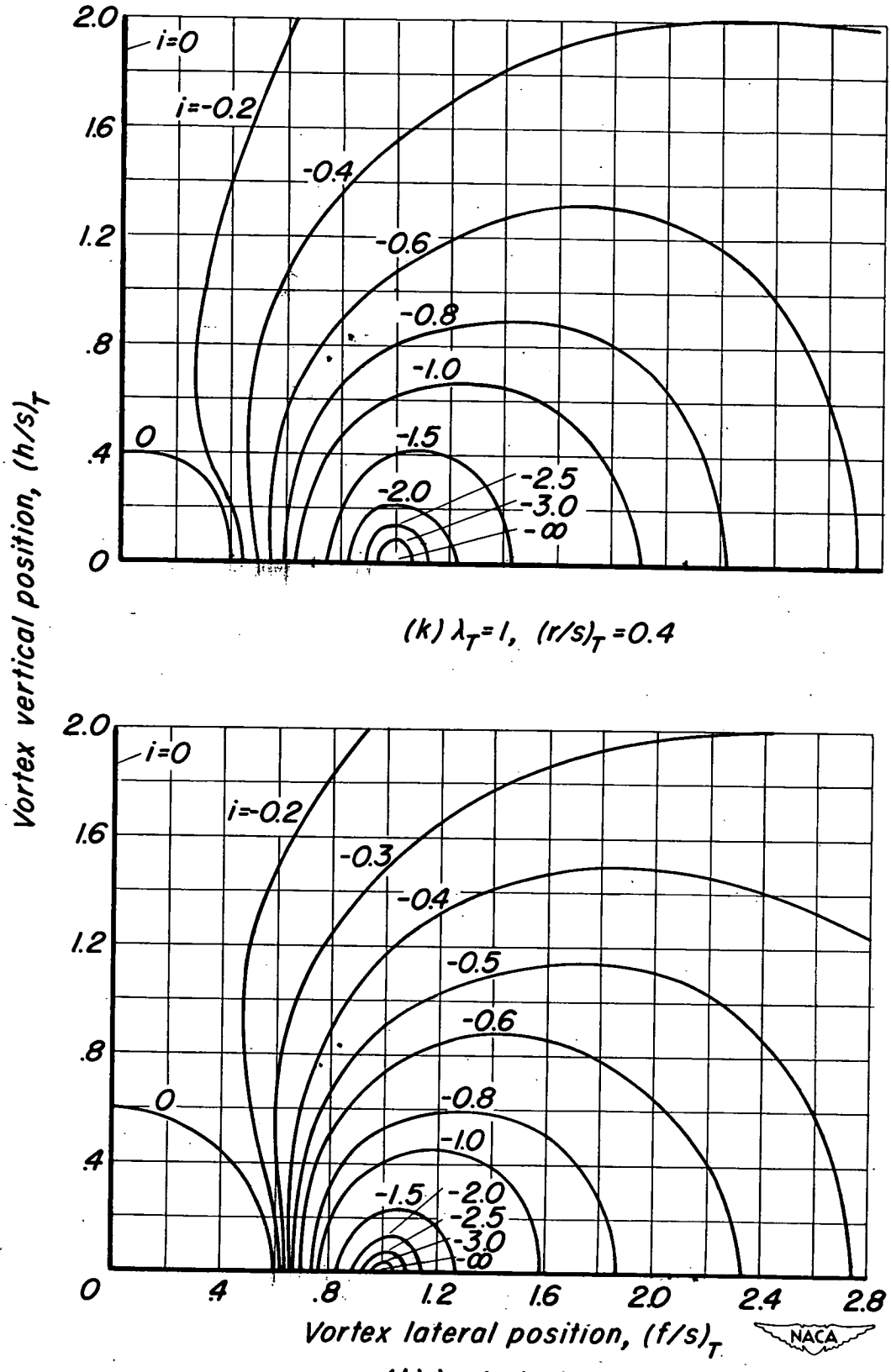

(k) $\lambda_T = 1$, $(r/s)_T = 0.4$

(l) $\lambda_T = 1$, $(r/s)_T = 0.6$

Figure 13. – Concluded.

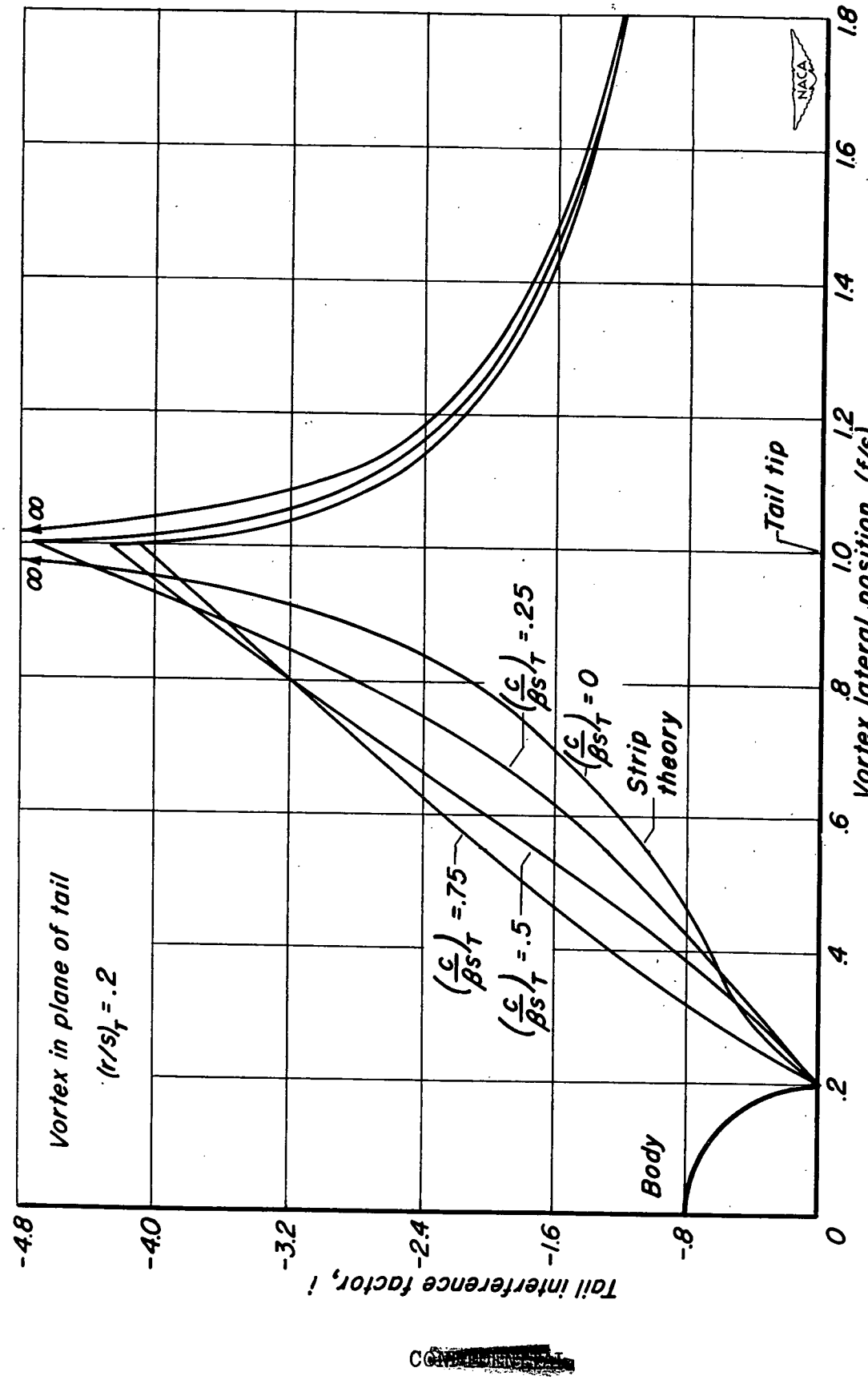

Figure 14. – Effect of chord–span ratio on lift of rectangular tail due to wing vortex as determined by Alden–Schindel technique.

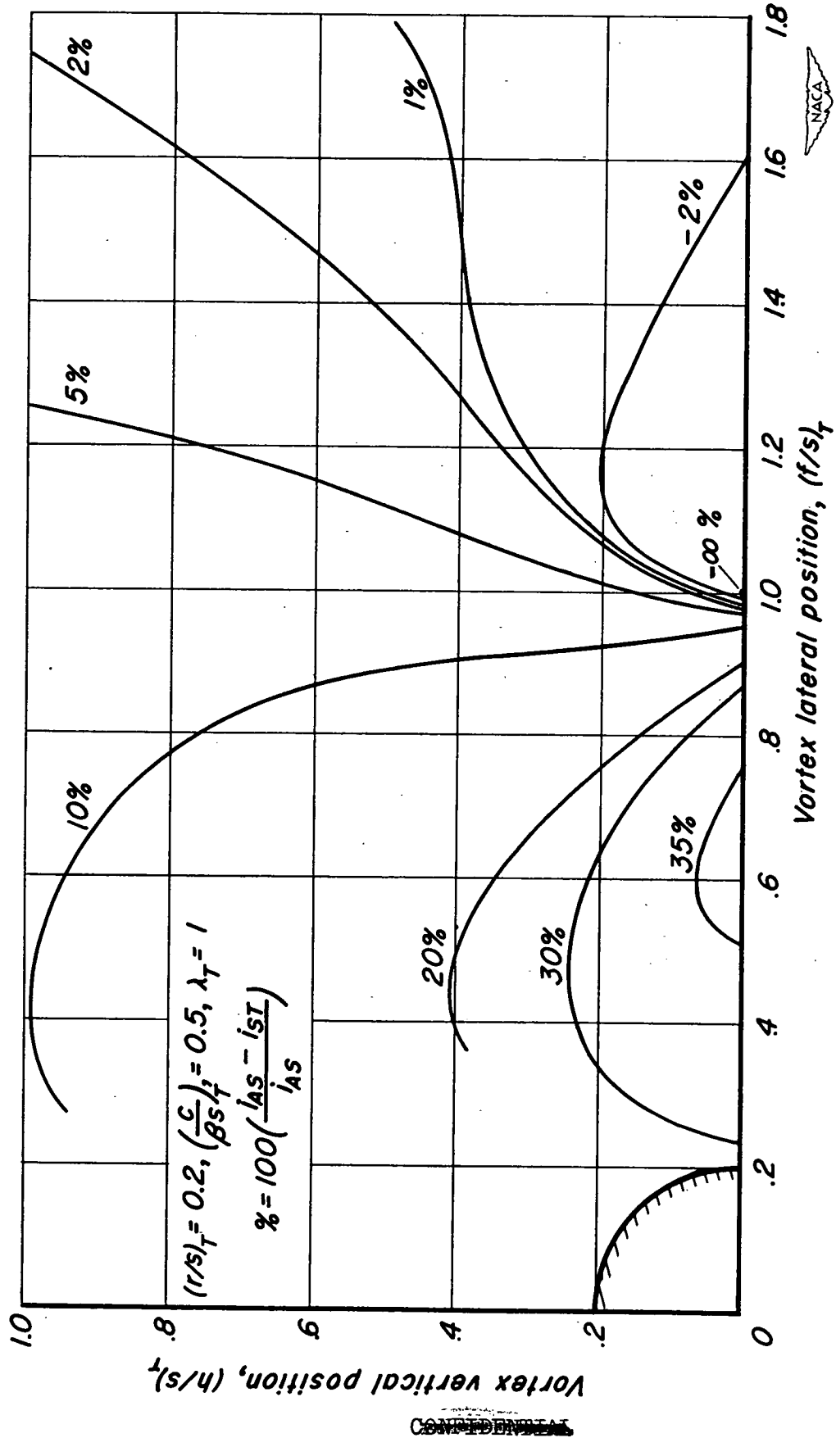

Figure 15.- Error due to use of strip theory in estimation of loads on rectangular tail section due to wing vortices.

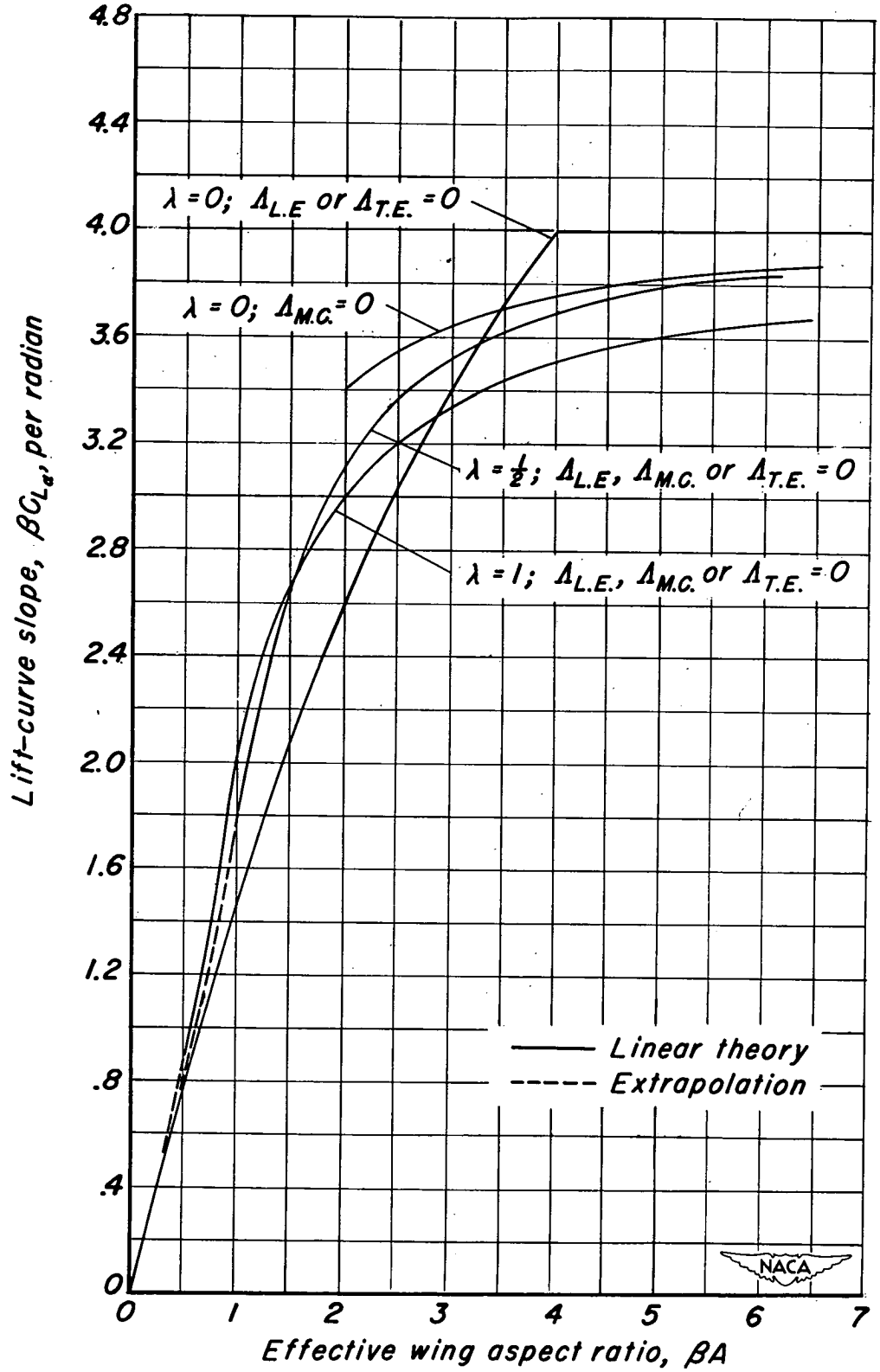

Figure 16. – Lift-curve slopes of supersonic wings as determined by linear theory.

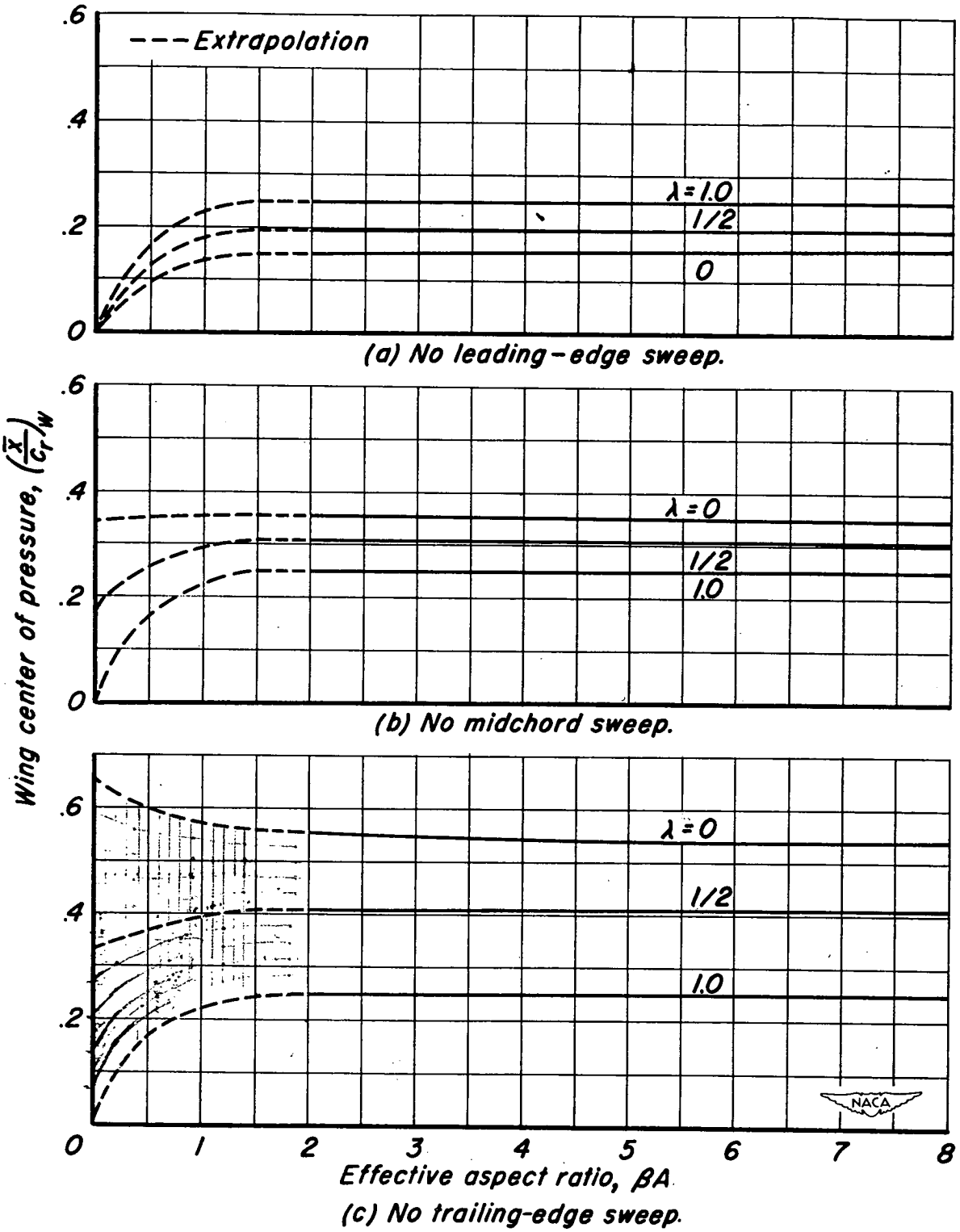

Figure 17. - Charts for determination of wing-alone center of pressure at subsonic speeds as determined by lifting-line theory.

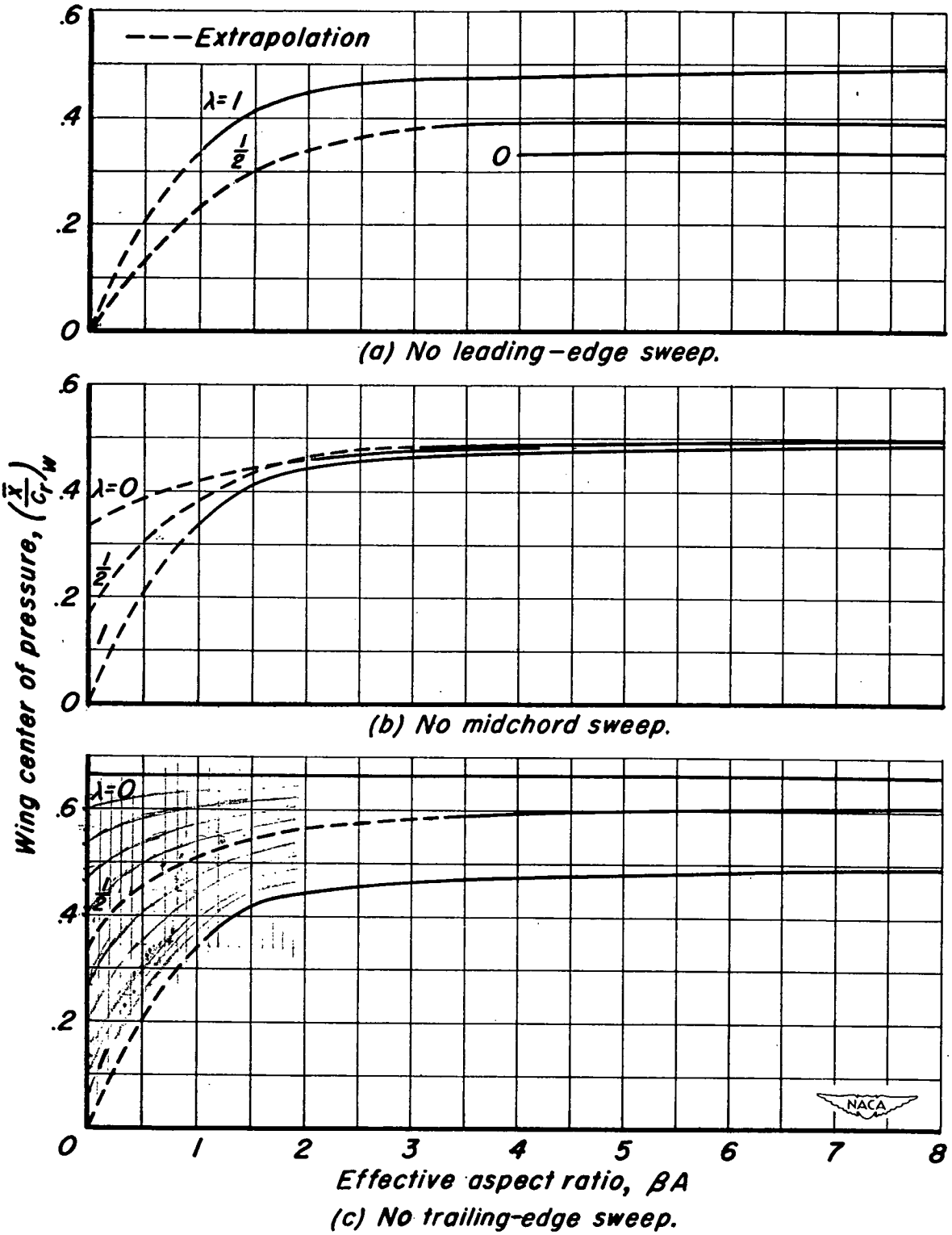

Figure 18.- Charts for determination of wing-alone center of pressure at supersonic speeds as determined by linear theory.

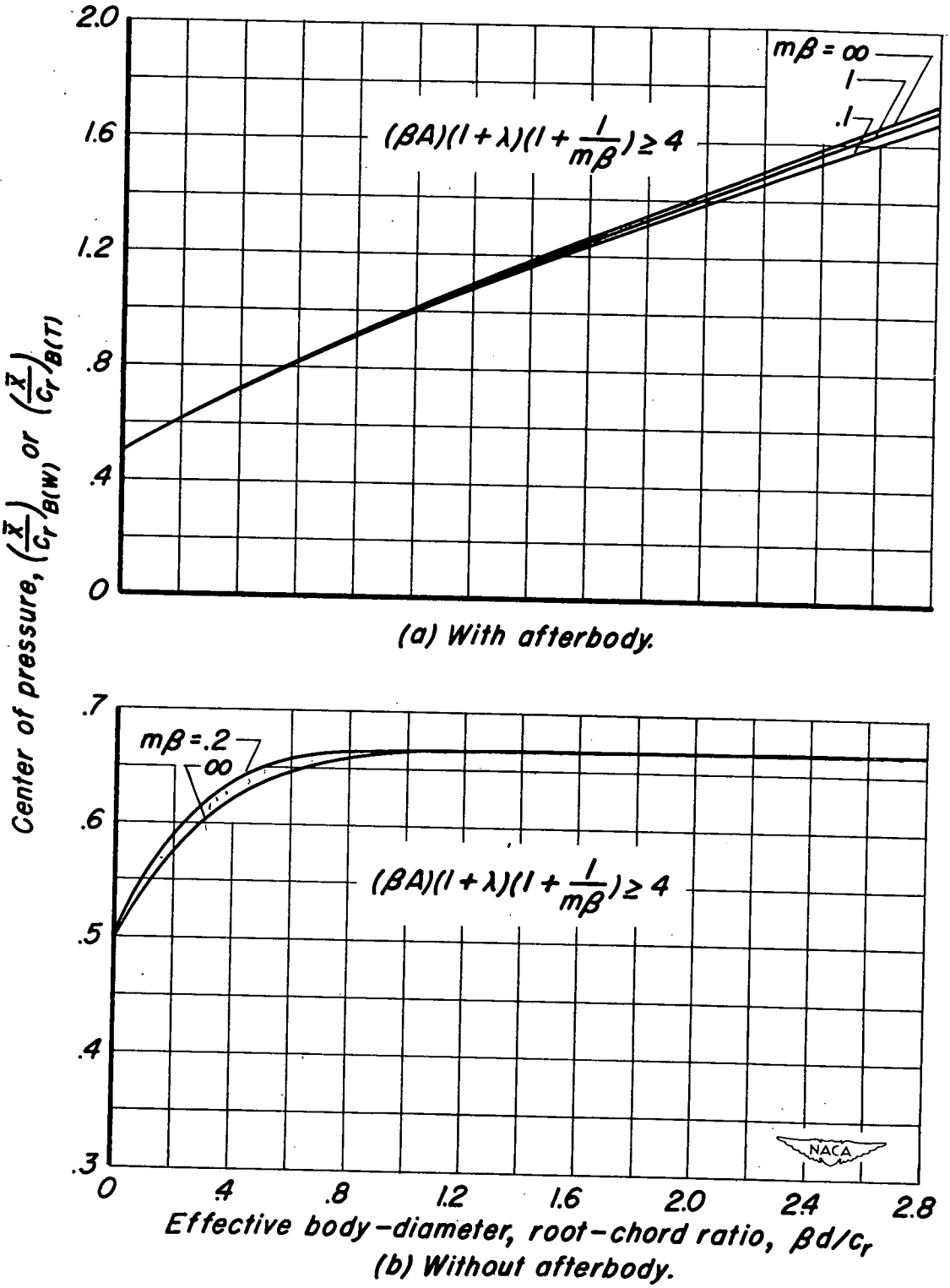

Figure 19. -Charts for determination of $(\frac{\bar{x}}{c_r})_{B(W)}$ or $(\frac{\bar{x}}{c_r})_{B(T)}$ at supersonic speeds.

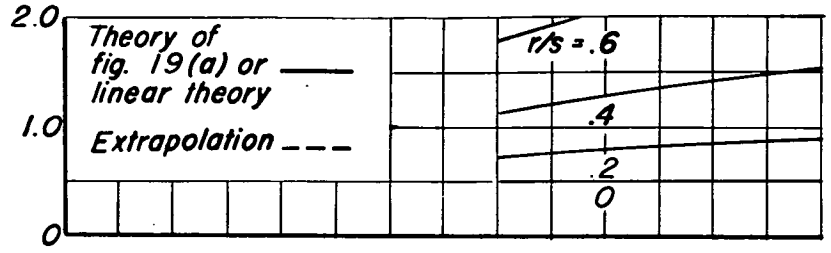

(a) No leading-edge sweep, $\lambda = 0$.

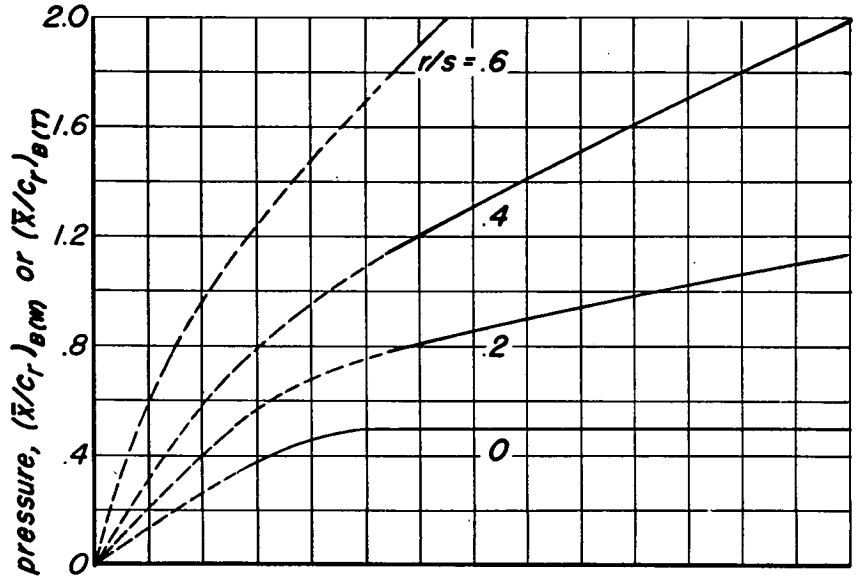

(b) No leading-edge sweep, $\lambda = 1/2$.

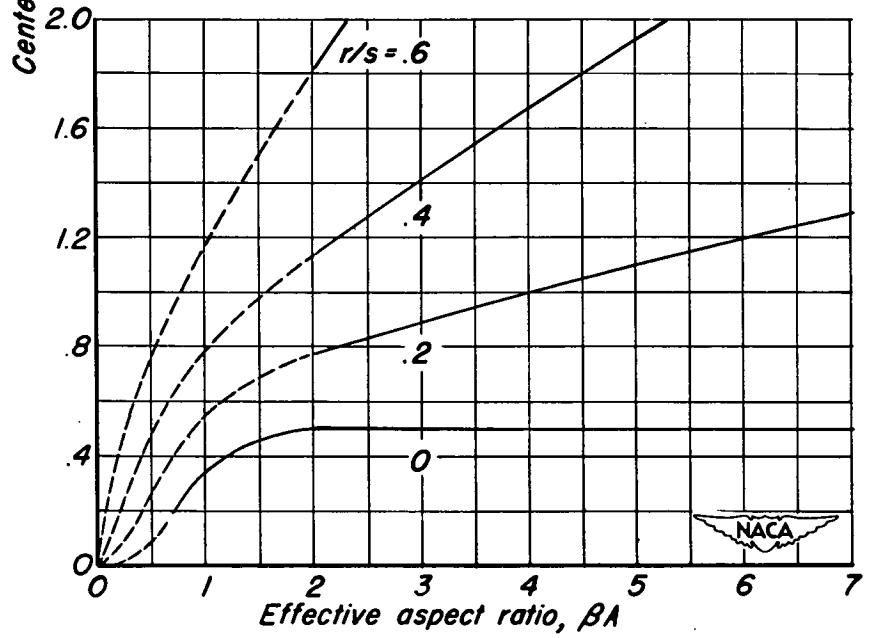

(c) No leading-edge sweep, $\lambda = 1$.

Figure 20. — Charts for determination of $(\frac{\bar{x}}{c_r})_{B(W)}$ or $(\frac{\bar{x}}{c_r})_{B(T)}$ at supersonic speeds for wings and tails with afterbodies.

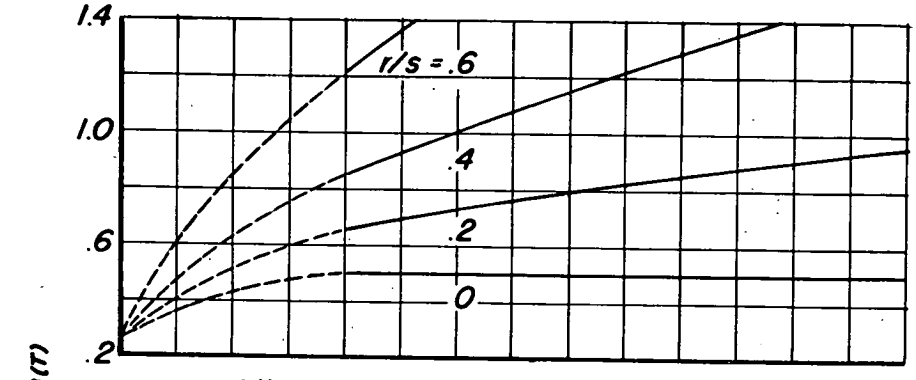

(d) No midchord sweep, $\lambda = 0$.

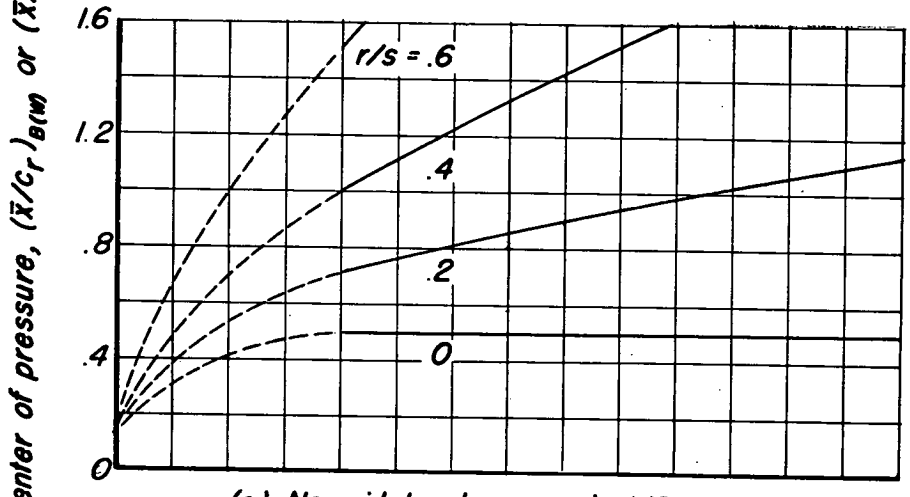

(e) No midchord sweep, $\lambda = 1/2$.

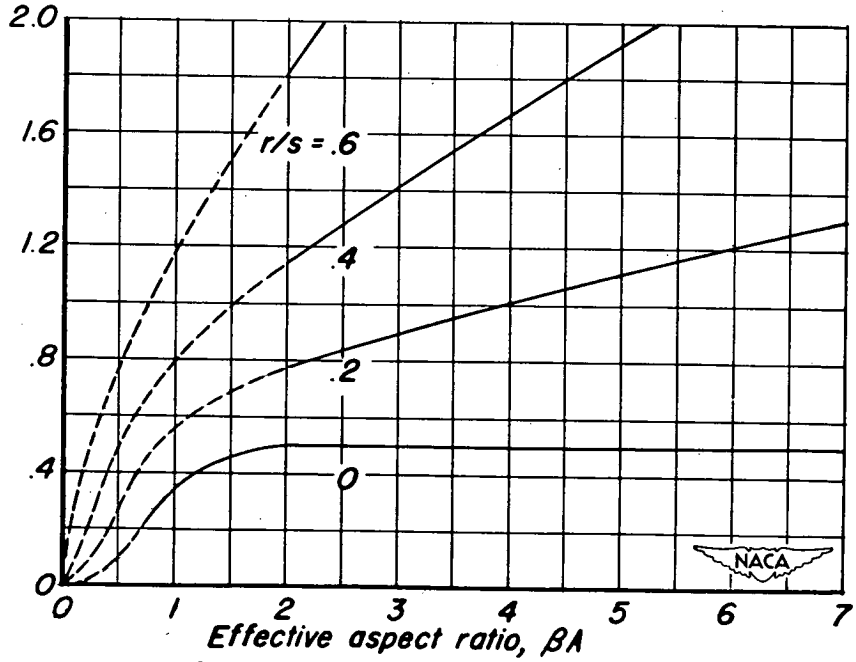

(f) No midchord sweep, $\lambda = 1$.

Figure 20.- Continued

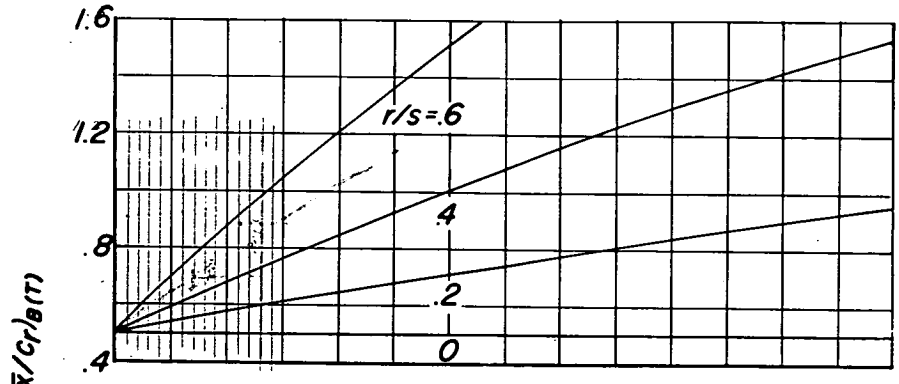

(g) No trailing-edge sweep, $\lambda = 0$.

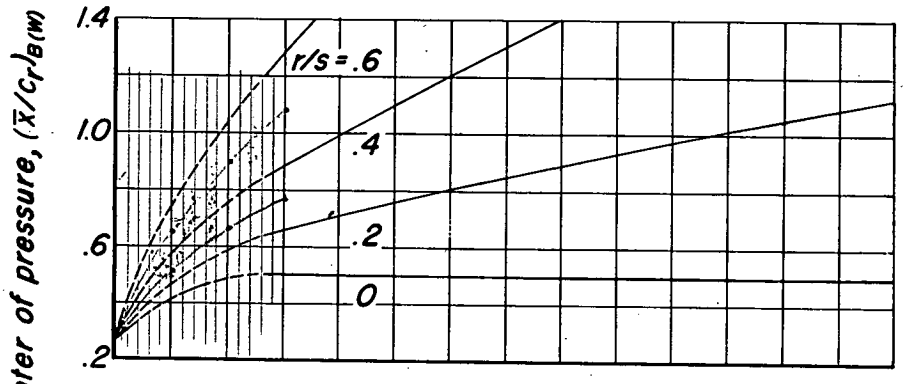

(h) No trailing-edge sweep, $\lambda = 1/2$.

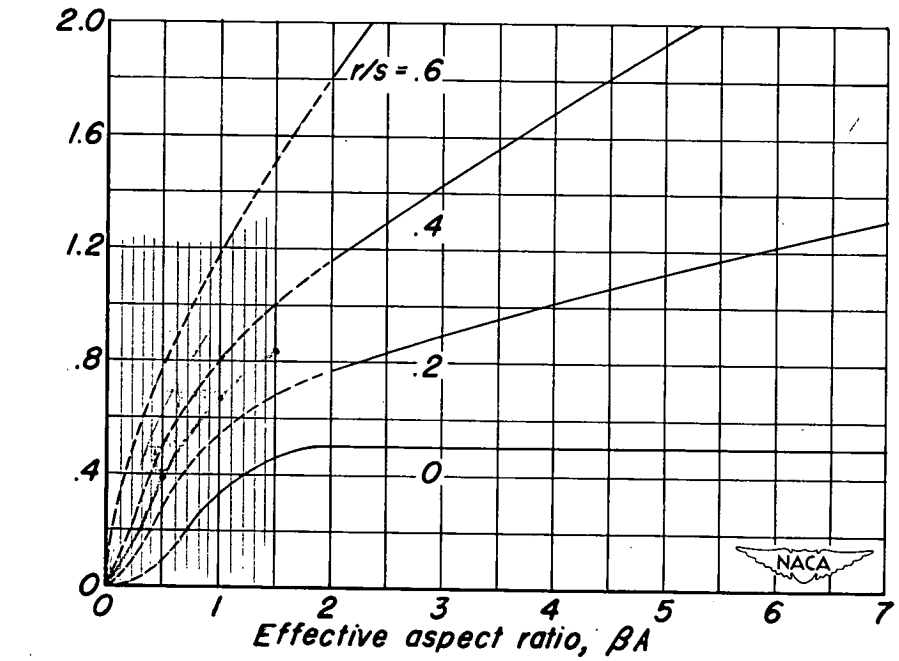

(i) No trailing-edge sweep, $\lambda = 1$.

Figure 20.- Concluded

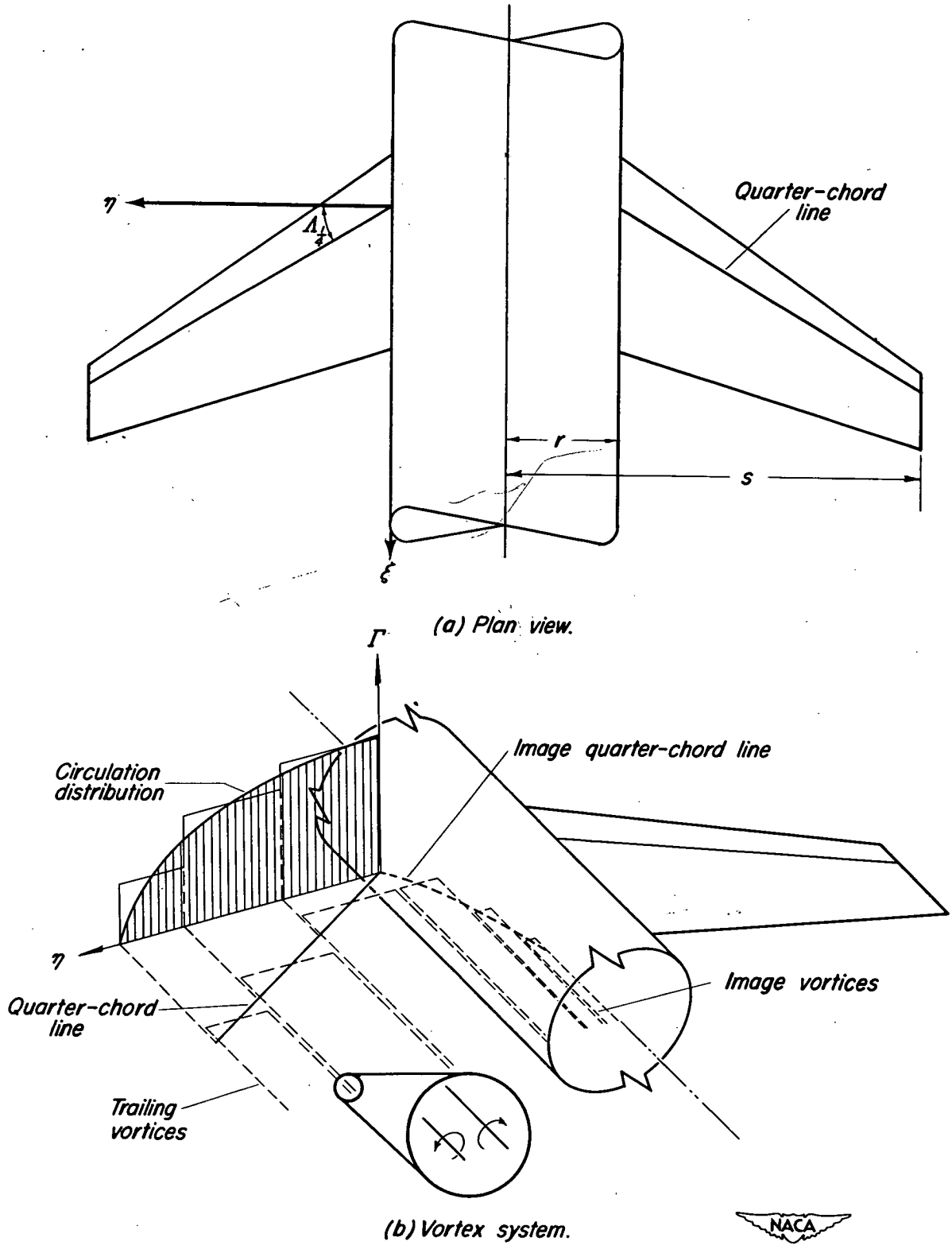

Figure 21.–Vortex model for determining center of pressure of body in presence of wing or tail at subsonic speeds.

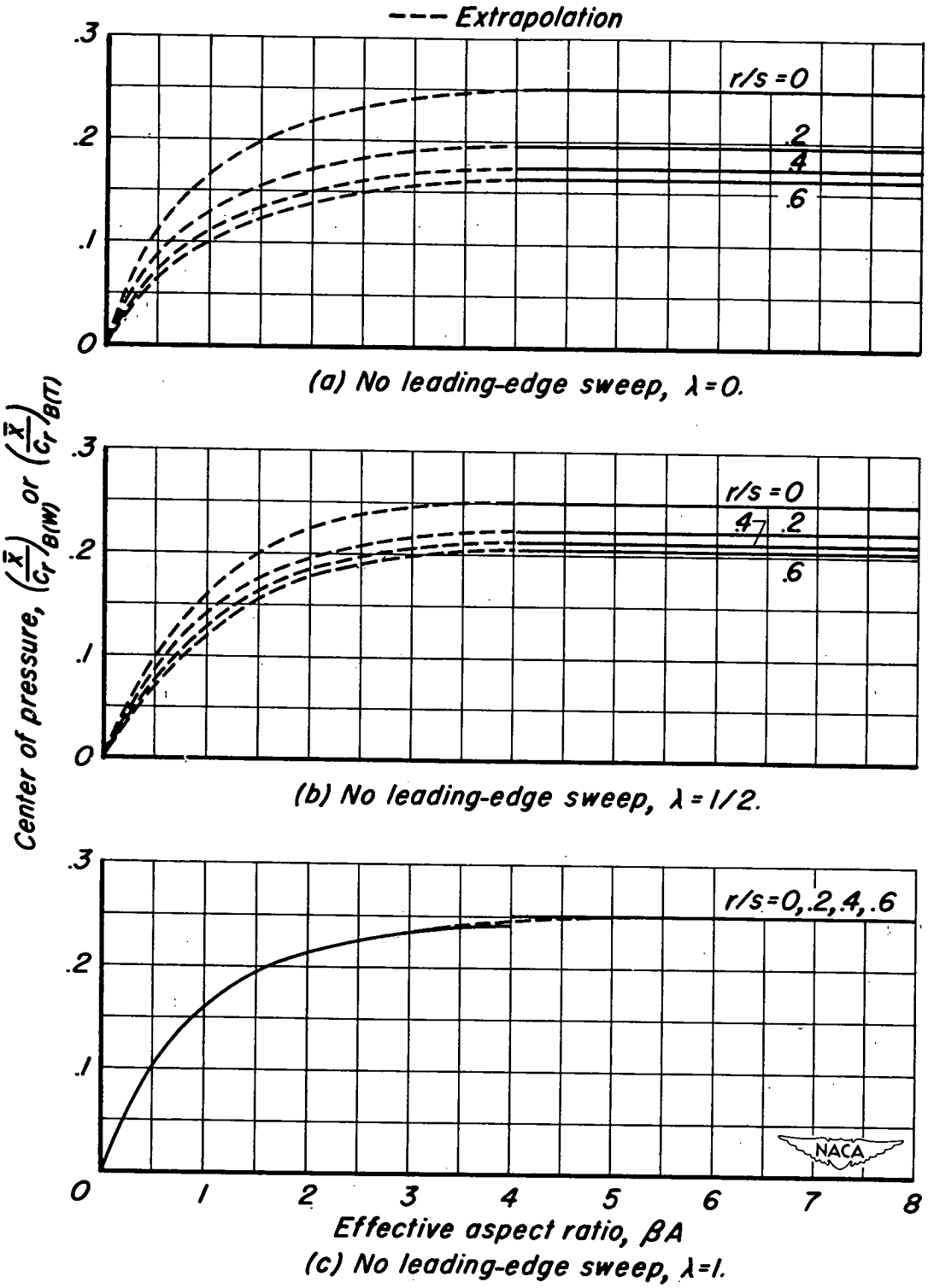

Figure 22.- Charts for determination of $(\frac{\bar{x}}{c_r})_{B(W)}$ or $(\frac{\bar{x}}{c_r})_{B(T)}$ at subsonic speeds.

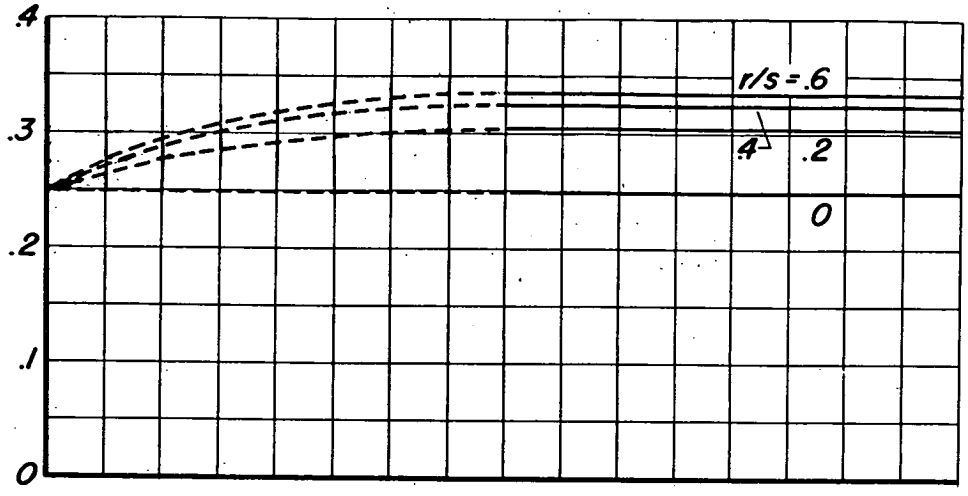

(d) No midchord sweep, $\lambda = 0$.

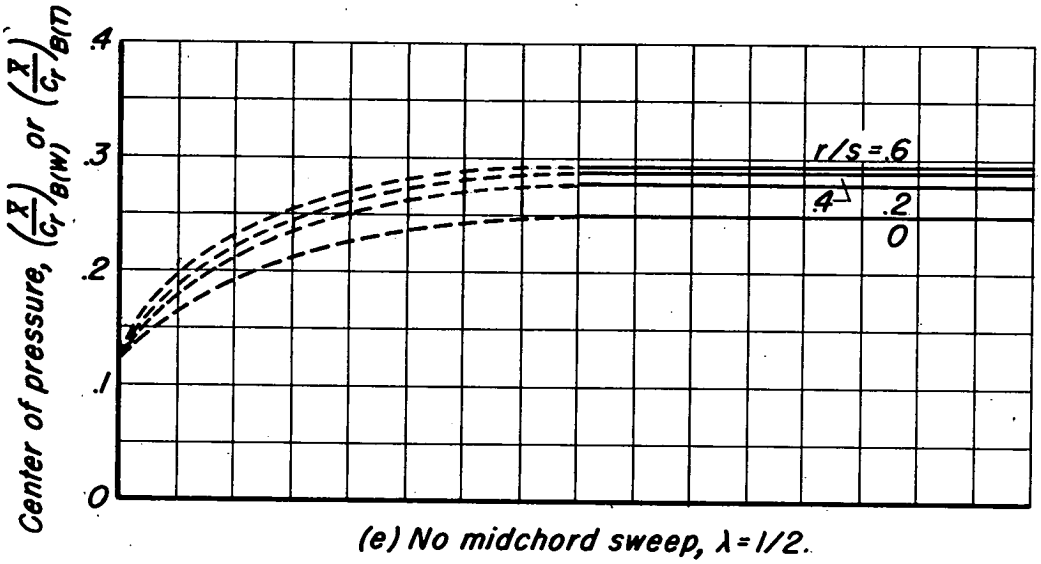

(e) No midchord sweep, $\lambda = 1/2$.

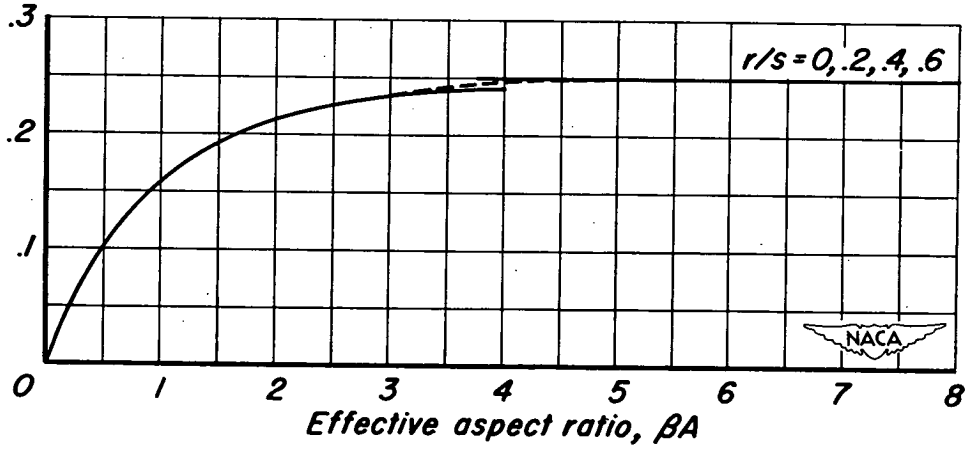

(f) No midchord sweep, $\lambda = 1$.

Figure 22.- Continued.

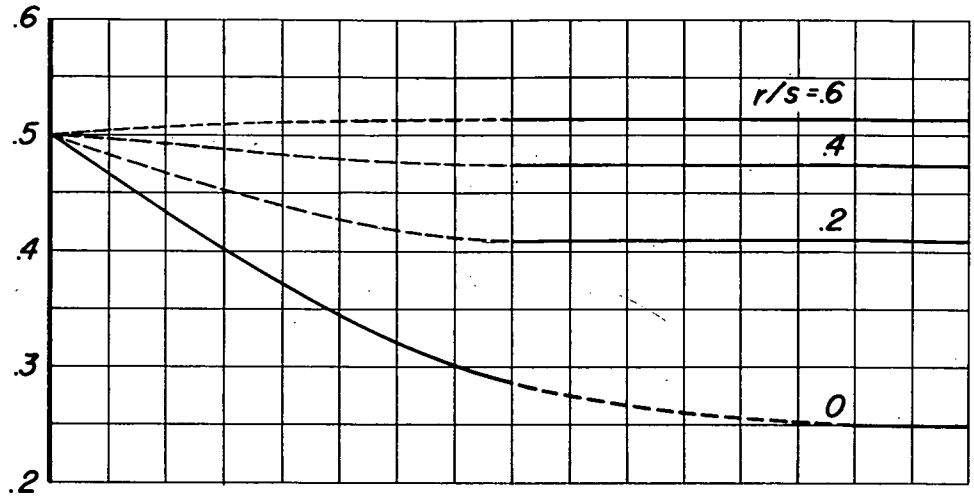

(g) No trailing-edge sweep, $\lambda = 0$.

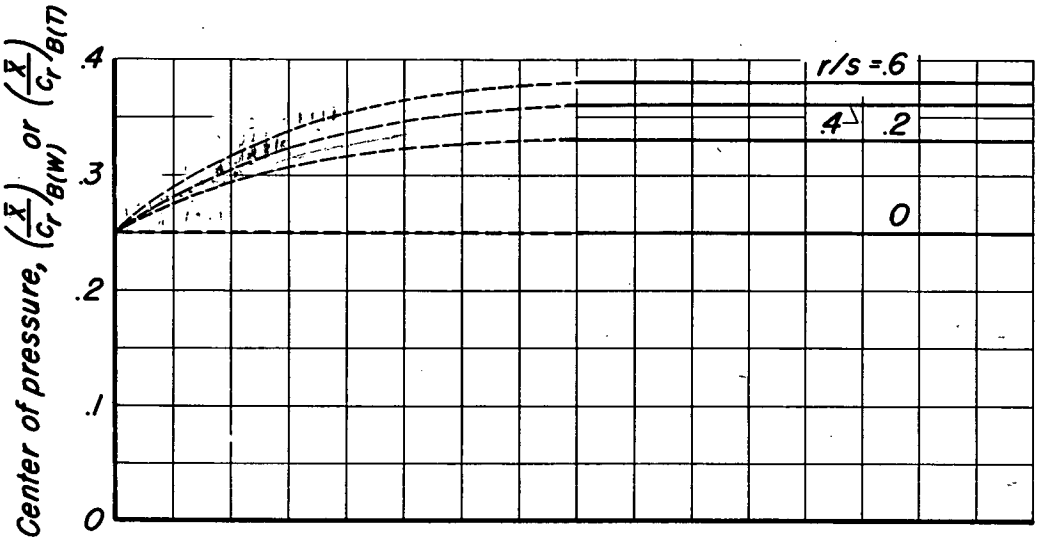

(h) No trailing-edge sweep, $\lambda = 1/2$.

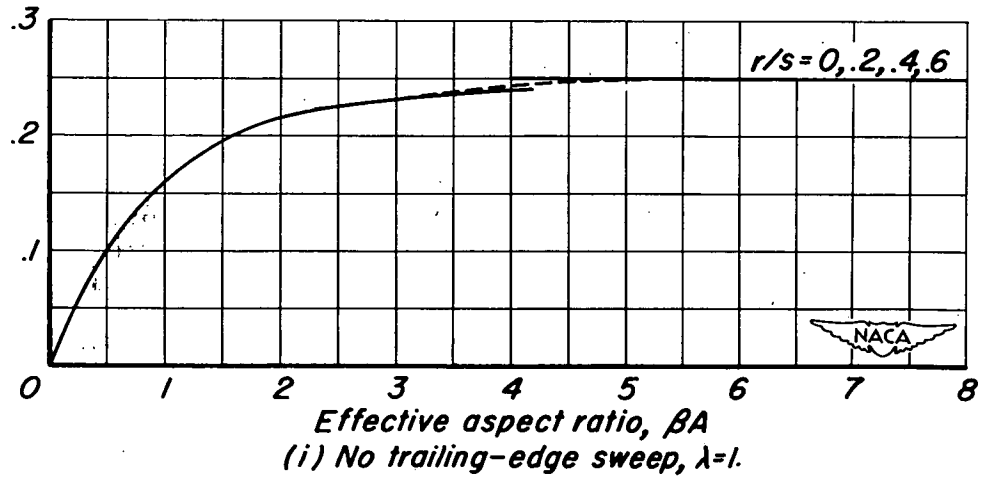

(i) No trailing-edge sweep, $\lambda = 1$.

Figure 22.-Concluded.

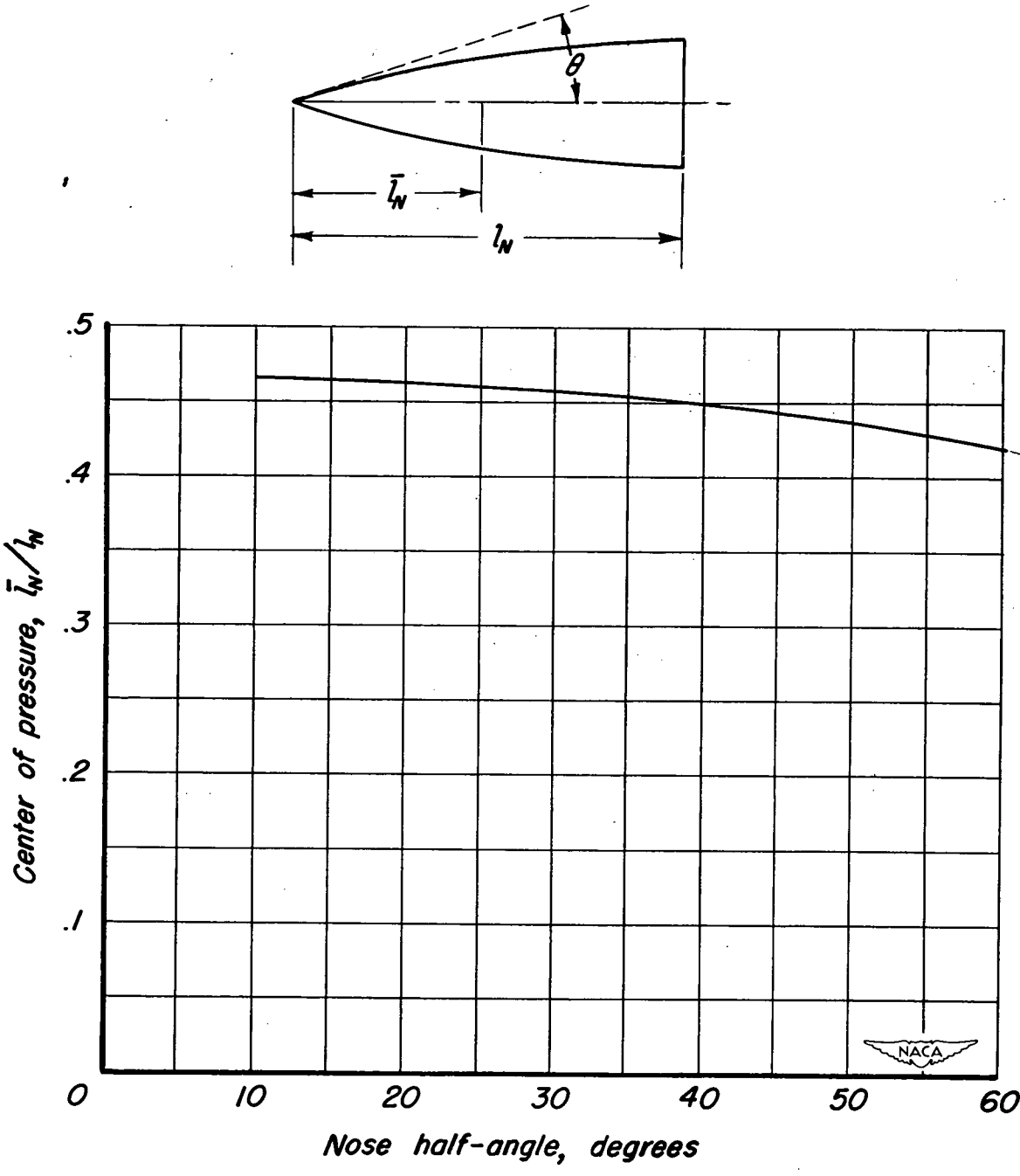

Figure 23.—Center of pressure of ogival nose as determined from slender-body theory.

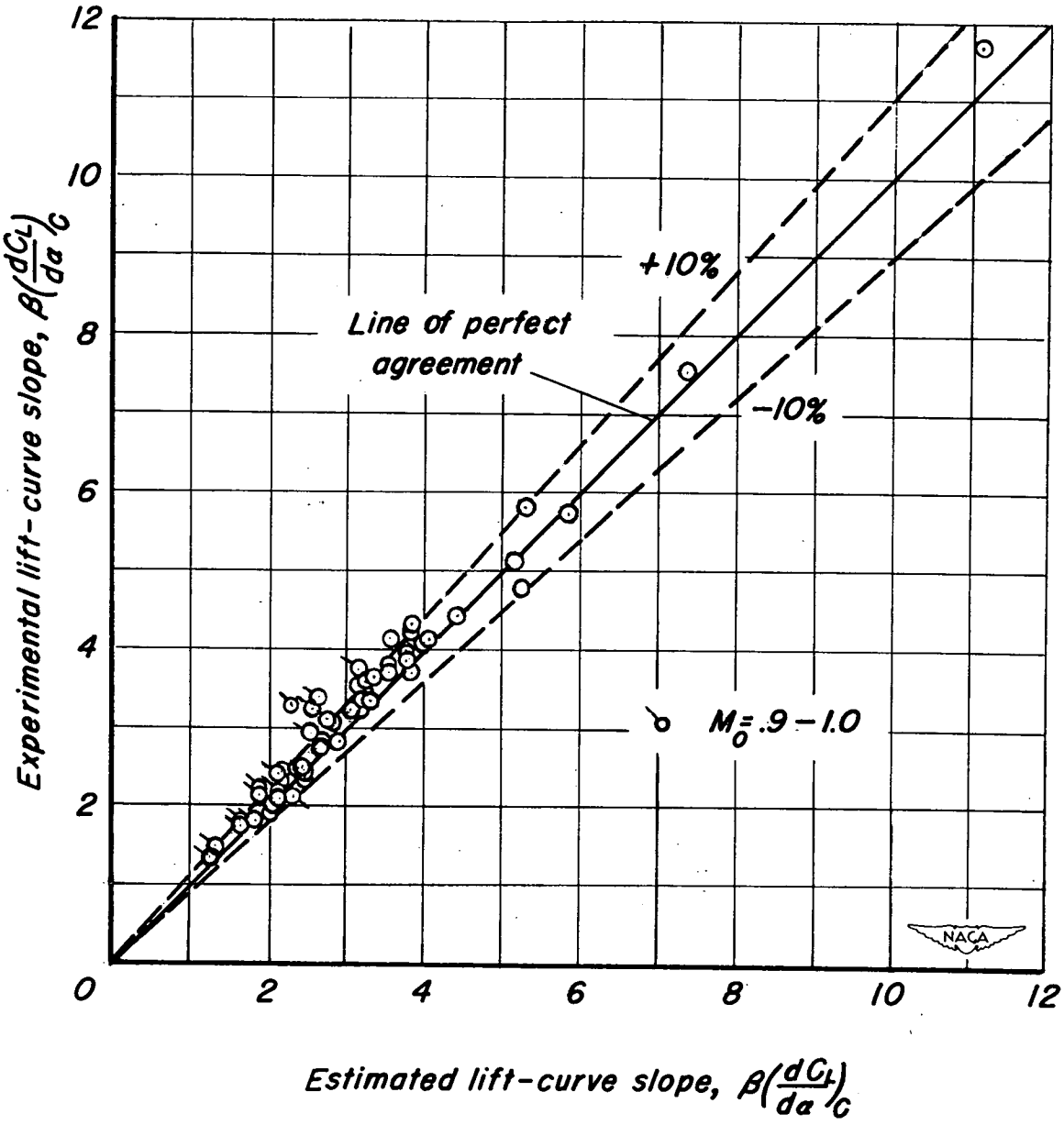

Figure 24.- Correlation between experimental and estimated lift-curve slopes for subsonic wing-body combinations.

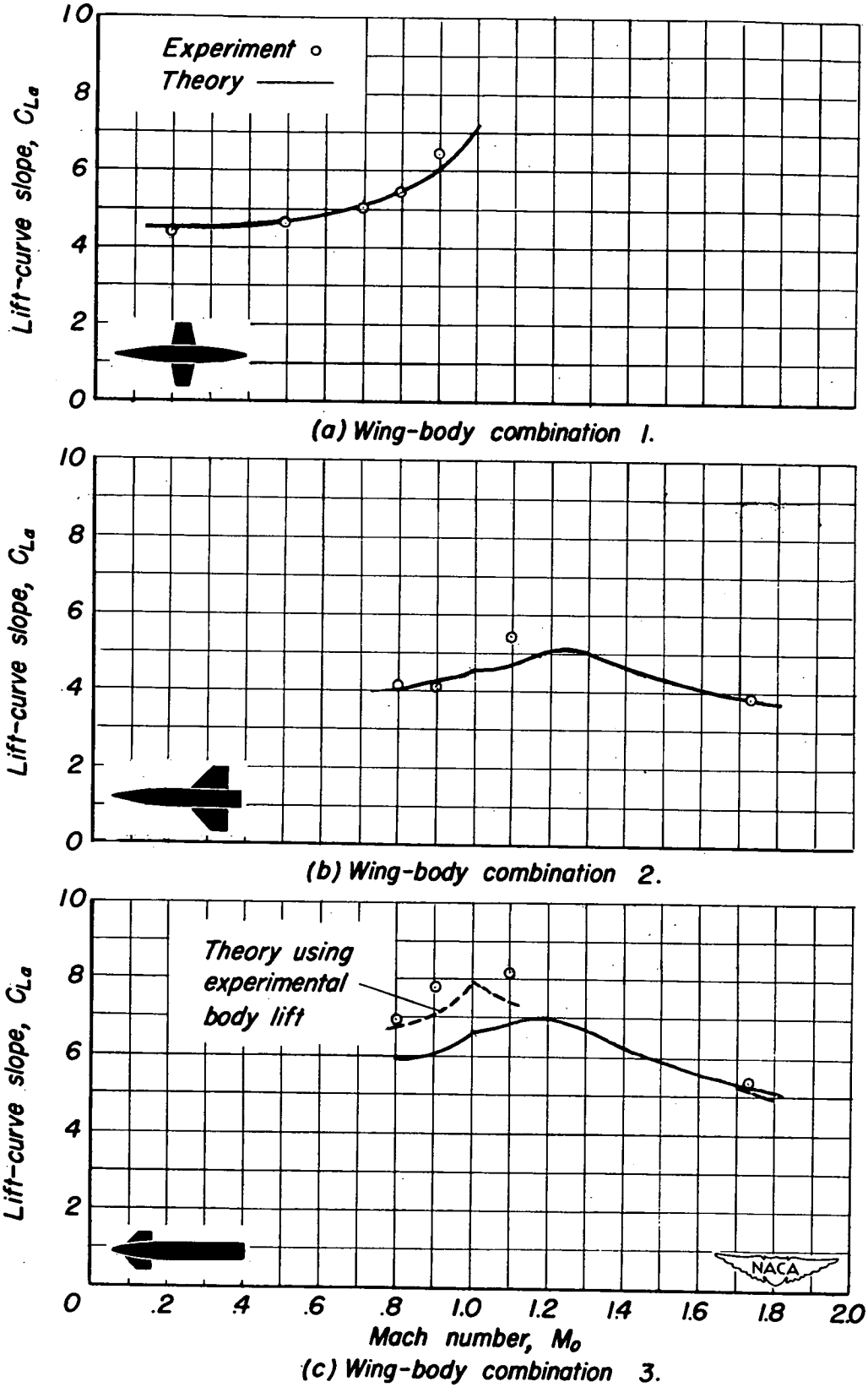

Figure 25.—Variation with Mach number of lift-curve slope of wing-body combinations.

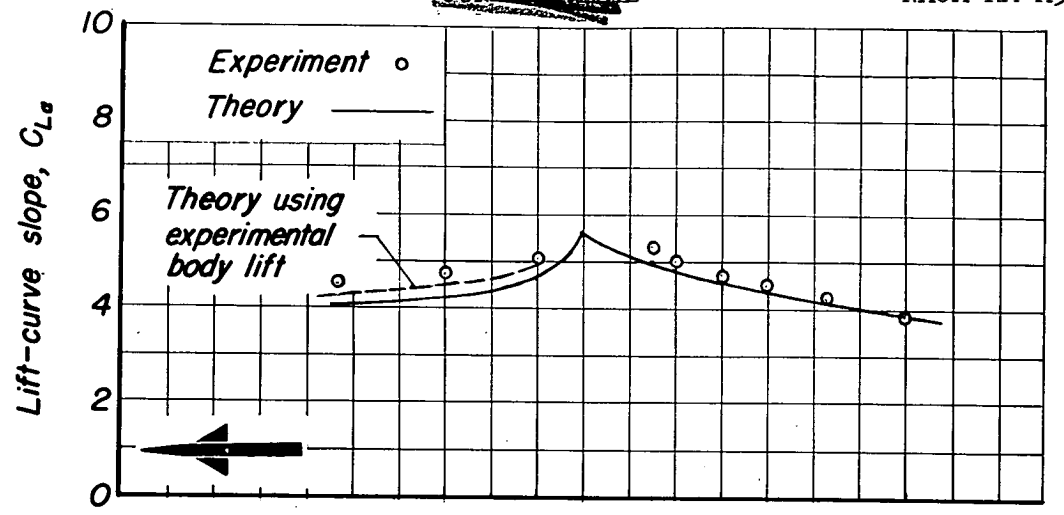

(d) Wing-body combination 4.

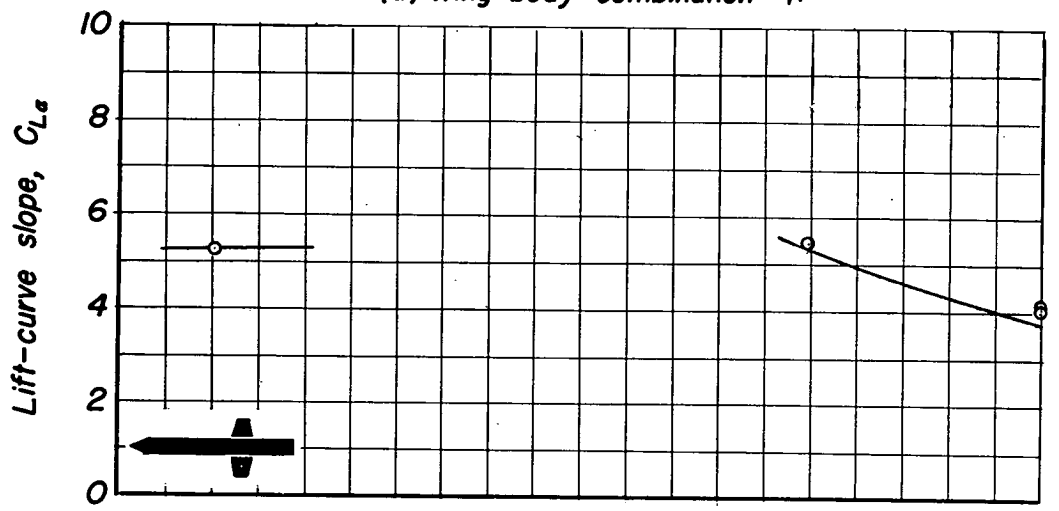

(e) Wing-body combination 7.

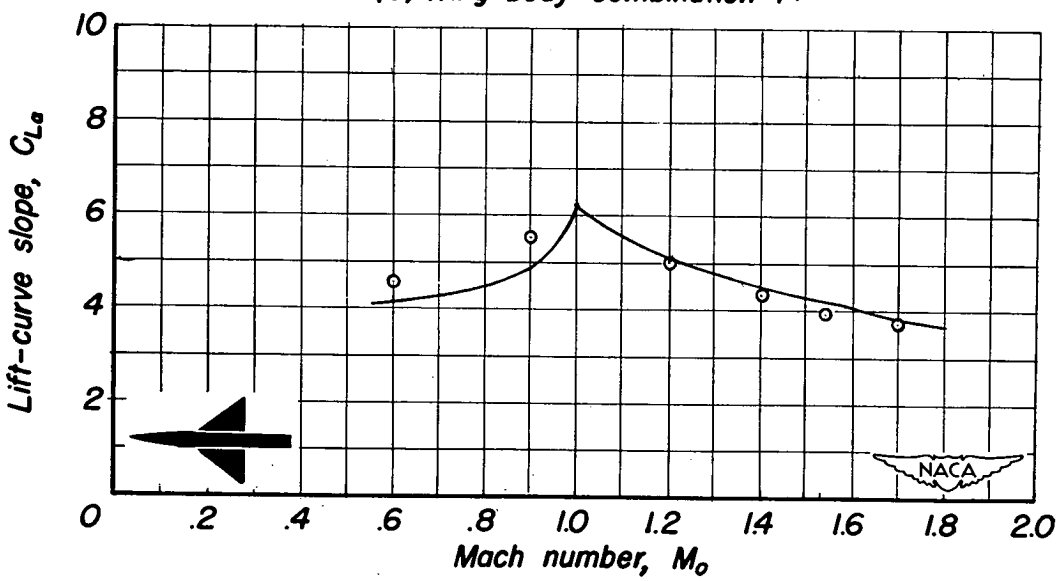

(f) Wing-body combination 8.

Figure 25. – Continued.

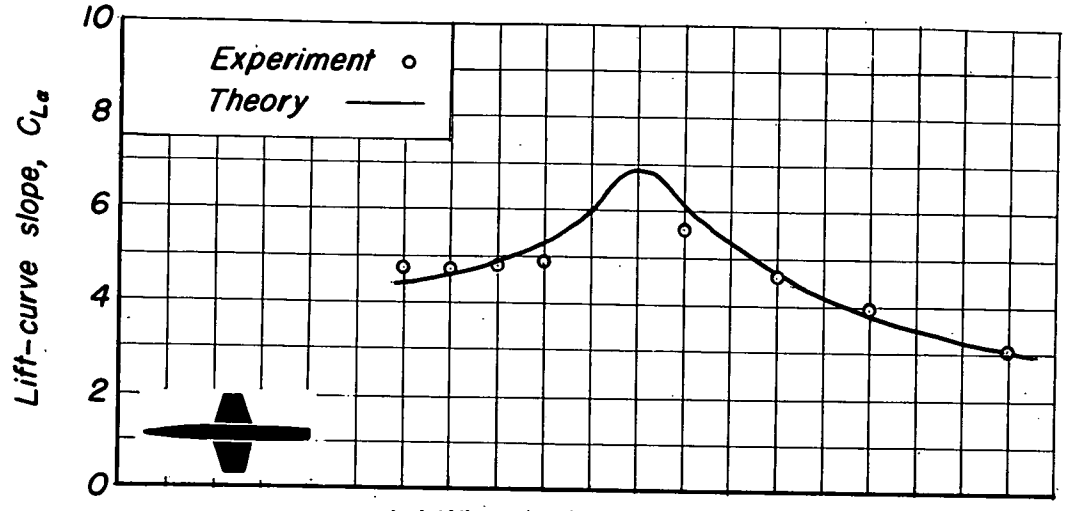

(g) Wing–body combination 9.

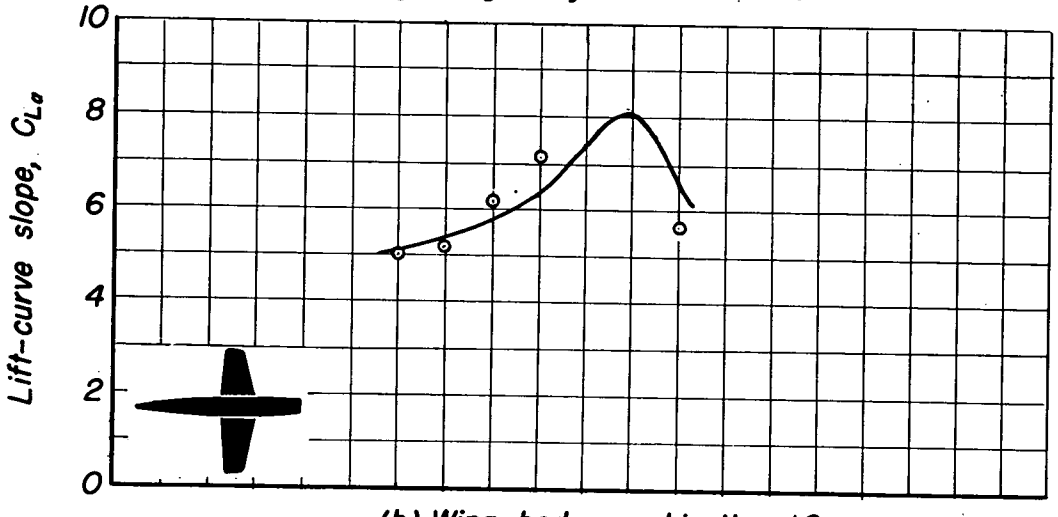

(h) Wing–body combination 10.

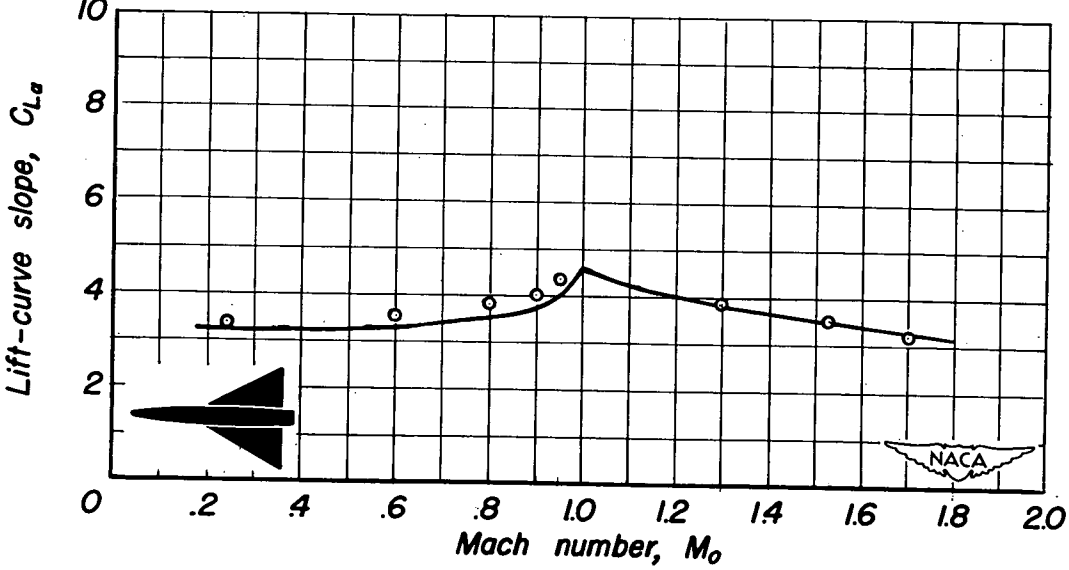

(i) Wing–body combination 11.

Figure 25.—Continued.

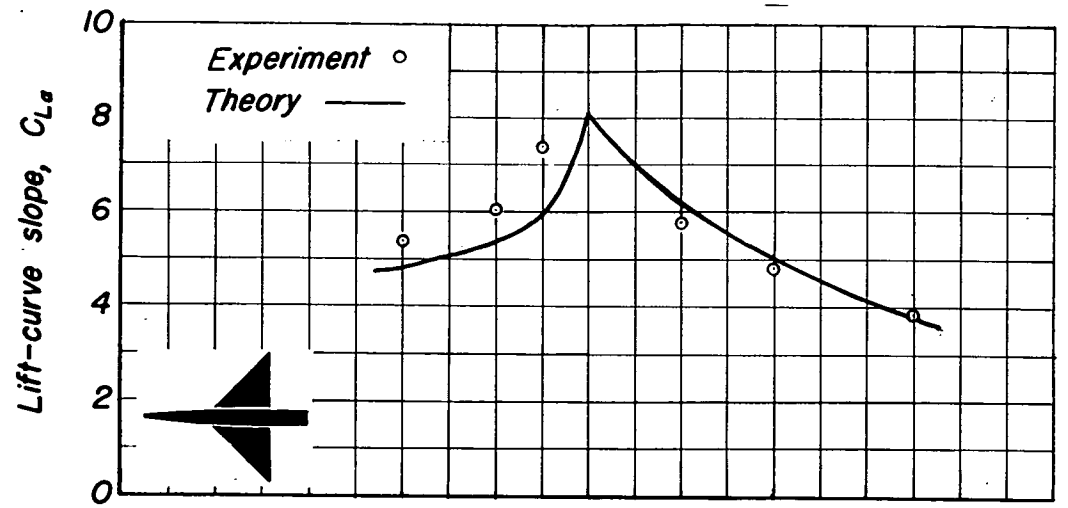

(j) Wing-body combination 12.

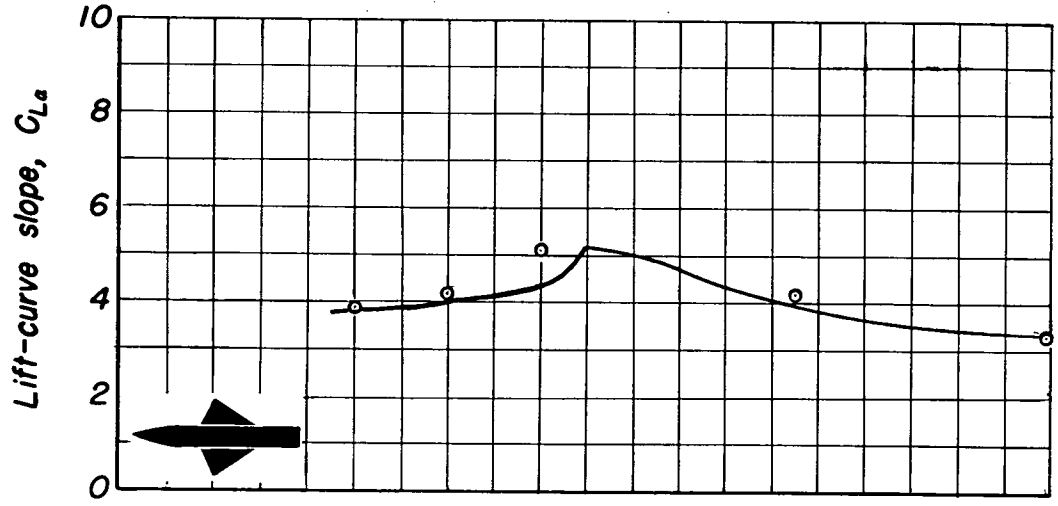

(k) Wing-body combination 13.

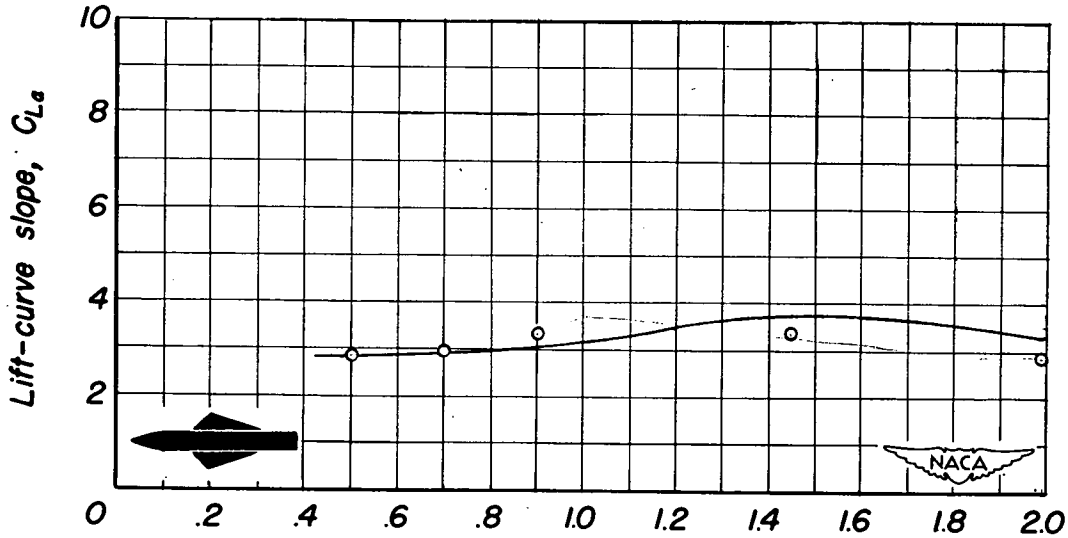

(l) Wing-body combination 14.

Figure 25. – Concluded.

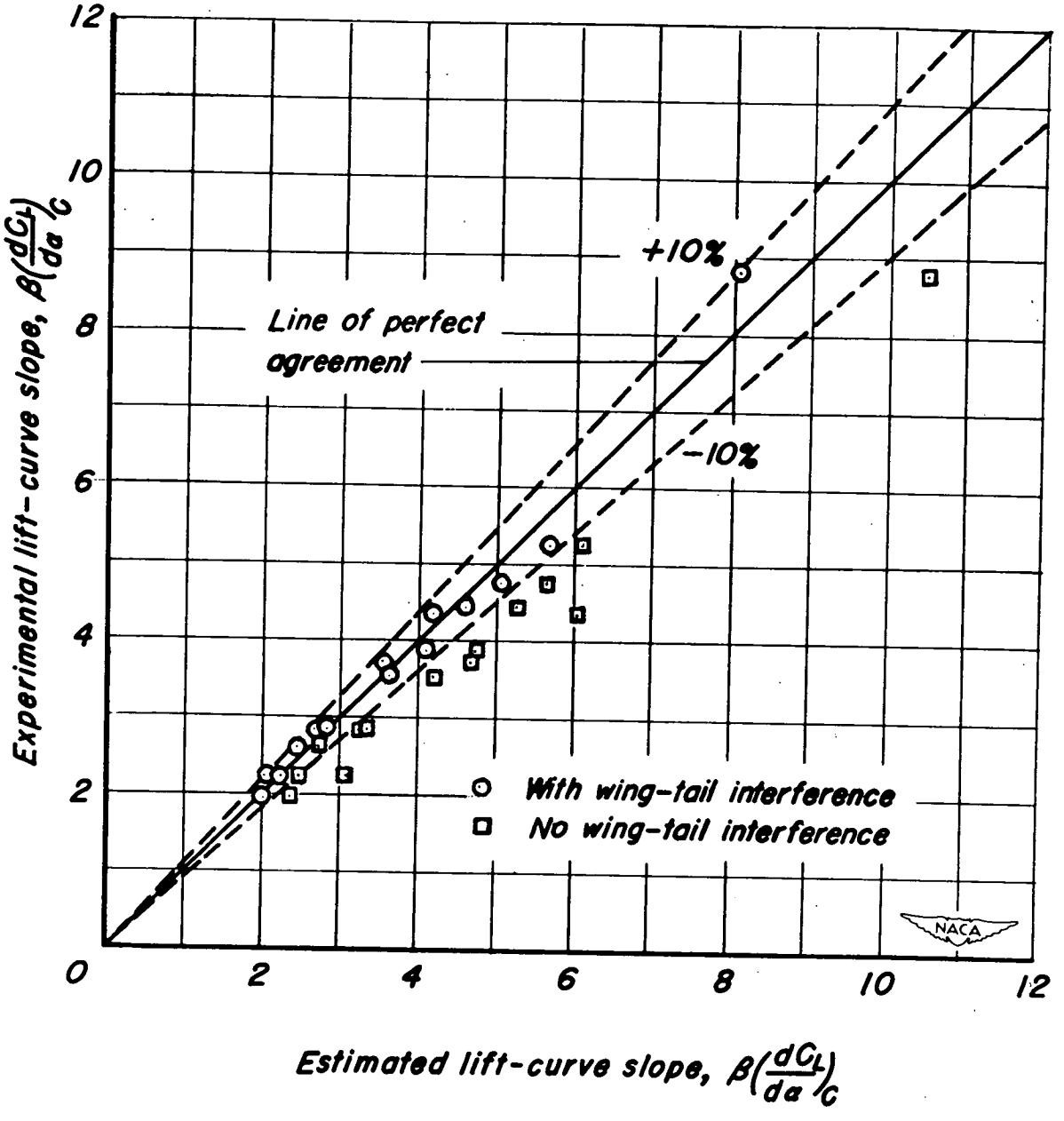

Figure 26.–Correlation between experimental and estimated lift-curve slopes for subsonic wing-body-tail combinations at $\alpha=0$.

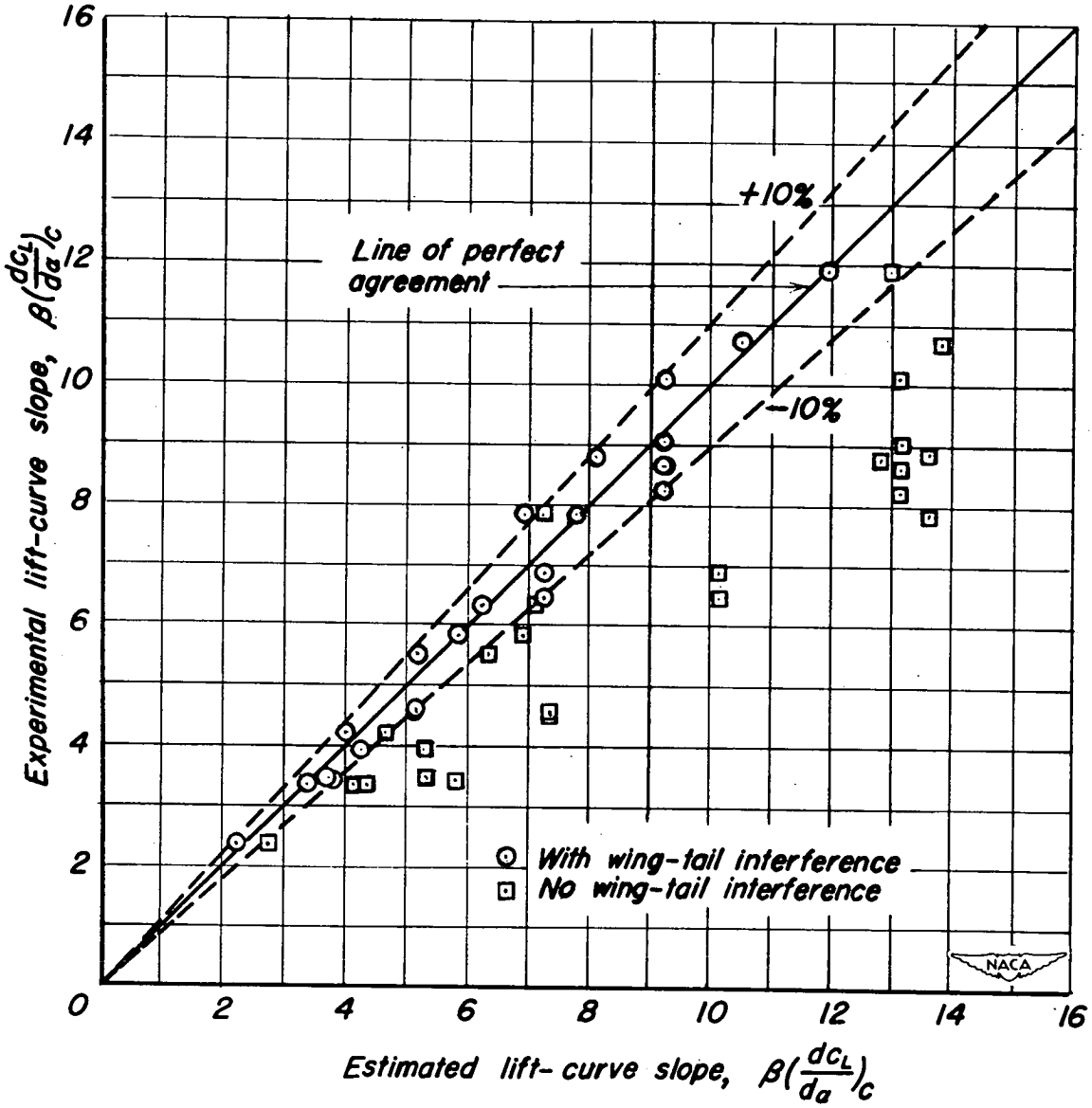

Figure 27.—Correlation between experimental and estimated lift-curve slopes for supersonic wing-body-tail combinations at $\alpha=0$.

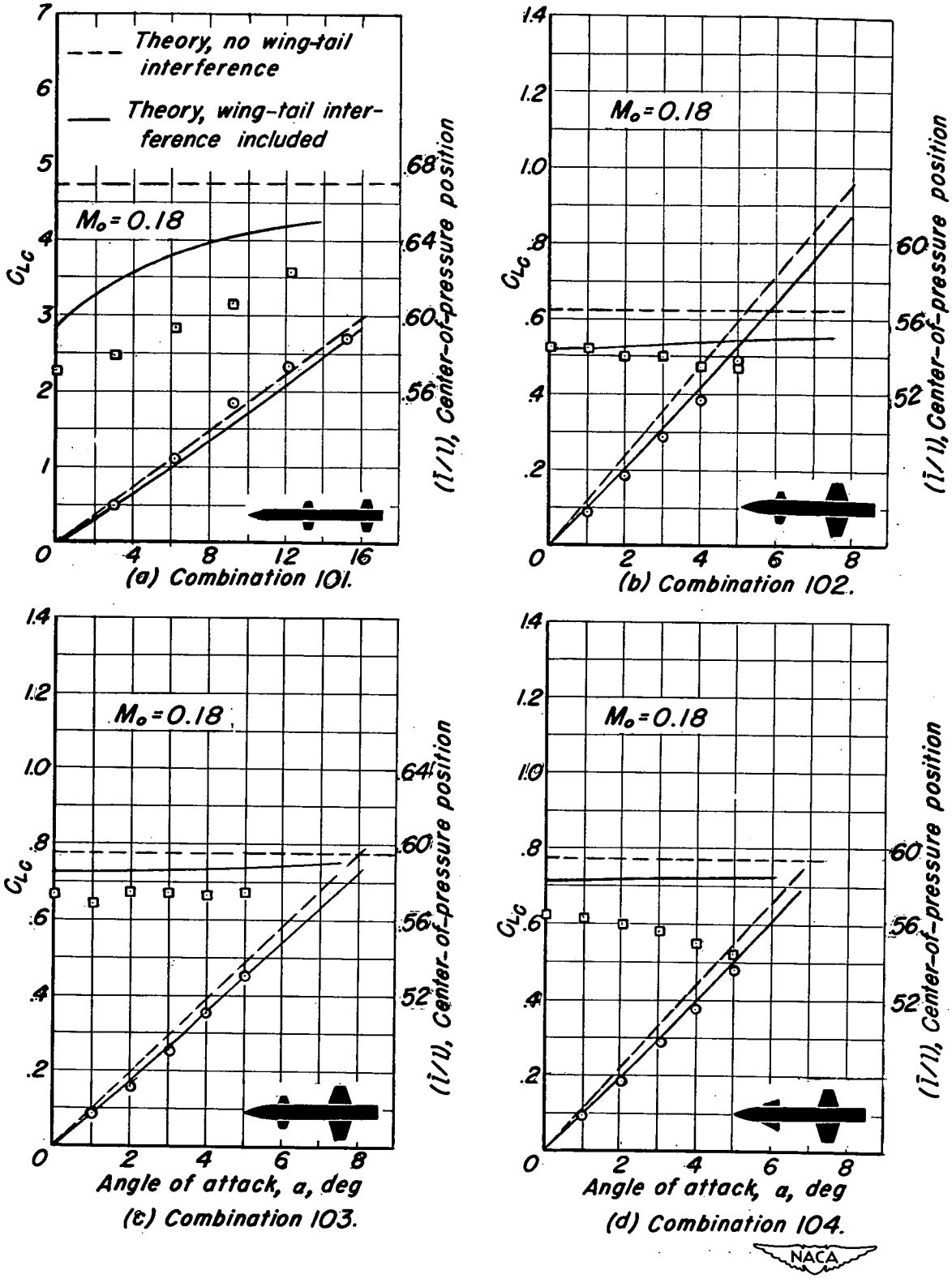

Figure 28.- Lift and center-of-pressure characteristics of subsonic wing-body-tail combinations.

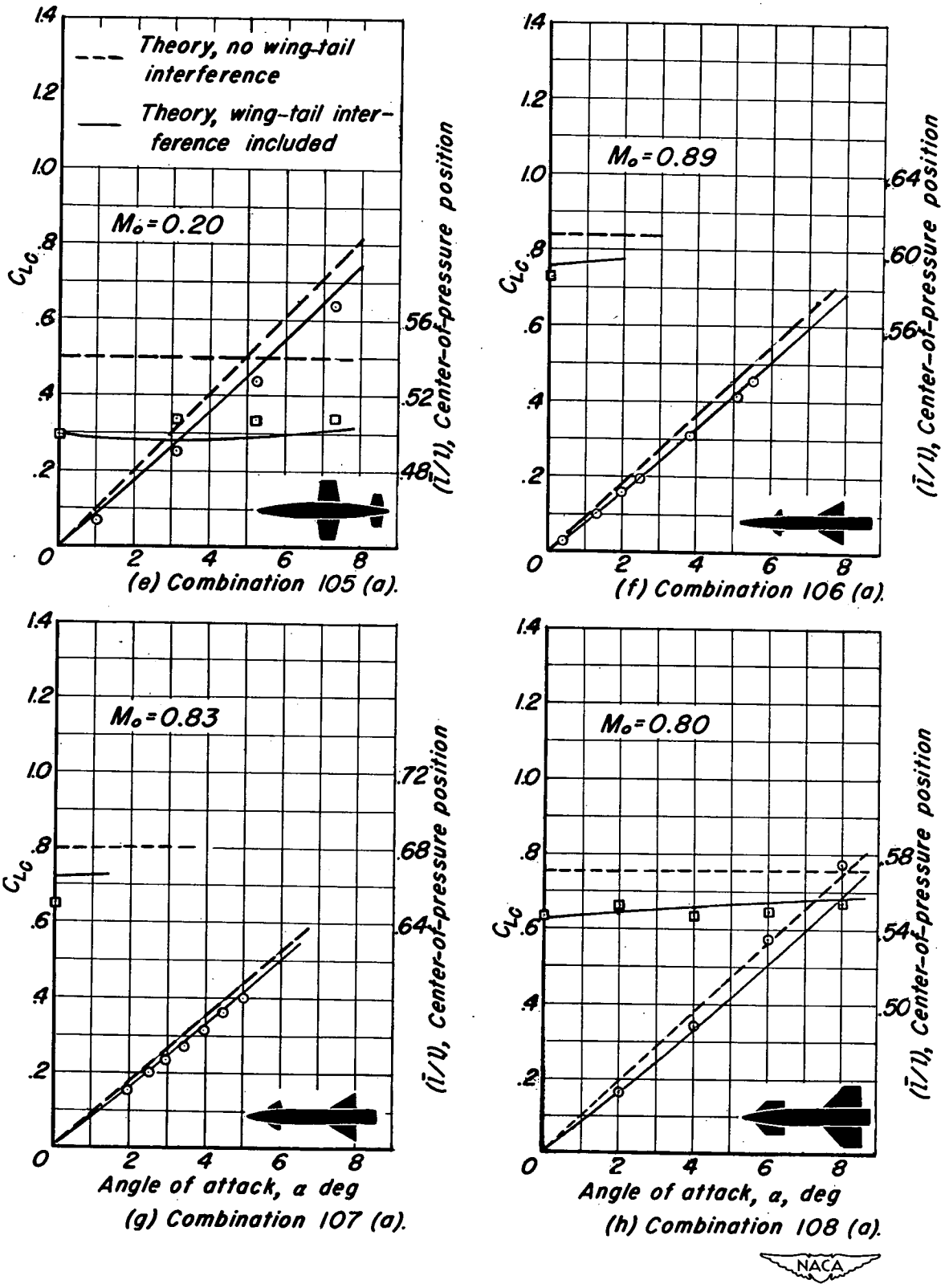

Figure 28.- Continued.

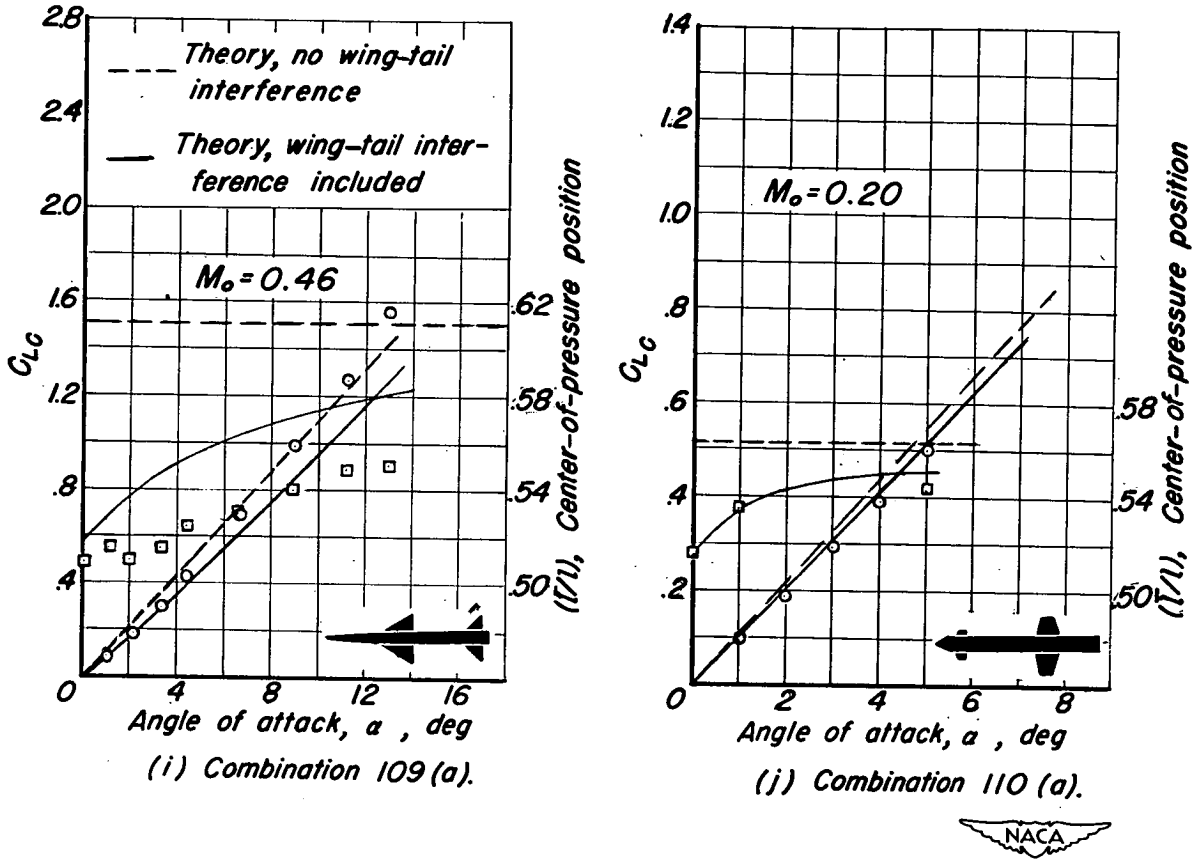

Figure 28.- Concluded.

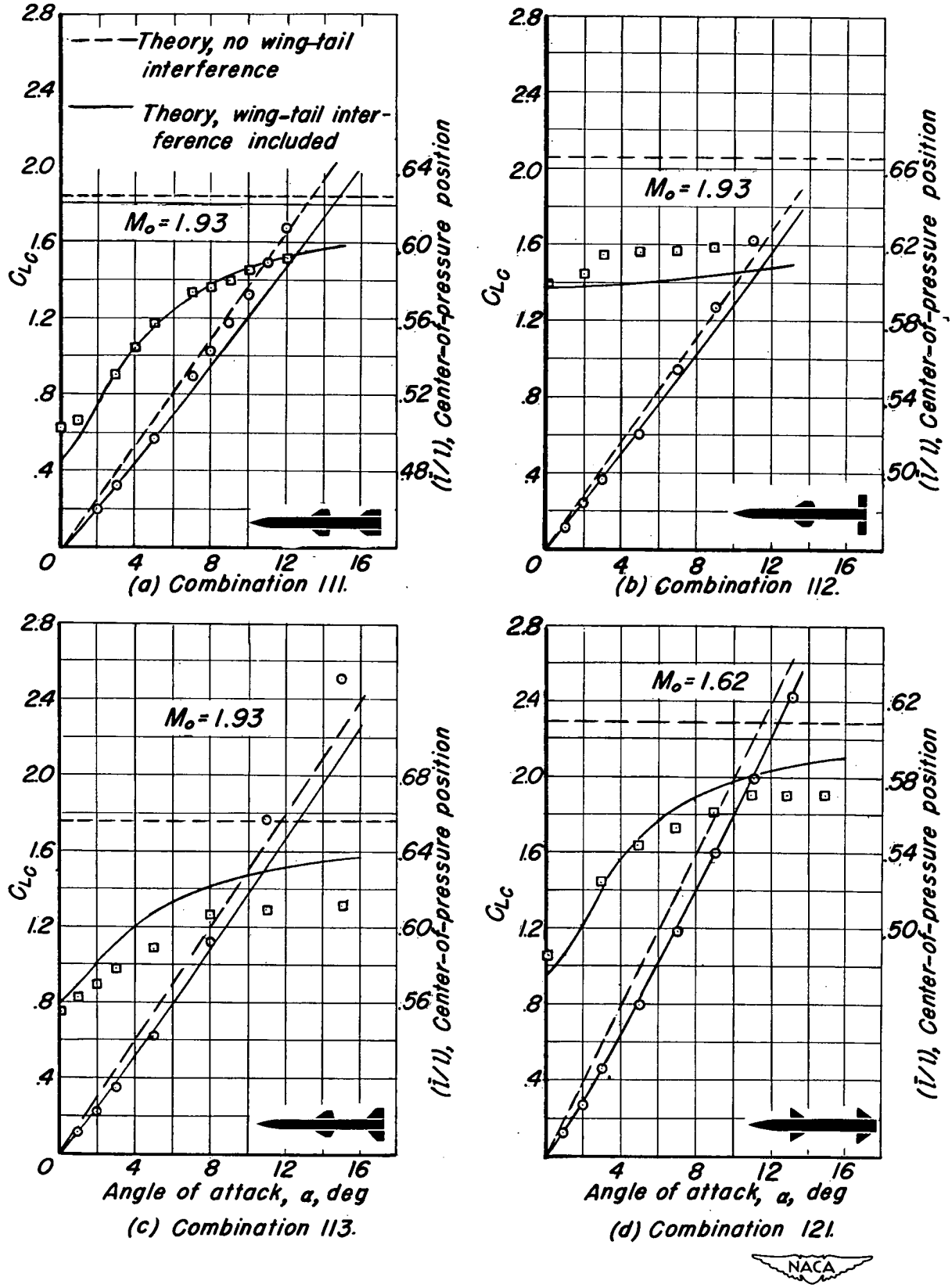

Figure 29.- Lift and center-of-pressure characteristics of supersonic wing-body-tail combinations.

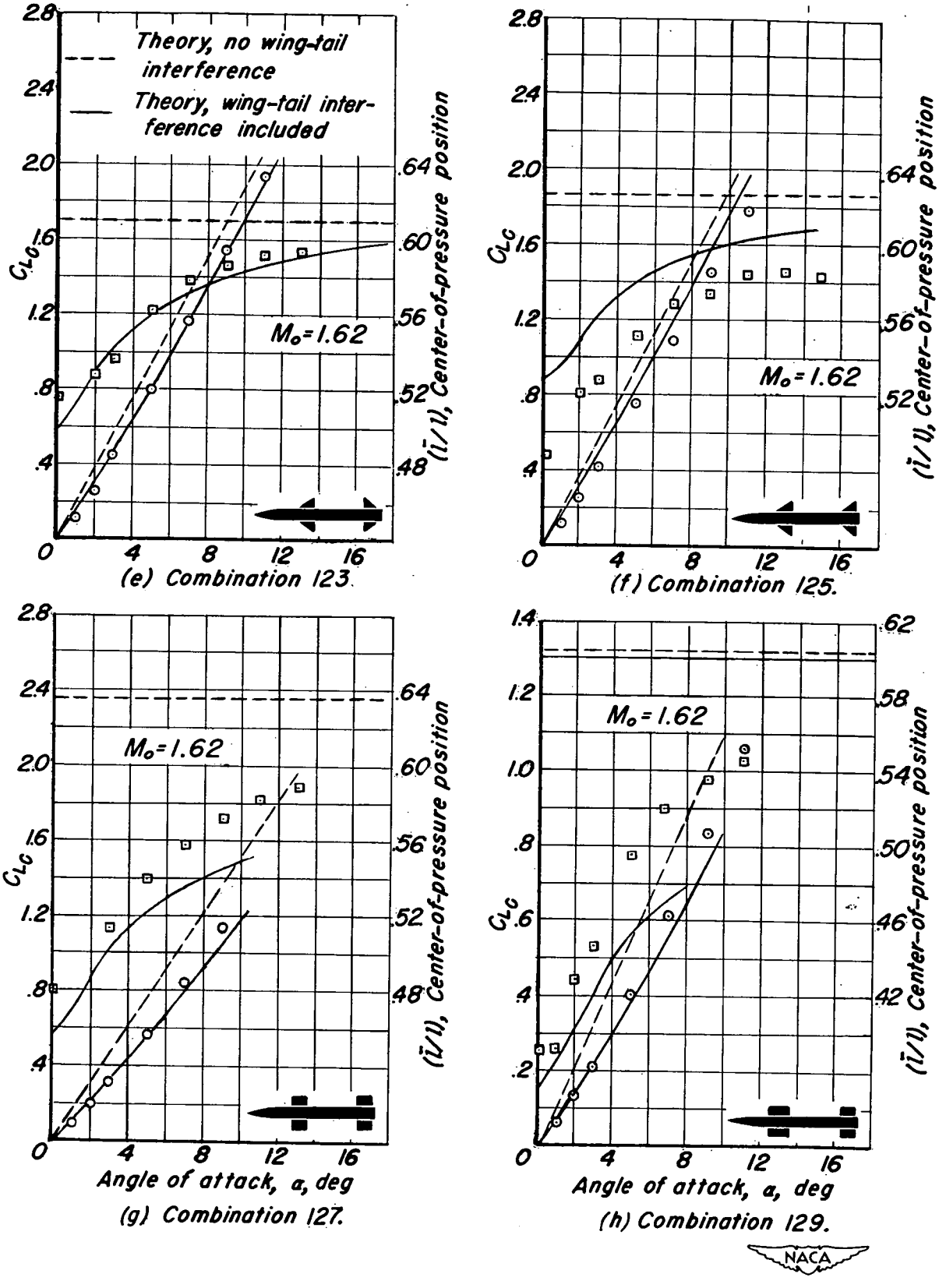

Figure 29.- Continued.

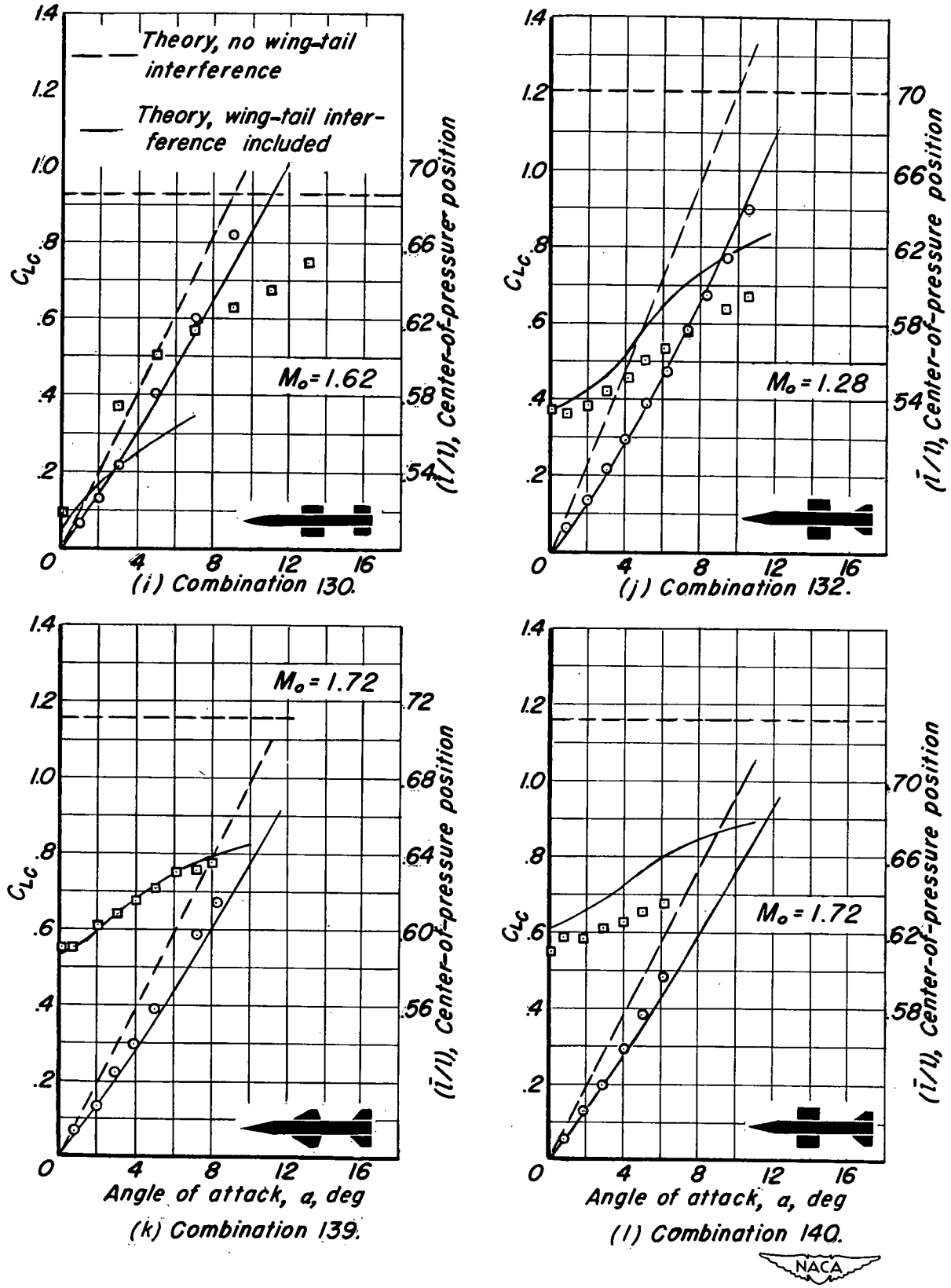

Figure 29.- Concluded.

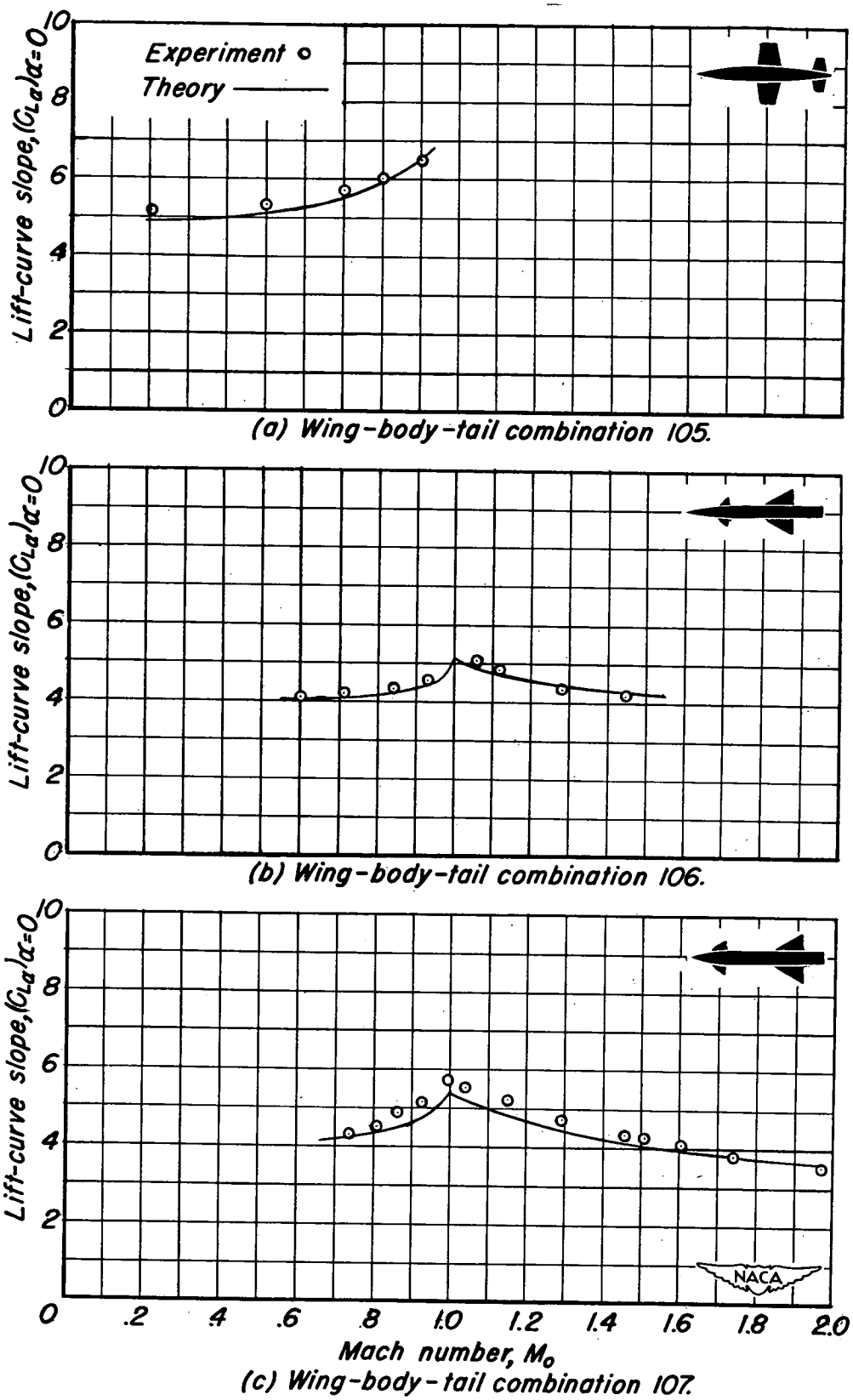

Figure 30. —Variation with Mach number of lift-curve slope or lift coefficient of wing-body-tail combinations.

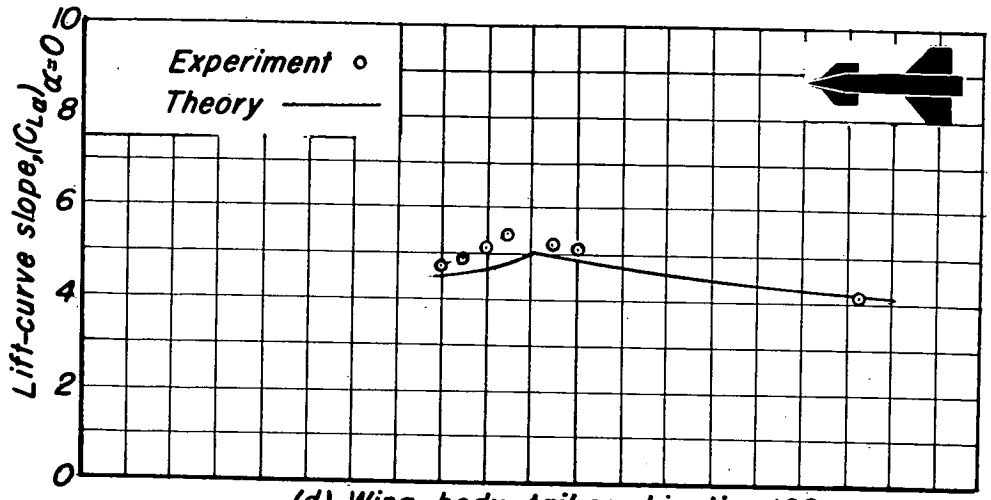

(d) Wing-body-tail combination 108.

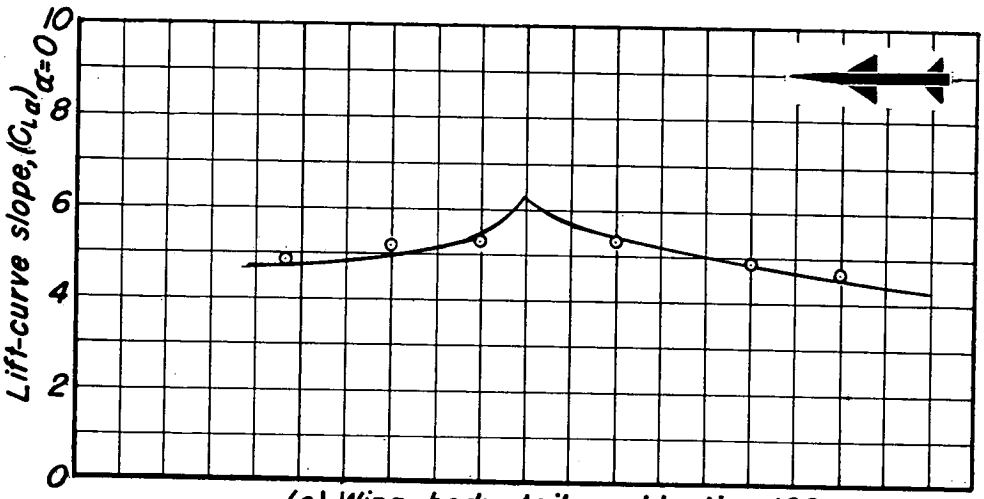

(e) Wing-body-tail combination 109.

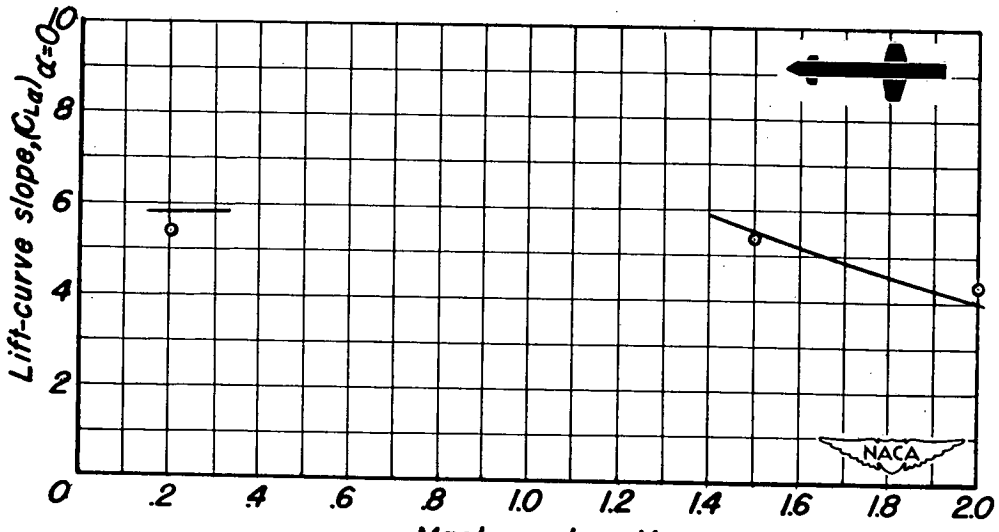

(f) Wing-body-tail combination 110.

Figure 30. - Continued.

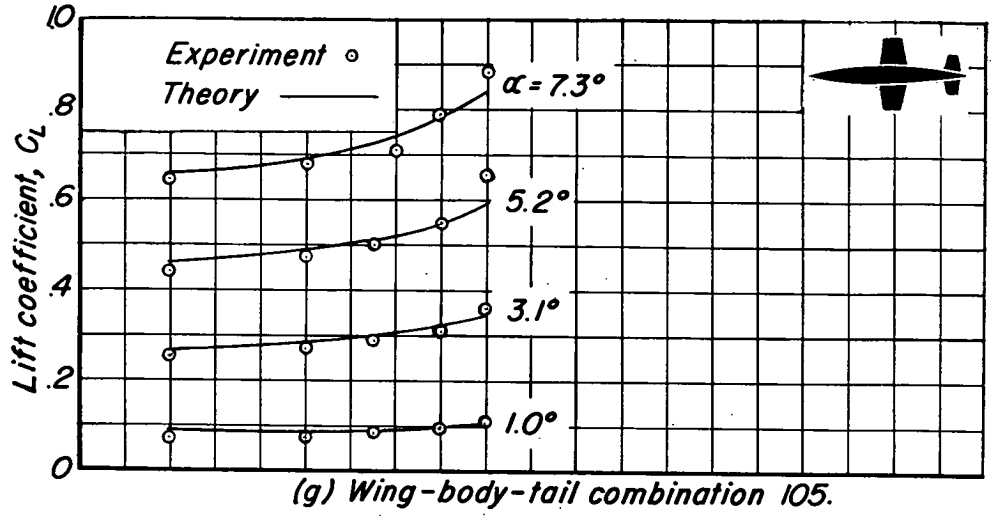

(g) Wing-body-tail combination 105.

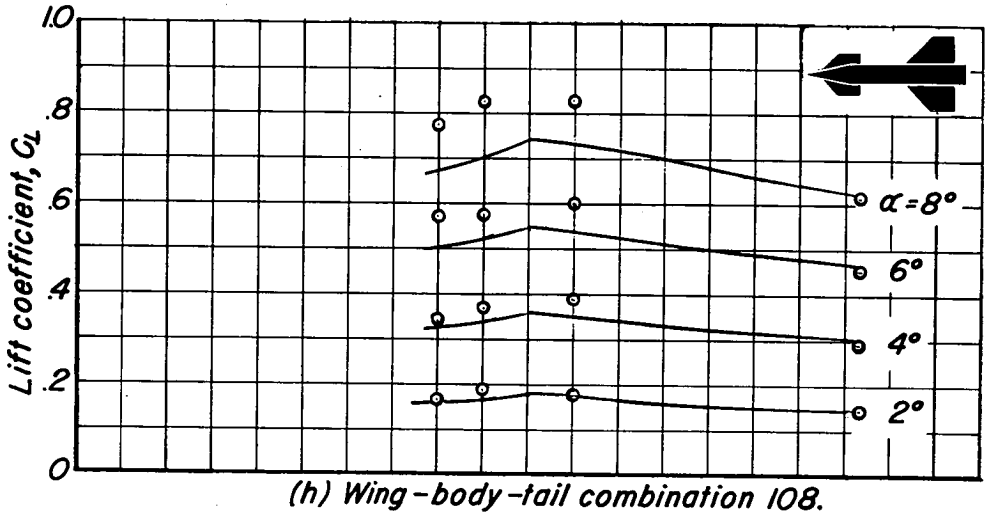

(h) Wing-body-tail combination 108.

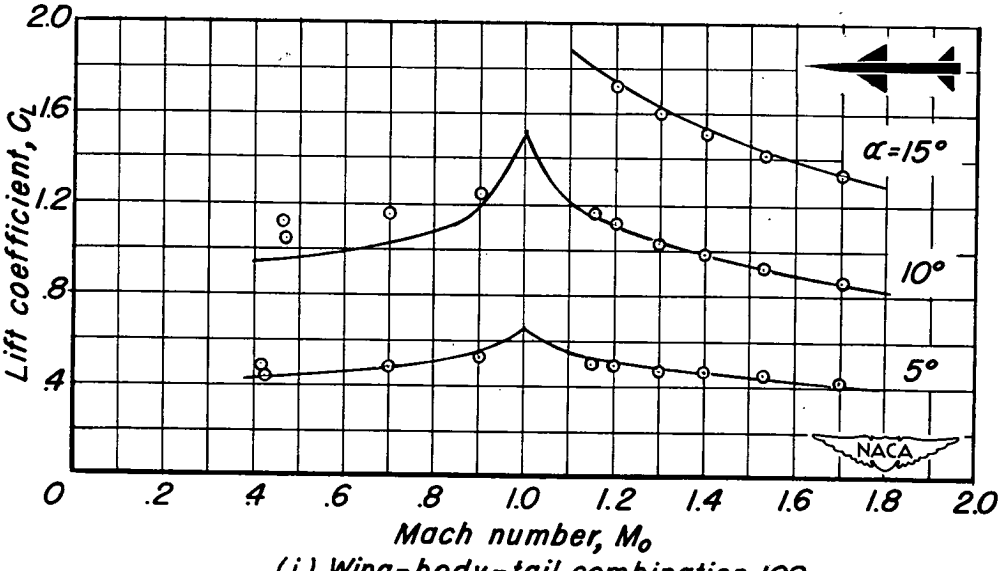

(i) Wing-body-tail combination 109.

Figure 30. —Continued.

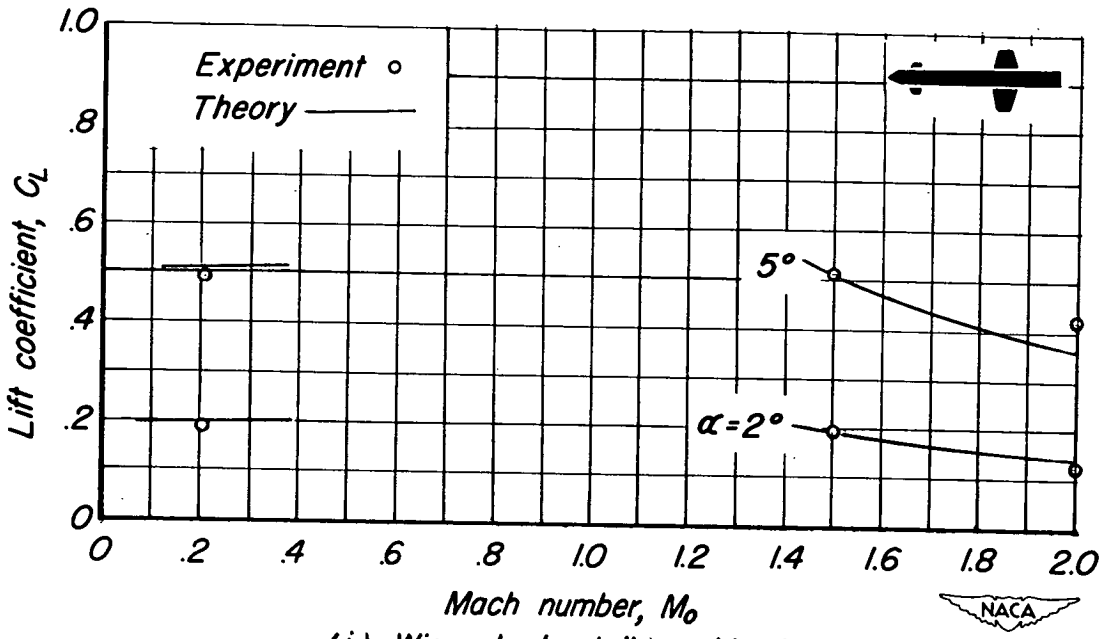

(j) Wing – body – tail combination 110.

Figure 30.- Concluded.

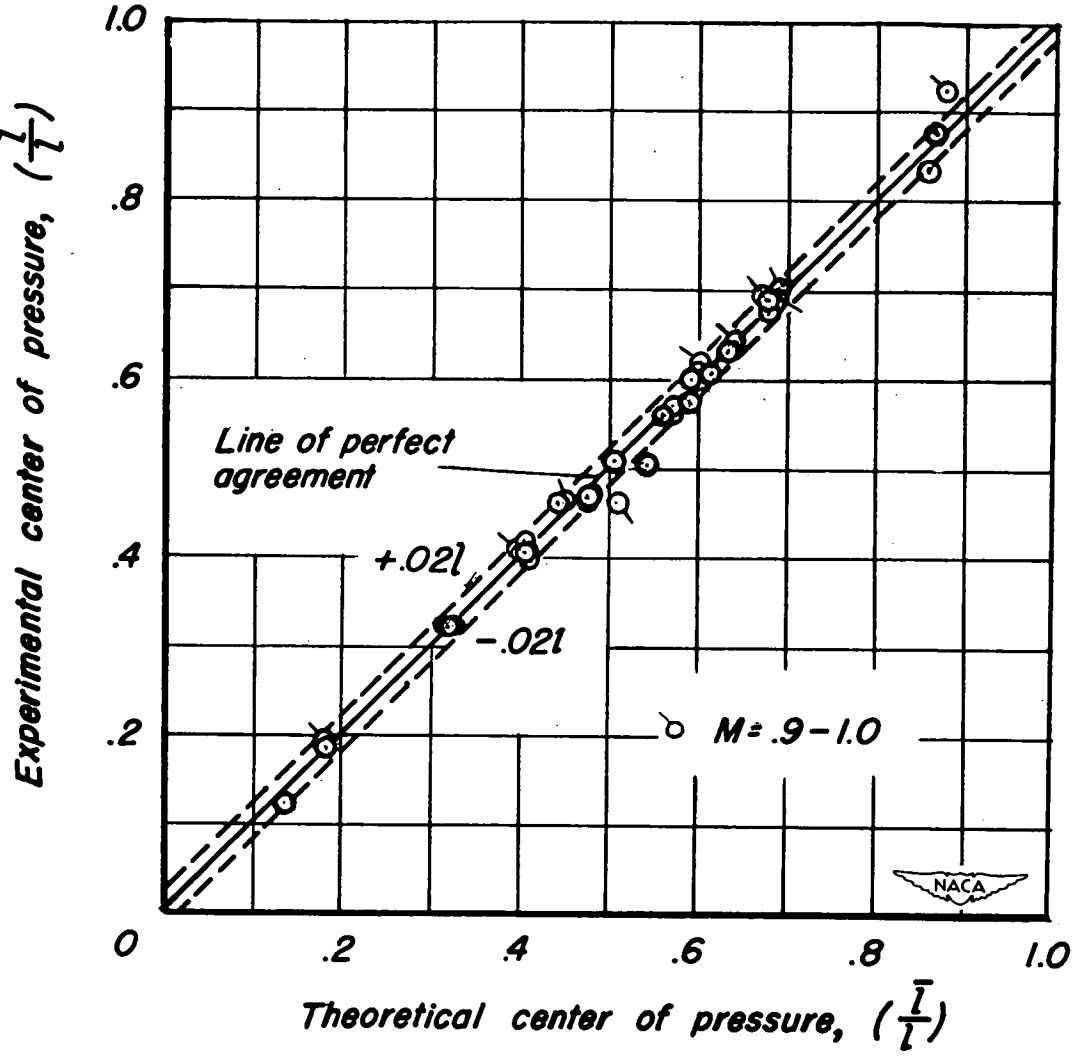

Figure 31.—Correlation between experimental and estimated centers of pressure for subsonic wing–body combinations.

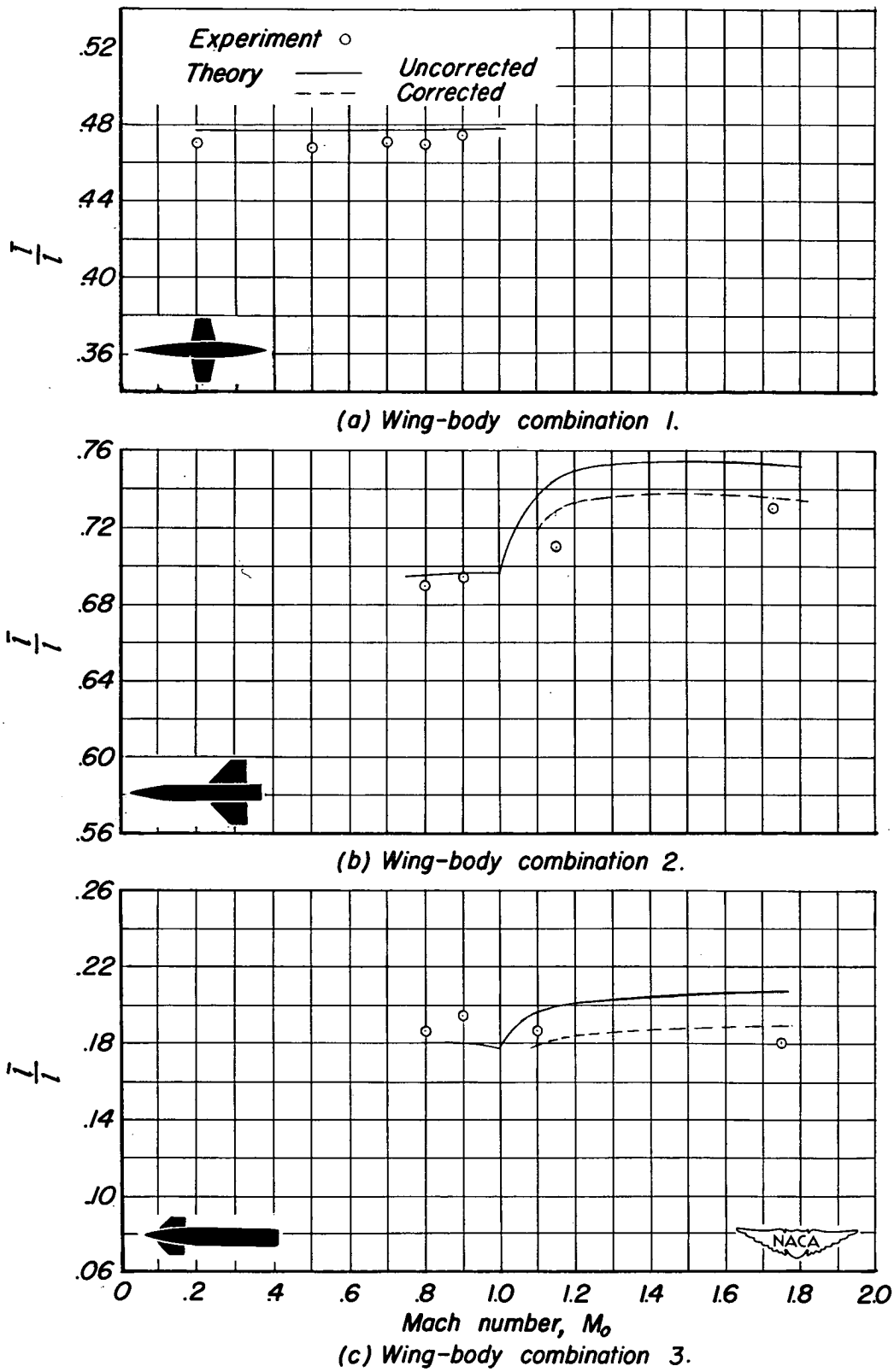

Figure 32.—Variation with Mach number of center-of-pressure positions for wing-body combinations.

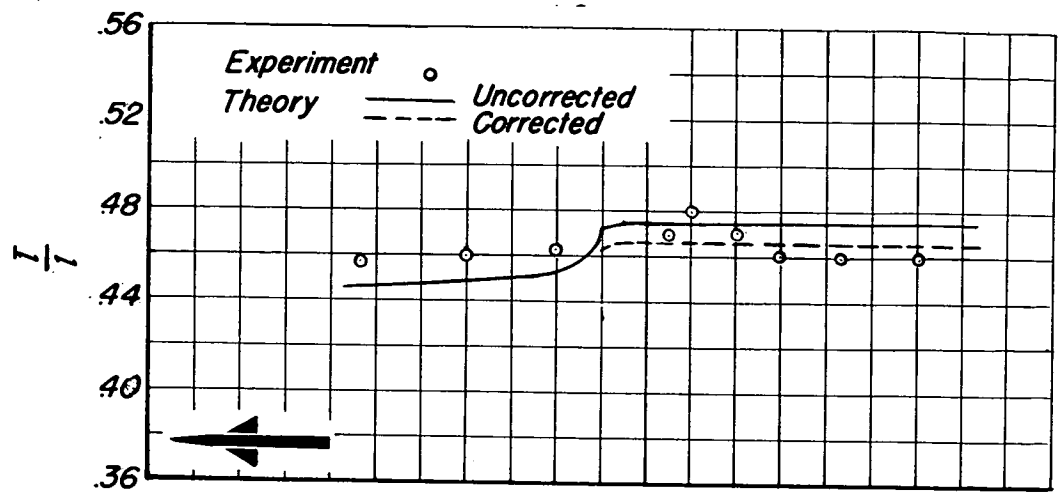

(d) Wing-body combination 4.

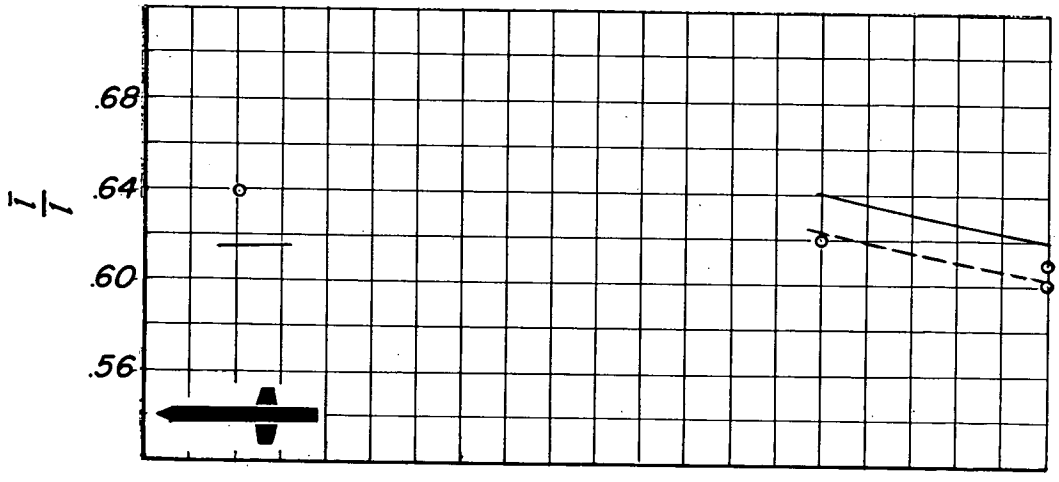

(e) Wing-body combination 7.

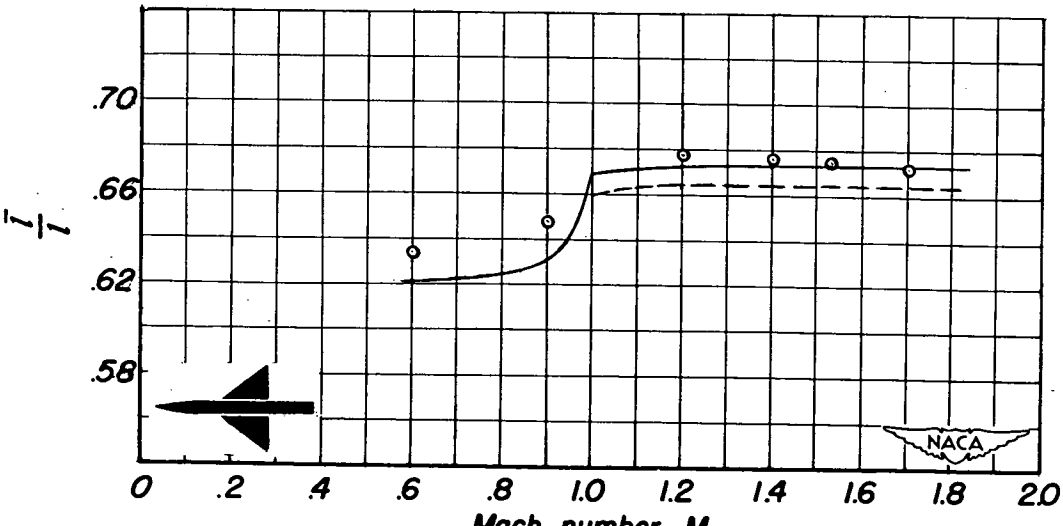

(f) Wing-body combination 8.

Figure 32. – Continued.

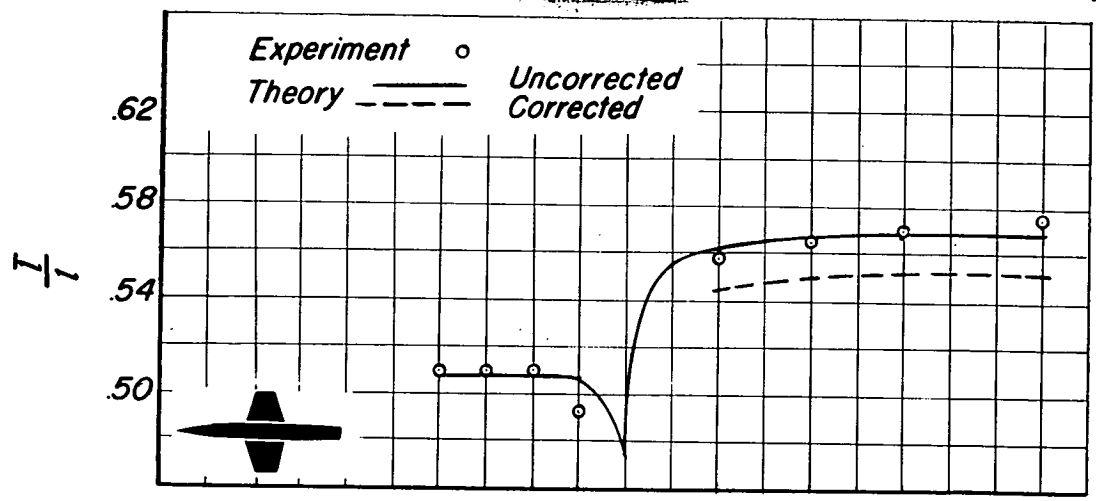

(g) Wing-body combination 9.

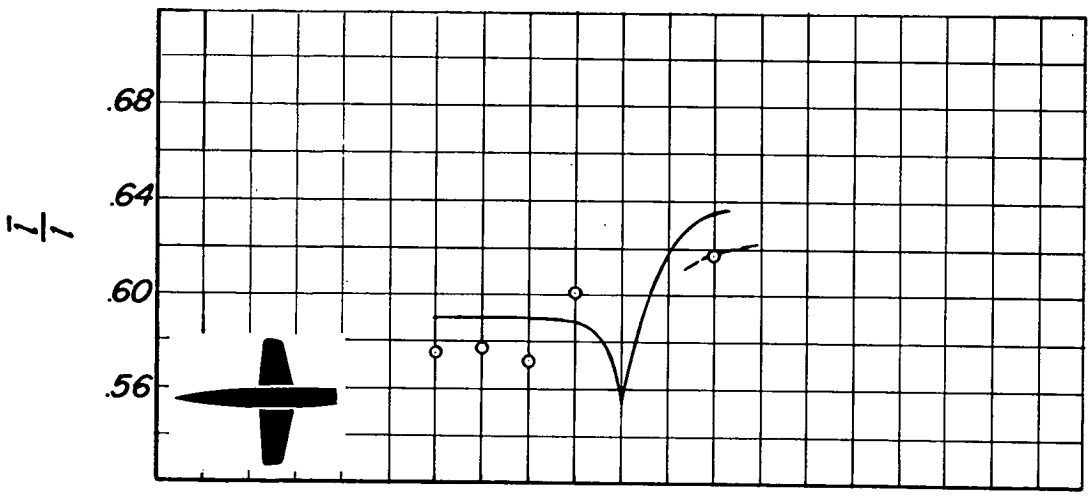

(h) Wing-body combination 10.

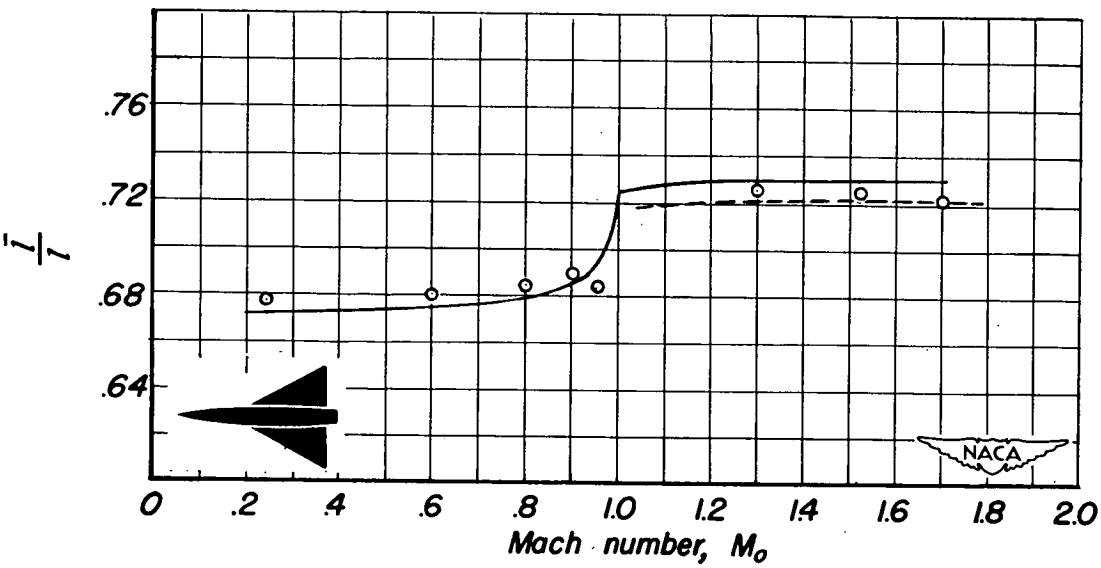

(i) Wing-body combination 11.

Figure 32.—Continued.

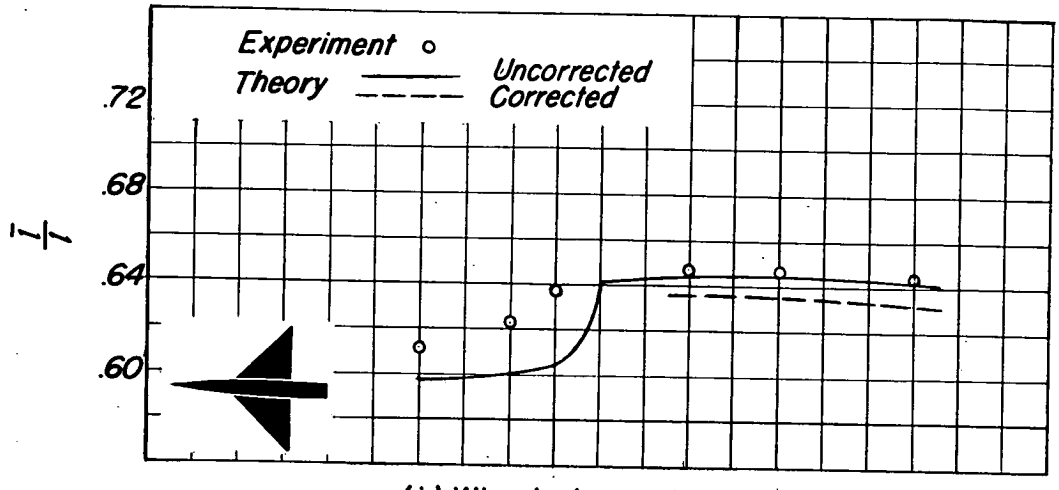

(j) Wing-body combination 12.

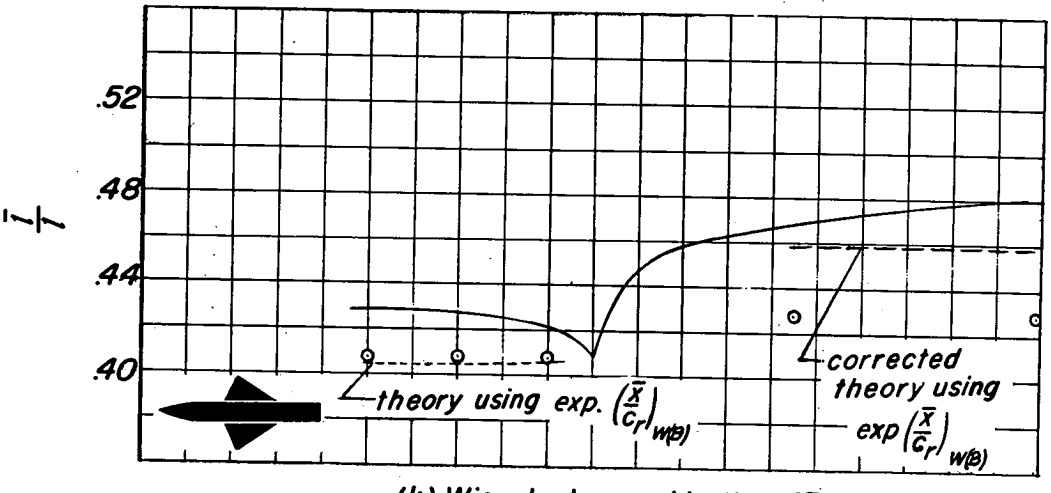

(k) Wing-body combination 13.

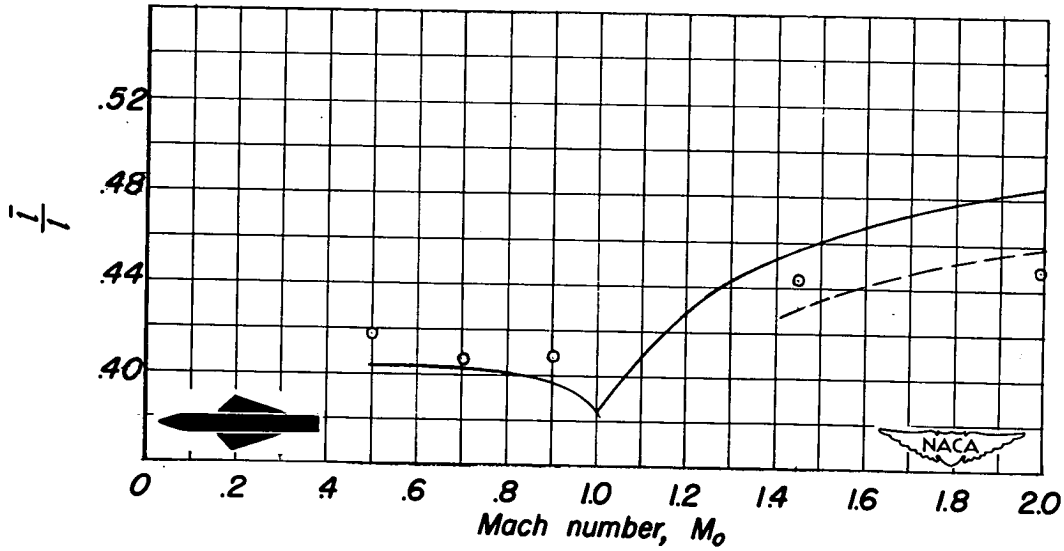

(l) Wing-body combination 14.

Figure 32.—Concluded.

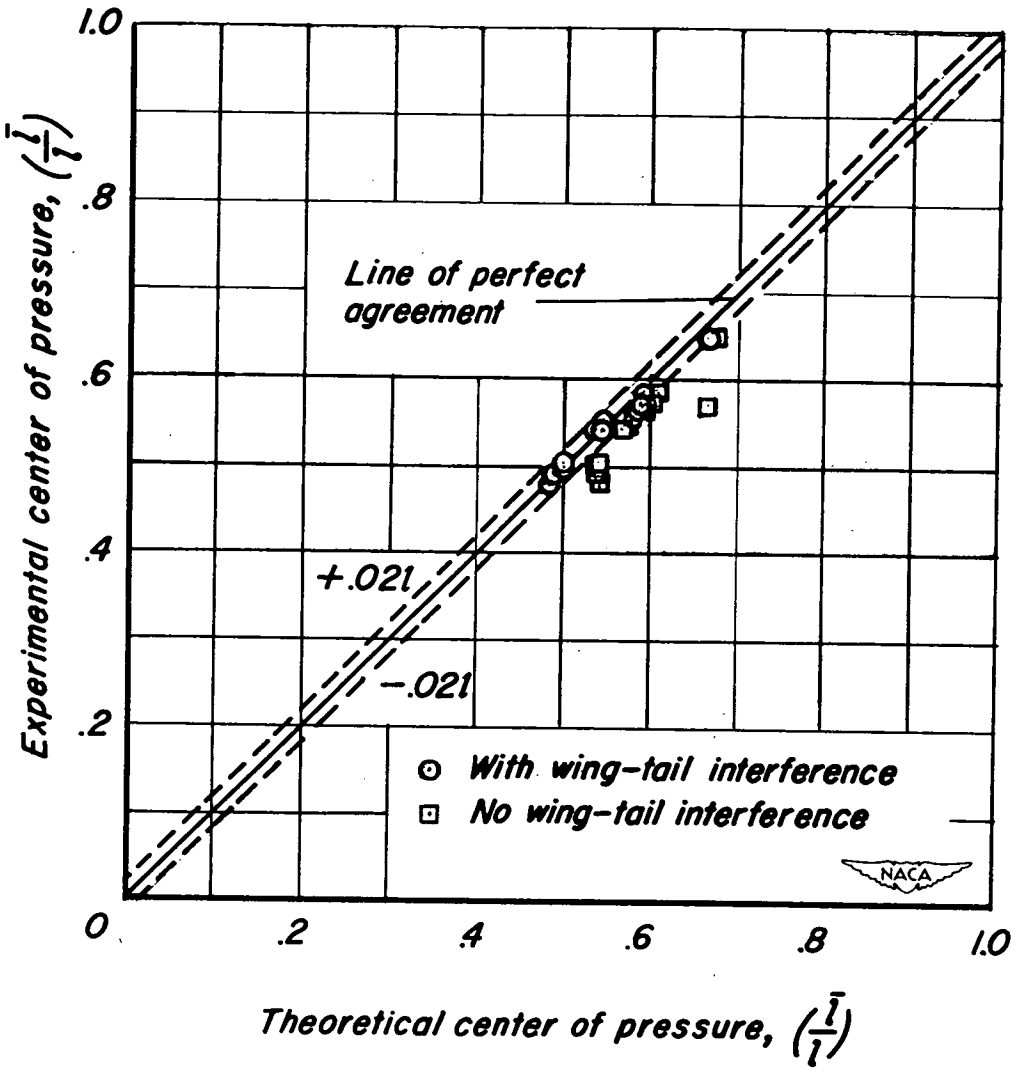

Figure 33.– Correlation between experimental and estimated centers of pressure for subsonic wing-body-tail combinations at $\alpha = 0$.

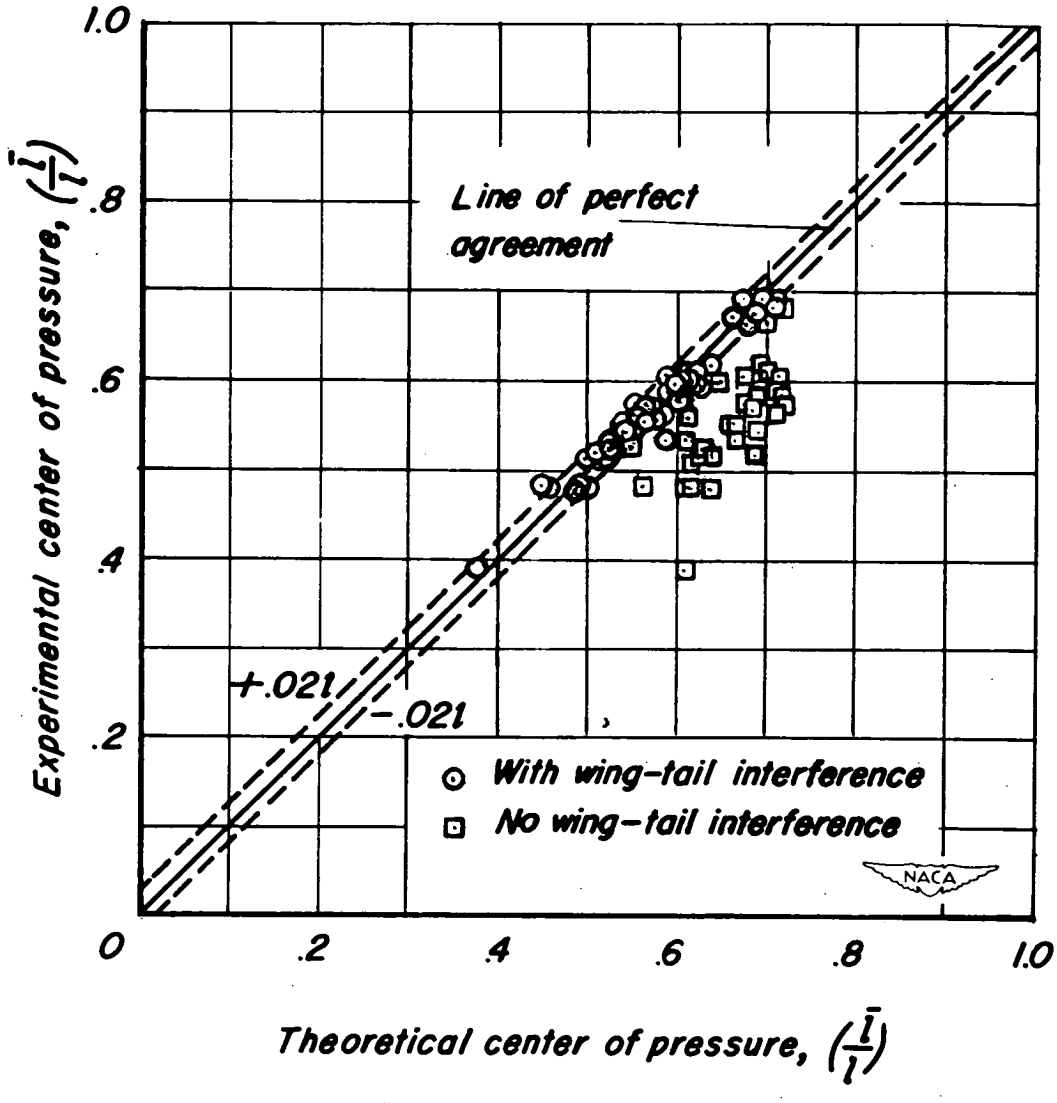

Figure 34.- Correlation between experimental and estimated centers of pressure for supersonic wing-body-tail combinations at $\alpha=0$.

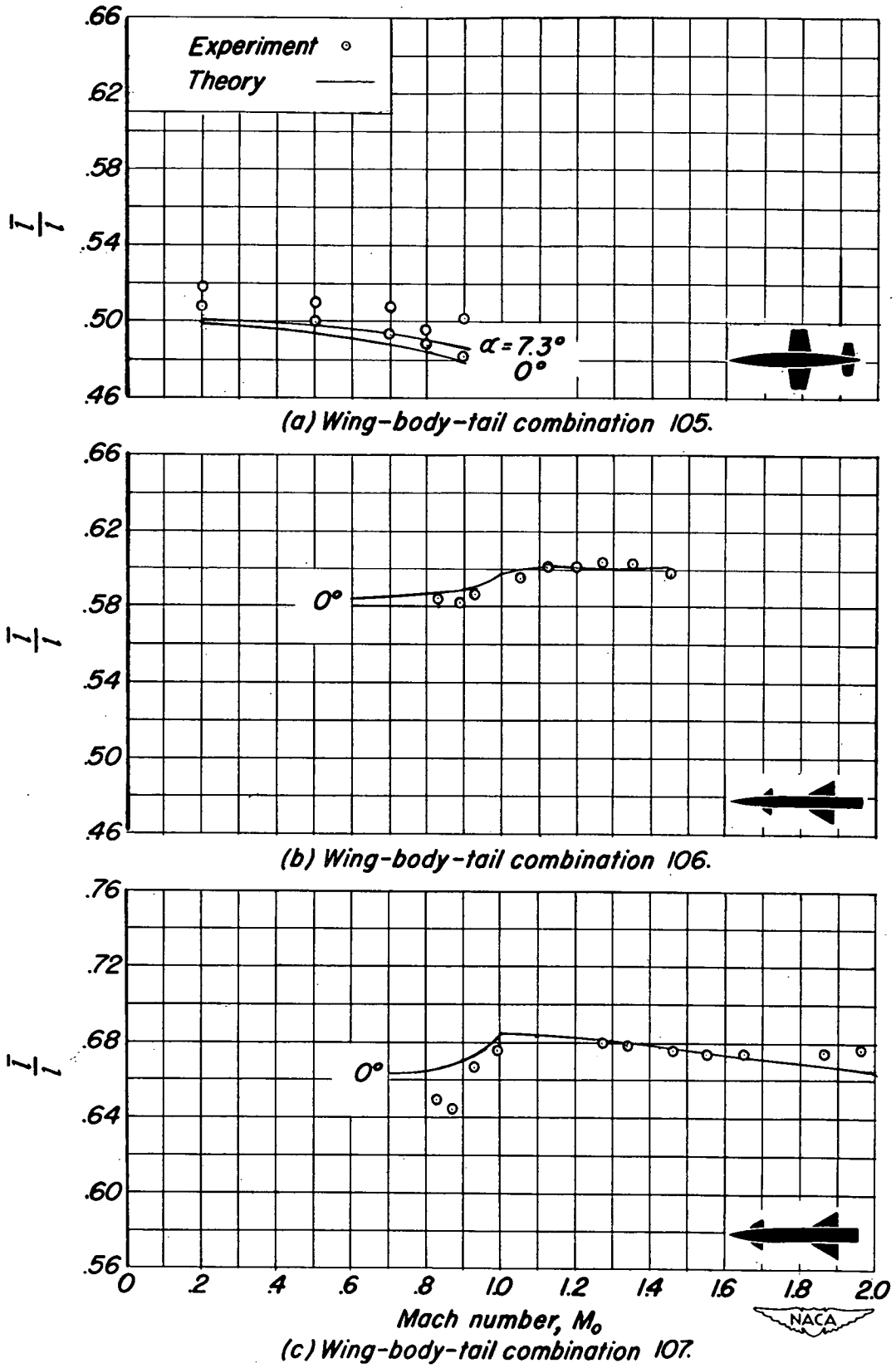

(a) Wing-body-tail combination 105.

(b) Wing-body-tail combination 106.

(c) Wing-body-tail combination 107.

Figure 35.- Variation with Mach number of center-of-pressure location of wing-body-tail combinations.

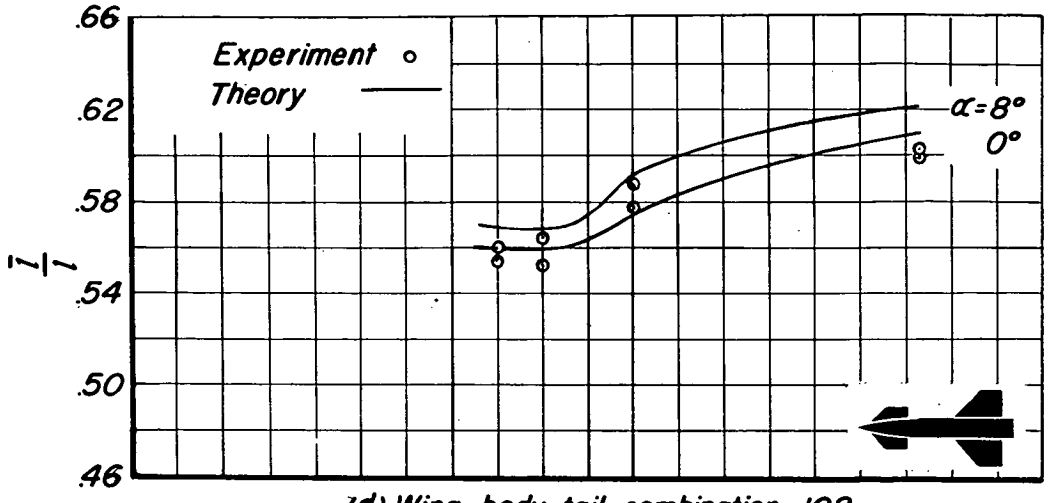

(d) Wing-body-tail combination 108.

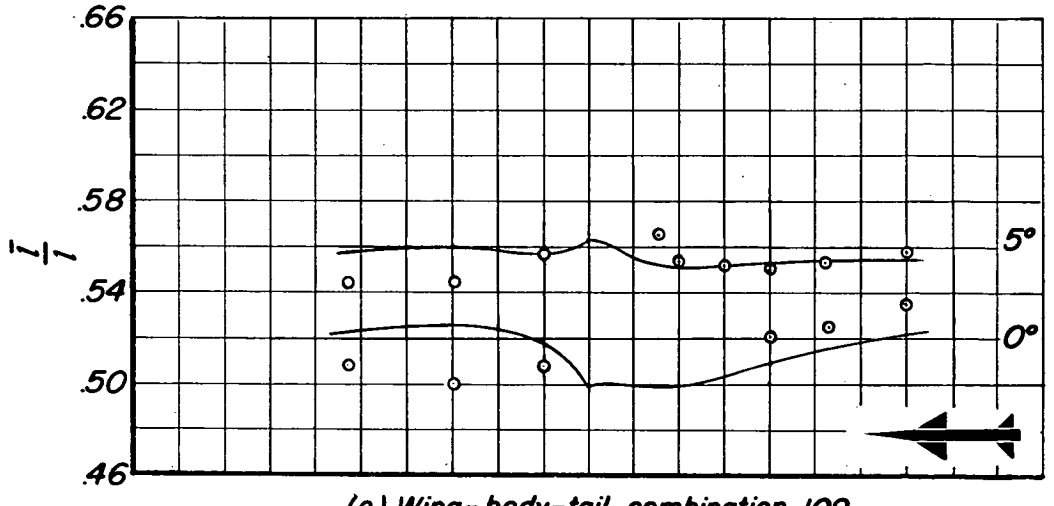

(e) Wing-body-tail combination 109.

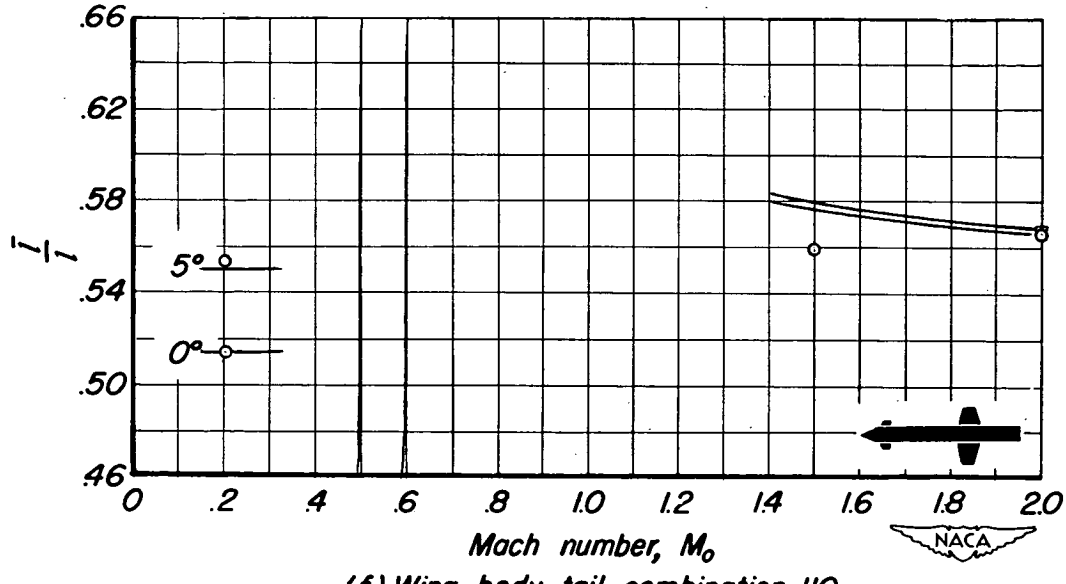

(f) Wing-body-tail combination 110.

Figure 35.—Concluded.

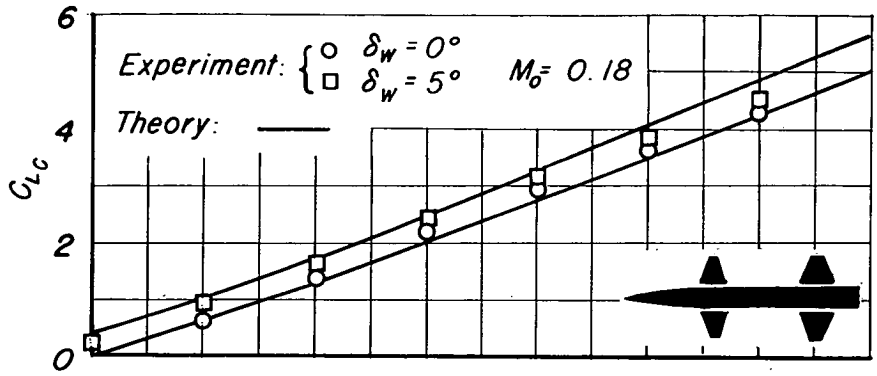

(a) Lift.

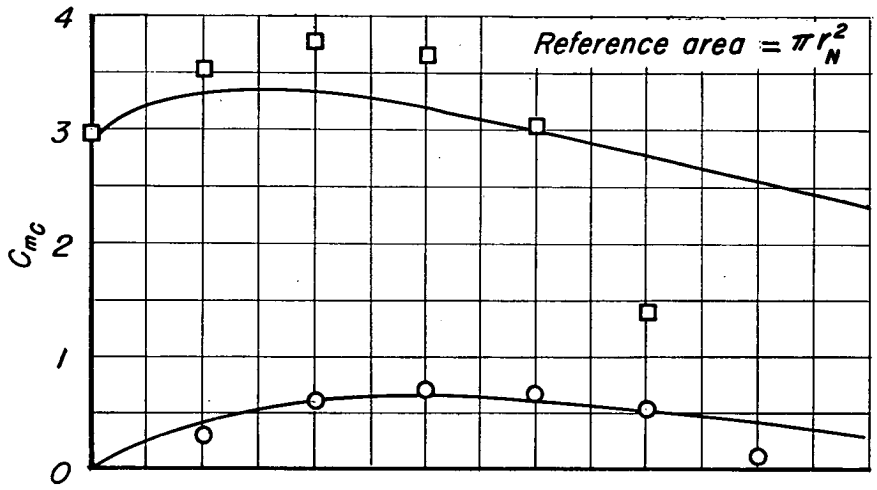

(b) Moment.

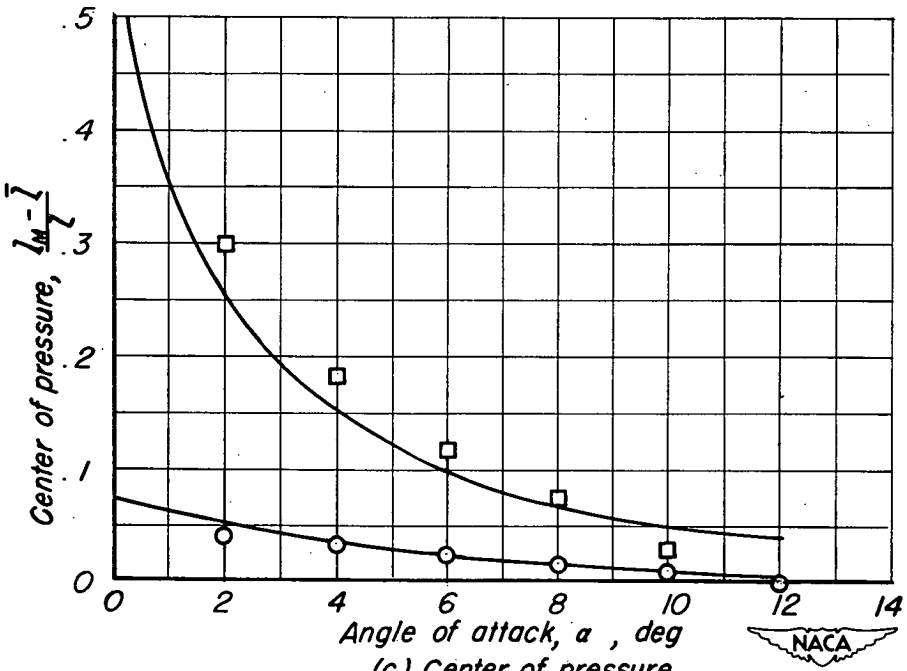

(c) Center of pressure.

Figure 36.- Comparison between estimated and experimental effects of wing incidence for combination 101.

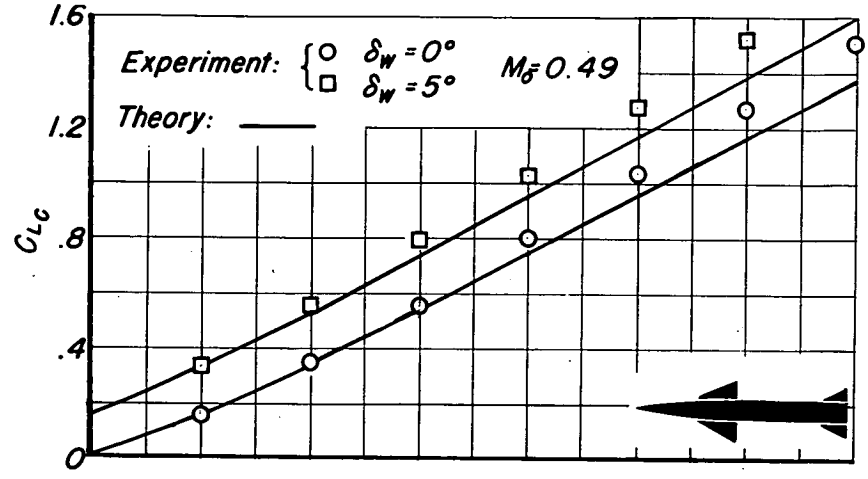

(a) Lift

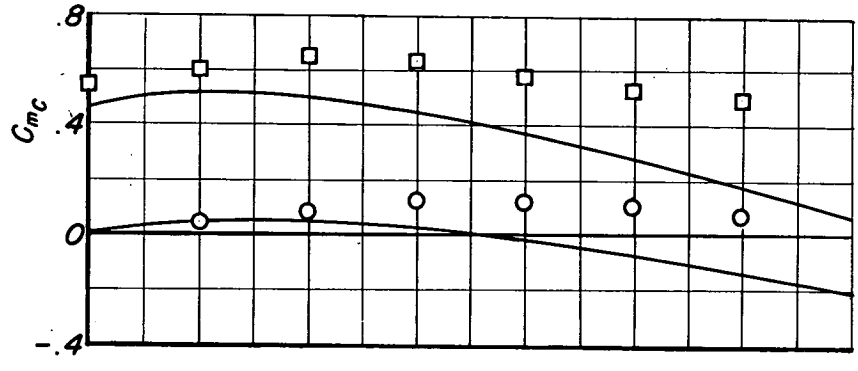

(b) Moment

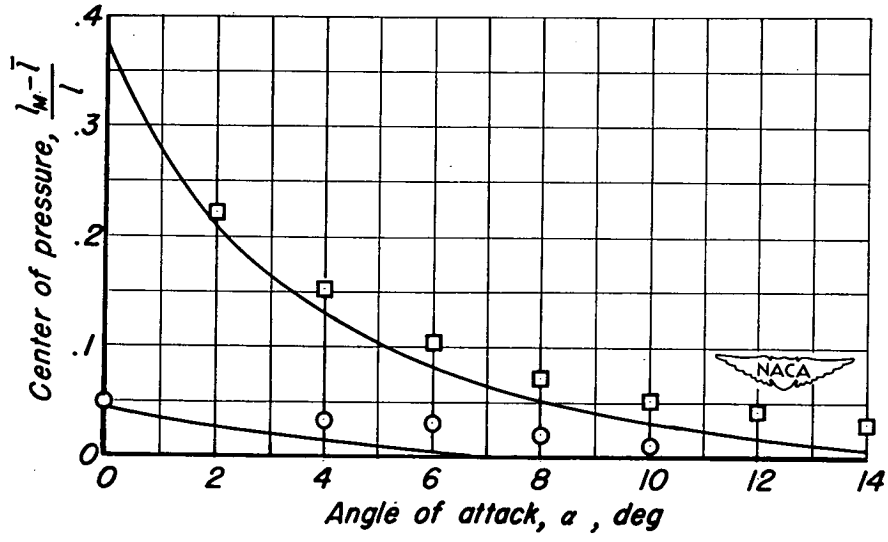

(c) Center of pressure.

Figure 37. – Comparison between estimated and experimental effects of wing incidence for combination 143.

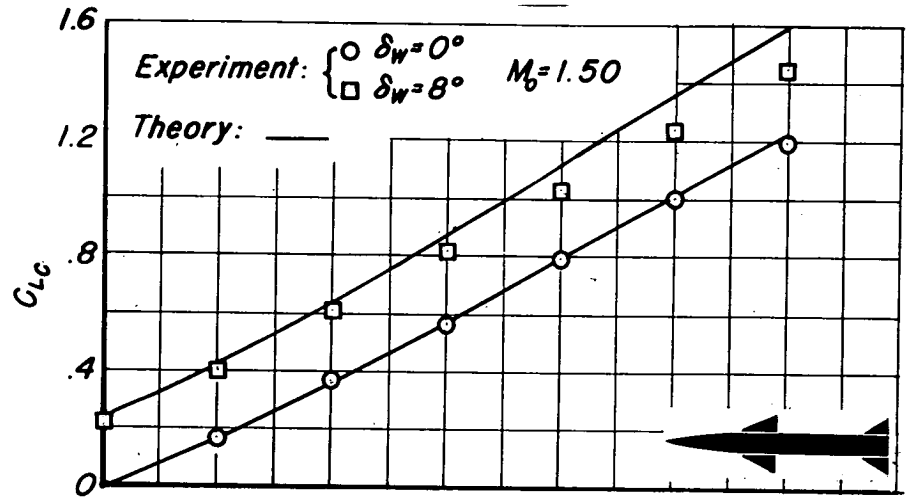

(a) Lift

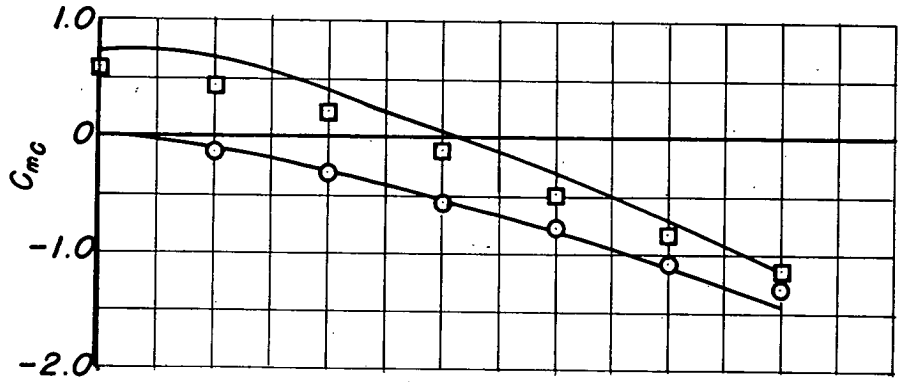

(b) Moment

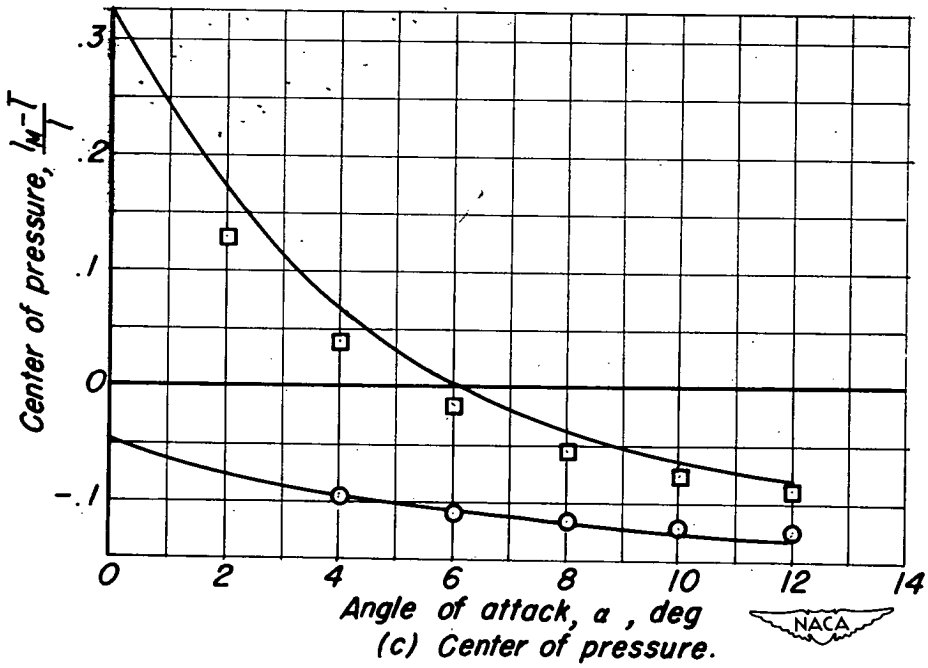

(c) Center of pressure.

Figure 38.— Comparison of estimated and experimental effects of wing incidence for combination 144.

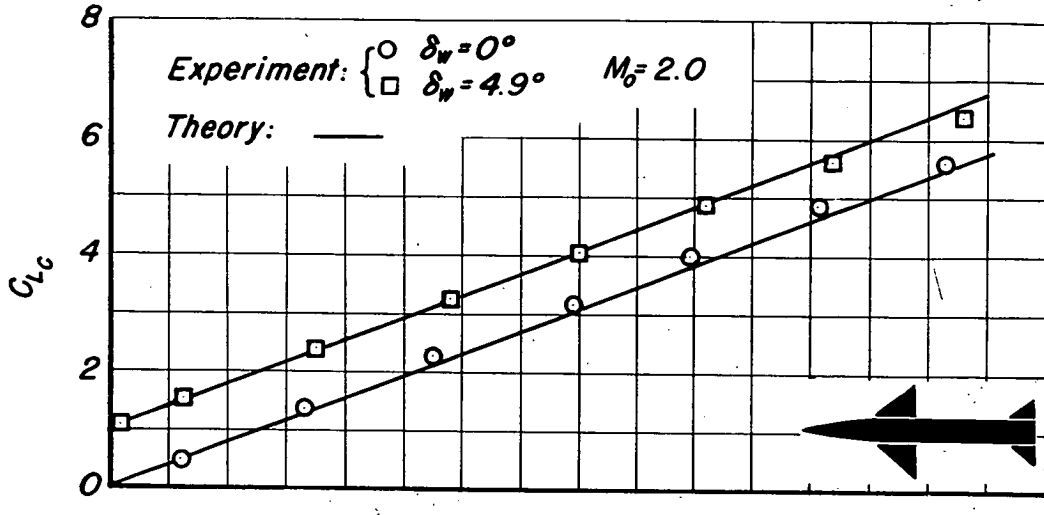

(a) Lift

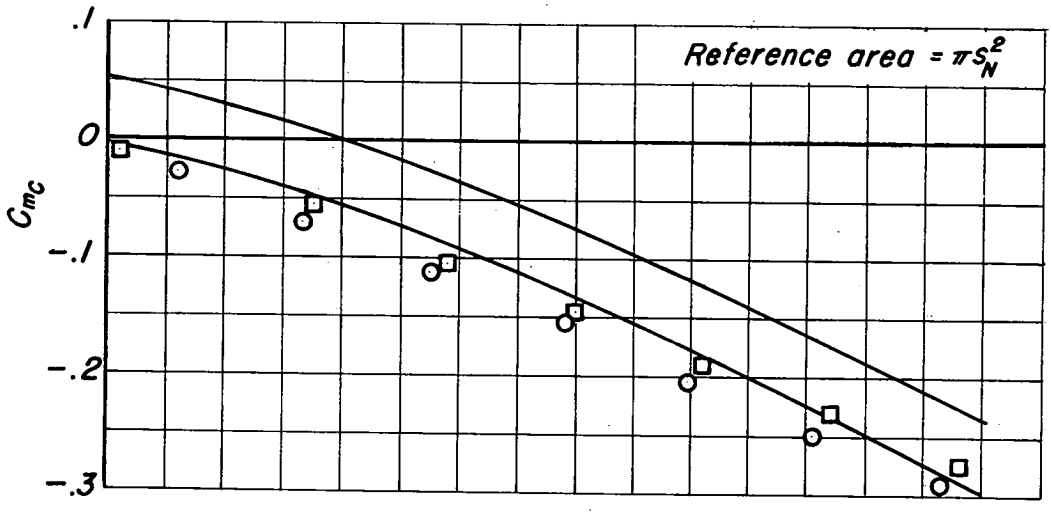

(b) Moment

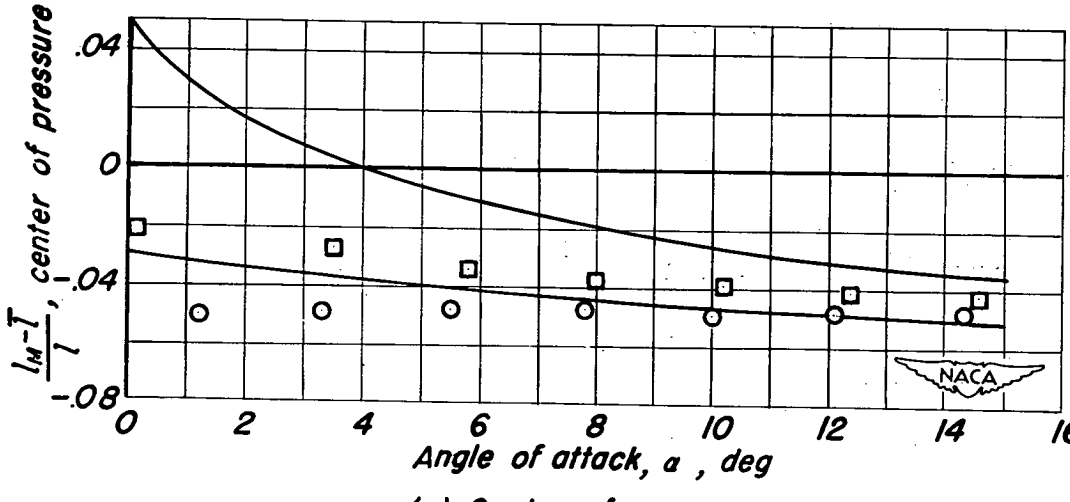

(c) Center of pressure

Figure 39.- Comparison between estimated and experimental effects of wing incidence for combination 145.

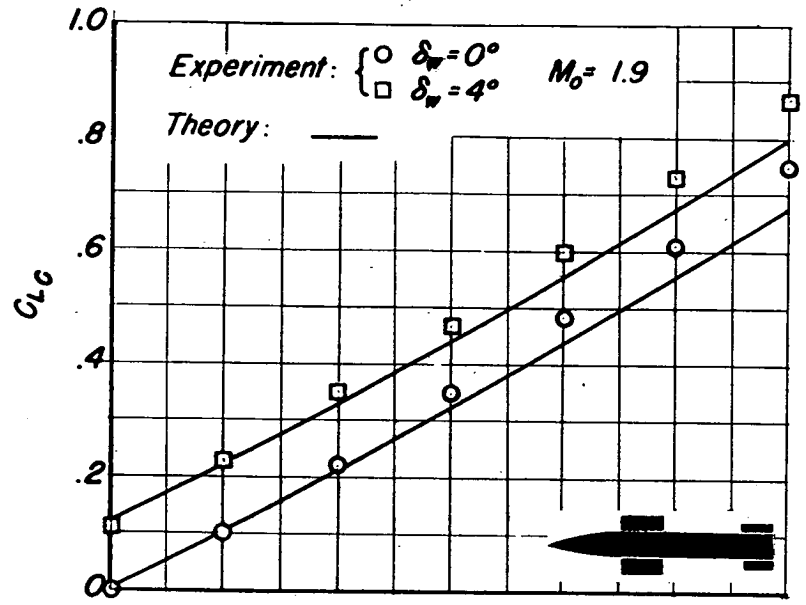

(a) Lift

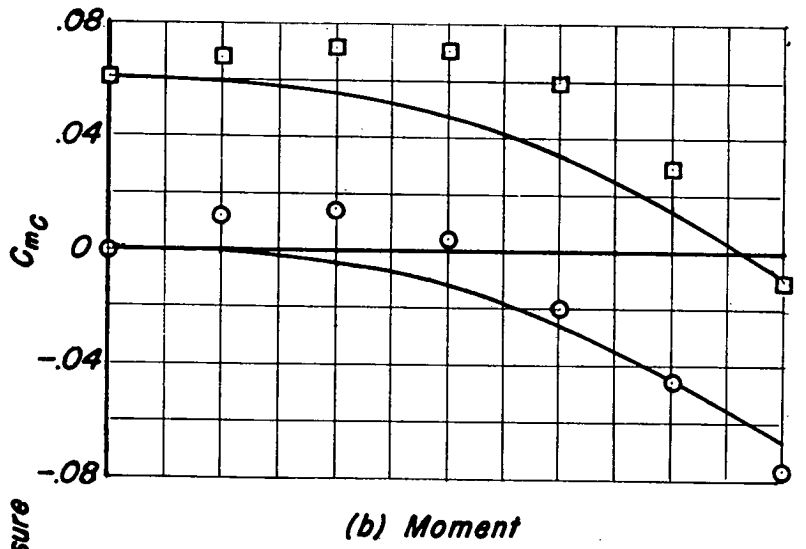

(b) Moment

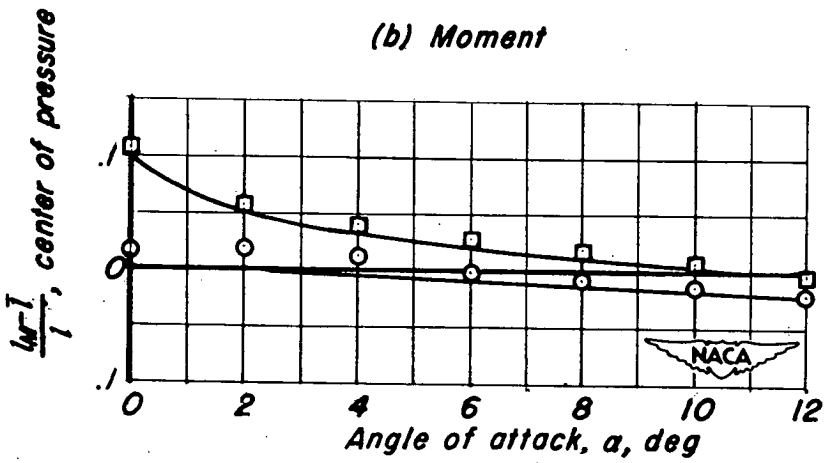

Angle of attack, α, deg

(c) Center of pressure.

Figure 40.- Comparison between estimated and experimental effects of wing incidence for combination 146.

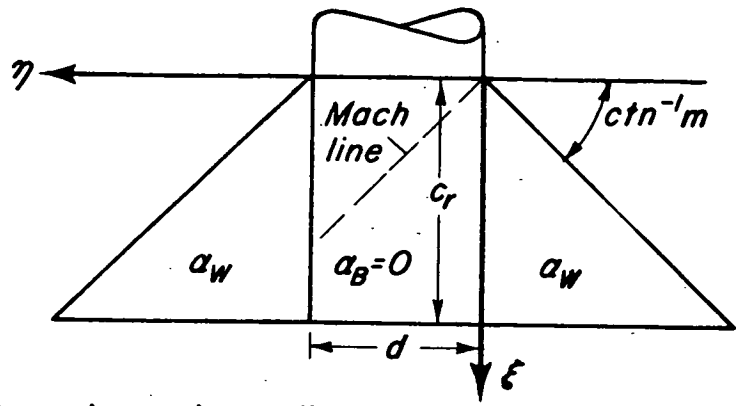

Figure 41.– Geometry and coordinate system used to obtain $K_{B(W)}$ and $K_{B(T)}$ for no afterbody.

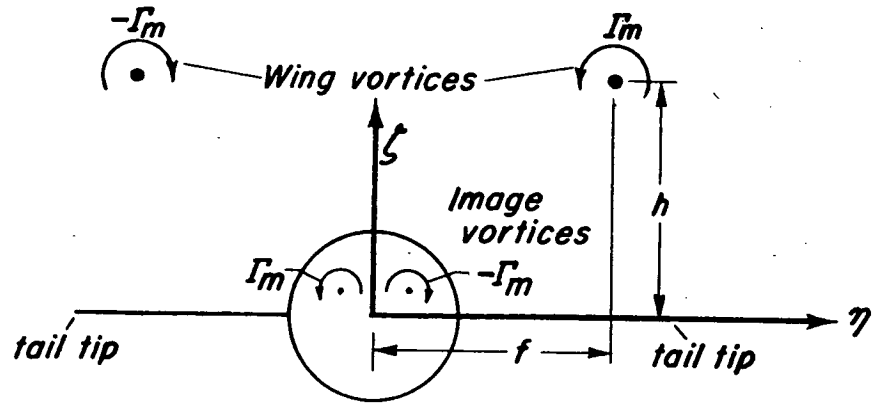

(a) Wing vortices in cross-flow plane of tail.

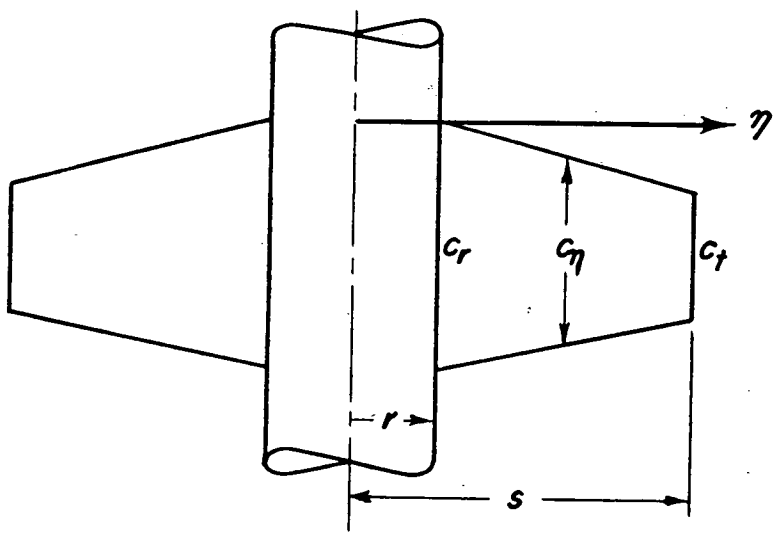

(b) Tail plan form dimensions.

Figure 42.– Model and dimensions for determination of tail interference factor by strip theory.

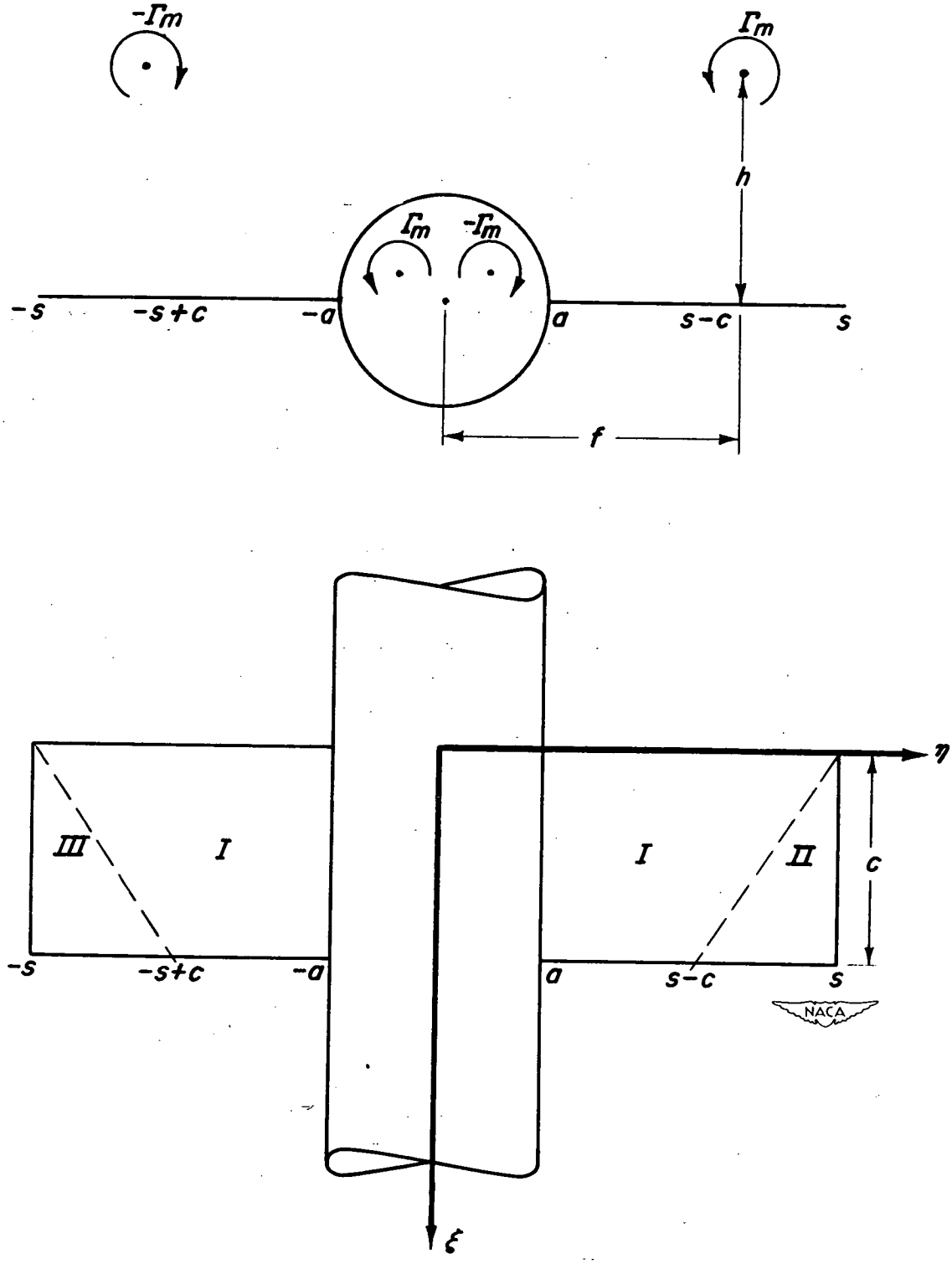

Figure 43.–Geometry of model used for determining tail interference factor for rectangular tail by Alden-Schindel technique.

NACA-Langley - 11-12-53 - 325